A synthetic lipid scramblase built from DNA

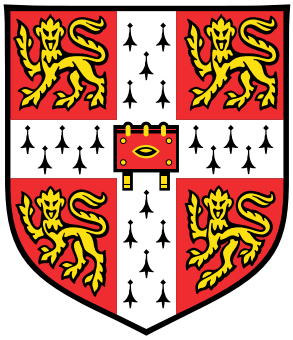

Alexander Ohmann

Department of Physics
University of Cambridge

This dissertation is submitted for the degree of
Doctor of Philosophy

Trinity Hall August 2019

Declaration

This dissertation is the result of my own work and includes nothing which is the outcome of work done in collaboration except as specified in the text. It is not substantially the same as any that I have submitted, or, is being concurrently submitted for a degree or diploma or other qualification at the University of Cambridge or any other University or similar institution except as specified in the text. I further state that no substantial part of my thesis has already been submitted, or, is being concurrently submitted for any such degree, diploma or other qualification at the University of Cambridge or any other University or similar institution except as specified in the text. This thesis does not exceed the word limit of 60,000 words set by the Physics and Chemistry Degree Committee, including abstract, tables, footnotes and appendices.

Alexander Ohmann
August 2019

A synthetic lipid scramblase built from DNA

Alexander Ohmann

Abstract

The programmable self-assembly facilitated by DNA nanotechnology provides unparalleled capabilities to construct functional devices at the nanoscale. Recently, DNA nanostructures have been developed to interact with biological membranes and serve as artificial counterparts of natural ion channels, or membrane bending, scaffolding, or fusion proteins. In this thesis, we design a synthetic DNA-built enzyme that facilitates rapid lipid mixing between the two leaflets of a lipid bilayer. It thereby mimics the function of yet another class of membrane proteins – lipid scramblases. Characterising this DNA nanostructure with gel electrophoresis, dynamic light scattering, atomic force and transmission electron microscopy, we find that the cholesterol groups required for membrane insertion, also induce clustering. Hence, we establish an easy-to-implement strategy to control hydrophobically mediated aggregation thereby introducing a solution to a common problem of amphiphilic DNA constructs. With a combination of fluorescence microscopy experiments and molecular dynamics simulations, we identify the mechanism behind the scrambling activity. The spontaneous membrane insertion of our DNA scramblase induces a toroidal pore that is lined by the lipid headgroups. This DNA-stabilised pore connects the inner and outer bilayer leaflet thereby facilitating diffusive lipid transport that rapidly equilibrates the membrane's lipid composition. In good agreement between experiments and simulations, we find the scrambling rate catalysed by our DNA-made enzyme to exceed 10^7 lipids per second, orders of magnitude faster than natural scramblase proteins. We thereby pioneer the use of self-assembled DNA nanostructures for controlling the lipid composition of biological membranes, opening new avenues for applications of membrane-interacting DNA systems in biophysical research and medicine.

Für meine liebe Familie
und meine liebste Itzy

Acknowledgements

My time in Cambridge would not have been as enjoyable without the presence and support of numerous people in my life. The ones mentioned here only account for a small part of those who accompanied me on my journey of obtaining my PhD.

First of all, I wish to thank my supervisor Prof. Ulrich F. Keyser for always being approachable and having steered this PhD work into the most successful direction. Despite my resistance, I valued his efforts in trying to teach me that sometimes 'good enough' is really good enough. He has a talent for spotting where students still lack experience and seeks to support them to develop it, making a PhD what it is supposed to be – a learning experience. I am very thankful for his mentorship and for always providing me with support and opportunities to develop my career further.

The insights gained in this thesis would not have been possible without the help of numerous colleagues and collaborators. Particularly, I want to thank Prof. Aleksei Aksimentiev from the University of Illinois at Urbana-Champaign and his group members Christopher Maffeo, Chen-Yu Li, Jejoong Yoo, and Himanshu Joshi. Our ongoing collaboration was key in understanding many fundamental aspects of this work and yielded many interesting results. And Christopher Maffeo's atomistic representation of our DNA scramblase provides a beautiful eye catcher at the end of this thesis. I am also thankful to Rebecca F. Thompson and Prof. Neil A. Ranson from the University of Leeds as they helped me to 'see' my DNA nanostructures for the first time.

I want to particularly thank every member of the Keyser group – past and present – as they were all an integral part of my PhD experience. I am thankful to Karolis Misiunas for entertaining conversations about watches but also insightful discussions about science and for taking me in when I was briefly homeless; Silvia Hernández-Ainsa for introducing me to various assays in the beginning of my PhD; Maria Ricci for beautiful AFM images; Kevin Baumann for keeping the cells alive; Queeny van der Spek for not giving up on the current measurements and succeeding in the end; Michael Schaich for frequently bringing

the group together for social events (at least whenever he is in his ‘optimistic Michael’ state); Niklas Ermann and Jehangir Cama for exciting foosball matches; Kaikai Chen for never letting anyone work alone late at the office; Diana Sobota for successfully continuing the work with synthetic DNA scramblases as well as proof-reading parts of this thesis, along with Nikki Weckman and Jinbo Zhu; and finally my office mates: Kareem Al Nahas (who mastered the Dark Arts of vesicle formation), Jannes Gladrow (who mastered the Dark Arts in general), Soichiro Tottori and our latest addition Filip Bošković, who all had to bear with me during the writing process. I am particularly thankful for the cooperative and supportive atmosphere in our group which made this PhD experience much more enjoyable and many of the obtained results even possible.

I am especially thankful to Kerstin Göpfrich. Her enthusiastic talk at a DPG meeting in Dresden got me in touch with Ulrich which ultimately brought me to Cambridge. She received me on my first day at the Cavendish Laboratory, helped me on my last day before handing in this thesis with final corrections, and gave me advice that guided my next steps afterwards. Her cheerful spirit and passion for discovering and spreading new knowledge was always inspiring.

Also outside the group, I am thankful for having made new friendships that will hopefully last beyond my time in Cambridge. My roommates Mia Kim, Huw Batts, Stine Ravnå and Gudlaug Jonasdottir when we lived in College at Wychfield and fought the squirrel together. And Sascha Feldmann for many fun hours at work and the gym, and for holding everything together at home when I did not have the time.

Foremost, I am grateful for the constant source of support from my family which is a fundamental cornerstone in my life. My brother Robin, who always took the first step making it easier for me to follow, and who made me, together with his wife Sylvie, an uncle of three during my PhD. And my parents, Marion and Wolfgang, who provided me with the opportunities and the support to explore the world, yet roots to always come back home to. It was incredibly calming to know that I could always count on them. Vielen Dank für alles.

Finally, I want to thank my suegris, Ana Bertha†, and my suegro, Carlos, who welcomed me with open arms into the family and always made me feel at home in Mexico. And of course, my Itzy, who stood by my side during the whole time of this PhD and became my fiancée towards the end of it. Whenever I need it, she is always there to put everything into perspective, and to remind me of what is really important in life. Gracias por todo.

List of Publications

Peer-reviewed publications

A. Ohmann, K. Göpfrich, H. Joshi, R. F. Thompson, D. Sobota, N. A. Ranson, A. Aksimentiev, and U. F. Keyser. 'Controlling aggregation of cholesterol-modified DNA nanostructures.' *Nucleic Acids Research*, 47(21):11441–11451 (2019). doi:10.1093/nar/gkz914.

A. Ohmann, C. Y. Li, C. Maffeo, K. Al Nahas, K. N. Baumann, K. Göpfrich, J. Yoo, U. F. Keyser, and A. Aksimentiev. 'A synthetic enzyme built from DNA flips 10^7 lipids per second in biological membranes.' *Nature Communications*, 9:2426 (2018). doi:10.1038/s41467-018-04821-5.

K. Göpfrich, C. Y. Li, M. Ricci, S. P. Bhamidimarri, J. Yoo, B. Gyenes, **A. Ohmann**, M. Winterhalter, A. Aksimentiev, and U. F. Keyser. 'Large-conductance transmembrane porin made from DNA origami.' *ACS Nano*, 10(9):8207–8214 (2016). doi:10.1021/acsnano.6b03759.

K. Göpfrich, C. Y. Li, I. Mames, S. P. Bhamidimarri, M. Ricci, J. Yoo, A. Mames, **A. Ohmann**, M. Winterhalter, E. Stulz, A. Aksimentiev, and U. F. Keyser. 'Ion channels made from a single membrane-spanning DNA duplex.' *Nano Letters*, 16(7):4665–4669 (2016). doi:10.1021/acs.nanolett.6b02039.

Preprints

A. Ohmann, C. Y. Li, C. Maffeo, K. Al Nahas, K. N. Baumann, K. Göpfrich, J. Yoo, U. F. Keyser, and A. Aksimentiev. 'Outperforming nature: Synthetic enzyme built from DNA flips lipids of biological membranes at record rates.' *bioRxiv*, 241166 (2017). doi:10.1101/241166.

Conference papers

A. Ohmann, C. Y. Li, C. Maffeo, K. Al Nahas, K. N. Baumann, K. Göpfrich, J. Yoo, U. F. Keyser, and A. Aksimentiev. 'Outperforming nature: Synthetic enzyme built from DNA flips lipids of biological membranes at record rates.' *Biophysical Journal*, 114(3):15a (2018). doi:10.1016/j.bpj.2017.11.128.

K. Göpfrich, **A. Ohmann**, S. P. Bhamidimarri, M. V. S. V. Duvvuri, C. I. Bercea, B. Gyenes, M. Winterhalter, and U. F. Keyser. 'From ion-channels to porins: Engineering DNA-based synthetic counterparts.' *Biophysical Journal*, 110(3):351a (2016). doi:10.1016/j.bpj.2015.11.1889.

List of Abbreviations

1C	DNA nanostructures (CP2 design) with 1 cholesterol tag
2C	DNA nanostructures (CP2 design) with 2 cholesterol tags
6HP	Six-helix pore
ABD	Aminobenzoxadiazole
AFM	Atomic force microscopy
ATP	Adenosine triphosphate
bp	base pair
BSA	Bovine serum albumin
C6	Hexane
chol-DNA	cholesterol-modified ssDNA
CMC	Critical micelle concentration
CP	Cambridge pore
Dithionite	Sodium dithionite / hydrosulfite
DLS	Dynamic light scattering
DMEM	Dulbecco's modified Eagle's medium
DMSO	Dimethyl sulfoxide
DNA	Deoxyribonucleic acid
DOPE	1,2-dioleoyl-sn-glycero-3-phosphoethanolamine
DPhPC	1,2-diphytanoyl-sn-glycero-3-phosphatidylcholine
DPhPE	1,2-diphytanoyl-sn-glycero-3-phosphoethanolamine
dsDNA	double-stranded DNA
dsGUV	droplet-stabilised GUV
EColi	E. Coli Polar Lipid Extract
EDTA	Ethylenediaminetetraacetic acid

eggPC	L-α-phosphatidylcholine (Egg, Chicken)
FCS	Fetal calf serum
FRAP	Fluorescence recovery after photobleaching
GUV	Giant unilamellar vesicles
HPLC	High performance liquid chromatography
ITO	Indium tin oxide
kb	kilobase
LUV	Large unilamellar vesicles
MD	Molecular dynamics
NBD	Nitrobenzoxadiazole
NBD-SE	NBD-succinimidyl ester
nt	nucleotide
OPOE	n-Octylpolyoxyethylene
p-p	Peak-to-peak
PAGE	Polyacrylamide gel electrophoresis
PBS	Phosphate-buffered saline
PEG	Polyethylene glycol
poly-T	poly-thymine
POPC	1-palmitoyl-2-oleoyl-sn-glycero-3-phosphatidylcholine
PS	Phosphatidylserine
PTFE	Polytetrafluoroethylene (Teflon)
SD	Standard deviation
SDS	Sodium dodecyl sulfate
ssDNA	single-stranded DNA
SUV	Small unilamellar vesicles
TBE	Tris-Borate-EDTA
TE20	10 mM Tris, 1 mM EDTA, 20 mM $MgCl_2$, pH 8.0
TEG	Triethylene glycol
TEM	Transmission electron microscopy
TEMED	N,N,N',N'-Tetramethylethylenediamine
TLC	Thin layer chromatography
UV-vis	Ultraviolet-visible
wt%	weight%

Table of Contents

Chapter 1

Introduction & Motivation

> *As we go down in size, there are a number of interesting problems that ... we will have to be ready to design for. But I am not afraid to consider the final question as to whether, ultimately – in the great future – we can arrange the atoms the way we want; the very atoms, all the way down! What would happen if we could arrange the atoms one by one the way we want them?*
>
> – Richard P. Feynman

On December 29th in 1959, theoretical physicist and Nobel laureate Richard Feynman voiced these words in his famous lecture "There's plenty of room at the bottom" given at the annual meeting of the American Physical Society at Caltech, California [1]. In his speech, he invited the audience to consider a new field of physics – a physics at the smallest of scales. He illustrated the tremendous opportunities that lie in studying the "problem of manipulating and controlling things on a small scale". With his vision of arranging atoms and molecules one by one, he is today considered to be the father of the modern-day history of nanotechnology. Presumably unbeknownst to Feynman, the material that made his dream become a reality, was deoxyribonucleic acid – or DNA. In 1982, crystallographer Nadrian Seeman laid the theoretical groundwork for creating large, periodic networks made from DNA, thereby pioneering the field of 'DNA nanotechnology' [2]. DNA is hereby taken out of its biological context of storing the genetic information of an organism. Instead, the DNA sequence is used to direct the assembly of structural motifs and connect them with each other. DNA molecules themselves are composed of 0.34 nm long nucleotides that assemble into polymer chains, the DNA strands. In contrast to the self-assembly of amino acid chains into highly ordered

protein structures, the interactions of DNA strands with each other are well understood. These characteristics of having ångström-scale building blocks, each individually addressable due to the known DNA sequence, and a profound understanding of how these blocks interact with each other, make DNA an ideal building material at the nanoscale.

Of considerable interest in recent years, was the use of DNA nanotechnology for biological and biophysical applications [3, 4]. Notably, the study of biophysical processes at cell membranes or model lipid bilayers has become a prominent and successful area in DNA nanotechnology [5]. Rather than a top-down approach of, for example, modifying natural proteins, DNA allows us to build synthetic counterparts ourselves from the bottom up, just like in Feynman's vision. This approach enables us to develop an understanding of which features are essential to reproducing biological function. The feasibility of the bottom-up assembly of synthetic protein analogues has already successfully been demonstrated by mimicking natural protein ion channels with a variety of rationally-designed, DNA-built counterparts. Since the first DNA-made ion channel introduced by Langecker *et al.* in 2012 [6], several designs have been developed spanning multiple orders of magnitude in conductance, similar to natural ion channel proteins [7].

However, only recently the interface between the membrane-inserted DNA and the lipids the membrane is composed of, has become the focus of attention. In parallel to the beginning of this thesis work, we have shown that a hydrophobically modified and membrane-inserted, single DNA duplex induces the formation of a toroidal, water-filled lipid pore surrounding the duplex [8]. This observation sparked the idea that such a DNA-induced, toroidal pore could potentially allow lipids to translocate between the two bilayer leaflets. Such so-called 'lipid flipping' events are an important mechanism for cells to modulate the lipid composition in their cell membrane. As the two leaflets of a mammalian cell's plasma membrane are made up from chemically distinct mixtures of phospholipids, the lipid distribution across bilayer leaflets is typically asymmetric [9]. A loss of the asymmetry can trigger unregulated apoptosis [10] and could lead to the development of Alzheimer's disease [11]. Therefore, controlling this lipid distribution is critically important to the cell's health and functions.

Three protein families – flippases, floppases and scramblases [12, 13] – can move lipids between the bilayer leaflets. While flippases and floppases require energy in the form of ATP (adenosine triphosphate) to maintain the asymmetric lipid composition, scramblase proteins can be activated to passively dismantle the lipids' asymmetric distribution at scrambling rates of up to 10^4 lipids per second [14–17]. Cells use this as a signalling mechanism typically required during critical events such as cell activation, blood coagulation and apoptosis [18–21]. Defective enzyme-catalysed, phospholipid scrambling activity in blood cells has been shown to hinder thrombin formation leading to a bleeding disorder called Scott syndrome [22].

Controlled lipid scrambling activity is a crucial process in marking cells as apoptotic which, if impaired, has been linked to weaken the immune system and induce autoimmune responses by exposing self antigens [23]. Therefore, the development of biocompatible and controllable synthetic counterparts to repair and/or regulate lipid scrambling activity in cell membranes is of considerable medical interest.

In this doctoral thesis, we will introduce the novel and innovative application of using DNA nanotechnology to modulate the lipid composition in biological membranes. We will devise a DNA nanostructure design that is able to self-insert into lipid membranes and mix lipids between the bilayer leaflets at extraordinary high rates, significantly outperforming natural lipid scramblase proteins. To the best of our knowledge, we thereby pioneer the application of DNA nanotechnology to build a synthetic lipid scramblase.

Throughout this dissertation we will progressively increase the complexity of the DNA nanostructure design and the experimental methods to analyse lipid scrambling activity. In Chapter 2, we will first provide a brief introduction to the design and assembly principles of DNA nanostructures. Previous work focussing on interfacing DNA constructs with lipid membranes will be reviewed with special emphasis on membrane-spanning DNA nanostructures. Our current understanding about the interactions between membrane-inserted DNA constructs and the lipids of a lipid bilayer will be summarised and how this relates to the aim of this dissertation to build an artificial lipid scramblase. The chapter will furthermore provide an overview of natural lipid scramblases and their biological role, as well as previous attempts to create artificial counterparts. Lastly, we will discuss an experimental method, termed 'dithionite reduction assay' [24], that will be key in determining the lipid scrambling activity of our artificial DNA scramblase.

In Chapter 3, we will introduce the design of the DNA scramblase and provide an in-depth analysis of its assembly and structural characteristics. Gel electrophoresis will be employed as a cost-efficient and rapid bulk analysis method to gauge the assembly yield of the DNA nanostructures. Using single-molecule techniques such as atomic force (AFM) and transmission electron microscopy (TEM), we will verify the correct assembly and geometry of the folded constructs. Several new designs will be introduced and compared against existing layouts. We will ultimately highlight the advantages of our particular DNA nanostructure design that will be employed to demonstrate its lipid scrambling activity.

As the lipid bilayer's hydrophobic core presents a high energetic barrier for the negatively charged DNA [25], hydrophobic modifications are required for the stable membrane insertion of DNA nanostructures. Although there are several tags applicable, the commercial availability in a variety of modification options made cholesterol the most prominent of them.

However, a common issue of hydrophobically modified DNA constructs is their tendency to aggregate. In order to understand and avoid this problem, we will study the aggregation behaviour of cholesterol-modified ssDNA, dsDNA, and of our DNA nanostructure design introduced in the previous chapter. In a collaboration with the group of Aleksei Aksimentiev from the University of Illinois at Urbana-Champaign, we will employ a combination of all-atom molecular dynamics (MD) simulations, gel electrophoresis and dynamic light scattering to study the aggregation depending on the DNA sequence, and the number and modification position of the cholesterol groups. Our results reveal an interaction of ssDNA with cholesterol that can be exploited to shield the hydrophobic group. We thereby introduce an easy-to-implement mechanism to control aggregation of DNA nanostructures simply by design.

Building up on this acquired knowledge, we will investigate the DNA constructs' interaction with lipid membranes in Chapter 5. Electrophysiology experiments verify that our cholesterol-modified DNA structure self-inserts into a lipid bilayer and induces an ionic current across it. However, the insertion efficiency will prove to be very low. We will then employ the dithionite reduction assay where scrambling activity is assessed from the fluorescence reduction of dye-labelled lipids located in the membrane of artificial lipid vesicles. After characterising and optimising several assay parameters, different cholesterol-modified DNA nanostructures will be tested for their lipid scrambling activity. We will demonstrate that the conventional dithionite assay of using ~200 nm-sized vesicles and bulk fluorescence spectroscopy measurements, is not sensitive enough to measure scrambling activity of the DNA nanostructures as their insertion efficiency is most likely too low to induce a detectable signal.

In Chapter 6, we will again employ atomistic simulations with the help of Aleksei Aksimentiev's group to verify that the DNA nanostructure indeed scrambles lipids when membrane-insertion is assured. The results will not only reveal the stable formation of a toroidal pore but also that this DNA-induced pore allows lipids to translocate between bilayer leaflets at rates on the order of 10^7 lipids per second. To experimentally complement these results, we will adapt the dithionite reduction assay to giant unilamellar vesicles thereby compensating for the DNA structures' low insertion efficiency and allowing us to directly trace lipid scrambling activity at the single-vesicle level using confocal fluorescence microscopy. Strikingly, experiments indicate similarly high scrambling rates as demonstrated by the simulations. Our *de novo* designed DNA-built lipid scrambling enzyme can thereby outperform any known biological scramblase by several orders of magnitude. This demonstrates the enormous power and still unexplored opportunities of controlling lipid homeostasis using DNA nanotechnology.

Chapter 2

DNA nanotechnology & lipid scrambling

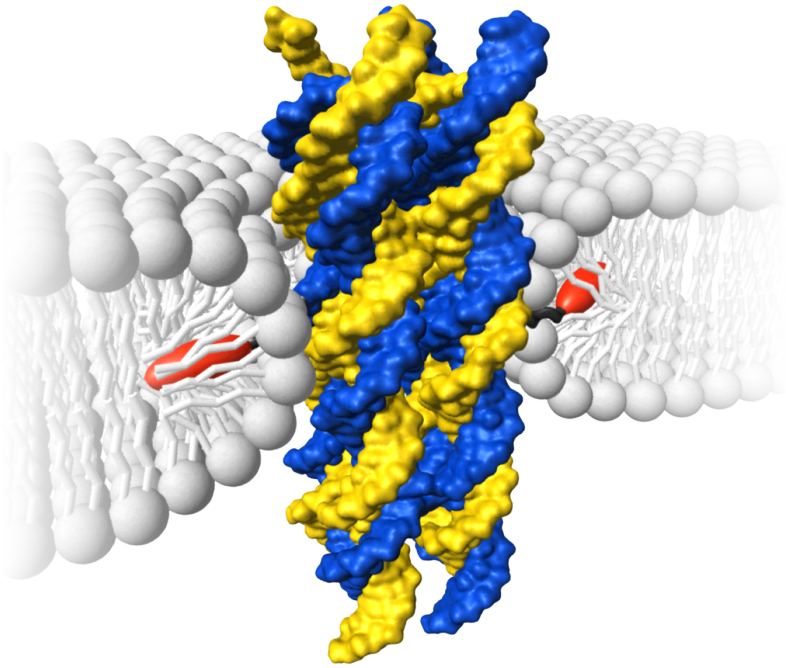

Parts of this work previously appeared in:

A. Ohmann, K. Göpfrich, H. Joshi, R. F. Thompson, D. Sobota, N. A. Ranson, A. Aksimentiev, and U. F. Keyser. 'Controlling aggregation of cholesterol-modified DNA nanostructures.' *Nucleic Acids Research*, 47(21):11441–11451 (2019).

2.1 Folding DNA into 3D shapes

Some people see a DNA robot and say,
'You can build a robot.'
Some people see a robot and say,
'You can build anything.'

– William M. Shih

DNA is an organic molecule composed of nucleotides that, via covalent bond formation, arrange into long polymers – the DNA single strands. Nucleotides contain one of four nitrogenous bases: adenine (A), cytosine (C), guanine (G), or thymine (T) (Fig. 2.1a). The number of nucleotides (nt) determines the length and their order determines the sequence of a DNA strand. Due to the formation of hydrogen bonds between complementary bases (A with T and G with C), a process called 'hybridisation', stable 'base pairs' are formed, turning single-stranded DNA (ssDNA) into double-stranded DNA (dsDNA). This dsDNA then typically adopts the characteristic double-helical structure as first proposed by Watson and Crick in 1953 [26] based on X-ray scattering experiments by Franklin *et al.* [27]. While DNA is used in living cells to store genetic information, with a distance between base pairs of 0.34 nm and a diameter of 2 nm, DNA is ideally suited as a building material at the nanoscale.

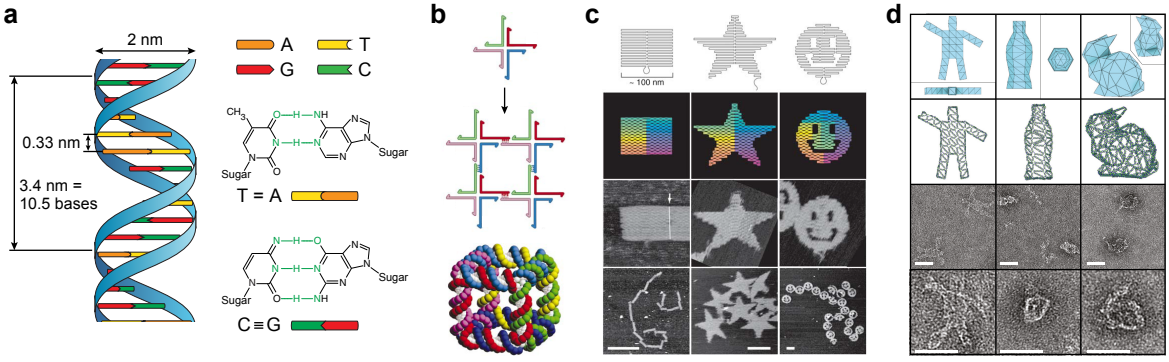

Fig. 2.1 Development of DNA nanotechnology. (**a**) Structure of B-form dsDNA with Watson-Crick base pairing [26] and an axial rise per base pair (bp) of 0.33 nm [28]. (**b**) Seeman's design of branched DNA junctions (top), 2D latices (middle) and a DNA cube (bottom). Adapted with permission [29]. Copyright 2003, Springer Nature. (**c**) Rothemund's DNA origami constructs shown with their scaffold pathways (top half) and AFM images (bottom half). Scale bars are 1 μm (left) and 100 nm (middle and right). Adapted with permission [30]. Copyright 2006, Springer Nature. (**d**) DNA origami structures of a stick figure, a bottle and a version of the Stanford bunny designed from 3D meshes (top half) and analysed with TEM (bottom half). Scale bars are 50 nm. Adapted with permission [28]. Copyright 2015, Elsevier Ltd. Entire figure adapted with permission [31]. Copyright 2019, Elsevier Ltd.

After laying the theoretical groundwork for DNA nanotechnology in 1982, Nadrian Seeman further developed the technique experimentally, demonstrating the successful self-assembly of structured materials out of DNA (see Fig. 2.1b) [29, 32, 33]. Other researchers followed with increasingly complex shapes like an octahedron by Shih *et al.* in 2004 [34]. Another milestone in the history of DNA nanotechnology was the introduction of the 'DNA origami' technique by Paul W. K. Rothemund in 2006 (see Fig. 2.1c) [30]. The method is based on directing the folding of a kilobase-long, viral ssDNA strand (termed 'scaffold') into a desired, pre-programmed geometry through the specific hybridisation of ~200 synthetic ssDNA strands (termed 'staples'), each typically between 20 to 50 nt long [35].
A crucial step in the simplification of designing DNA constructs was the development of the open-source programme 'caDNAno' by Douglas *et al.* in 2009 [36]. Desired shapes are designed graphically and the software calculates the necessary staple strand sequences which can then be synthesised by a company. This considerably sped up the design process while reducing the error rate facilitating the move from 2D to complex 3D shapes [35]. Another major step towards the analysis of DNA structures was made in 2011 with the web-based tool CanDo that can simulate 3D DNA origami shapes and provide an idea about their flexibility and stability [37]. Multiple design and modelling tools have been developed in recent years and many are still under active development [28, 38–42]. The advances in experimental expertise and design software have led to a vast range of applications of DNA nanostructures [3, 43], particularly regarding nanofabrication with synthetic nanomaterials [44], arranging pathways for chemical reactions [45, 46], biomolecule- [47] and force-sensing [48, 49], drug delivery [50, 51] and creating higher order structures (Fig. 2.1d) [28, 52].
In 2012, an alternative technique to DNA origami emerged, where the scaffold is omitted and only short synthetic ssDNA strands are employed [53]. This enabled the assembly of significantly more complex shapes than previously demonstrated solely based on short oligonucleotides. Still, the assembly of scaffolded DNA origami and non-scaffolded DNA constructs have certain common experimental characteristics. As the melting temperature of the DNA strands depends on their length and sequence, the folding reaction usually happens by mixing the DNA strands, heating them to above 90 °C to ensure complete separation, and then cooling them down slowly to room temperature (Fig. 2.2). This thermal annealing protocol can take from a few minutes up to several days depending on the complexity of the design [37, 54]. To overcome the repulsive electrostatic forces between the negatively charged DNA strands, this one-pot reaction typically takes place in a salt buffer with divalent ions such as 10 to 20 mM magnesium chloride ($MgCl_2$) [35], although folding with only monovalent ions at higher concentration, such as 1 to 2 M sodium chloride, has been successfully demonstrated as well [55].

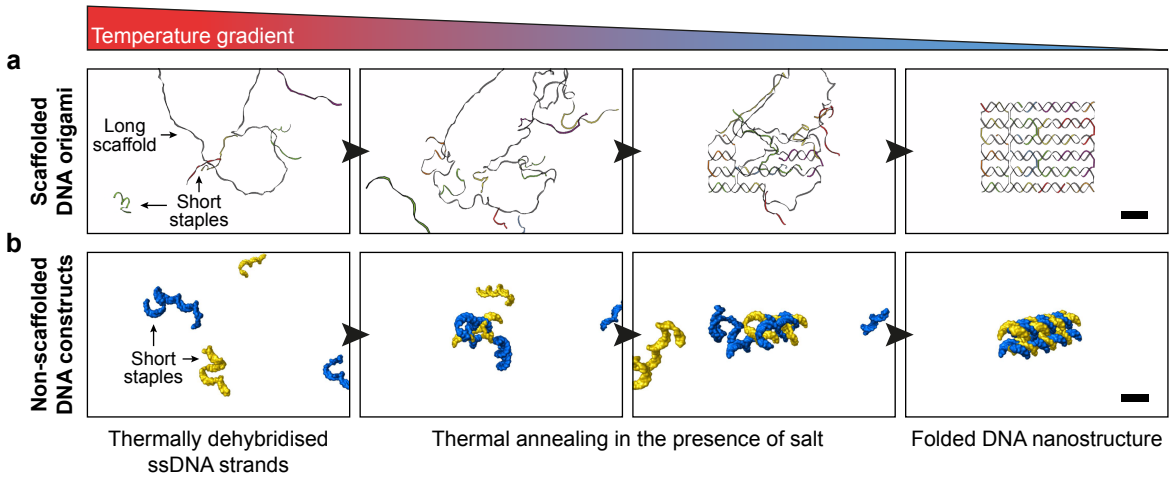

Fig. 2.2 Comparison of DNA origami assembly techniques. Snapshots of folding animations of scaffolded (**a**) and non-scaffolded (**b**) DNA nanostructure assembly during a temperature gradient typically from > 90 °C down to room temperature (**a** is adapted from [56, 57]).

For the aim of this dissertation to design a synthetic DNA-built mimic of a lipid scramblase, using only chemically synthesised oligonucleotides rather than employing the DNA origami technique has several advantages:

1. Iteration steps in design optimisation are much shorter and more cost-efficient as much fewer staple strands are needed.

2. As DNA origami structures are generally folded with an excess of staple strands over the scaffold strand, they require a post-assembly purification step [58]. Non-scaffolded structures, being assembled at equimolar concentrations of the DNA strands, generally do not require purification.

3. The design space can be expanded to smaller DNA constructs, as not the entire usually ~7,000 to 8,000 nt long scaffold strand needs to be incorporated into the structure. This facilitates the creation of designs with a molecular weight more similar to their protein-based counterparts.

4. Smaller DNA structures allow for significantly longer all-atom MD simulations, as the computing time required for large DNA origami constructs is very costly and time-consuming, and therefore typically not feasible. This advantage will be particularly beneficial in Chapter 6 of this dissertation.

5. Not being limited by the scaffold strand, purely staple-based designs can easily be produced at micromolar concentrations. This is several orders of magnitude higher than the nanomolar concentration range typically yielded for DNA origami structures.

While the larger, scaffolded DNA origami constructs allow for the incorporation of a higher number of functional groups in the design, we will see in this thesis that an impressive amount of modifications can be included already in structures made from a few ssDNA strands. This is also facilitated by the advantage that every DNA strand can be modified while, in contrast, modifications cannot easily be placed on the viral scaffold DNA. Furthermore, particularly the scalability of the DNA nanostructure folding concentrations, while maintaining low production costs, is the most striking benefit of the non-scaffolded design approach. It does not only broaden the spectrum of experimental opportunities but is a crucial requisite for possible medical applications in the future. Due to these advantages, this dissertation will employ non-scaffolded DNA nanostructures rather than the DNA origami technique.
In summary, the versatility, programmability and possibility to design and modify shapes with nanoscale precision, make DNA nanotechnology an ideal approach to build controllable structures that could potentially mimic the function of natural proteins.

2.2 Interfacing DNA nanostructures with lipid bilayers

Due to the immense structural control, the biocompatibility of DNA, and the ease of precisely modifying DNA with functional groups, interfacing DNA constructs with biology has gained significant importance in recent years [3, 4, 59]. Particularly, the targeted interaction of DNA with lipid bilayers has become a popular application of DNA nanotechnology [5, 60].
Negatively charged DNA interacts with cationic lipids, particularly under low salt conditions [61], as well as zwitterionic lipids in the presence of divalent cations such as Mg^{2+} or Ca^{2+} [62–64]. However, for a targeted and stable interface without significant dependence on the lipid composition, and to control the directionality of the insertion, DNA is typically conjugated to lipids or hydrophobic molecules. While a variety of membrane anchors such as azobenzene [65], porphyrin [8, 66, 67], ethyl phosphorothioate [68, 69], or tocopherol [70] have been employed, cholesterol is by far the most prominent [6, 54, 65, 71–84]. Its abundance in natural cell membranes and the commercial availability of cholesterol-tagged DNA with a variety of linker chemistries render it an ideal functional group to interface DNA nanostructures with biological and artificial lipid membranes.
Lipophilic DNA-conjugates have been used to functionalise polymersomes [73], microfluidic droplets [85] and, most prominently, lipid vesicles and planar lipid bilayers [86]. Herein, lipid-DNA linkers have been employed for drug delivery [87], biosensing [88] and to assemble size-controlled liposomes [89] or stimuli-responsive liposome networks [65, 71]. DNA-built mimics of membrane bending [76, 77], membrane scaffolding [90] and fusion proteins [91, 92] are other prominent classes of membrane-interacting DNA constructs.

Of particular interest and success has been the application to design DNA nanostructures that can spontaneously self-insert into lipid membranes and induce ionic currents across them, thereby mimicking the function of natural protein ion channels [6]. An impressively large variety of designs across multiple scales ranging from a single DNA duplex [8], via small non-scaffolded constructs [66–68, 72, 73, 93], to large-conductance DNA origami transmembrane porins [70, 74] has been devised in recent years.
Interestingly, our work on the smallest of these structures, a porphyrin-modified DNA duplex, was of particular importance for this dissertation [8]. This membrane-inserted DNA nanostructure did not possess a hollow, ion-conducting cavity. Yet it still induced stable ionic currents across a lipid bilayer suggesting an ionic current flow at the DNA-lipid interface (see schematic in Fig. 2.3a). MD simulations showed that the lipid headgroups rearrange towards the amphiphilic transmembrane part of the DNA duplex thereby forming a water- and ion-filled toroidal lipid pore. However, no efforts investigating the movement of lipid molecules between the bilayer leaflets were made at that point.

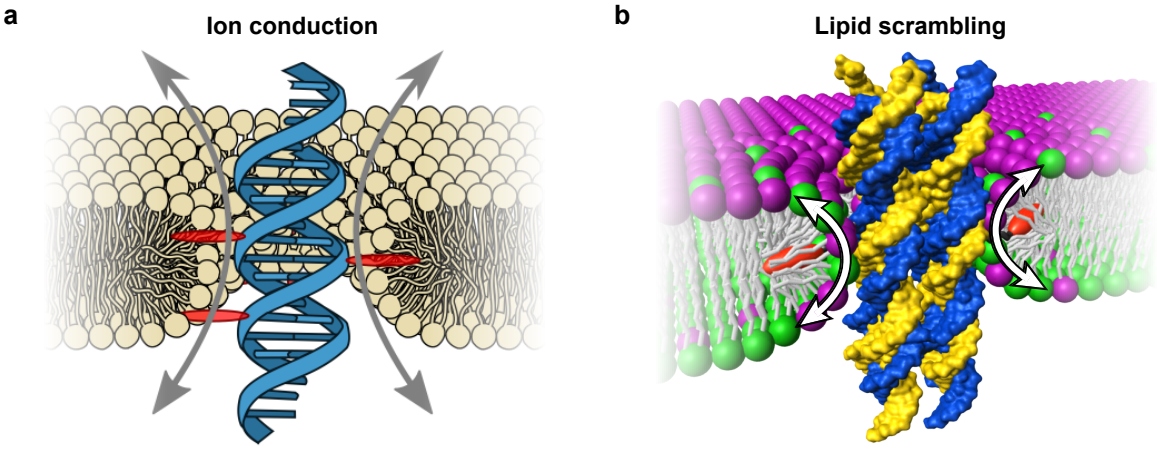

Fig. 2.3 Schematics of membrane-inserted DNA duplex and DNA scramblase. (**a**) DNA duplex (blue) modified with porphyrin (red ellipses) and its envisioned placement inside a lipid bilayer inducing a toroidal DNA-lipid pore that facilitates an ionic current flux across the lipid bilayer (grey arrows). Adapted with permission [8]. Copyright 2016, American Chemical Society. (**b**) Schematic of the membrane-inserted DNA scramblase design employed in this dissertation and its envisioned lipid scrambling mechanism. Lipids initially residing at opposite bilayer leaflets (purple and green) can translocate between the leaflets via the DNA-induced toroidal pore (indicated by white arrows).

In this dissertation, we hypothesise that such a DNA-induced toroidal pore can not only conduct ions, as demonstrated previously, but also connects the bilayer leaflets such that lipid molecules can translocate between them (see Fig. 2.3b). It can thereby mimic the function of natural lipid scramblase proteins to equilibrate the lipid composition across bilayer leaflets.

2.3 Lipid scrambling in biological membranes

Living cells use membranes for numerous physiological processes such as compartmentalisation of functions, segregation and protection, cell-cell interaction and many others [94]. One way to control these functions and to communicate with the extracellular environment is to specifically modulate the lipid composition of the plasma membrane. In all animal cells, there is an asymmetric distribution of phospholipids between the inner and outer leaflet of the cell's lipid bilayer [95]. A crucial step in controlling the lipid composition is to overcome the high energetic barrier of the bilayer's hydrophobic core. To translocate a phospholipid headgroup from one bilayer leaflet to the other through the hydrophobic core, a process called 'lipid flip-flop' [96], an energy barrier of > 20 kcal mol^{-1} must be overcome [97]. The rates of spontaneous lipid flipping events depend on the chemistry of the lipid headgroup, their fatty acid chains, the membrane composition and its physical state [98]. However, spontaneous translocation of phospholipids is generally a very slow process happening at time scales of several hours to days [96–99]. Nevertheless, lipid flip-flop at rates significantly faster than passive lipid translocations is essential for a cell's health. It is required for cell growth, cellular responses to physiological stimuli, membrane homeostasis, and to cooperate with proteins in creating intracellular vesicles [97]. Therefore, a transbilayer lipid flipping mechanism is essential to actively control the lipid composition of the plasma membrane.
Mainly three protein families facilitate lipid flipping: flippases, floppases and scramblases (Fig. 2.4) [97]. While flippases and floppases are ATP-dependent and work against a concentration gradient to establish and maintain lipid asymmetry, scramblases are ATP-independent working along concentration gradients to equilibrate the lipid composition [100].

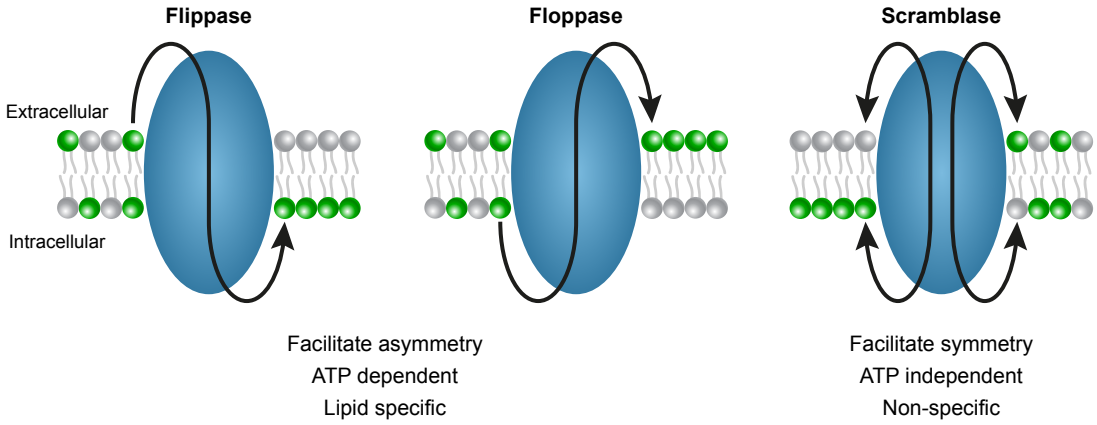

Fig. 2.4 Comparison of lipid-flipping proteins. Flippases flip lipids from the extracellular to the intracellular leaflet (fl**i**ppases flip to the **i**nside), floppases flip lipids the other way (fl**o**ppases flip to the **o**utside). Scramblases flip lipids in both directions. While flippases and floppases flip/flop only specific lipids, scramblases scramble lipids non-specifically [97].

Cell function, differentiation and growth depend on the precise modulation of the lipid distribution between bilayer leaflets [98]. To exert control over the equilibration of the lipid composition induced by lipid scramblases, their activity needs to be regulated. This is typically mediated by caspases (a family of cysteine proteases) or by adjusting the concentration of Ca^{2+} ions in the cell [95, 98, 101]. As phosphatidylserine (PS) and phosphatidylethanolamine (PE) lipids are primarily found in the intracellular (cytoplasmic) leaflet of the plasma membrane [102], activation of scramblase activity results in their increased concentration in the extracellular (exoplasmic) leaflet. Particularly the exposure of PS lipids to the cell surface is connected to critical events such as marking cells as apoptotic to trigger their removal by macrophages [103]. PS exposure has also been linked to the activation of blood platelets to regulate blood coagulation by enhancing thrombin production [104], cell fusion [105] and aiding bone mineralisation [106, 107]. This demonstrates that controlling the lipid composition is essential for a broad spectrum of physiological processes. Particularly uncontrolled scrambling activity has been linked to severe illnesses such as sickle cell disease [108] or Scott syndrome, a rare bleeding disorder [109].
Although already in 1985, Rosing *et al.* demonstrated that impaired scramblase activity causes Scott syndrome, only in 2010, Suzuki *et al.* were able to identify a specific molecule, transmembrane protein 16F (TMEM16F), as a calcium-dependent phospholipid scramblase [95, 110]. In 2014, Brunner *et al.* then obtained the X-ray structure of a TMEM16 fungal homologue from *Nectria haematococca* (nhTMEM16) (see Fig. 2.5) [111].

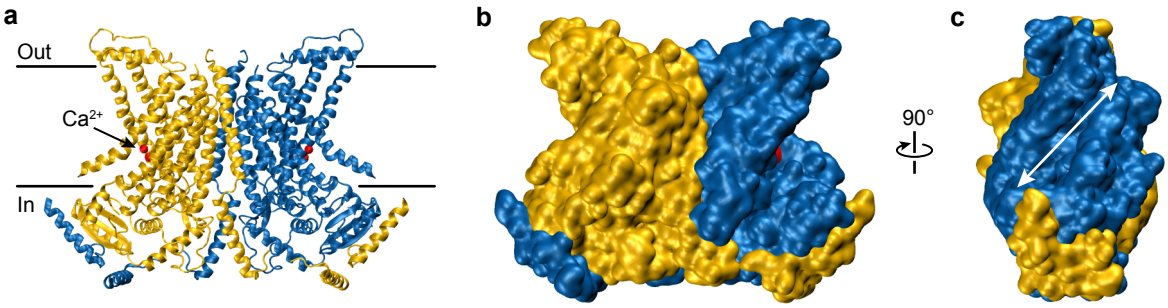

Fig. 2.5 Structure of nhTMEM16 scramblase. Side view from the membrane (indicated by black horizontal lines) using a cartoon (**a**) or a surface representation (**b**). Yellow and blue illustrate the two subunits of the homodimeric protein. Red indicates the position of bound calcium ions. (**c**) Rotated view of **b** with a white double-headed arrow indicating the hydrophilic groove. Images were created using VMD [112] and structure 4WIT [111] from the Protein Data Bank [113].

The TMEM16 protein family consists of Ca^{2+}-activated Cl^- channels as well as Ca^{2+}-dependent channels that are at the same time also lipid scramblases [114, 115]. Particularly the fungal homologues afTMEM16 and nhTMEM16, and human TMEM16E and TMEM16F

proteins, have been shown to possess this dual function [115], with TMEM16F being the one that has been studied the most and its physiological role understood best [21, 116–120]. When fully activated by Ca^{2+} ions, lipid transport rates of scramblases have been estimated to be $\geq 10^4$ lipids per second [14, 115, 121]. A more detailed discussion on scrambling rates will be presented in Section 6.3.6 in Chapter 6.

Unregulated scramblases, such as the G protein-coupled receptor opsin [15], that constitutively scramble lipids exist as well which is thought to be mediated by a transient hydrophilic groove opened through a conformational change [17]. Oligomerisation of single-helix peptides, such as antimicrobial peptides [122] or the pore-forming protein perforin [123], have been shown to form toroidal pores that can facilitate phospholipid flip-flop. But also monomeric single-helix peptides, typically with several repeated sequences in the hydrophobic core and decorated by positively charged residues at both termini [120], have also been demonstrated to induce constitutive, unregulated phospholipid scrambling activity [124, 125]. Despite ample research, the precise mechanism how scramblases translocate lipid molecules is still poorly understood [120]. The generally accepted 'credit card' model (see Fig. 2.6) suggests that scramblases possess a membrane-exposed hydrophilic cavity, or a groove (see Fig. 2.5c), which phospholipid headgroups can move through [97, 115, 126].

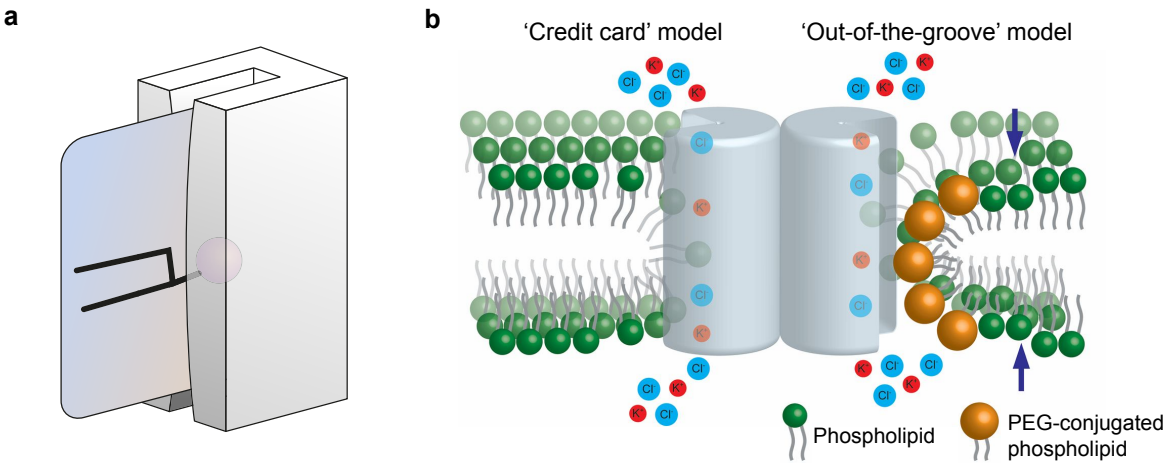

Fig. 2.6 Models for lipid scrambling mechanism. (**a**) Schematic illustration of the credit card model in which a lipid translocating through the hydrophilic groove of a scramblase protein is envisaged as a credit card being swiped through a card reader. Adapted with permission [17]. Copyright 2018, Elsevier Ltd. (**b**) Comparison of 'credit card' (left) and 'out-of-the-groove' model (right). While in the credit card model lipids only translocate through the groove, together with ion permeation, in the out-of-the-groove model local membrane deformation (indicated by blue arrows) facilitates lipid transfer outside the groove. Adapted with permission [127].

Nevertheless, the question if the ion permeation and lipid scrambling pathways are always the same or can be separate is an ongoing debate [127]. In 2013, a study concluded a separate pathway for ions and lipids of afTMEM16 [14]. A more recent publication suggested that ion and lipid conduction pathways are physically the same [128] which had subsequently been confirmed for the fungal scramblase nhTMEM16 [129]. However, translocations of lipids with headgroups much larger than the cavity width have been observed which suggests an additional 'out-of-the-groove' transport mechanism (see Fig. 2.6b) [115]. This hypothesis is supported by a recent structural study of TMEM16F using electron cryo-microscopy with results indicating that an additional mechanism based on membrane distortion could independently scramble lipids without requiring a hydrophilic groove [130]. This ongoing controversy and particularly the still poorly understood mechanism of how lipids enter the hydrophilic groove make this subject a particularly interesting area of active research.
Although a few previous studies were able to create artificial lipid scramblases via synthesised cationic steroids [131] or synthetic peptides [125, 132], reported scrambling rates were generally rather low. Efforts involving the insertion of DNA nanostructures in a lipid bilayer have so far only been focused on creating ion channels. No results have been reported on designing an artificial scramblase using DNA making it a highly interesting and innovative approach. The important biological role and the prevailing controversy about the lipid translocation mechanism make scrambling activity a particularly intriguing area of study.

2.4 Determining lipid scrambling activity

As the lipid translocation between bilayer leaflets cannot be observed directly, several indirect detection methods using chemically modified lipid probes have been developed [133]. A common factor among them is that an asymmetry between the inner and outer bilayer leaflet is established first. Scrambling activity is then assessed by monitoring how this asymmetry returns back to a uniform distribution over time [98]. To study lipid scrambling under controlled conditions, model membrane systems present an ideal environment as they avoid the complex interplay of active processes found in natural systems.
Scrambling activity has been investigated by electron paramagnetic resonance of spin-labelled [96], by proton nuclear magnetic resonance of isotopically labelled [134, 135], or by extraction (using BSA [14] or liposomes [136]) or reduction of fluorescently labelled lipids [133]. Herein, the most established assay to determine scrambling activity in model membrane systems is the 'dithionite reduction assay' [14, 24, 115, 131, 132, 137–142]. Artificial lipid vesicles are prepared containing a low proportion (~0.5 %) of lipids chemically modified with the fluorescent dye nitrobenzoxadiazole (NBD). While only weakly fluorescent

in water, its fluorescence intensity and lifetime increases when located in a hydrophobic environment [142]. The fluorescence intensity of such NBD-containing lipid vesicles is then monitored, typically in bulk, using fluorescence spectroscopy. Sodium hydrosulfite $Na_2S_2O_4$, also termed 'sodium dithionite', which dissociates in aqueous solution into 2 Na^+ and $S_2O_4^{2-}$ (dithionite), is then added to the vesicle suspension. In the presence of dithionite, the nitro group (-NO_2) on the NBD dye is irreversibly reduced to an amino group (-NH_2) forming the non-fluorescent derivative aminobenzoxadiazole (ABD; see Fig. 2.7).

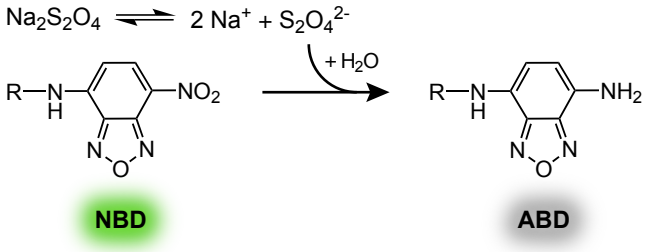

Fig. 2.7 Chemical reaction of dithionite reduction. Sodium hydrosulfite dissociates in aqueous solutions into 2 Na^+ and $S_2O_4^{2-}$ (dithionite) [24]. Dithionite then irreversibly bleaches NBD fluorescence by reducing the NBD's nitro group (-NO_2) to an amino group (-NH_2). R denotes a chemical group the NBD is attached to, for example a lipid tail.

A fundamental feature of this assay is that due to the double negative charge, dithionite does not permeate through membranes [15, 24]. This means that in the absence of scrambling activity, only NBD-labelled lipids in the outer bilayer leaflet are reduced in their fluorescence. Assuming an equal distribution of labelled lipids in the inner and outer bilayer, the normalised fluorescence per vesicle thereby exhibits an intensity reduction to half of the initial value over time (see Fig. 2.8a). This typically occurs at a time scale of a few minutes where spontaneous lipid flip-flop is negligible. Thus, the fluorescence reduction establishes an asymmetric lipid distribution between the bilayer leaflets, a fundamental characteristic of lipid scrambling assays mentioned at the beginning of this section.

To test the scrambling activity of a scramblase protein or, in our case, a membrane-inserting DNA nanostructure, prior to addition of dithionite the vesicles are either formed with the lipid-scrambling complex or are incubated with it to allow membrane insertion to take place. The same dithionite reduction assay is then performed. If lipid scrambling activity is induced, NBD-labelled lipids on the inner bilayer leaflet that were previously inaccessible to be bleached by dithionite, are now transported to the outer bilayer leaflet where their fluorescence can be irreversibly reduced. Given a complete exchange of lipid molecules between both bilayer leaflets, the fluorescence intensity should then over time approach 0 (Fig. 2.8b). Example traces of lipid vesicles constituted without or with a calcium-regulated afTMEM16 scramblase obtained via fluorescence spectroscopy are shown in Fig. 2.8c.

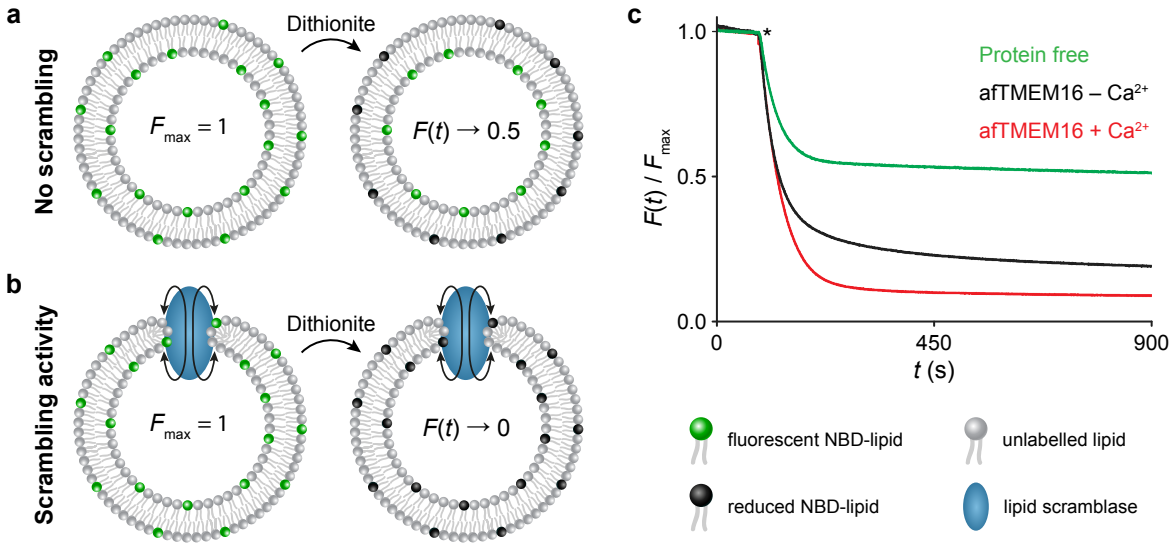

Fig. 2.8 Dithionite reduction assay to experimentally verify scrambling activity. (**a,b**) Scheme of lipid vesicles containing a low percentage of NBD-labelled lipids (green) which are fluorescently reduced (black) upon addition of dithionite. (**a**) In the absence of lipid scrambling activity the normalised fluorescence is reduced to 0.5 over time. (**b**) If lipid flip-flop is induced by a scramblase, the fluorescence intensity is eventually reduced to 0. (**c**) Example traces of fluorescence reduction obtained via fluorescence spectroscopy [14]. Upon addition of dithionite (asterisk) the normalised fluorescence approaches a value of ≈ 0.5 without a scrambling protein present (green trace). If vesicles were constituted with the afTMEM16 scramblase the fluorescence intensity rapidly decreases below 0.5 at a calcium-dependent rate (black and red traces). The fluorescence does not approach 0 as not all lipid vesicles contain scramblase proteins. Adapted with permission [14]. Copyright 2013, Springer Nature.

For the dithionite assay, lipids can be labelled with NBD at different positions: either at their headgroup or at their fatty acid tails typically via a hexane (C6) or a dodecane (C12) linker (see Fig. 2.9). A previous study employed differential spin-label quenching to determine the position of the NBD dye within the lipid membrane [143]. Interestingly, the location of the NBD group of tail-labelled (6-NBD-PC and 12-NBD-PC) and headgroup-labelled lipids (NBD-PE) was found to be very similar (see Fig. 2.9) [144, 145]. This also provides an explanation why NBD can at the same time exhibit enhanced fluorescence due to the hydrophobic environment but still be accessible for reduction by the dithionite anion. An important aspect for the interpretation of the results is to ascertain that through all stages of the assay, membrane-impermeability of the dithionite is maintained. This will be discussed more in detail in Section 6.3.5 in Chapter 6. Furthermore, as the signal indicative of scrambling activity is assessed from the translocation of NBD-labelled 'reporter' lipids, there is an uncertainty of how representative the determined scrambling rates are for the unlabelled lipids the vesicles are composed of. Due to the presence of the fluorescent tag on

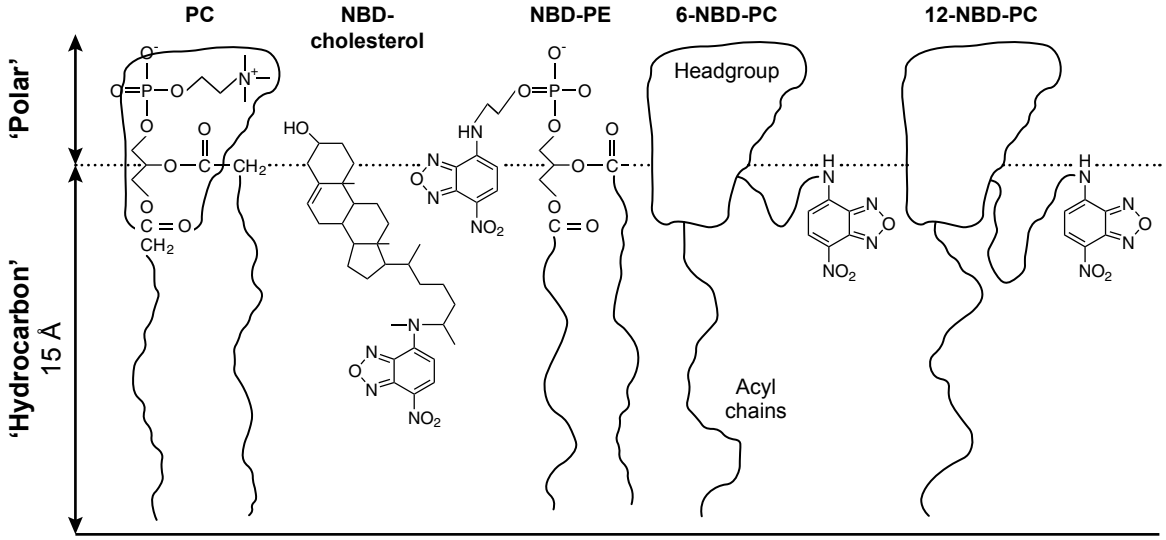

Fig. 2.9 Schematic diagram of one bilayer leaflet illustrating the location of NBD-labelled lipids as determined by differential spin-label quenching. Bottom line refers to the centre of the lipid bilayer. Adapted with permission [144]. Copyright 1990, Elsevier Ltd.

the lipid, its flipping kinetics could differ from the kinetics of the general, unlabelled lipid composition [133]. However, a recent study employed a perdeuterated variant of 1-palmitoyl-2-oleoyl-sn-glycero-3-phosphatidylcholine (POPC) as the labelled reporter lipid [135]. The difference compared to unlabelled POPC is minimal as only some of the hydrogen atoms were replaced with deuterium. Using proton nuclear magnetic resonance (H^1-NMR) as a readout method, they determined flip-flop rates comparable to a previous study that used lipids tail-labelled with NBD [146]. This suggests that the presence of the NBD dye at the lipid tail might not significantly affect the measured scrambling kinetics which agrees with another report stating that the lipid headgroup charge is a more significant determining factor for lipid flip-flop than a modification on the fatty acid chain [133].

One drawback of the dithionite reduction assay is that the observed intensity traces are a superposition of two processes: (a) scrambling of NBD-labelled lipids between the bilayer leaflets, and (b) their fluorescence reduction by dithionite. If the lipid translocation occurs very rapidly, the dithionite reduction will be the rate-limiting process. Therefore, estimating the lipid scrambling rate from the trace of fluorescence reduction can underestimate the actual rate of lipid flip-flop. We will discuss this in more detail in Section 6.3.6 in Chapter 6. However, the comparative ease of performing the dithionite reduction assay, the ample previous research published on it, and the existing equipment and expertise to form and analyse model lipid bilayer systems in our group, render this assay the ideal choice in this thesis to determine the scrambling activity of our synthetic, DNA-built lipid scramblase.

Chapter 3

DNA nanostructure design and assembly

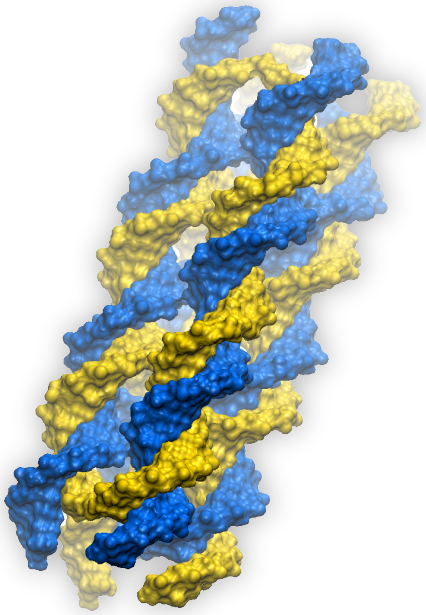

Parts of this work previously appeared in:

A. Ohmann, K. Göpfrich, H. Joshi, R. F. Thompson, D. Sobota, N. A. Ranson, A. Aksimentiev, and U. F. Keyser. 'Controlling aggregation of cholesterol-modified DNA nanostructures.' *Nucleic Acids Research*, 47(21):11441–11451 (2019).

A. Ohmann, C. Y. Li, C. Maffeo, K. Al Nahas, K. N. Baumann, K. Göpfrich, J. Yoo, U. F. Keyser, and A. Aksimentiev. 'A synthetic enzyme built from DNA flips 10^7 lipids per second in biological membranes.' *Nature Communications*, 9:2426 (2018).

3.1 Introduction

Part of it is DNA and getting DNA to form interesting and exciting and useful shapes ...
– Nadrian C. Seeman

In this chapter, we will introduce the DNA nanostructure design which will later be employed as an artificial lipid scramblase. Optimising the folding yield of monomeric structures and performing an in-depth structural analysis will lay the foundation for subsequent experiments focusing on the effects of cholesterol modifications, studying lipid membrane insertion, and lipid scrambling activity.
Polyacrylamide gel electrophoresis will initially be employed as a rapid and cost-efficient tool to study the folding yield of the DNA nanostructure. It will allow to verify the correct assembly of the DNA nanostructure in bulk by providing insight on the amount of formed monomers, dimers and aggregates. This method will then be utilised to optimise the folding yield depending on the $MgCl_2$ concentration in the assembly buffer. We will furthermore discuss the influence of ssDNA overhangs at the ends of the design, particularly which nucleotides prevent stacking interactions best and how many are needed.
While gel electrophoresis is the ideal tool to verify folding yields, it does not allow to determine the actual size and geometry of the assembled nanostructures at a single-molecule level. After optimising the folding yield, we will therefore employ atomic force and transmission electron microscopy, two prevalent techniques in the field of DNA nanotechnology [3], to confirm that the most prominent band in the gel actually represents monomeric structures approximately matching the expected design both in shape and size.
Lastly, the optimised design will be compared to previously reported nanostructures able to insert into lipid membranes and alternative designs devised in this thesis work. We will compare them regarding the pathways of the ssDNA staple strands and the distribution of crossovers providing structural stability. Using the computational tool 'CanDo' the rigidity will be analysed to identify undesirable fluctuations or instabilities in the design. Gel electrophoresis will furthermore allow for a quick estimate of their respective folding yields. The designs will also be compared regarding their ease and flexibility to introduce modifications at various positions. This will become specifically important later on for the incorporation of cholesterol tags to facilitate membrane insertion and fluorescent dyes to track the DNA nanostructures with fluorescence microscopy.
A fundamental comprehension and optimisation of the design is a crucial step as these aspects need to be kept in mind when designing future experiments and interpreting their results.

3.2 Materials & Methods

3.2.1 DNA nanostructure assembly

DNA nanostructures were designed using caDNAno software [36]. In order to maximise specificity of the different strands, sequences were optimised using the web-based analysis tool NUPACK [38]. DNA oligonucleotides were purchased from Integrated DNA Technologies, Inc. (IDT) using standard desalting and delivery at 100 µM in IDTE buffer (10 mM Tris, pH 8.0, 0.1 mM EDTA). If not stated otherwise, required DNA strands for a specific construct were mixed at a final concentration of 1 µM in TE20 buffer (10 mM Tris, 1 mM EDTA, 20 mM $MgCl_2$, pH 8.0). DNA nanostructure assembly was performed as described previously [54]. Briefly, the mixture was heated to either 85 or 95 °C for 5 min, subsequently cooled to 25 °C over 18 hours and finally stored at 4 °C. Heating to 95 °C reduced the visible aggregation of the folded DNA nanostructures upon analysis with PAGE and was therefore the superior protocol. For the assembly it was important that all DNA strands were at the same concentration. Therefore, the minimum final amount of assembly mix was 100 µl in order to not pipette less than 1 µl per DNA strand. Furthermore, the concentration of purchased DNA strands was measured using UV-vis spectroscopy (NanoDrop 2000, Thermo Fisher Scientific) to verify that it is indeed approximately 100 µM.

3.2.2 Polyacrylamide gel electrophoresis

Gel electrophoresis, a well-established experimental technique in molecular biology, is one of the most cost-efficient and powerful tools for the characterisation of DNA nanostructures. Upon applying an electric field across a gel formed from cross-linked polymers, the negatively-charged DNA migrates through the porous gel matrix against the direction of the field. When keeping the applied voltage, the pore size of the gel, and the buffer conditions constant, the migration distance of the DNA nanostructure primarily depends on its size and shape [147]. Thereby information can be gained about the different structural conformations of the DNA sample, e.g. folded and misfolded populations can be separated. To maximise the separation resolution, the average pore size of the gel matrix needs to be chosen appropriately regarding the size of the molecule to be analysed. As a macromolecule separation method, agarose gel electrophoresis is best suited for analysing large DNA constructs, such as DNA origami. The size of the here designed DNA nanostructures is on the order of ~10 nm. This makes non-denaturing (native) polyacrylamide gel electrophoresis (PAGE) with pore sizes in the low nanometre range (depending on the acrylamide concentration [148, 149]) the optimal tool, as used previously for a DNA structure of similar size [54].

Gel preparation, running conditions & staining

All chemicals were acquired from Sigma-Aldrich and all gel equipment from Bio-Rad. Gels were hand-cast at a concentration of 10 % polyacrylamide supplemented with 0.5x Tris-borate-EDTA and 11 mM $MgCl_2$, as described previously [54]. The detailed recipe is listed in Table 3.1.

Table 3.1 Recipe for casting one 10 % PAGE gel. For two gels all amounts are doubled.

Gel mixture recipe	Amount	Concentration	Order #
Acrylamide/Bis-acrylamide, 30 % solution	5 ml	10 %	A3699
10x Tris-Borate-EDTA (TBE) pH 8.3	750 µl	0.5x	T4415
0.5 M $MgCl_2$	330 µl	11 mM	M2393
H_2O	8.92 ml		
Total volume	15 ml		
Polymerisation initiators			
10 % (w/v) ammonium persulfate (APS)	150 µl	0.1 %	A3678
N,N,N',N'-Tetramethylethylenediamine (TEMED)	10 µl	0.07 %	T9281

Mini-PROTEAN® spacer plates with 1.0 mm integrated spacers (1653311, Bio-Rad) were used together with Mini-PROTEAN® short plates (1653308), clamped together, and mounted in a Mini-PROTEAN® Tetra Cell casting stand. Once assembled, APS and TEMED were added to the 15 ml gel mixture. The mixture was then immediately vortexed, poured between the spacer plates using a glass Pasteur pipette, and the gel comb was inserted. The gel was left to polymerise for 1 to 2 hours.
Gels were run in a Mini-PROTEAN® Tetra Cell (Bio-Rad) which was embedded in crushed ice a few minutes prior. The gel was run for 90 min at 100 V in running buffer containing 0.5x TBE and 11 mM $MgCl_2$ (for recipe see Table 3.2). DNA was stained by immersing the gel slab for 10 min in GelRed® 3x in water (Biotium). Subsequent imaging was performed on a GelDoc-It™ (UVP) using UV excitation.

Table 3.2 Recipe for PAGE running buffer sufficient for one run.

Running buffer recipe	Amount	Concentration
10x Tris-Borate-EDTA (TBE) pH 8.3	40 ml	0.5x (44.5 mM Tris-borate, 1 mM EDTA)
0.5 M $MgCl_2$	17.6 ml	11 mM
H_2O	742.4 ml	
Total volume of running buffer	800 ml	

A detailed collection of advice and troubleshooting guidance for performing PAGE with DNA nanostructures can be found in Appendix A.1.

Sample loading & DNA ladder

2 µl of DNA nanostructures at 1 µM were mixed with 0.4 µl custom-made 6x orange loading dye (for detailed recipe see Table 3.3). The loading dye was prepared using TE20 (10 mM Tris, 1 mM EDTA, 20 mM $MgCl_2$, pH 8.0) as the main buffer and stored at room temperature. 2 µl of the mixture were loaded into the well using 0.5 mm thick Corning® gel-loading tips (CLS4853, Sigma-Aldrich).

Table 3.3 Recipe for 6x orange loading dye. Amount of Orange G can be approximate as it is only used to add visibility for sample handling (typically the tip of a spatula is sufficient). For loading DNA nanostructures the dye was made with TE20 buffer. Note that the concentration of this buffer should not be at 6x even though the recipe is for the 6x loading dye.

6x loading dye recipe	Amount	Concentration	Order #
Ficoll®-400	150 mg	15 % (w/v)	F2637
Orange G	9 mg	0.9 % (w/v)	O3756
Buffer solution	fill to 1 ml		
Total volume of 6x loading dye	1 ml		

Reference DNA markers were either L: GeneRuler Low Range DNA Ladder (SM1191, Thermo Fisher Scientific), or L*: 50 bp DNA ladder (N3236, New England Biolabs). With the loading dye described above diluted in TE20 buffer, DNA ladder L can be prepared ready-to-load using the recipe listed in Table 3.4. The ladder was stored at 4 °C and between 1.2 and 2 µl were typically loaded onto the gel.

Table 3.4 Recipe for preparing 120 µl of ready-to-load DNA ladder L.

DNA ladder recipe	Amount
GeneRuler Low Range DNA Ladder, 0.5 µg µl^{-1}	12 µl
6x orange loading dye (prepared with TE20 buffer)	20 µl
TE20 buffer	88 µl
Total volume of ready-to-load DNA ladder L	120 µl

Image analysis

Gel images were analysed using Fiji [150]. Images were cut, the colour scale was inverted and the background was subtracted using the integrated rolling ball method at a radius of 300 pixel (> 30 % of the shortest image dimension). Using the gel analyser tool intensity plots per lane were generated. The background for each lane was again subtracted by drawing a line from the intensity level before the gel pocket to the level after the furthest band.

Monomer, dimer and multimer peaks were identified, and approximated by lines following the contour of the peak from the full width half maximum downwards. The areas under these approximated monomer, dimer and multimer peaks was then measured using the wand tool. The obtained values were normalised to the sum of their respective lane which compensated for a possible variation in sample loading volume and therefore allowed the comparison of folding yields between different lanes.

3.2.3 Atomic force microscopy of DNA nanostructures

5 µl of DNA nanostructures (typically at a concentration of 10 nM) in TE20 buffer were deposited on a freshly cleaved mica surface (Agar Scientific) and incubated for 90 s. To remove excess sample the surface was rinsed three times with 1 ml Milli-Q water and blow-dried with nitrogen. Imaging was carried out by M. Ricci using a Cypher S AFM (Oxford Instruments) in amplitude modulation in air and at room temperature using AC240TS cantilevers (Olympus) with a nominal spring constant of 2 N m^{-1}. The set-point to free amplitude ratio was generally kept at around 70 % with a free oscillation amplitude of 20 nm. The frequency of excitation was set close to the resonance of the first flexural mode (around 70 kHz) and a repulsive mode was preferred. The scan speed was set to either 1 or 2 Hz obtaining an image of 256 $\times$ 256 pixels. Images were flattened and band-pass filtered using Gwyddion [151]. For analysis of DNA nanostructure dimensions, a height mask was applied and an ellipse was automatically fitted to these areas approximating major and minor axes which was interpreted as length and width of the nanostructures, respectively.

3.2.4 Transmission electron microscopy of DNA nanostructures

3 µl of DNA nanostructure solution (1 µM in TE20 buffer) were deposited onto an electron microscopy grid (Agar) with a continuous carbon layer treated by glow discharge before use (30 s, 10 mA). Sample was blotted away and the surface of the grid was washed twice with water and once with 1 % (w/v) uranyl acetate staining solution. 3 µl staining solution was then incubated on the surface of the grid for 30 s. Subsequently the excess was blotted away. Grids were imaged by R. F. Thompson with an FEI Spirit G2 12 BioTWIN transmission electron microscope with a Gatan US1000XP 2k x 2k CCD camera.

3.3 Results & Discussion

3.3.1 Design overview

An overview of the design of the DNA nanostructure used throughout this thesis work is presented in Fig. 3.1. The structure consists of eight ssDNA strands (Fig. 3.1a) that, in the presence of Mg^{2+} ions and subject to a thermal annealing protocol, self-assemble into four interconnected DNA duplexes giving the design an overall cuboid shape (Figs. 3.1b-d). The required DNA strands range from 23 to 47 nt in length and are listed in Table 3.5.

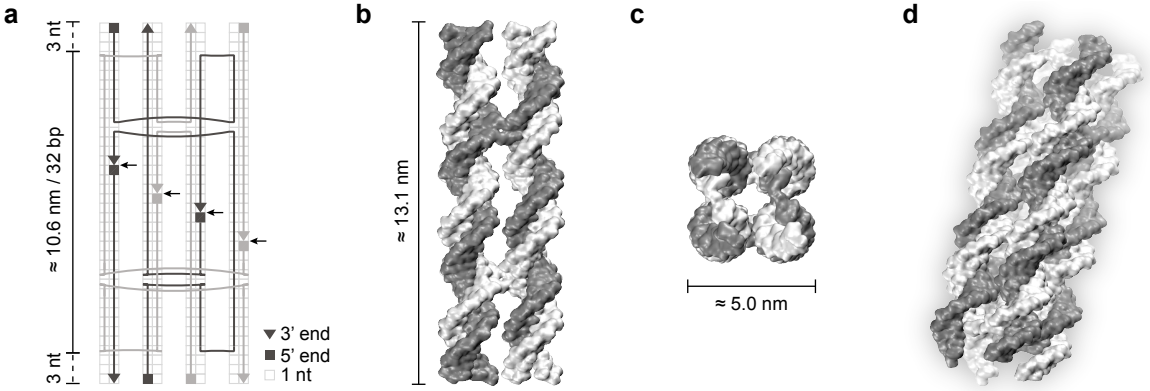

Fig. 3.1 Design of DNA nanostructure. (**a**) 2D illustration highlighting the pathways of the ssDNA strands as well as the crossover positions. Complementary strands are displayed in light and dark grey. Black arrows indicate DNA nicks that facilitate the incorporation of modifications on the DNA 3' and 5' terminal ends. View from side (**b**), top (**c**) and perspective (**d**) of a 3D representation of the folded nanostructure. The 3D model was created by converting the caDNAno file to a protein data bank (PDB) file format using an open-source online tool [42] and then depicted using a surface representation in VMD software [112].

The assembled DNA construct has a length of ≈ 13.1 nm and a width of ≈ 5.0 nm, assuming an axial rise per bp of 0.33 nm [28], a mean distance between two bases of 0.43 nm for ssDNA [152], a dsDNA diameter of 2.25 nm [37], and an interhelical distance of 2.7 nm [153]. The layout follows the caDNAno design rules which suggest DNA crossovers at specific locations when neighbouring DNA strands are close to each other with respect to their helical rotation [36]. In the central region there are four DNA nicks (see Fig. 3.1a) which allow the incorporation of cholesterol modifications on the 3' or 5' terminal ends which will facilitate the insertion of the DNA nanostructure into a lipid bilayer. These nicks are strategically placed at positions that face away from the nanostructure to the outside as the helical pitch of the DNA is taken into account. This will be discussed more in detail in Chapter 4 and is specifically highlighted in Fig. 4.10.

Table 3.5 DNA sequences and strand names used to assemble DNA nanostructures.

Name	Sequence (5' to 3')	Length (nt)
sc1	CCTTTCCACGAACACAGGGTTGTCCGATCCTATATTACGACTCCTTT	47
sc2	TTTGGGAAGGGGTTCGCAAGTCGCACCCTAAACG	34
sc3	TCTTATCCTGCATCGAAAGCTCAATCATGCATCTTT	36
sc4	TTTATGTTGAAGGCTCAGGATGC	23
st1	TTTATCGGACATTCAACATGGAGTCGTGGTGCGACT	36
st2	TGCGAACAGGATAAGACGTTTAGAATATAGGTTT	34
st3	TTTTTCGATGCCCCTTCCCGATGCATGAAGGGCATCCTGAGCCACCC	47
st4	TGTGTTCGTGGAATTGAGCTTTT	23

The square-lattice arrangement of the four DNA duplexes leads to a small, central lumen along the long axis of the nanostructure (see Fig. 3.1c). While this cavity would be large enough to allow ions to pass [154, 155], we have previously demonstrated that ion permeation can also occur at the DNA-lipid interface [8]. It is therefore anticipated that this DNA construct creates a passage for ions when inserted into a lipid bilayer. This can be exploited to verify the insertion capabilities of the DNA nanostructure design by performing single-molecule current recordings across lipid bilayers, as typically employed to verify the successful membrane insertion of DNA constructs [6, 66, 68]. This aspect will be focused on in Chapter 5.
Lastly, the design is composed of a dsDNA core section ($\approx$ 10.6 nm / 32 bp) flanked at both ends by eight ssDNA overhangs (see Fig. 3.1a) to prevent stacking interactions between the nanostructures which will be discussed in detail in the following section.

3.3.2 Single-stranded overhangs to avoid stacking

An initial hurdle to overcome was to optimise the yield of monomeric DNA nanostructures. A crucial design element are four single-stranded DNA overhangs at each end of the design (blue in Figs. 3.2a,b). PAGE analysis of the folded structures shows that without any ssDNA overhangs (–) the DNA nanostructures formed clusters that remained in the gel pocket (see Fig. 3.2c). This is caused by stacking interactions between the blunt double-strand ends [156, 157] and enhanced by the presence of the divalent Mg^{2+} ions in the buffer solution [158]. Introducing four, single-nucleotide ssDNA overhangs at either end of the nanostructure resulted in the appearance of two additional bands in the gel which are interpreted as DNA nanostructure monomers and dimers (see Fig. 3.2c). While cytosine overhangs (C) do not mitigate clustering, a monomer band appears for both guanine (G) and adenine (A) overhangs. However, the highest monomer band intensity was observed for thymine overhangs (T). This makes thymine nucleotides most efficient at preventing stacking interactions consistent with calculations on free stacking energies [159]. Further extension of

the overhangs to up to three thymine nucleotides (TTT) almost entirely eliminated aggregation leaving an intense monomer band with low presence of dimers.
Although the structure is formed from 128 bp and 24 nt of ssDNA overhangs, the monomer band appears slightly below the 400 bp mark. As DNA ladders are composed of pieces of double-stranded DNA of various lengths, they can only be used as a relative comparison for DNA nanostructures, for example across different gels, as the geometry of the nanostructure is different from dsDNA which alters its running behaviour in the gel. To verify that this most intense band indeed refers to monomeric nanostructures, transmission electron microscopy was employed which will be discussed in Section 3.3.4.

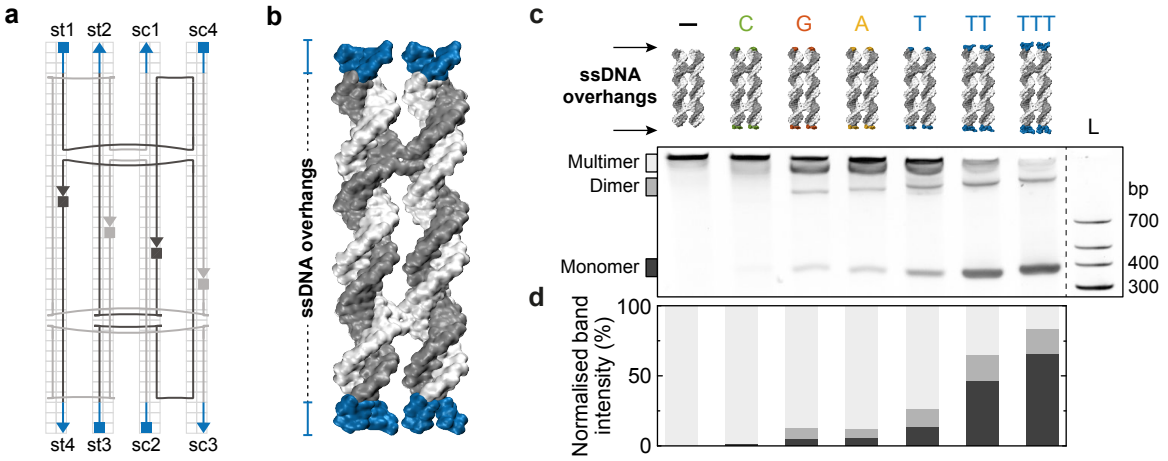

Fig. 3.2 Dependence of inter-structural stacking on the ssDNA overhang type. (**a**) 2D layout of the nanostructure design including strand names. Single-stranded DNA overhangs are highlighted in blue. (**b**) 3D representation illustrating the position of the ssDNA overhangs. (**c**) PAGE analysis of DNA nanostructures folded with various overhanging ssDNA bases on all eight ends ranging from single nucleotides (C, G, A, or T) to multiple thymines (TT and TTT). Specific DNA sequences for each design are listed in Table A.1 in the Appendix. The amount of monomeric structures increases while aggregation in the pocket decreases the more thymine overhangs are employed. L denotes a DNA ladder (see Section 3.2). Samples and ladder were run on the same gel but space between them was omitted as indicated by the dashed line. (**d**) Histogram plotting the intensities of monomer, dimer, and multimer bands normalised to their sum per lane.

Determining the band intensity of monomers, dimers and multimers normalised per lane, results in a quantitative analysis of their respective yield (see Fig. 3.2d). The optimised structure with TTT overhangs yields a band intensity of 66 % for monomers, 18 % for dimers, and 16 % for multimers. However, it needs to be pointed out that larger DNA structures result in more intense bands as the signal is determined by the number of dye molecules that intercalate into the DNA, which is larger for bigger structures. Therefore, simply judging by

the intensity of the dimer and multimer bands, their actual share in the sample mixture will be overestimated thereby underestimating the monomer yield. Assuming a linear relationship between DNA nanostructure size and intercalating number of dye molecules, Equation 3.1 can be used to achieve a more representative estimate:

$$\begin{aligned} \%_{Monomer} &= 100 - \%_{Dimer} - \%_{Multimer} \\ &= 100 - \frac{I_{Dimer}}{2} - \frac{I_{Multimer}}{n} \end{aligned} \tag{3.1}$$

where $n \geq 3$ is the number of monomeric structures the multimers are formed of, and I_{Dimer} and $I_{Multimer}$ are the percental proportion of dimers and multimers judging by their respective band intensity (as plotted in Fig. 3.2d). For $n = 3$, to gauge a lower limit of the monomer yield, Equation 3.1 results in a monomer folding yield of ≈ 86 %. This means that in a solution of folded DNA nanostructures with TTT overhangs, roughly 86 % can be assumed as being monomeric. Following the trend of increasing monomer band intensity with higher number of thymine ssDNA overhangs, this yield could possibly be even more improved by adding a fourth thymine nucleotide to the overhangs. Interestingly, the same trend is not observed in the dimer band intensities (12 % for T, 19 % for TT and 18 % for TTT). This could mean that dimer formation is not caused by stacking interactions but rather due to misfolding.

Studying the number of single TTT extensions on each side of the design revealed that all eight overhangs (four on each side) are necessary to effectively reduce clustering (see Fig. 3.3). Including overhangs on only one side of the construct resulted in a mixture of clustering and a pronounced band at a shorter run length (4|0 in Fig. 3.3). As this design favours dimer formation of DNA nanostructures via stacking interactions of the blunt double-stranded DNA ends on one side, the intense, slow migrating band can be identified as DNA nanostructure dimers, confirming the initial interpretation.

Due to the results of these experiments, the DNA nanostructure will always be folded with eight TTT overhangs, unless stated otherwise.

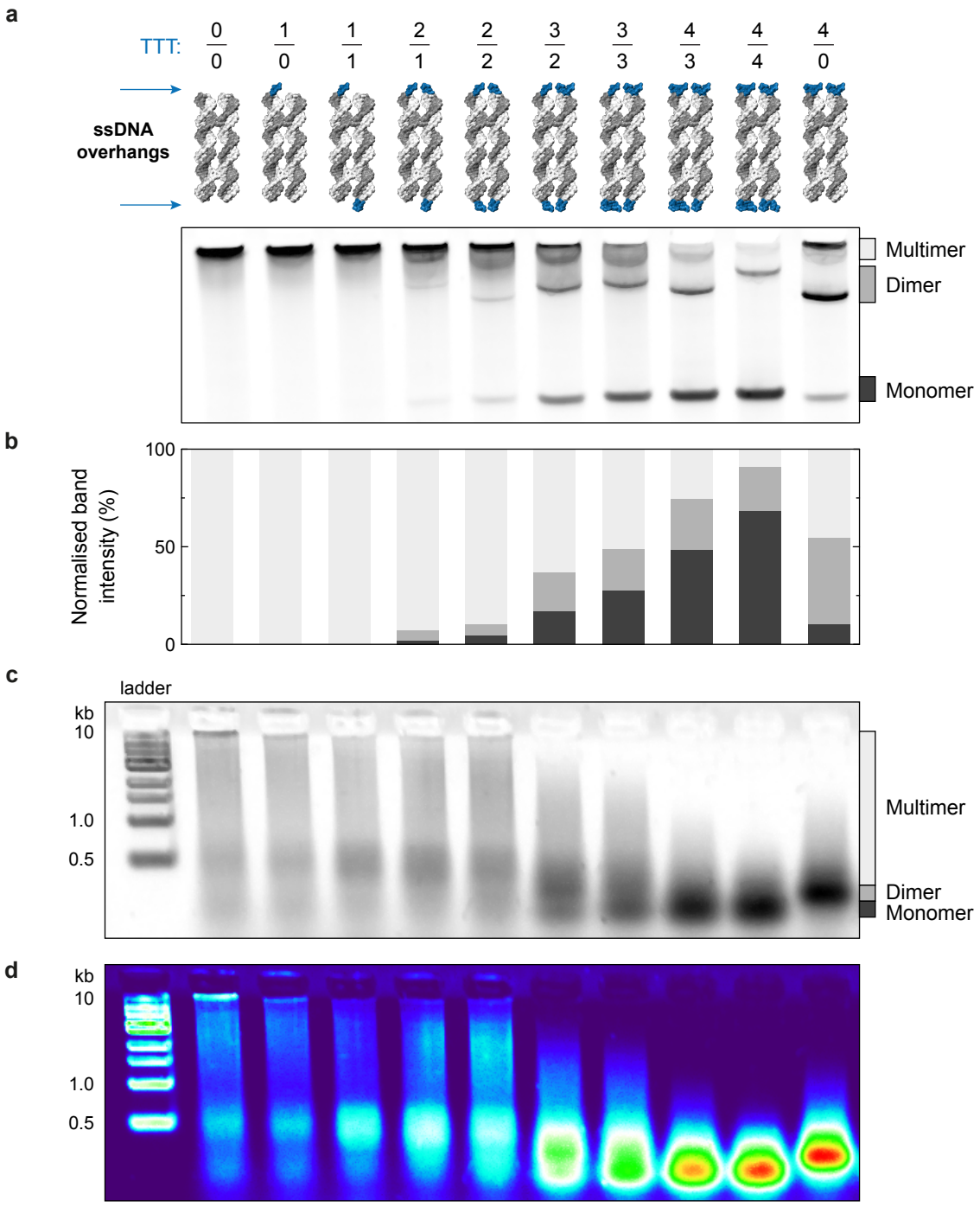

Fig. 3.3 Dependence of inter-structural stacking on the number of TTT overhangs. (**a**) PAGE analysis of DNA nanostructures folded with gradually increasing numbers of TTT overhangs on each side of the nanostructure. (**b**) Histogram plotting the intensities of monomer, dimer, and multimer bands normalised to their sum per lane. (**c,d**) 2 % agarose gel of samples analysed in **a** shown as greyscale (**c**) and false colours (**d**) to highlight changes in band intensities. Ladder refers to 1 kb DNA ladder (New England Biolabs). For an overview of the stepwise introduction of DNA strands with TTT overhangs, see Table A.2 in the Appendix.

3.3.3 Folding yield dependence on magnesium concentration

In the previous section, the DNA nanostructures were folded in 1x TE and 20 mM $MgCl_2$. This buffer was chosen as a starting point as it has previously been successfully employed to fold a DNA construct of similar geometry [54]. To explore how our particular design folds at different Mg^{2+} concentrations, the DNA nanostructure has been assembled at various concentrations of $MgCl_2$ and analysed with PAGE (see Fig. 3.4a).

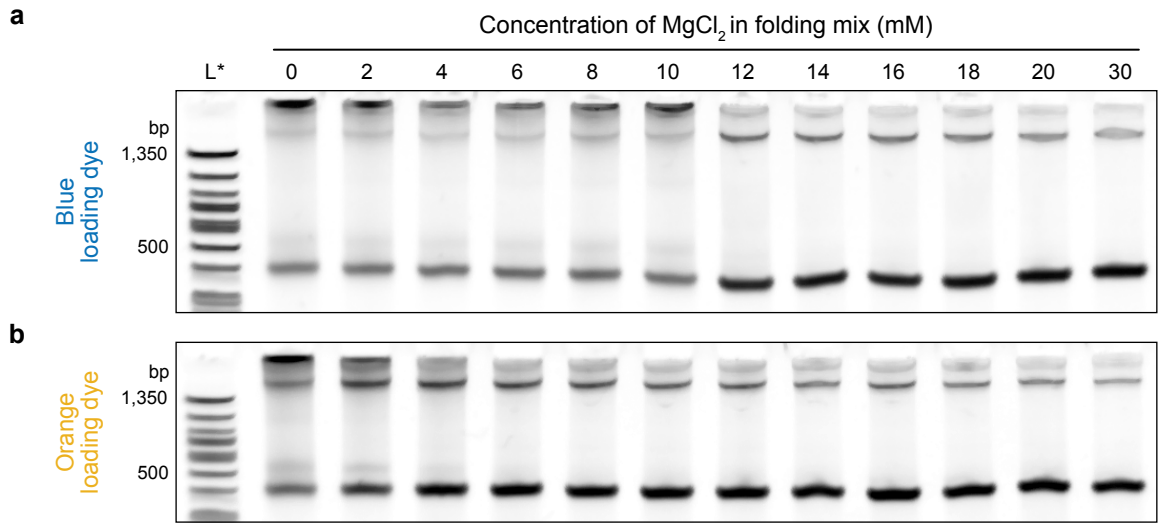

Fig. 3.4 Influence of loading dye on DNA nanostructure analysis. DNA nanostructures were folded at varying concentrations of $MgCl_2$ between 0 and 30 mM and loaded into the gel pocket either using blue (**a**) or orange (**b**) loading dye each at 1x final concentration (for buffer contents see Table 3.6). L* refers to a 50 bp DNA ladder (New England Biolabs).

The gel shows that even without additional Mg^{2+} ions during the assembly, a certain amount of structures fold to form monomers. This could be explained by the fact that the DNA nanostructure is very small and electrostatic repulsion of the DNA strands does not impair folding as much as it would for larger DNA origami constructs. However, for $MgCl_2$ concentrations up to 10 mM a significant portion of structures remains as clusters in the gel pocket. From 12 mM onwards, these clusters are suddenly reduced and the results are comparable to previous ones obtained when studying single-stranded overhangs. While this suggests that this DNA nanostructure design only folds well for $MgCl_2$ concentrations above 10 mM, the result is actually an artefact of the loading dye used to load the samples into the gel pockets. At the final 1x concentration used for loading, the employed, commercially available blue loading dye still contains 11 mM EDTA in it (for dye contents see Table 3.6). EDTA is a chelator for metal ions with the following hierarchy in binding affinity:

$$Fe^{3+} > Cu^{2+} > Pb^{2+} > Zn^{2+} > Cd^{2+} > Co^{2+} > Fe^{2+} > Mn^{2+} > Ca^{2+} > Mg^{2+}$$ [160].

Table 3.6 Comparison of blue and orange loading dye contents at 1x concentration. Orange dye was prepared using TE20 buffer. As DNA nanostructure samples are already in TE20 buffer, the 6x orange dye only needs to match it but does not need to be more concentrated.

	1x Blue loading dye	1x Orange loading dye	Unit
Dye	Bromophenol blue	Orange G	
	0.015	0.15	% (w/v)
Ficoll®-400	2.5	2.5	% (w/v)
EDTA	11	0.17	mM
Tris-HCl	3.3	1.7	mM
SDS	0.017	—	%
$MgCl_2$	—	3.3	mM
pH	8.0	8.0	

While its affinity is higher for other metal ions, EDTA is still a very effective chelator for Mg^{2+} ions. This means that loading the sample with the commercially available blue dye results in a reduction of free Mg^{2+} ions as they are captured by EDTA in a 1:1 ratio [161]. Although this reduction is post-assembly and only during the gel sample preparation and loading, EDTA could even chelate Mg^{2+} ions that are already bound to the DNA. The magnitude of this effect can be highlighted by loading the same exact samples onto a gel using a custom-made gel loading dye with only 0.17 mM EDTA (see Table 3.6 for orange dye contents). The resulting gel reveals that DNA nanostructure aggregation only occurs at very low $MgCl_2$ concentrations and is already significantly reduced from ~6 mM onwards (Fig. 3.4b). This means, that the EDTA-containing blue loading dye affected the interpretation at which $MgCl_2$ concentrations the DNA constructs fold well. The sudden change between assembly at 10 mM and 12 mM supports this interpretation as this exactly bridges the 11 mM threshold of EDTA. It also shows that depletion of Mg^{2+} ions leads to DNA nanostructure aggregation, even after they have been correctly assembled beforehand.
It should be noted that the custom-made 6x loading dye (orange dye) contains 20 mM $MgCl_2$. However, this is not expected to significantly interfere with the results as this change in $MgCl_2$ concentration only happens after the folding process. If the assembly was successful, it should not reduce the yield. If the assembly was not successful, it will not significantly increase the yield as most structures aggregate without proper thermal annealing (Fig. 4.12b). For these reasons, the custom-made dye will be used exclusively from here on.
For large DNA origami nanostructures, typically a rather narrow range of $MgCl_2$ concentration yields successfully folded structures [35, 55]. To determine if there is such an optimal concentration for this nanostructure design, the band intensities of monomers, dimers and multimers have been analysed as illustrated in Fig. 3.5. From approximately 6 mM $MgCl_2$ onwards, monomer band intensities dominate compared to aggregates. Increasing the $MgCl_2$

concentration to 20 mM further enhances the monomer intensities from 54 % to 68 %, while both dimer and multimer formation decrease from 29 % to 20 % and 18 % to 12 %, respectively. Even though 30 mM improves the monomer yield even slightly more, some experiments require a low amount of $MgCl_2$, which would be more difficult to achieve after assembly without diluting the DNA nanostructures too much. Furthermore, a number of protocols have been established previously on DNA nanostructures folded at 20 mM in our group. For these reasons, the optimal $MgCl_2$ concentration to fold this design at was chosen to be 20 mM and, if not stated otherwise, was used from here onwards.

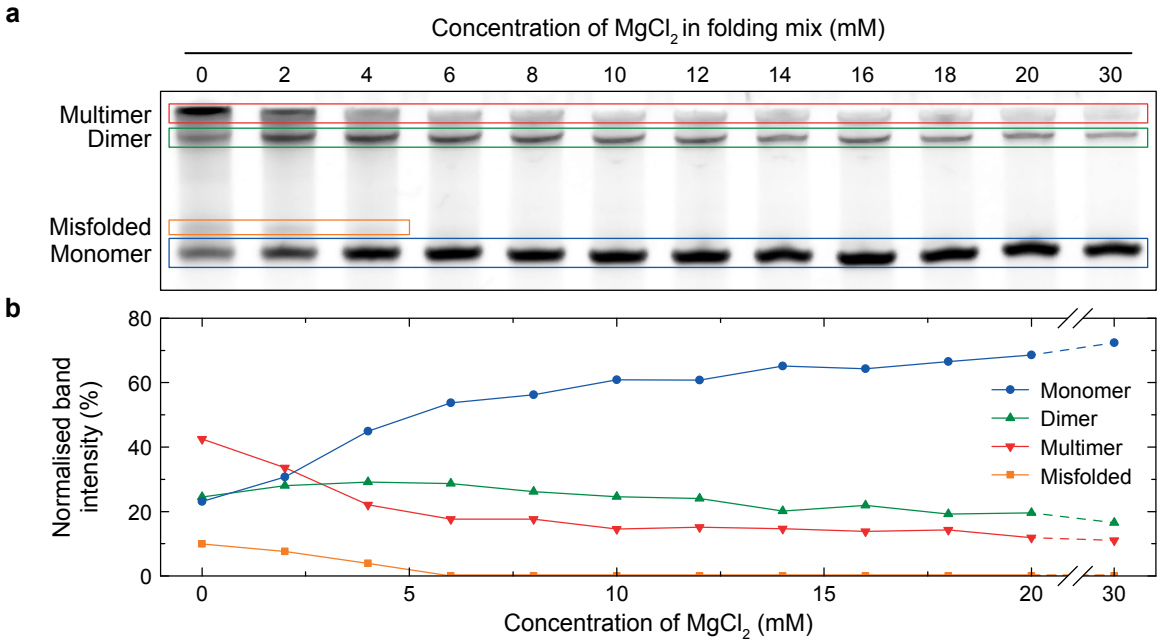

Fig. 3.5 Dependence of DNA nanostructure folding yield on the concentration of $MgCl_2$ in the folding mix. (**a**) Same PAGE analysis of DNA nanostructures folded at different concentrations of $MgCl_2$ as shown in Fig. 3.4b. Coloured sections highlight monomer, dimer, and multimer bands, as well as a small population of misfolded nanostructures at low $MgCl_2$ concentrations. (**b**) Graph showing the normalised intensity of bands referring to monomeric, dimeric, multimeric, or misfolded nanostructures as shown in **a**. For the analysis, care was taken that none of the band intensities were saturated.

3.3.4 Size verification of DNA nanostructures with AFM & TEM

AFM measurements

In the previous sections we have applied gel electrophoresis to analyse the different size populations of the folded DNA nanostructures which allowed us to optimise the design and folding protocol to maximise the amount of monomeric structures. However, DNA reference

ladders cannot be used to judge the absolute size and geometry of the DNA nanostructures. Atomic force microscopy (AFM) has previously been applied successfully to measure the size and geometry of assembled DNA nanostructures [30, 45, 54, 74, 162, 163]. To determine the dimensions of this particular design, assembled structures were deposited on a mica surface and imaged in air. The recorded AFM images shown in Figs. 3.6a,b reveal a relatively homogeneous distribution of elevated spots resembling the DNA nanostructures.

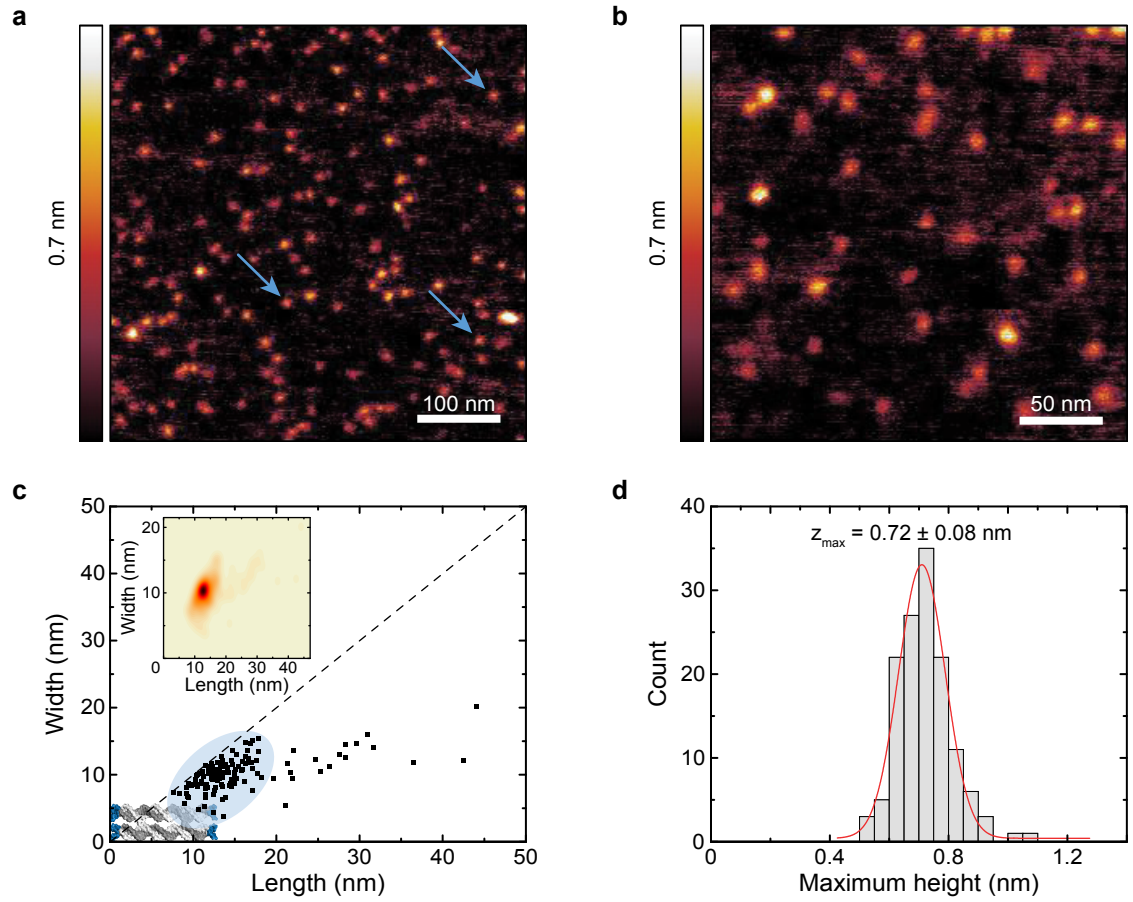

Fig. 3.6 Atomic force microscopy analysis of DNA nanostructures. (**a,b**) Topographic AFM images showing DNA nanostructures deposited on a mica surface and imaged dry. Arrows indicated likely monomeric structures. Images were acquired by M. Ricci. (**c**) Graph depicting the lengths and widths derived from ellipses fitted to the nanostructures shown in **a**. The dashed line indicates circularly shaped structures. Blue area highlights data most likely referring to monomeric nanostructures. The model of the DNA nanostructure in the lower left corner is scaled to the theoretical dimensions. Inset shows a 2D density plot peaking at $\approx$ 12.8 nm and $\approx$ 10.3 nm length and width, respectively. (**d**) Histogram of the maximum height distribution of DNA constructs. Red line represents a Gaussian fit. Data in **c,d** was obtained from 136 structures identified in **a**.

The dimensions, measured from ellipses automatically fitted to the structures, show a clear asymmetry due to the deviation from the dashed line which would indicate a circular shape (see Fig. 3.6c). The majority of data points is localised at the low end of the size spectrum between ~10 and 20 nm which most likely represent monomeric DNA nanostructures (see blue area and inset in Fig. 3.6c). The low number of determined larger structures could refer to dimeric or multimeric structures. The fact that the larger measured constructs increase in asymmetry could indicate that the dimeric and multimeric DNA constructs might be connected longitudinally on their short edge. However, due to the sample density the larger sizes could also be monomers located too close to each other to be successfully resolved.
The average length (a_{major}) and width (a_{minor}) for monomeric DNA nanostructures (blue shaded area in Fig. 3.6c) was determined to be 13.2 ± 2.3 nm and 9.9 ± 2.1 nm (mean ± SD), respectively. The length matches very well with the theoretical value of ≈ 13.1 nm given that tip convolution could cause the structures to appear larger [164]. The width, however, amounts to roughly double of the expected value of ≈ 5.0 nm which could have several reasons. The dimensions of the nanostructures might be smaller or on the order of the size of the AFM tip which would represent a measurement of the tip geometry rather than the actual sample. Another possibility for the constructs approximately doubling in width could be that they might have adhered onto the surface due to the positive Mg^{2+} ions present during the sample deposition. Lastly, sample deformation could occur due to the applied forces onto the DNA constructs by the oscillating, probing AFM tip. The latter explanation would agree with the maximum height distribution averaging only at z_{max} = 0.72 ± 0.08 nm (mean ± SD; Fig. 3.6d). Such a height has previously been reported for DNA embedded in a salt layer imaged in air together with the observation that DNA height was always less than the theoretical value when determined with AFM (even without a salt layer) due to elastic deformation caused by the interaction of the tip with the sample [165].

TEM measurements

Although atomic force microscopy did provide some more information about the size and geometry of the DNA nanostructures, the determined dimensions only matched in length with the expected value but not in width. While these results could eventually be the actual sizes of the DNA nanostructures, meaning that it did not assemble as expected, multiple reasons were presented why and how the AFM measurement method inherently could have influenced the result to cause the increased width. A further improvement of measuring the dimensions of the DNA constructs could be expected by performing transmission electron microscopy (TEM). TEM imaging has frequently been employed to determine the dimensions of assembled DNA nanostructures [35, 36, 166–168]. By applying this technique, the lowest

resolvable, structural feature is not related to a tip size and no elastic deformations due to compression forces would bias the measurements.

Figure 3.7 summarises the results obtained from TEM analysis of positively stained DNA nanostructures. Heavy ions in the uranyl acetate staining solution accumulate on the DNA constructs which results in an increased scattering probability for electrons in the beam due to the larger cross-section of the uranium ions. Therefore, areas with higher contrast are associated with the DNA constructs (Figs. 3.7a,b,d).

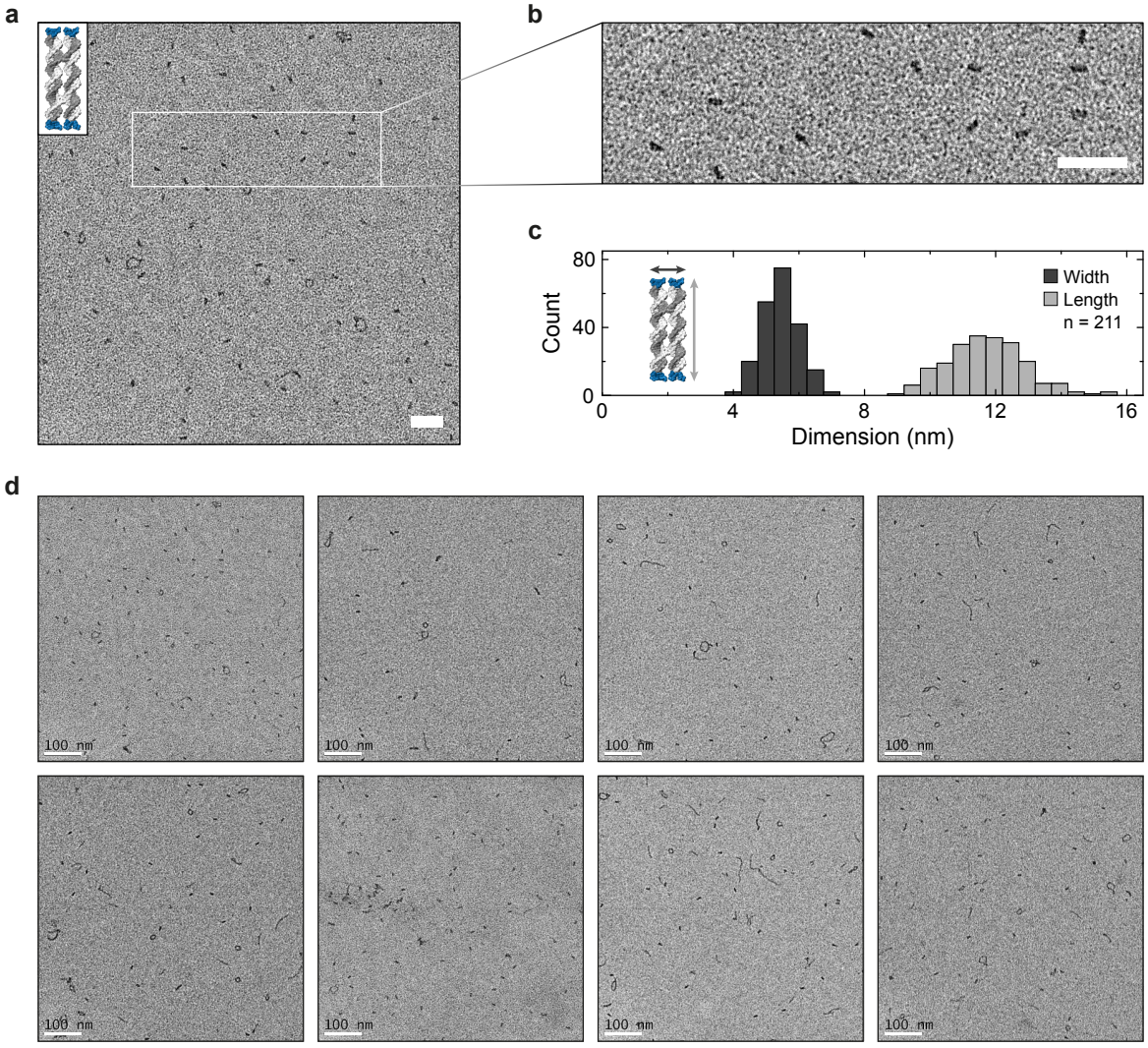

Fig. 3.7 Transmission electron microscopy analysis of DNA nanostructures. (**a**) Example TEM micrograph of positively stained DNA nanostructures. A magnified view (**b**) shows the monomeric DNA nanostructures as dark, rectangular shapes. White scale bars denote 50 nm. (**c**) Histogram of the length and width distribution of monomeric DNA nanostructures obtained from 211 structures. (**d**) TEM micrographs used for size distribution analysis. White scale bars denote 100 nm. Images were acquired by R. F. Thompson.

In agreement with the PAGE results, only a small amount of multimeric structures is observed. The magnified view in Fig. 3.7b illustrates that the majority of structures is of similar size and rectangular geometry which is consistent with monomeric nanostructures laying flat on the TEM grid. The images in Fig. 3.7d also show that aggregates predominantly adopt chain- or ring-like structures which could represent multimers caused either by stacking interactions or incorrect strand hybridisation. However, these were not observed with AFM analysis so they could also be an artefact emerging from the sample preparation, for example due to uranyl acetate staining.

Analogously to the analysis of the AFM data, images were flattened, an intensity mask was applied and ellipses were automatically fitted to obtain the dimensions of the DNA structures. As predominantly the size and geometry of monomeric constructs were of interest, masked regions of aggregated structures were excluded. The lengths and widths of over 200 monomeric DNA nanostructures were measured from the images shown in Fig. 3.7d yielding an average length of 11.7 ± 1.2 nm and width of 5.4 ± 0.6 nm (mean ± SD; Fig. 3.7c). The length matches well with the expectations given that only the central 10.6 nm of the DNA constructs consist of double-stranded DNA. While the overhanging TTT ssDNA bases extend the total length to $\approx$ 13 nm, their reduced contrast is likely to bias the measurement towards shorter dimensions. An explanation for the slightly wider than expected $\approx$ 5 nm width could be electrostatic repulsion between the DNA strands of the structure. Cryo-electron microscopy of larger DNA origami structures has shown that the distance between the midpoints of neighbouring duplexes can vary between 1.85 nm (at DNA crossover positions) and 3.6 nm [168]. Furthermore, as the structures were positively stained, the slightly larger width could result from uranyl atoms predominantly binding to the DNA backbone [169] making the DNA structures appear wider without affecting their length.

In summary, while AFM measurements provided some insight into the size and geometry, particularly the width of the DNA nanostructures significantly differed from the expected value possibly due to tip-sample interaction. Analysis with TEM, however, introduced fewer possible biases and provided results closer to the theoretically expected ones. The currently applied method of determining dimensions by fitting ellipses to the structures might have introduced some deviation as well. A most likely more accurate approach would be to perform class-averaging on a large sample size of imaged structures and measure the geometry from this. Furthermore, negatively stained nanostructures could yield even more representative dimensions as well. Nevertheless, we could conclude from these results that the DNA nanostructures fold correctly with approximately the expected size and geometry.

3.3.5 Comparison to alternative DNA nanostructure designs

Figure 3.8 presents an overview of different DNA nanostructure designs comparing previous ones to the ones devised in this work. Each design is accompanied by a mechanistic simulation using the web-based tool CanDo [37] which provides a rapid computational feedback on the 3D structure and flexibility (right in Fig. 3.8). All of these structures were designed to be used for insertion into lipid bilayers. The ones devised in our group (CP = Cambridge Pore) are all based on a 4-helical architecture differing in length and strand layout. While CP1 was designed previously [54], CP2 to CP4 were created within this thesis work. The 6HP design has been devised and studied extensively by another group [72].
In order to compare the designs, all structures have been assembled at 1 µM in TE20 buffer using the 18 hour folding protocol described in Section 3.2. The necessary sequences to fold each structure are summarised in Table A.3 in the Appendix. These sequences were also used to determine the molecular weights of the nanostructures. The folded constructs have then been analysed with PAGE (see Fig. 3.9a).
The gel shows clear monomer bands for all designs while the amount of dimer and multimer formation varies between them. Although the DNA ladder cannot be used as a direct size reference, the nanostructures themselves could. The graph in Fig. 3.9b plots the molecular weight of the DNA nanostructures over their run length in the gel. For dimer structures, simply double the monomer weight was assumed. The linear fit to both monomers and dimers agrees very well with the linear fit to only the monomers, which further confirms that the often observed upper intensity band in the gel refers do dimeric nanostructures. Interestingly, the designs CP1, CP2, CP3 and 6HP have very similar molecular weights yet quite different run lengths. This could be explained by their varying structural rigidity. The CanDo simulations show that CP3 is the most rigid, followed by CP2, then CP1, and 6HP being the most flexible. As additional flexibility increases the hydrodynamic radius, more flexible designs will travel slower through a gel matrix and more rigid designs will travel faster. The fact that these differences are confirmed in the gel in turn verifies that the simulated mechanical properties of the DNA nanostructures could indeed indicate realistic design-specific characteristics. In the following section the advantages and disadvantages of each design will be discussed.

CP1. This design has previously been employed in our group and demonstrated lipid membrane insertion and ion conduction with gating and voltage-switching behaviour [54]. The staple pattern follows a previously introduced DNA tiles principle to form arbitrary two-dimensional DNA shapes [53]. While this design yields a distinctive monomer band in the gel with little clustering in the pocket, some additional bands between the monomer

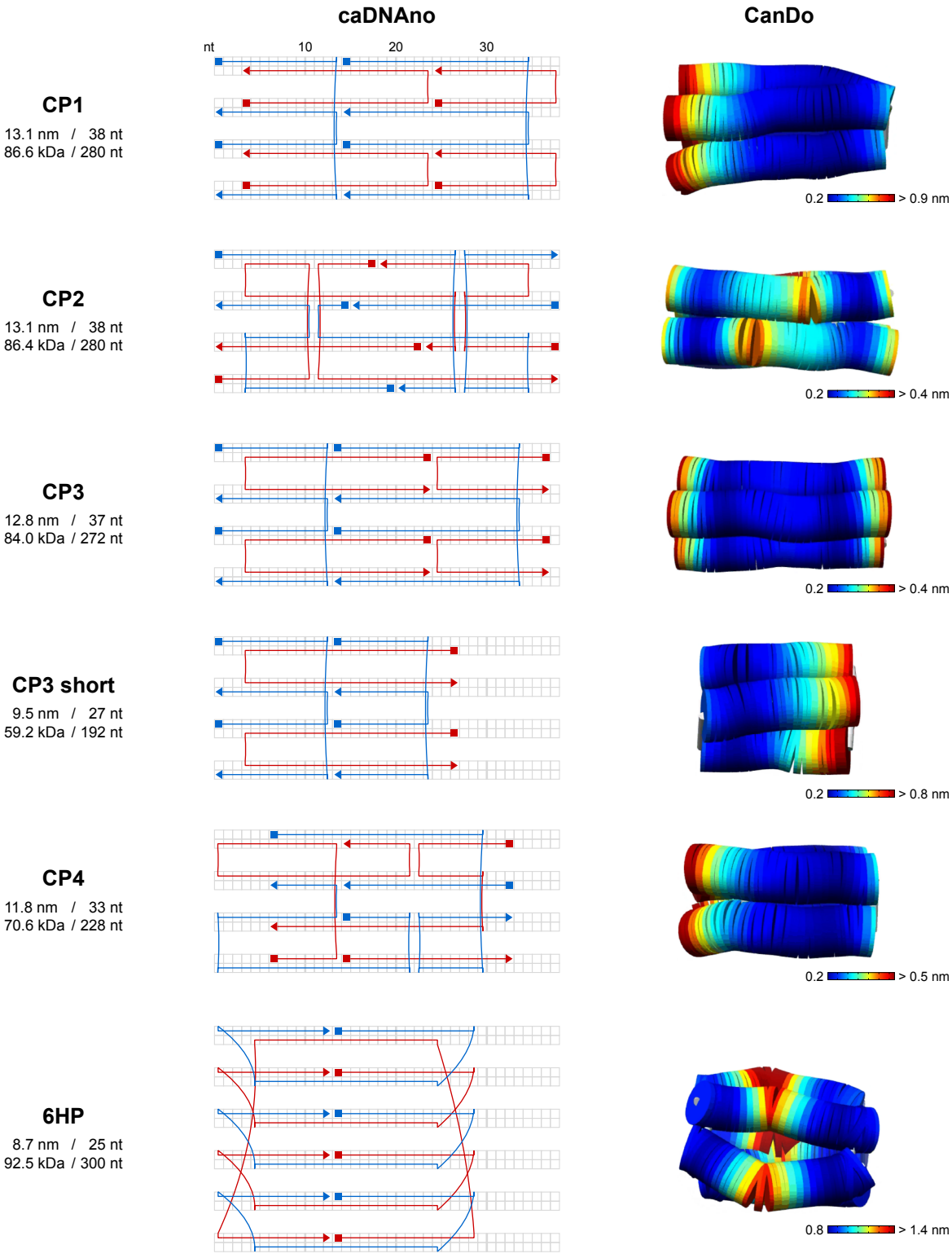

Fig. 3.8 Overview of different DNA nanostructure designs. CP1 and 6HP have been published previously [54, 72]. All other designs have been devised in this work. Lengths are approximated similarly as for the design presented in Fig. 3.1 in Section 3.3.1.

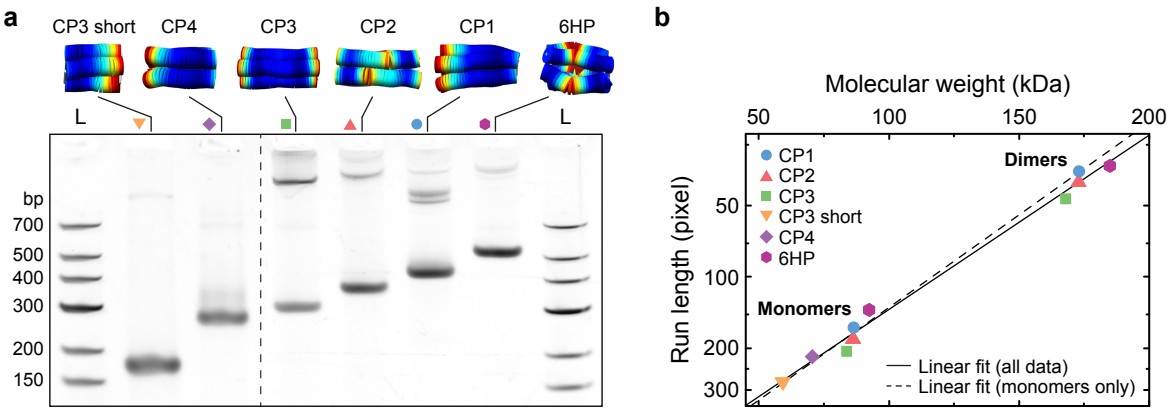

Fig. 3.9 Analysis of different DNA nanostructure designs. (**a**) PAGE analysis of different, assembled DNA nanostructure designs together with their CanDo simulations at the top. Samples were run on the same gel but space between them was omitted as indicated by the dashed line. (**b**) Graph displaying the run length of the monomer and dimer bands from the gel shown in **a** over the respective molecular weight of the different DNA nanostructures. Dimer molecular weights were simply assumed to be double the monomer weight. Run lengths were measured in pixel with respect to the particular well of each lane. Linear fits are either to all data points (solid) or to monomers only (dashed).

and dimer band are visible. These indicate the formation of some intermediate structures of unknown size and geometry. Furthermore, the design has a significant asymmetry regarding the distribution of crossovers that interconnect the helices. The caDNAno design shows that the first crossover appears after 14 nucleotides, approximately one third of the total design length. The CanDo simulations confirm that this asymmetric crossover distribution leads to an asymmetry in the rigidity of the structure showing increased noise on the left end of the construct. Lastly, the design does not follow the suggested crossover positions in the caDNAno software. While the crossover pattern works well for a large 2D plane, it could induce torsional stress in this design as the DNA strands are not close to each other at the crossover position due to their helical pitch. It also makes it less clear which way incorporated modifications would face in the design.

CP3. In this design, the previously discussed asymmetric crossover distribution of CP1 has been remedied simply by switching the orientation of four staples strands (red in Fig. 3.8). This creates a balanced distribution of crossovers and overall homogenises the noise and rigidity of the structure which is also visible in the CanDo simulations. However, the design still does not follow the typical pattern to place crossovers where the helical pitches of adjacent DNA strands are closest, similar to CP1, possibly inducing torsional stress.

Furthermore, the gel reveals a very prominent dimer band and some clustering. This could possibly be remedied by choosing different staple sequences.

CP3 short. This layout is based on CP3 but shortened by one section. Interestingly, this almost completely diminishes dimer or multimer formation, leaving the cleanest monomer band for all designs. However, this comes again at the cost of an asymmetric rigidity. While the small size of this construct could aid its membrane insertion potential, a significant downside is that it limits the amount of modifications that can be incorporated in the design. For DNA strands with a single modification, only two modifications can be placed in the central region which limits the options to place cholesterol tags to facilitate membrane insertion. Although it is possible to add two modifications to a single DNA strand, typically this increases the price while the yields are very low.

CP4. This is the second design with barely any tendency to form multimeric structures. The monomer band shows a slight smear which could be due to the floppy ssDNA loops on one end of the design. The advantage of this layout is that multiple cholesterol modifications can be placed in the central region. They can also be added slightly off-centre, adjacent to the ssDNA loop. This would allow the cholesterol to be shielded by the presence of the ssDNA, a feature which will be discussed more detailed in Chapter 4. While the design presents an asymmetry in the rigidity, the distribution of crossovers is rather homogeneous and they also follow the caDNAno design rules, which should avoid torsional stress.

6HP. While this 6-helical design is significantly different to the other designs, it is presented here as it has been the subject of multiple publications [72, 73, 78, 79, 93, 170, 171]. The six helices are interconnected by ssDNA loops, composed of four thymines each, which make this structure the least rigid which is also reflected in the CanDo simulations (note the different size range of the colour scale). This flexibility could pose a problem for example for single-molecule current measurements as it could add to the noise and induce a variety of conductances. The design allows for placing multiple cholesterol modifications in the central region. However, it does not easily facilitate the incorporation of fluorescent dyes as they would also have to be placed in the central region, possibly interfering with the membrane interaction, or modified internally to a DNA strand which is typically more expensive. Lastly, as it is a 6-helical pore, the hollow central lumen allows for transport of molecules. While this could be exploited, in this work it is a disadvantage as it creates a passage for dithionite which is undesirable in the lipid scrambling assay that will be discussed more in depth in Chapters 5 and 6.

CP2. In this direct comparison, many advantages of this design become apparent. Due to the array of DNA nicks around the central region, it can be equipped with up to eight modifications at once while still only using single-modified DNA strands. Alternatively, modifications can be placed on the outer edges of the design which is ideal to separate functional parts. For example cholesterol modifications to facilitate membrane insertion can be placed in the central part while fluorescent dyes to track the structures can be positioned at the ends, thereby not interfering with the membrane-inserted middle region. Furthermore, the design follows the crossover rules of caDNAno which should minimise torsional stress. It also allows to place the central nicks at positions where modifications on the 3' and 5' ends are diagonally facing away from the structure. Although the PAGE results do show some dimer and slight multimer formation, it is comparable to previously employed designs. Lastly, the layout is point symmetric to the centre, giving it no preferred directionality and homogeneous rigidity throughout as confirmed by the CanDo simulations. The design therefore strikes a balance between homogenous structural properties that follow caDNAno crossover rules, high yield of monomeric structures, and large customisability with chemical modifications. This is why it was chosen as the basic structure to create a synthetic lipid scramblase.

3.4 Conclusion

In this chapter, the fundamental design of the DNA nanostructure was presented that will be used throughout this work. PAGE was employed for the initial analysis to optimise the yield of folded monomeric structures. A folding buffer with 1x TE and 20 mM $MgCl_2$ yielded the highest amount of monomers without using excessive amounts of $MgCl_2$ which could cause problems in later experiments. Overhanging ssDNA strands were incorporated at the ends of the design to reduce nanostructure aggregation caused by base pair stacking interactions. It was shown with PAGE that overhangs composed of three thymines reduced aggregation best, leading to a monomer yield of ≈ 86 %. Possibly four thymines could improve the folding yield slightly further and could be implemented in future experiments using the CP2 design. While AFM measurements could roughly confirm the length of the DNA nanostructure, the width was wider than expected. This could be explained by the AFM tip being of a similar size as the DNA nanostructure and possible deformation of the DNA constructs due to sample-tip interaction. TEM analysis remedied these measurement artefacts and indeed yielded a length of 11.7 ± 1.2 nm and width of 5.4 ± 0.6 nm which are very close to the expected values. A further improvement in determining the precise dimensions could be to use negatively-stained DNA nanostructures rather than positively-stained ones. In summary, gel electrophoresis confirmed a high proportion of monomeric structures, and TEM measurements verified that these monomers are of the expected size and geometry.
Compared to previous and alternative DNA nanostructure layouts, the CP2 design stood out due to its balance of homogeneous rigidity, structural symmetry, comparatively high folding yield, and the advantageous location and high number of modification positions, and will therefore be used for further applications in this work. However, the smaller CP3 short design, despite the limited number of modification positions, could still be interesting as it formed almost exclusively monomers and its small form factor could aid membrane insertion. Also the CP4 design could potentially be used in future experiments as it had a high folding yield and cholesterol modifications could be adjacent to ssDNA loops which could shield their hydrophobicity and reduce aggregation (a method discussed further in Chapter 4).
The gained information from the in-depth analysis of the CP2 design presented in this chapter will provide an important basis for judging the results of further experiments involving cholesterol modifications, membrane insertion, and the application of this nanostructure as an artificial DNA scramblase.

Chapter 4

Controlling aggregation of cholesterol-modified DNA nanostructures

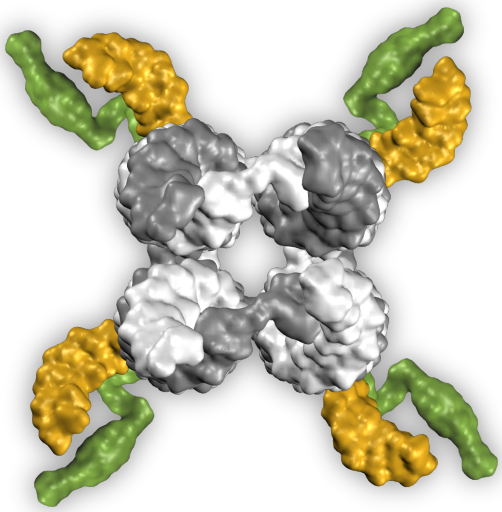

Parts of this work previously appeared in:

A. Ohmann, K. Göpfrich, H. Joshi, R. F. Thompson, D. Sobota, N. A. Ranson, A. Aksimentiev, and U. F. Keyser. 'Controlling aggregation of cholesterol-modified DNA nanostructures.' *Nucleic Acids Research*, 47(21):11441–11451 (2019).

A. Ohmann, C. Y. Li, C. Maffeo, K. Al Nahas, K. N. Baumann, K. Göpfrich, J. Yoo, U. F. Keyser, and A. Aksimentiev. 'A synthetic enzyme built from DNA flips 10^7 lipids per second in biological membranes.' *Nature Communications*, 9:2426 (2018).

4.1 Introduction

... and the other part of it is to modify DNA. But to do things with modified DNA is very hard – that takes a lot of work by talented people.

– Nadrian C. Seeman

The previous chapter focused exclusively on understanding and optimising the DNA nanostructure itself. With the CP2 design having shown the most promising characteristics, the next step is to equip it with the capability to self-insert into a lipid bilayer such as a cell membrane. The key to inserting the negatively charged DNA into lipid membranes are hydrophobic groups specifically positioned on the DNA constructs. As outlined in Section 2.2 in Chapter 2, cholesterol is the most prominent hydrophobic modification to facilitate the insertion of DNA nanostructures into lipid bilayers. However, a fundamental challenge is the strong tendency of DNA-cholesterol conjugates to aggregate [70, 79–81, 172]. While aggregation can be exploited as a switching mechanism [80] or to grow DNA crystals [173], it is undesirable for most applications as a precise structure-function relationship requires well-defined monomeric components. Krishnan *et al.* designed a large DNA-built channel decorated with 57 hydrophobic anchors which demonstrated increased membrane interaction but aggregated in solution [70]. Johnson-Buck *et al.* reported reduced hybridisation kinetics by ~6 to 9 times of cholesterol-modified ssDNA compared to unmodified ssDNA [81]. They also observed clustering of DNA-cholesterol nanostructures forcing them to use fewer cholesterol modifications to reduce aggregation. Already two cholesterol moieties have been shown to induce oligomerisation in the assembly of DNA origami blocks [172]. Cholesterol-mediated aggregation was also observed to cause extremely low binding efficiencies to artificial lipid vesicles [174]. Even after successful insertion, DNA nanostructures with three cholesterol moieties have been reported to form aggregates in a lipid bilayer [78].
Nevertheless, higher numbers of cholesterol tags on a DNA construct are desirable and often necessary to facilitate spontaneous membrane insertion [70]. Their collective free energy gain upon membrane incorporation reduces the energy barrier for DNA nanostructures to self-insert into a lipid bilayer [74, 175], thereby facilitating more efficient membrane interaction. This intricate balance between an increased number of hydrophobic moieties while keeping aggregation at a minimum is typically only found by time-consuming trial and error. To overcome this long-standing challenge, this chapter will provide systematic insight into the factors that govern the aggregation of cholesterol-modified ssDNA, dsDNA and DNA

nanostructures. With non-denaturing (native) PAGE and all-atom molecular dynamics (MD) simulations, we initially analyse the aggregation of cholesterol-tagged ssDNA (chol-DNA). We then establish a mechanism to reduce cholesterol-mediated interactions of a DNA duplex by incorporating ssDNA overhangs adjacent to the hydrophobic group. Using transmission electron microscopy, PAGE and dynamic light scattering (DLS), we characterise our devised DNA nanostructure and its aggregation behaviour depending on the cholesterol number, modification position and linker type. Finally, we show that ssDNA overhangs adjacent to the cholesterol can be applied as a universal mechanism to control the aggregation of hydrophobically modified DNA nanostructures.

4.2 Materials & Methods

4.2.1 DNA nanostructure assembly

DNA nanostructures were designed using caDNAno software [36]. In order to maximise specificity of the different strands, sequences were optimised to minimise secondary structure and unwanted base pairing using the web-based DNA analysis tool NUPACK [38]. Unmodified DNA oligonucleotides were purchased from Integrated DNA Technologies, Inc. (IDT), purified by standard desalting or PAGE, and delivered at 100 µM in IDTE (10 mM Tris, pH 8.0, 0.1 mM EDTA). Required DNA strands for a specific construct were mixed at a final concentration of 1 µM in TE20 buffer (10 mM Tris, 1 mM EDTA, 20 mM $MgCl_2$, pH 8.0). The mixture was heated to 85 °C or 95 °C for 5 min, subsequently cooled to 25 °C over 18 hours and finally stored at 4 °C, as described previously [75]. If not stated otherwise, 3'-modified cholesterol strands were purchased from IDT with a triethylene glycol (TEG) linker, while 5'-modified strands were acquired from biomers.net with either a TEG or a C6 linker. Chol-DNA strands were HPLC-purified, delivered dry, and only then diluted in Milli-Q water (Merck Millipore) to a concentration of 100 µM and stored at 4 °C. Prior to addition to the assembly mix, chol-DNA strands were vortexed briefly, spun down in a tabletop centrifuge and heated to 55 °C for 10 min. Chol-DNA was incorporated into the DNA nanostructure by adding it to the assembly mix at 1 µM final concentration (1:1 ratio towards unmodified strands) while the respective unmodified oligonucleotide with the same sequence was omitted.

4.2.2 Non-denaturing polyacrylamide gel electrophoresis

Chemicals were acquired from Sigma-Aldrich and gels were run in a Mini-PROTEAN Tetra Cell (Bio-Rad). Gels were hand cast at a final concentration of 10 % polyacrylamide supplemented with 0.5x Tris-borate-EDTA (TBE) and 11 mM $MgCl_2$. Per 15 ml gel mixture, 150 µl 10 % (w/v) ammonium persulfate solution (aliquots kept at −20 °C and freshly thawed each time) and 10 µl N,N,N',N'-Tetramethylethylenediamine (TEMED) were added to start the polymerisation which was typically left to set for at least 1 hour before running the gel. 2 µl of assembled DNA nanostructures at 1 µM were mixed with 0.4 µl custom-made 6x loading dye (6x: 15 % Ficoll 400, 0.9 % Orange G diluted in TE20) and 2 µl of the mixture were loaded into the well, as described in Chapter 3. For chol-DNA only, 1 µl of 100 µM chol-DNA solution (pre-heated as described in DNA nanostructure assembly) was mixed with 9 µl Milli-Q water and 2 µl of custom loading dye (this time prepared in Milli-Q water instead of TE20) and between 1 and 3 µl of this mixture were loaded. For

duplexes of DNA and chol-DNA, strands were mixed at a 1:1 stoichiometric ratio in 50 mM NaCl and left at room temperature for 30 min before loading. GeneRuler Low Range (L; Thermo Fisher Scientific Inc.) or a 50 bp DNA ladder (L*; New England Biolabs) were employed as reference DNA ladders. Gels were run in 0.5x TBE supplemented with 11 mM $MgCl_2$ at 100 V for 90 min on ice which are typical conditions for the analysis of DNA nanostructures [36, 55]. DNA was stained by immersing the gel slab for 10 min in 3x GelRed (Biotium). Subsequent imaging was performed on a GelDoc-It^{TM} (UVP). Image analysis was performed as described in Section 3.2.2 in Chapter 3. All operations were homogeneously applied to the whole image.

4.2.3 MD simulations of cholesterol-modified ssDNA and dsDNA

All-atom MD simulations described in this chapter were carried out by H. Joshi and A. Aksimentiev at the University of Illinois at Urbana-Champaign. The simulations were performed using the NAMD2 programme [176]. Initial atomistic ssDNA and dsDNA models were constructed using AMBERTOOLs [177] and the cholesterol was covalently linked to the DNA backbone [75]. CHARMM General Force Field (CGenFF) parameters [178] were used to describe the cholesterol-TEG's bonded and non-bonded interaction with surrounding atoms of DNA, water, and ions. The DNA's negative charge was compensated by Mg^{2+} hexahydrates, as used in experiment, and the system was submersed in water and 100 mM NaCl using VMD software [112]. Subsequently, the system was subjected to energy minimisation and equilibration at constant number of atoms, pressure, and temperature. The particle mesh Ewald (PME) method was used to calculate the long-range electrostatic interactions in NAMD2 [176], the Nose-Hoover Langevin piston [179, 180] and Langevin thermostat [181] were used to maintain the system's constant pressure and temperature. CHARMM36 force field parameters [182, 183] along with NBFIX modifications for non-bonded interaction [184, 185] were used to describe interatomic potential among water, ions, and nucleic acids. SETTLE [186] algorithm was applied to maintain rigid water molecules and RATTLE [187] algorithms were used to constrain all other covalent bonds involving hydrogen atoms. 500 ns equilibrium MD simulations were performed for each system using periodic boundary conditions. To improve sampling of the conformational space, two sets of simulations for each system were performed. Analysis and post-processing of simulation trajectories were performed using VMD [112] and CPPTRAJ [188].

4.2.4 Lipid membrane attachment of DNA duplex and nanostructure

Membrane attachment experiments were performed by K. Göpfrich, Max Planck Institute for Medical Research, Germany. Small unilamellar vesicles (SUVs) were formed as described previously [189]. Briefly, 99.5 mol% 1-palmitoyl-2-oleoyl-sn-glycero-3-phosphatidylcholine (POPC, Avanti Polar Lipids, USA) and 0.5 mol% Atto488-labelled 1,2-dioleoyl-sn-glycero-3-phosphoethanolamine (Atto488-DOPE, ATTO-TEC GmbH, Germany) were mixed in chloroform. The lipid mixture was dried under a gentle stream of nitrogen and subsequently placed in a desiccator for 2 hours. Lipids were resuspended in 10 mM Tris, pH 8.0, 1 mM EDTA at a concentration of 2.2 mM, vortexed for 10 min and extruded through a 50 nm polycarbonate membrane (Avanti Polar Lipids, USA). SUVs (final concentration: 1.1 mM) were mixed with the respective DNA duplexes or nanostructures (final concentration: 0.5 µM) in TE20 buffer. The mixture was encapsulated into surfactant-stabilised water-in-oil droplets via the aqueous inlet of a microfluidic T-junction device. The oil phase contained HFE-7500 fluorinated oil (3M, Germany) with 1.4 wt% perfluoropolyether-polyethylene glycol (PFPE-PEG) block-copolymer fluorosurfactants (Ran Biotechnologies, Inc., USA) and 10.5 mM PFPE-carboxylic acid (Krytox, MW: 7,000–7,500 g mol^{-1}, DuPont, Germany). Under these conditions, SUVs fuse at the droplet periphery and form a spherical supported lipid bilayer (droplet-stabilised GUV or dsGUV). The attachment of DNA structures was then monitored with optical microscopy. For details see [189–191].

4.2.5 Confocal fluorescence imaging

Confocal fluorescence imaging was performed to monitor the attachment of the DNA duplexes and nanostructures to lipid membranes of dsGUVs. For this purpose, a Leica SP5 confocal laser scanning microscope (Leica Microsystems GmbH, Germany) was used, equipped with an argon and a white light laser as well as a 40x water immersion objective (HC PL APO 40x/1.10 w, CORR CS2, Leica Microsystems GmbH, Germany). The pinhole aperture was set to one Airy Unit and experiments were performed at room temperature. Recorded images were brightness- and contrast-adjusted, and analysed with ImageJ (NIH, USA).

4.2.6 Dynamic light scattering

Dynamic light scattering measurements were performed on a Zetasizer Nano ZSP (Malvern Panalytical) with an excitation wavelength of 633 nm. The refractive index of DNA was set to 1.46 [192]. Water was selected as the dispersant in the software. DNA nanostructures were measured at 25 °C and a concentration of 1 µM in TE20 buffer.

4.3 Results & Discussion

4.3.1 Sequence-dependence of cholesterol-tagged ssDNA aggregation

Most commonly, the cholesterol moiety is connected to the 3' end of ssDNA via a triethylene glycol (TEG) linker as shown in Fig. 4.1. This linker is covalently bound to the 3' oxygen of the phosphate atom of the terminal nucleotide. The fully stretched length of the linker is ≈ 2 nm and of the cholesterol is ≈ 1.7 nm which was determined from their chemical structures in ChemiBio3D Ultra (PerkinElmer).

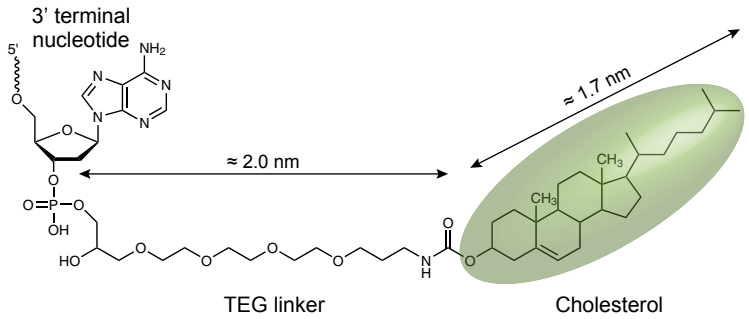

Fig. 4.1 Chemical structure of cholesterol modified to a DNA 3' end. Cholesterol (green ellipsoid) is covalently bound to a phosphate group at the ssDNA 3' end via a TEG linker. A terminal nucleotide is shown as an example.

As non-denaturing polyacrylamide gel electrophoresis is able to precisely resolve differences in molecular size and conformation in a quick and cost-efficient manner, it represents an ideal tool to visualise cholesterol-mediated interactions of chol-DNA molecules. To probe the aggregation behaviour of chol-DNA, three different sequences (a, b, c; for sequences see Table 4.1) with mixed nucleotides were analysed with non-denaturing 10 % PAGE (see Fig. 4.2). In order to assure that the observed aggregation behaviour is not an artefact of the specific production batch of the chol-DNA, three separate production batches were ordered and compared for each chol-DNA sequence.

Table 4.1 DNA sequences used to show sequence-dependent chol-DNA aggregation.

DNA strand	Sequence (5' to 3')
a (-CholTEG)	AAAACGCTAAGCCACCTTTAGATCCAAA(-CholTEG)
b (-CholTEG)	AAACTCCCGGAGTCCGCTGCTGATCAAA(-CholTEG)
c (-CholTEG)	GGATCTAAAGGACTTCTATCAAAGACGGGACGACTCCGGGAG(-CholTEG)

The gel reveals a different aggregation behaviour for each sequence ranging from smeared bands, indicating transient interactions between DNA strands (a), to complete aggregation in

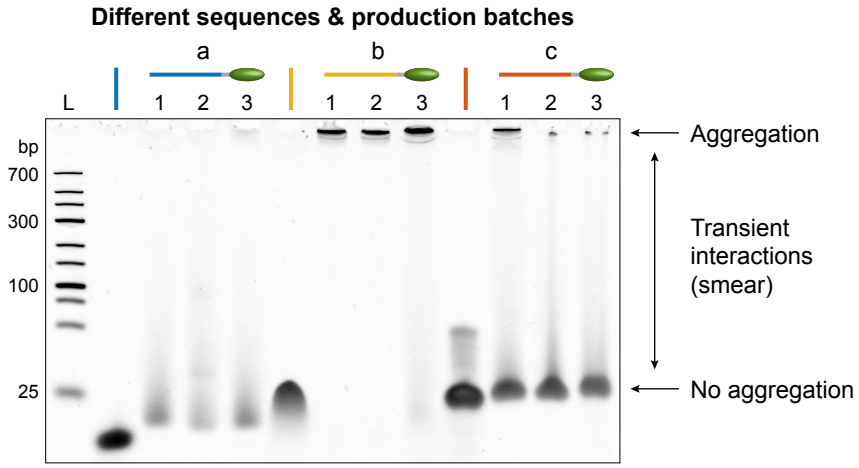

Fig. 4.2 Sequence dependence of cholesterol-modified ssDNA. PAGE analysis of three different ssDNA sequences (a, b, c) with and without cholesterol tag. Numbers indicate different production batches ordered three months apart from each other from IDT (28.10.2014, 29.01.2015, and 29.04.2015, respectively). For sequences see Table 4.1.

the gel pocket (b), or a mixture of defined bands (indicating monomeric DNA strands) and aggregation (c). Importantly, no difference between production batches is observed. This illustrates that the behaviour of cholesterol-modified ssDNA is purely sequence-dependent. To determine the origin of the sequence-dependent behaviour, we first verified if any secondary structure or multimer formation could have been the cause. For this purpose, we tested if the particular, unmodified DNA sequences showed secondary structure formation using the web-based nucleic acid structure prediction tool NUPACK [38]. Calculations were performed at a temperature of 18 °C and a DNA concentration of 8 µM with 50 mM NaCl and 11 mM $MgCl_2$. Except for the additional NaCl, these parameters match the experimental conditions chol-DNA strands were subjected to during PAGE (see Section 4.2). While sequence (a) was predicted to exclusively remain monomeric, both sequences (b) and (c) showed tendencies to form multimeric structures (Fig. 4.3). We analysed other DNA sequences, and even with relatively low predicted dimerisation tendencies, they also aggregated in the gel pockets if modified with cholesterol (see Fig. A.1 in the Appendix). Such tendency to form multimeric structures could explain their aggregation behaviour once modified with cholesterol.

To test if we can prevent aggregation by reducing multimer formation, we altered one specific base which aided dimerisation in sequence (b) (black arrow in Fig. 4.3b). By changing it from guanine to adenine, terming the resulting sequence (b*), the amount of monomeric structures predicted by NUPACK increased from 45 % to 93 % (Figs. 4.4a,b). PAGE analysis of sequence (b) and (b*) showed that aggregation in the pocket is completely averted (Fig. 4.4c). However, a remaining long smear still indicates transient cholesterol-mediated interactions.

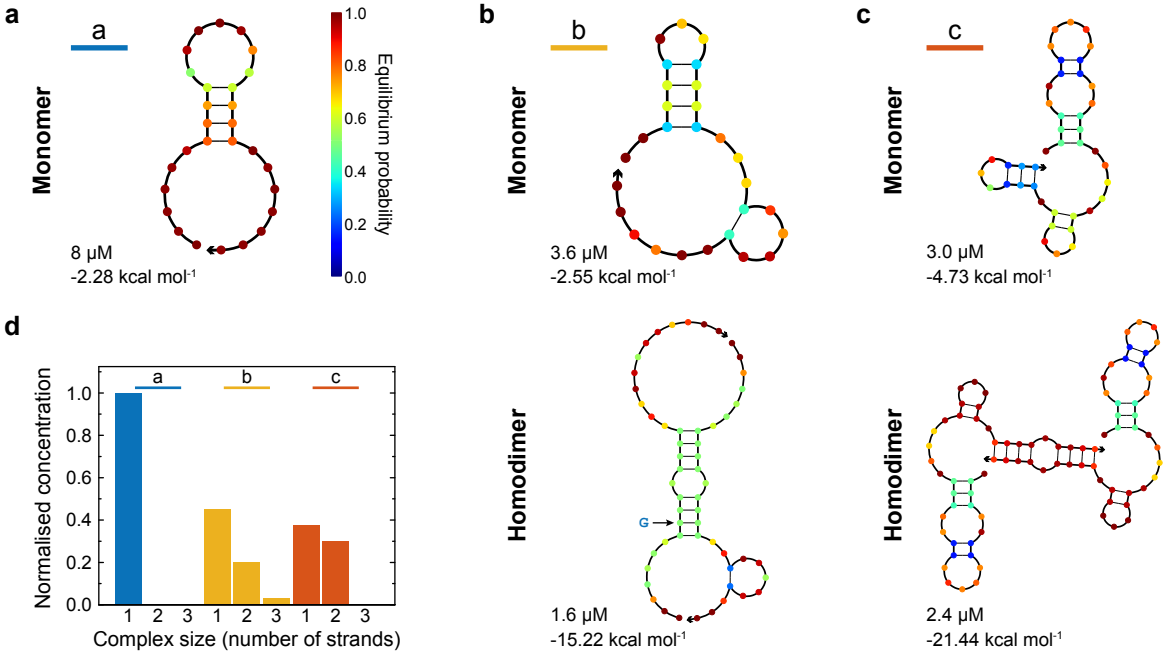

Fig. 4.3 NUPACK minimum free energy calculations of secondary structures of DNA sequences. (**a-c**) Probability shading representation of the secondary structure predicted by NUPACK of sequences a, b, and c. Each secondary structure is shown with its calculated free energy and the predicted concentration based on a total concentration of 8 µM. Arrow in **b** highlights a base that will later be altered to reduce multimerisation. (**d**) Histogram showing the normalised concentration for monomers, dimers, and trimers for the analysed sequences.

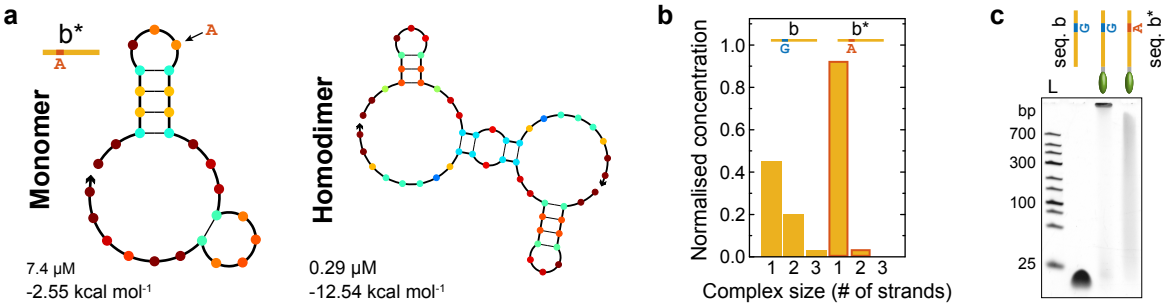

Fig. 4.4 Influence of multimerisation on chol-DNA aggregation. (**a**) NUPACK secondary structure calculations of monomer and homodimer of sequence (b*). Sequence (b*) differs from sequence (b) by the ninth base which was changed from guanine to adenine to reduce dimer formation. (**b**) Histogram illustrating reduced multimerisation of sequence (b*) compared to sequence (b). (**c**) PAGE analysis contrasting the decreased aggregation behaviour of sequence (b*) by having changed a single base and thereby reducing multimer formation.

Although sequences with tendencies to form dimers or multimers were identified to be prone to significant aggregation once modified with cholesterol, even without or low multimerisation, cholesterol-mediated interactions were still present, like the smear of sequence (a) in Fig. 4.2, or the smear of sequence (b*). We therefore set out to further determine indicators for the sequence-dependent aggregation. For this purpose, we tested poly-thymine (poly-T) sequences as they represent the most simplified DNA sequences and are not prone to stable secondary structure formation [193]. At the same time, we probed the dependence on the length of the sequence, as this could for example influence the formation of micelles. The gel in Fig. 4.5a compares cholesterol-modified poly-T sequences ranging from 20 to 50 nucleotides, which are relevant lengths for the assembly of DNA nanostructures [35].

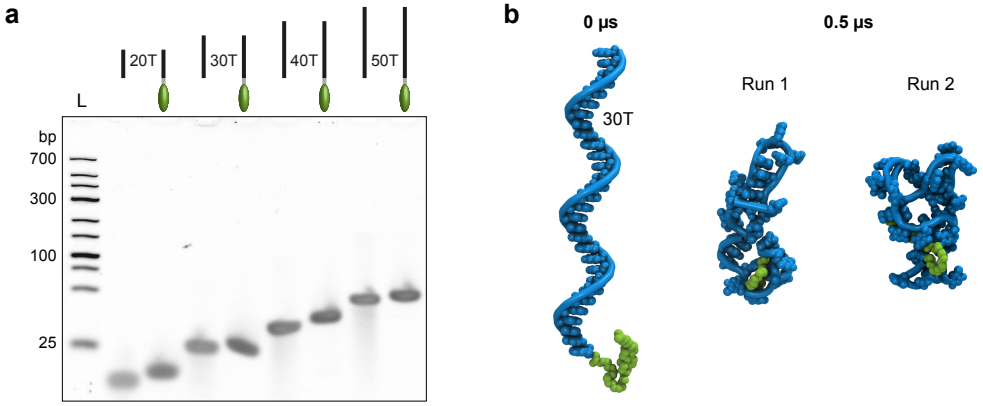

Fig. 4.5 PAGE and MD simulation of cholesterol-modified poly-T ssDNA. (**a**) PAGE of poly-T sequences ranging from 20 to 50 thymine bases are shown without and with a cholesterol modification at the 3' end. (**b**) Snapshots of all-atom MD simulation of cholesterol-modified 30 thymine ssDNA (30T) at the beginning (0 µs) and end (0.5 µs) of two independent simulation runs starting from the same initial configuration. The ssDNA wraps around the cholesterol group in both simulation runs. Water and ions are not shown for clarity. For an image sequence throughout the simulation see Fig. A.2 in the Appendix. A movie of the simulation can be found in the Supplementary Information of the published article [194].

As expected, the longer the DNA strand, the slower the migration in the gel due to the increasing hydrodynamic radius. Furthermore, chol-DNA strands are slightly shifted to shorter run lengths compared to the corresponding unmodified strand due to the increased hydrodynamic radius attributed to the cholesterol group. Notably, all cholesterol-modified strands form similarly sharp bands as unmodified ones showing no aggregation nor transient interactions at all. This indicates that neither the interaction between the chol-DNA strands nor the interaction of the cholesterol group with the gel matrix has a significant effect on the migration of the DNA.

To gain insight into the molecular interactions of the ssDNA with the cholesterol tag, we collaborated with the group of A. Aksimentiev at the University of Illinois at Urbana-Champaign, who performed all-atom MD simulations. An atomistic model of the cholesterol conjugated to a 30 thymine (30T) long ssDNA strand was built in explicit water, and extensive equilibrium MD simulations were performed at ambient temperature, pressure, and ionic concentrations comparable to those used in experiments (see Section 4.2). The snapshots in Fig. 4.5b illustrate that throughout the 0.5 µs simulation, the cholesterol group gets completely wrapped by the ssDNA, with the hydrophobic DNA bases facing the cholesterol moiety (see Fig. A.2 in the Appendix). A second, independent simulation, starting from the same initial configuration, yielded a similar result. We postulate that by wrapping around the cholesterol, the ssDNA effectively shields the cholesterol's hydrophobicity preventing intermolecular cholesterol-mediated interactions which agrees with the sharp bands observed in Fig. 4.5a. The simulations furthermore show that the bases immediately adjacent to the cholesterol tag also interact with it first (Fig. A.2 in the Appendix). This indicates that these terminal bases could have a more significant contribution to the sequence-dependent behaviour. We therefore placed special emphasis on the three bases adjacent to the cholesterol tag and altered these while maintaining the rest of the sequence to be thymine bases. PAGE results show no significant difference between three terminal thymine, adenine or cytosine bases (Fig. 4.6a). However, terminal guanine nucleotides induced transient intermolecular interactions, visible as a completely smeared band (GGG). In contrast, all unmodified DNA strands showed no aggregation nor transient interactions. This demonstrates that multiple terminal guanine bases can lead to transient cholesterol-mediated interactions between the chol-DNA strands. We then chose a sequence with mixed nucleotides that did not show any aggregation nor transient interactions even when modified with cholesterol (see sequence AAA in Fig. 4.6b). To determine the influence of the terminal bases we altered them to either TAT or GCG. Interestingly, this significantly affected the aggregation behaviour with a long smear for terminal TAT and both a smear and aggregation in the pocket for terminal GCG (see Fig. 4.6b). In order to verify that these differences only originate from the DNA sequence, we compared the synthesised oligonucleotides with terminal TAT and GCG from different suppliers (IDT or biomers.net) but no significant difference was observed between them (see Fig. 4.6b). We furthermore verified if the storage conditions of the particular sample could have induced the observed differences. Chol-DNA strands from IDT were acquired and diluted in Milli-Q water less than three weeks before the experiment. Chol-DNA strands from biomers.net were acquired dry in two aliquots from the same production batch for each DNA sequence. The 'Biomers 1' aliquots were dissolved to 100 µM in Milli-Q water 3 years and 11 months prior the experiment. 'Biomers 2' aliquots were stored dry at −20 °C and only dissolved

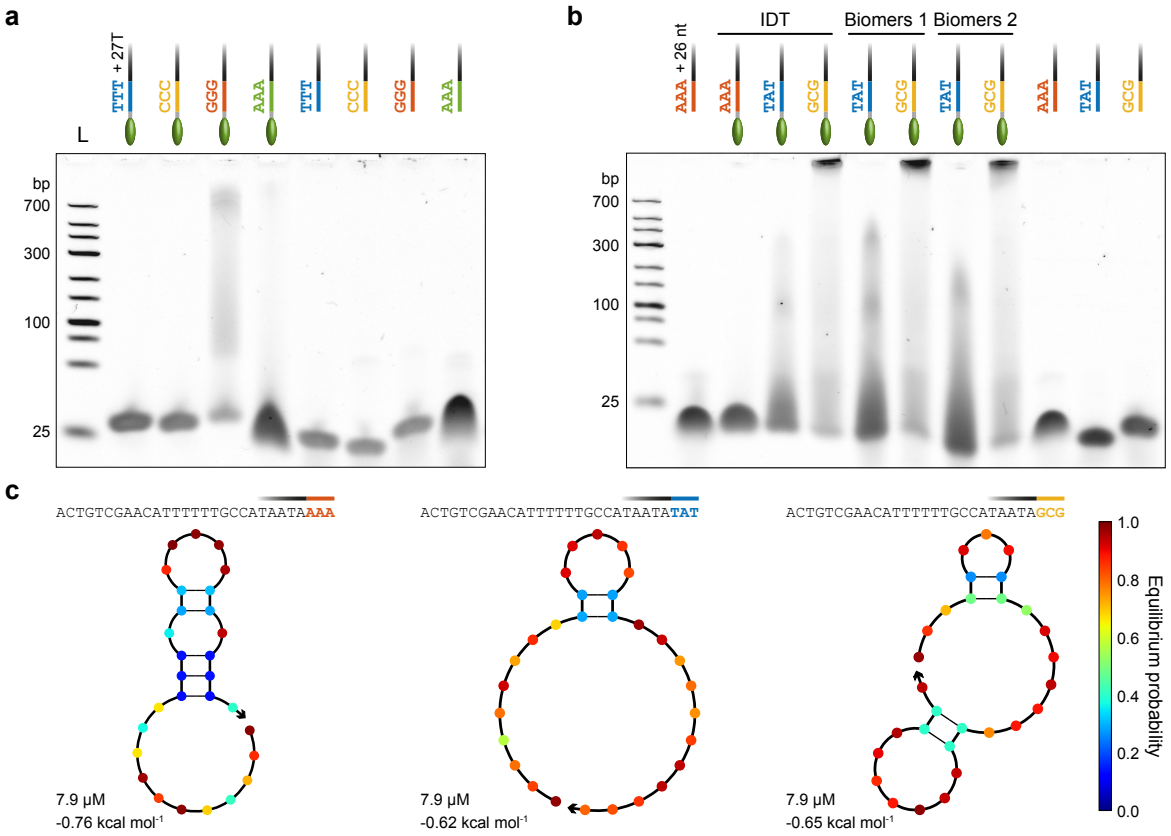

Fig. 4.6 Influence of terminal bases on chol-DNA aggregation. (**a**) Comparison of poly-T chol-DNA sequences containing different terminal bases. (**b**) Comparison of different terminal bases on a mixed DNA sequence shows a sequence-dependent aggregation behaviour of the cholesterol-modified strands but not of the unmodified strands. The behaviour is independent of supplier (IDT or Biomers) and storage conditions (Biomers 1 or Biomers 2). (**c**) NUPACK secondary structures calculations of the analysed DNA sequences. Dimer formation was below 0.7 % for all sequences.

two months prior the experiment. Once diluted in water, all chol-DNA strands were stored at 4 °C. Again, no significant difference was observed. Lastly, we also confirmed that the unmodified strands all result in sharp bands without any smears or signs of aggregation.

As shown before, tendencies to form multimeric structures could have caused the observed differences in aggregation. However, analysis with NUPACK reveals that over 99 % of the strands are predicted to be monomeric for all three sequences (Fig. 4.6c). This indicates that multimerisation is only partly responsible and other factors contribute to the sequence-dependent aggregation behaviour of chol-DNA. Additionally, all secondary structures of the monomers had a similarly low free energy of $\approx 1\ k_BT$. This indicates that multimerisation and secondary structure formation, as predicted by NUPACK for the unmodified sequences, do not provide a complete explanation for the sequence-dependent aggregation behaviour.

Our PAGE analysis of the sequence-dependent aggregation of cholesterol-modified ssDNA has shown that poly-T sequences can successfully inhibit cholesterol-mediated molecular interactions. This happens most likely due to the ssDNA wrapping around the cholesterol moiety, as indicated by MD simulations. Furthermore, sequences with certain tendencies to form dimers or multimers led to significant aggregation and should be avoided. While terminal thymines prevented aggregation best, the aggregation behaviour of mixed DNA sequences originates most likely from a more complex interplay of secondary structure formation and multimerisation. It has been shown that cholesterol and its esters can form stable complexes with DNA duplexes [195]. Furthermore, inter-cholesterol hydrophobic interactions have been demonstrated to stabilise nucleic acid complexes by up to 13 °C for duplexes and 30 °C for triplexes [196]. Such interactions could decrease the melting temperature of secondary structures thereby inducing the observed sequence-dependent aggregation of chol-DNA. Consequently, experiments involving cholesterol-modified ssDNA require careful consideration of the DNA sequence.

4.3.2 Shielding cholesterol group by an adjacent ssDNA overhang

As applications for cholesterol-modified DNA commonly involve double-stranded DNA, we investigated the cholesterol-mediated aggregation of a DNA duplex with a single cholesterol tag. Furthermore, we wanted to explore if the previously observed cholesterol-ssDNA interaction can be utilised to control aggregation simply by the design of the complementary, unmodified DNA strand. To test this, the clustering chol-DNA strand (sequence b in Fig. 4.2 and Table 4.1) was hybridised to complementary strands of various lengths ranging from 6 nucleotides shorter (−6) than the chol-DNA strand to a 10 nt ssDNA overhang adjacent to the cholesterol (for sequences see Table A.4 in the Appendix). PAGE results in Fig. 4.7a show that while the cholesterol-modified ssDNA strand (ss chol) aggregates in the pocket, hybridisation to a complementary strand eliminated these aggregates in all cases. A feasible explanation is that the previously demonstrated multimerisation tendencies of sequence (b) are inhibited by forming a DNA duplex.

Nevertheless, for complementary strands without overhang (−6 and 0) the bands in the gel still show long smears, indicating transient interactions either among the DNA duplexes or with the gel matrix. However, hybridisation with complementary strands with increasing ssDNA overhangs gradually eliminates these transient interactions. The longer the ssDNA overhang, the sharper the band of the duplex. A 6 nt overhang on the complementary strand is sufficient to obtain a clear band in the gel, successfully suppressing aggregation as well as transient interactions. Longer overhangs (+8 and +10) do not increase the band sharpness any further. The same aggregation prevention by adjacent ssDNA overhangs was achieved

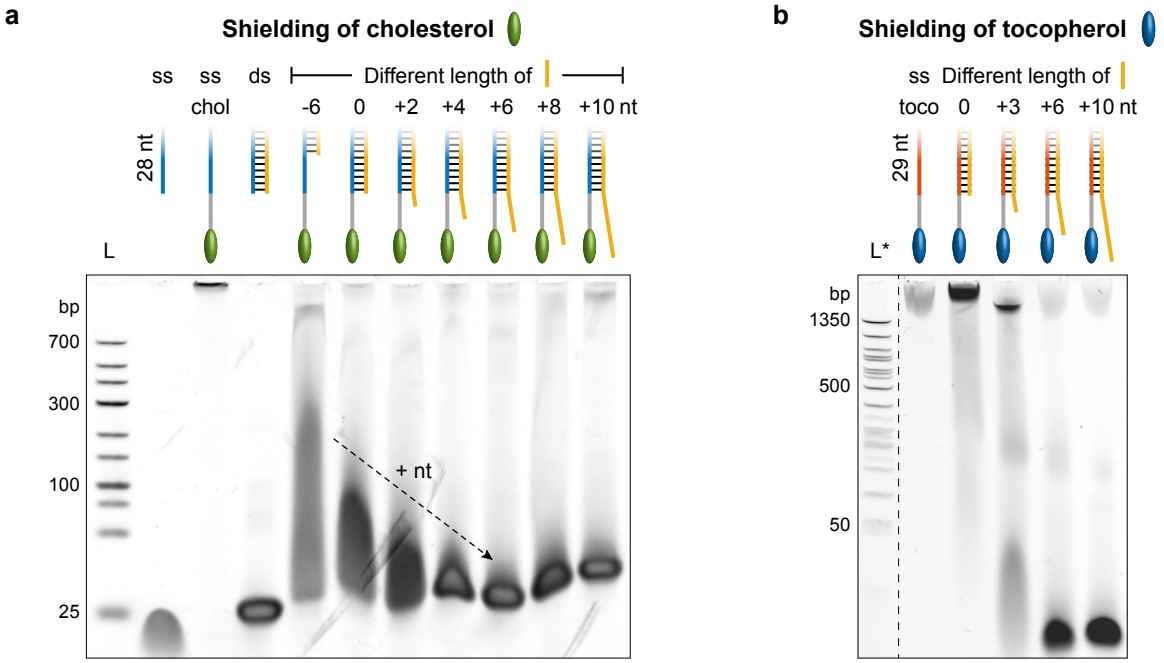

Fig. 4.7 Preventing aggregation of hydrophobically modified dsDNA by an adjacent ssDNA overhang. (**a**) PAGE analysis of cholesterol-modified ssDNA (ss chol, blue) and its duplex with a complementary DNA strand (orange) of varying overhang length ranging from −6 to +10 nucleotides with respect to the cholesterol-modified strand. (**b**) PAGE analysis of tocopherol-modified ssDNA (red) and its duplex showing reduced aggregation once modified with a complementary DNA strand (orange) of increasing overhang length.

for tocopherol-modified DNA in a separate experiment (see Fig. 4.7b and Table A.4 in the Appendix for DNA sequences). In both cases the overhang sequence was chosen randomly. We again utilised 0.5 µs long all-atom MD simulations to investigate the interaction of the cholesterol group with the DNA. Without overhang, the cholesterol remains freely accessible as there is no ssDNA present to wrap around it (Figs. 4.8a,b). This accessibility of the cholesterol is likely to mediate molecular interactions between modified duplexes giving rise to the observed smeared gel bands in Fig. 4.7a. In contrast, the simulation of the cholesterol-modified duplex with a 6 nt overhang shows that the cholesterol is wrapped by the ssDNA (Figs. 4.8c,d). This observation agrees with the simulation results for the cholesterol-modified ssDNA. The ssDNA overhang most likely presents a hydrophilic, steric hindrance, effectively preventing cholesterol-mediated interactions. For each system, an independent simulation repeat was performed, starting from the same initial configuration, demonstrating a similar interaction of the ssDNA with the cholesterol group (see image sequences in Fig. A.3 in the Appendix). The combined results of PAGE and MD simulations show that free cholesterol modifications are more prone to clustering than ones shielded by adjacent ssDNA.

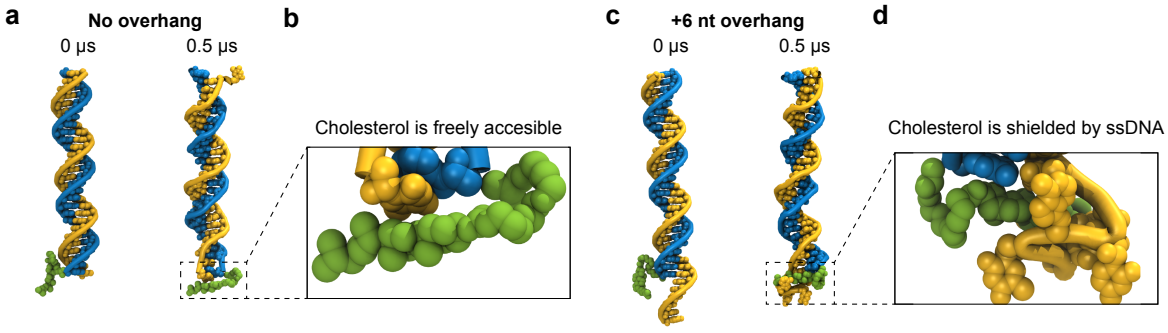

Fig. 4.8 Preventing aggregation of hydrophobically modified dsDNA by an adjacent ssDNA overhang. Instantaneous snapshots of all-atom MD simulations of the DNA duplex with one cholesterol tag either without overhang (**a,b**) or with a 6 nt overhang (**c,d**), each shown at the beginning (0 µs) and end (0.5 µs) of the equilibrium MD simulation. Close-ups illustrate that cholesterol is more freely accessible without overhang (**b**) but shielded by the ssDNA if the overhang is present (**d**). For image sequences of simulations see Fig. A.3 in the Appendix.

As the purpose of the cholesterol group is the interaction of DNA with lipid bilayers, we needed to ensure that the overhang does not impede membrane binding. We therefore incubated artificial, droplet-stabilised giant unilamellar vesicles (dsGUVs, see Section 4.2.4) with the cholesterol-modified duplex containing a 6 nt overhang. The complementary strand of the duplex was labelled on the 3' end with the fluorescent dye Cy3 which facilitated tracing the location of the DNA duplexes. Imaging the vesicles with confocal fluorescence microscopy showed bright fluorescent rings, co-localising with the lipid membranes, thereby showing successful insertion of the cholesterol into the membrane (see Fig. 4.9). This demonstrates that the presence of the overhang does not inhibit membrane binding.
From these experiments and simulations, we can conclude that the extension of the complementary DNA strand adjacent to the cholesterol moiety can be used as a universal strategy to avoid aggregation of cholesterol-tagged DNA duplexes.

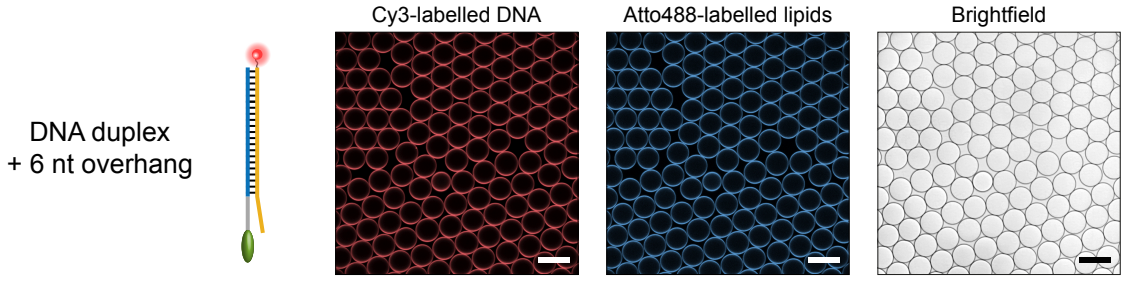

Fig. 4.9 Membrane attachment of shielded DNA duplex. Confocal microscopy images of Cy3-labelled, cholesterol-modified DNA duplexes (red) containing a 6 nt overhang demonstrating attachment to membranes of lipid vesicles containing 0.5 mol% ATTO488-labelled lipids (blue) together with brightfield images of the vesicles. Scale bars denote 50 µm.

4.3.3 Influence of cholesterol number and linker type on aggregation

After studying cholesterol-modified ssDNA and dsDNA, we investigated the cholesterol-mediated aggregation of the CP2 DNA nanostructure design as introduced in Chapter 3. It was important to characterise the influence of cholesterol modifications on the DNA nanostructure as the gained insights will be helpful to understand and optimise the design for insertion into lipid bilayers.

As mentioned in Chapter 3, a key feature of the design is an array of 3' and 5' ends in the central region of the DNA nanostructure, allowing for the specific positioning of cholesterol modifications (see Figs. 4.10a-c). Their strategical placement regarding the DNA's helical pitch facilitates that cholesterol modifications should face diagonally away from the structure, which could aid their accessibility after assembly (as illustrated in Fig. 4.10b). The ssDNA pathways are point-symmetric to the centre causing an overall symmetry of the design. These features facilitate the systematic analysis of the cholesterol-mediated interaction between the DNA nanostructures regarding cholesterol number, linker type, and modification position.

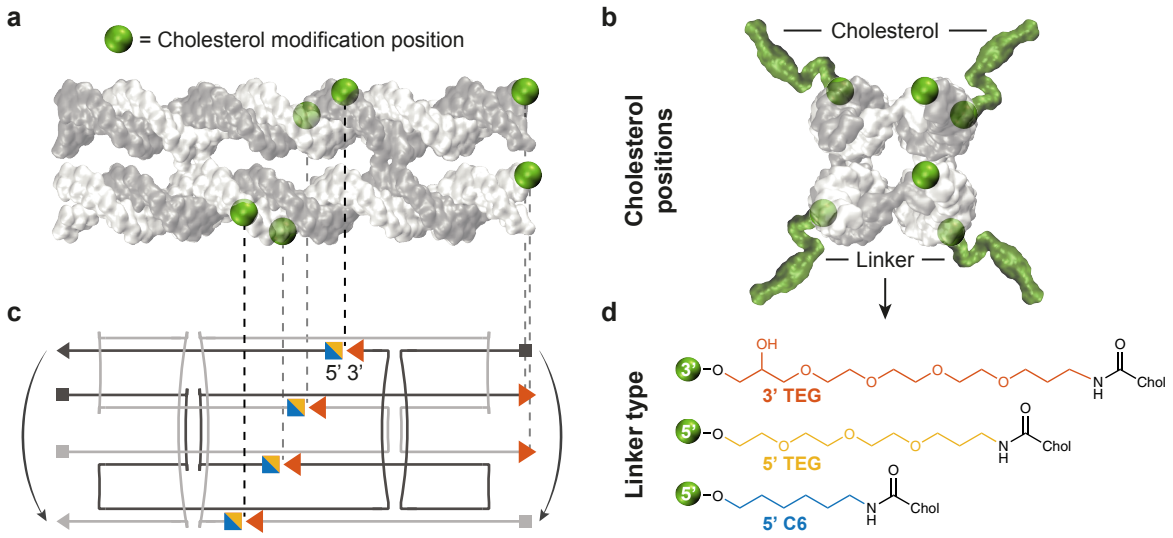

Fig. 4.10 Overview of cholesterol modification positions and linker types. Side view (**a**) and top view (**b**) of a 3D representation of the DNA nanostructure. Cholesterol modification positions, specifically the oxygen atoms to which the cholesterol is linked to (compare Fig. 4.1), are highlighted as green spheres. (**c**) 2D scheme illustrating the ssDNA pathways and modification positions within the DNA nanostructure design. Arrows illustrate the translation from the 2D and to the 3D architecture. (**d**) Chemical structures of three commercially available linker types. Colours in **c** indicate the possible modification positions for each linker type within the design. For a detailed overview of modification positions and DNA strand names see Fig. A.4 in the Appendix.

First, DNA nanostructures were assembled with 1 to 4 cholesterol modifications covalently bound to the central region of the DNA constructs. At the same time we wanted to determine if the type of linker employed between the cholesterol and the DNA had an influence on the cholesterol-mediated interactions. For this purpose, three different commercially available linker chemistries were tested: 3' and 5' end TEG-linkers, and a 5' hexane (C6) linker (see Fig. 4.10d). They differ in length, modification position (3' or 5'), and hydrophobicity with TEG being less hydrophobic than the C6 chain due to the additional oxygen atoms. PAGE analysis of DNA nanostructures folded with 1 to 4 cholesterol groups for each linker type reveals stepwise band shifts to shorter run lengths with each additional cholesterol group for all linker types (see Fig. 4.11). This can be explained by the increasing hydrodynamic radius of the nanostructures for each additional cholesterol tag.

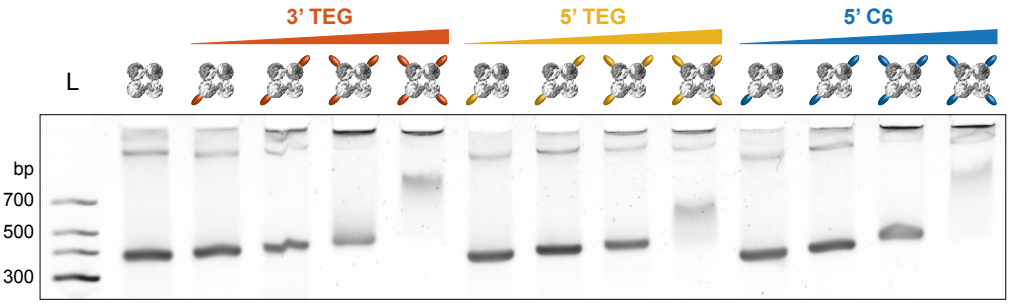

Fig. 4.11 PAGE analysis of DNA constructs assembled with 1 to 4 cholesterol tags for each linker type. For details on modified DNA strands see Tables A.5 and A.6 in the Appendix.

For 1 to 3 cholesterol groups, monomer bands remain relatively sharp, however, aggregation in the pockets gradually increases. For 4 cholesterol modifications, all structures show a smeared, less intense band with a much larger band shift than the previously observed consistent shifts for each cholesterol addition. This suggests that cholesterol-mediated interactions are now dominating and induce aggregation of the DNA nanostructures.
For all structures folded with cholesterol modifications in the central region of the design, an additional adenine nucleotide was included prior each cholesterol tag as a spacer (see Table A.5 in the Appendix). In previously reported work a longer spacer, composed of three adenine nucleotides prior the cholesterol group, was employed [54]. Here, this spacer was shortened to one adenine as this allows to position the cholesterol molecules more precisely on the DNA construct. At the same time, the adenine nucleotide prior the hydrophobic tag ensured that the attachment chemistry of the cholesterol was homogeneous for all modification positions, as it was demonstrated before that this can influence chol-DNA aggregation (see Fig. 4.6). Lastly, the additional nucleotide still provided the cholesterol anchor with a slightly increased range which could potentially be beneficial for membrane attachment.

Nevertheless, we wanted to ensure that this spacer did not have a significant influence on the observed differences in cholesterol-mediated aggregation. To test if the adenine spacer affected the folding yield of the DNA nanostructures, we assembled the constructs using DNA sequences that contained an additional adenine nucleotide but no cholesterol modification. PAGE analysis shows that the presence of the spacer does not significantly affect the folding yield of the DNA nanostructures (see Fig. 4.12a). We then folded the structures with 1 to 4 cholesterol modifications (as performed for Fig. 4.11) either with (+A) or without (−A) the spacer. The results of the subsequent PAGE analysis demonstrate that the additional adenine did not affect the overall observed trend of increased clustering with additional cholesterol tags (see Fig. 4.12b). Only for 3 cholesterol modifications a slight difference between the extent of the monomer band smear was observed, however, the band was sharper when the spacer was included. Therefore, the single adenine spacer was still included in the design for all further experiments involving centrally positioned cholesterol tags.

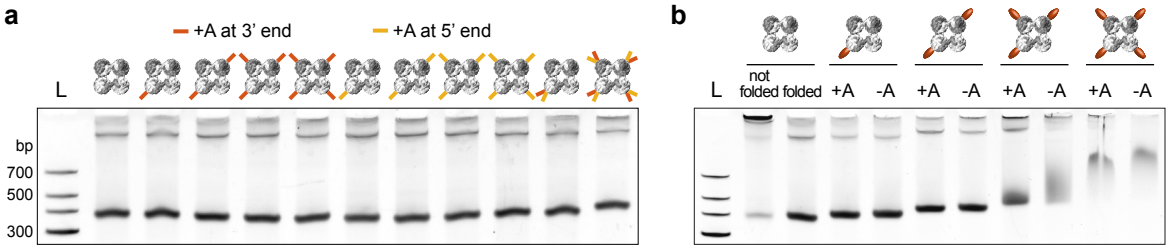

Fig. 4.12 Influence of additional adenine spacer on DNA nanostructure assembly. (**a**) PAGE analysis of DNA nanostructures assembled with additional adenine spacers at the 3' (red marker) or 5' ends (yellow marker) but without cholesterol modifications. (**b**) Comparison of DNA nanostructures assembled with 1 to 4 cholesterol-TEG modifications with (+A) and without (−A) adenine spacer. The first lane after the ladder shows a DNA nanostructure that did not undergo a folding protocol but was simply mixed together at room temperature.

4.3.4 Influence of the cholesterol modification position

Next, the influence of the cholesterol modification position was studied. For this, DNA nanostructures were assembled with cholesterol modifications either at the central region, or the end. Figure 4.13 shows the PAGE analysis of DNA nanostructures folded with 1 or 2 TEG-linked cholesterol groups (1C and 2C, respectively). While a single cholesterol tag in the central region shifts the monomer band, as discussed above, it does not change the band intensity nor induce aggregation. However, addition of a single cholesterol to the end of the design reduces the monomer band intensity to $\approx$ 35 % (compared to 77 % if on the side), while dimer and multimer intensities increased by 19 % and 23 %, respectively (Fig. 4.13a). Similar cholesterol-mediated dimerisation has been reported for a DNA cube construct [174].

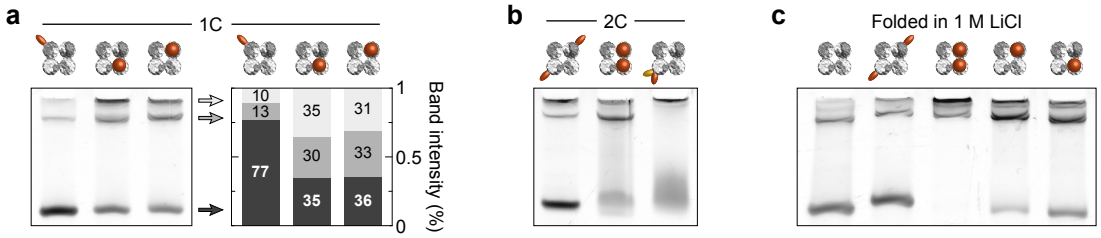

Fig. 4.13 Influence of modification position on DNA nanostructure aggregation. PAGE comparing DNA nanostructures modified with one (**a**) or two (**b**) cholesterol tags at different locations. Band intensities are normalised to the sum per lane. (**c**) PAGE illustrating that the position-dependent aggregation is even more pronounced when structures are folded in 1 M LiCl, 25 mM HEPES, pH 8. For DNA strands see Fig. A.4 and Table A.5 in the Appendix.

Two central cholesterol modifications at opposing sides also yield a sharp monomer band (see Fig. 4.13b). This contrasts with two cholesterol tags placed at the end of the structure causing a smeared monomer band with reduced intensity while the dimer band increases. Furthermore, placing two cholesterol tags right next to each other at the same location results in a significantly smeared monomer band.

These results suggest that aggregation not only depends on the number of cholesterol tags but also on their modification position. Particularly cholesterol at the end of the structure induces dimerisation or even aggregation. When folded in a monovalent salt solution such as 1 M LiCl, aggregation of end-modified structures is even more pronounced. While two central cholesterol modifications induce only very slight aggregation, most structures form only dimers or multimers for cholesterol modifications placed at the end (see Fig. 4.13c). This aggregation happens in a similar fashion as if base-stacking interactions are not prevented on one side of the DNA nanostructure, as demonstrated in Fig. 3.3a. The observed effects for end-modified structures are therefore possibly a combination of cholesterol-mediated interactions which are further stabilised by base-stacking interactions between the ssDNA overhangs. This indicates that the additional cholesterol-mediated interactions could enhance weaker molecular interactions already present in the design which should be taken into account in the design process.

4.3.5 Controlling cholesterol-mediated aggregation of DNA constructs

Having studied the cholesterol-mediated aggregation of our DNA construct, we then investigated if the previously observed cholesterol-ssDNA interaction can be applied to prevent aggregation of the DNA nanostructures. Similar to how cholesterol-mediated interactions could be prevented with an adjacent ssDNA overhang for the tagged DNA duplex, such overhangs can be introduced in the DNA nanostructure to control aggregation by ‘shielding’ the

cholesterol. For this purpose, we extended the 5' ends in the central region of the design by 2, 4 or 6 thymine nucleotides to obtain ssDNA overhangs adjacent to the central 3'-modified cholesterol tags (Fig. 4.14a). A 3D model representation of the DNA nanostructure provides an illustration of the location of the overhangs and cholesterol modifications (Figs. 4.14b,c).

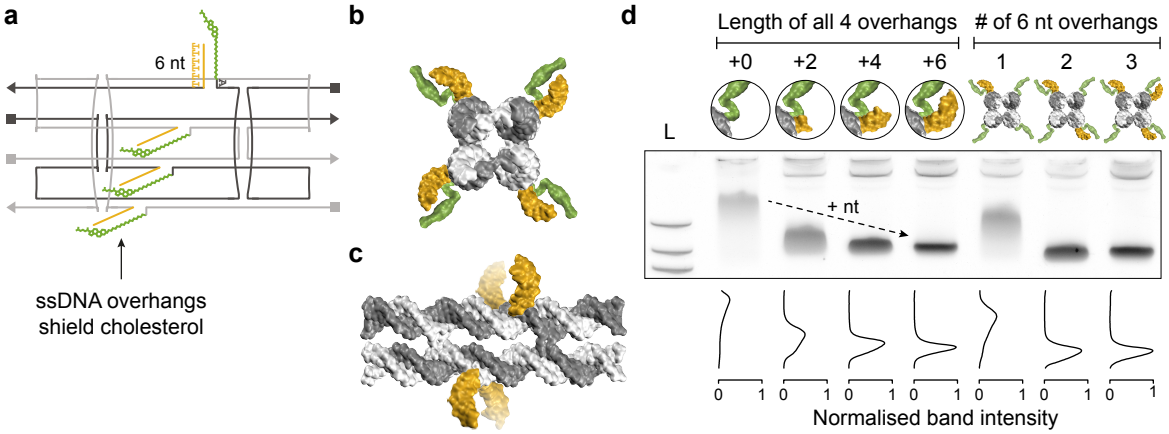

Fig. 4.14 Controlling cholesterol-mediated DNA nanostructure aggregation by ssDNA overhangs. (**a**) 2D scheme illustrating the positions of cholesterol tags (green) and ssDNA overhangs (orange). (**b,c**) 3D model of the DNA nanostructure including four 6 nt overhangs shown from top with four cholesterol modifications (**b**) or from the side with overhangs only (**c**). (**d**) PAGE of DNA constructs assembled with four 3' TEG-linked cholesterol groups and increasing ssDNA overhang length (+0 to +6 nt) or number of 6 nt overhangs adjacent to the cholesterol. Band intensity graphs are normalised to the +6 nt monomer band intensity and visualise the increasing run length and band sharpness when cholesterol tags are shielded.

As 4 central cholesterol modifications consistently induced aggregation, we assembled DNA nanostructures with 4 cholesterol tags without and with 2, 4, or 6 nt overhangs adjacent to all cholesterol groups, to test if aggregation can successfully be prevented. Structures without ssDNA overhangs again demonstrated clustering in PAGE, however, with increasing overhang lengths the initially smeared band gradually shifts to longer run lengths while increasing in band sharpness and intensity (Fig. 4.14d). This behaviour signifies a gradually decreasing hydrodynamic radius as well as increasing structural homogeneity, both indicative of successful aggregation suppression. An overhang length of 6 nt was sufficient to achieve a sharp monomer band, consistent with the results of the DNA duplex studies (compare Fig. 4.7). Varying the number of 6 nt overhangs furthermore showed that while one overhang was insufficient, already from two overhangs onwards a significantly sharper monomer band was observed suggesting successful aggregation prevention (Fig. 4.14d). This agrees with previous observations as it effectively reduces the system to two diagonally placed cholesterol modifications which generally did not show signs of cholesterol-mediated interactions.

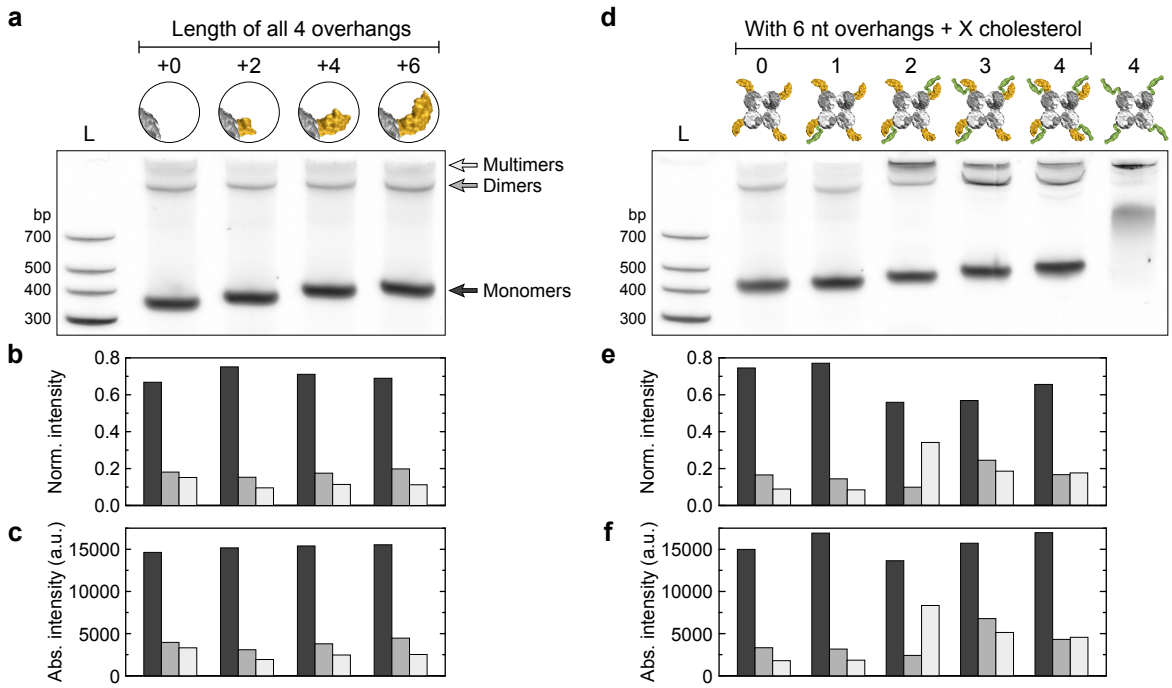

Fig. 4.15 Influence of ssDNA overhangs on DNA nanostructure assembly without and with cholesterol. (**a**) PAGE analysis of DNA nanostructures assembled with four overhangs of various lengths (+0 to +6 nt). (**b,c**) Histograms of monomer, dimer and multimer band intensities determined from **a** and normalised to the sum per lane (**b**) or absolute (**c**). (**d**) PAGE of DNA nanostructures with four 6 nt overhangs and increasing number of cholesterol modifications. (**e,f**) Histograms of monomer, dimer and multimer band intensities determined from **d** and normalised to the sum per lane (**e**) or absolute (**f**).

As a control, we confirmed that the added ssDNA overhangs do not interfere with the assembly of the DNA constructs. PAGE analysis shows slight shifts to shorter run lengths for increasing overhang lengths, as expected (Fig. 4.15a). At the same time, normalised band intensities remain approximately the same (Fig. 4.15b). Assuming a linear relationship between number of nucleotides and band intensity (as more staining dye can intercalate into the DNA), the observed slight increase for the absolute monomer intensities can be explained by the increasing DNA nanostructure size due to the additional overhang length (Fig. 4.15c). DNA structures that are folded with all four 6 nt overhangs, now also produced consistent band shifts for each additional cholesterol (Fig. 4.15d) without significant changes to the intensity of the monomer band (Figs. 4.15e,f). In conclusion, PAGE results suggest that ssDNA overhangs adjacent to cholesterol modifications can prevent cholesterol-mediated molecular interactions without significantly affecting the folding yield of the DNA nanostructures.

To show that the observed gel electrophoresis results are representative for the aggregation behaviour of the DNA constructs in solution, we performed DLS measurements. While DNA nanostructures without cholesterol groups showed no aggregation, modification with four cholesterol tags led to significant aggregation with diameters exceeding 1,000 nm (Fig. 4.16).

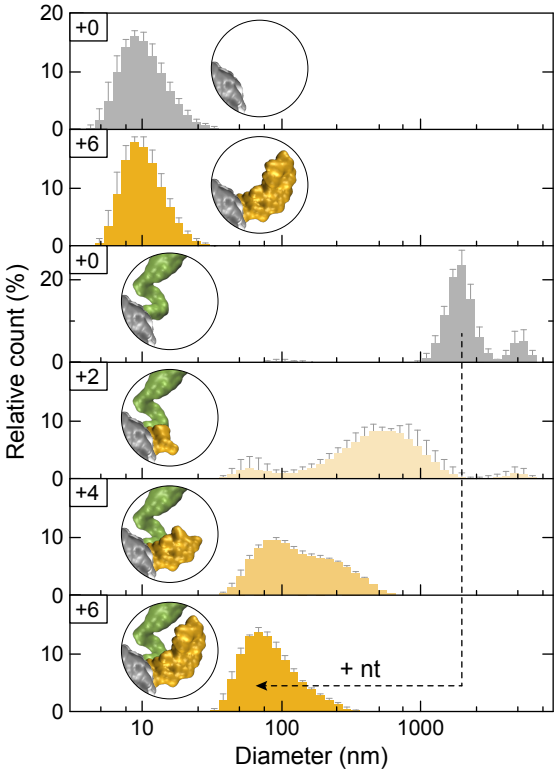

Fig. 4.16 DLS analysis of DNA nanostructures without and with four cholesterol tags demonstrating reduced aggregation if +2, +4, and +6 nt overhangs are employed. Histograms represent the average volume distribution of five measurements (error bars denote SD).

Upon addition of ssDNA overhangs, aggregation is gradually reduced with increasing overhang lengths, consistent with the PAGE experiments. Due to the non-spherical design of the DNA nanostructure, the contrasting interface with the surrounding water without or with hydrophobic cholesterol modifications (potentially affecting the hydrodynamic radius), and the polydispersity of the samples due to multimerisation and either complete or partial aggregation, reporting absolute sizes using DLS could be misleading which is why we only employed it to indicate the observed trend of reduced aggregation. In conclusion, DLS results confirm that our observed effects from non-denaturing PAGE are representative for the cholesterol-mediated aggregation behaviour of DNA nanostructures in solution.

Lastly, we ensured that DNA nanostructures with 4 cholesterol tags shielded by adjacent 6 nt overhangs, still bind to lipid bilayers. Analogous to experiments performed with the shielded DNA duplex, confocal microscopy of dsGUVs containing Cy3-labelled DNA nanostructures revealed that membrane attachment was not inhibited by the ssDNA overhangs (Fig. 4.17).

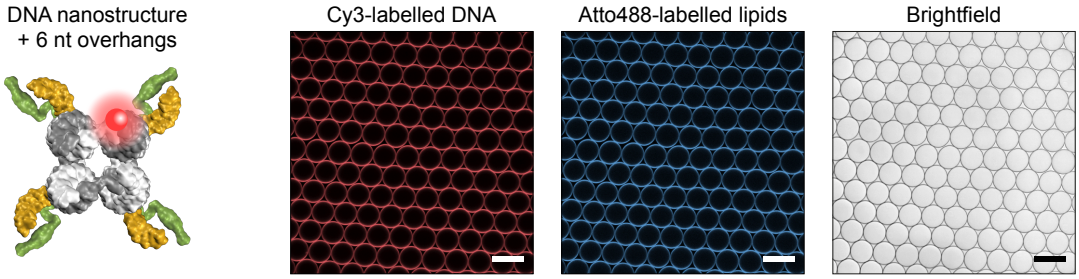

Fig. 4.17 Membrane attachment of shielded DNA nanostructures. Confocal microscopy images of Cy3-labelled, cholesterol-modified DNA nanostructures (red) with four 6 nt overhangs demonstrating attachment to membranes of lipid vesicles containing 0.5 mol% ATTO488-labelled lipids (blue) together with brightfield images of the vesicles. Scale bars denote 50 µm. Cy3 labels were incorporated on strands st2 and st4 (see Appendix, Table A.5).

4.4 Conclusion

The detailed analysis of cholesterol-modified ssDNA, dsDNA, and DNA nanostructures performed in this chapter shows that it is possible to control the aggregation of cholesterol-modified DNA nanostructures following a few simple design rules.

Cholesterol-modified ssDNA exhibits a sequence-dependent aggregation behaviour, independent of the production batch, supplier, or storage conditions. Sequences prone to forming dimers or multimers generally showed significant aggregation and should be avoided by optimising the sequences using structure prediction tools such as NUPACK [38]. Terminal thymine nucleotides generally avoided aggregation best, thus we recommend incorporating a poly-T section to precede the cholesterol moiety if the DNA sequence can be chosen freely. Our atomistic MD simulations of poly-T chol-DNA showed interactions of the hydrophobic nucleobases with the hydrophobic cholesterol moiety causing the ssDNA to wrap around the cholesterol group. For mixed DNA sequences, the behaviour is more complex. Consequently, experiments involving chol-DNA require careful consideration of the DNA sequence.

We further demonstrated that the incorporation of cholesterol tags into DNA nanostructures can be successfully analysed with non-denaturing PAGE with a visible shift for each additional cholesterol group. While nanostructure clustering does not significantly depend on the DNA-cholesterol linker type, it is the number and location of the hydrophobic tags that proved

to be the governing factors. The fact that DNA nanostructures with the same number of cholesterol tags can behave significantly different in PAGE suggests that interactions between the nanostructures rather than with the polyacrylamide gel matrix are governing. This is further supported by the DLS measurements performed in solution. The interactions between cholesterol-modified DNA strands described here can only be studied in non-denaturing conditions as earlier published results showed that surfactants can mask cholesterol-mediated aggregation [81]. Therefore, studying interactions between hydrophobically modified DNA nanostructures requires non-denaturing gel electrophoresis to accurately judge and precisely adjust aggregation of designs with a higher number of cholesterol tags.

Most importantly, we demonstrated that the hydrophobic interactions of cholesterol-tagged DNA can be easily controlled by incorporating an ssDNA overhang adjacent to the hydrophobic group. In agreement with the MD simulations, the ssDNA overhang most likely presents a steric hindrance, effectively preventing cholesterol-mediated aggregation. Due to the flexible nature of the ssDNA overhang, it does not impede insertion of the cholesterol-tagged DNA into a lipid bilayer membrane as we showed with confocal fluorescence imaging. Adjusting the length of the overhang can be utilised to precisely tune the degree of hydrophobic interaction. This allows for controlling cholesterol interactions simply by the rational design of the ssDNA overhang. The method also avoids the necessity of multi-unit membrane incorporation strategies and the use of surfactants, thereby circumventing the drawbacks of these strategies. Furthermore, it enables to increase the number of cholesterol modifications per DNA nanostructure, thereby facilitating enhanced membrane interaction.

The results of this study present a guide to control and prevent aggregation of cholesterol-modified ssDNA, dsDNA, and DNA nanostructures using simple DNA design rules and no additional components. This novel, cost-efficient, and easy-to-implement strategy to control aggregation of cholesterol-modified DNA nanostructures can readily be applied to existing designs without significant modifications. Additionally, it is not limited to cholesterol but can be applied to other hydrophobic modifications as already demonstrated for tocopherol.

The gained knowledge on the aggregation behaviour of the CP2 DNA nanostructure, once modified with cholesterol, will be the basis for subsequent applications presented in this thesis, particularly the design of the DNA-based lipid scramblase in Chapter 6. However, the method to prevent aggregation using ssDNA overhangs was only established after the work presented in Chapters 5 and 6 was performed. Without this shielding strategy, the DNA nanostructure modified with two cholesterol tags, diagonally positioned in the central region, showed the most consistent behaviour regarding high monomer yield and low aggregation tendency (compare Fig. 4.11). Therefore, this design was predominantly tested in further experiments presented in the next chapters.

Chapter 5

Dithionite reduction assay on LUVs

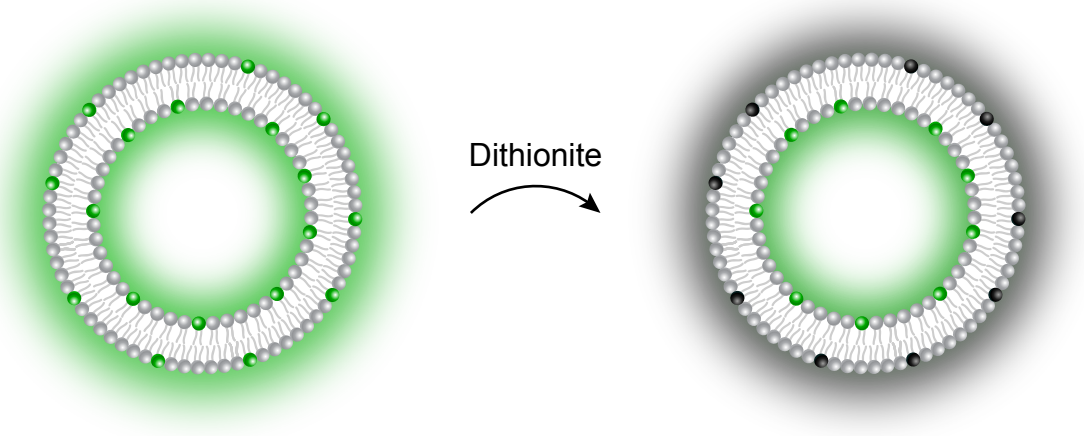

Parts of this work previously appeared in:

A. Ohmann, C. Y. Li, C. Maffeo, K. Al Nahas, K. N. Baumann, K. Göpfrich, J. Yoo, U. F. Keyser, and A. Aksimentiev. 'A synthetic enzyme built from DNA flips 10^7 lipids per second in biological membranes.' *Nature Communications*, 9:2426 (2018).

5.1 Introduction

It took a long time to figure out how to get these experiments to work.
– Nadrian C. Seeman

In the previous two chapters we studied the assembly characteristics of the CP2 DNA nanostructure first without and then with cholesterol modifications. In this chapter we will build up on this foundation and study if these cholesterol-modified DNA nanostructures can insert into lipid bilayers and, if so, can induce lipid scrambling between bilayer leaflets.
We will first perform electrophysiological measurements, a strategy that has been previously successfully employed to verify the membrane-insertion of DNA nanostructures [6, 8, 54, 66–68, 74]. A voltage is applied across a lipid bilayer and membrane-insertion of the DNA constructs can be identified by a sudden jump in the current to a stable plateau. With these experiments we will successfully demonstrate that the cholesterol-modified DNA structures can indeed insert into lipid bilayers and can therefore be termed *'DNA nanopores'*.
We will then utilise the dithionite reduction assay, as introduced in Chapter 2, to analyse the lipid scrambling activity of the DNA nanostructures. We will perform the assay as it is commonly reported in the literature, using lipid vesicles of ~100 to 200 nm in diameter and detecting the fluorescence signal from a bulk solution using a fluorescence spectrometer [14, 15, 24, 115, 137, 140, 197]. It has never previously been reported that this assay was employed to investigate scrambling activity of DNA nanostructures. Furthermore, as the dithionite reduction assay in general was also not established in our group, it was important to study and understand the fundamental characteristics and parameters that significantly affect the results of the assay. Such a foundation will prove valuable in the long run, in order to design targeted experiments and interpret their results more accurately. We will therefore initially characterise the assay regarding its dependence on the dithionite concentration, NBD labelling position, lipid composition, vesicle size, and the influence of surfactants.
From these experiments we will determine the optimal assay conditions and perform the dithionite reduction assay in the presence of cholesterol-modified DNA nanostructures to gauge if lipid scrambling can be observed. The basic principle will be to compare the dithionite-induced fluorescence reduction of plain vesicles (top in Fig. 5.1) with vesicles incubated with DNA nanostructures (bottom in Fig. 5.1). If the DNA nanostructures insert into the membrane and scramble lipids, a decrease of the normalised fluorescence intensity to values below 0.5 should be observed.
While we successfully demonstrate attachment of cholesterol-modified DNA nanostructures to the vesicles, no clear evidence for scrambling activity could be shown in this bulk assay.

One hypothesis is the low membrane insertion efficiency of the DNA structures, an issue that has been reported previously [47], and will also be confirmed in the electrophysiology experiments. We will therefore also attempt to facilitate increased membrane insertion using surfactants and electroporation.

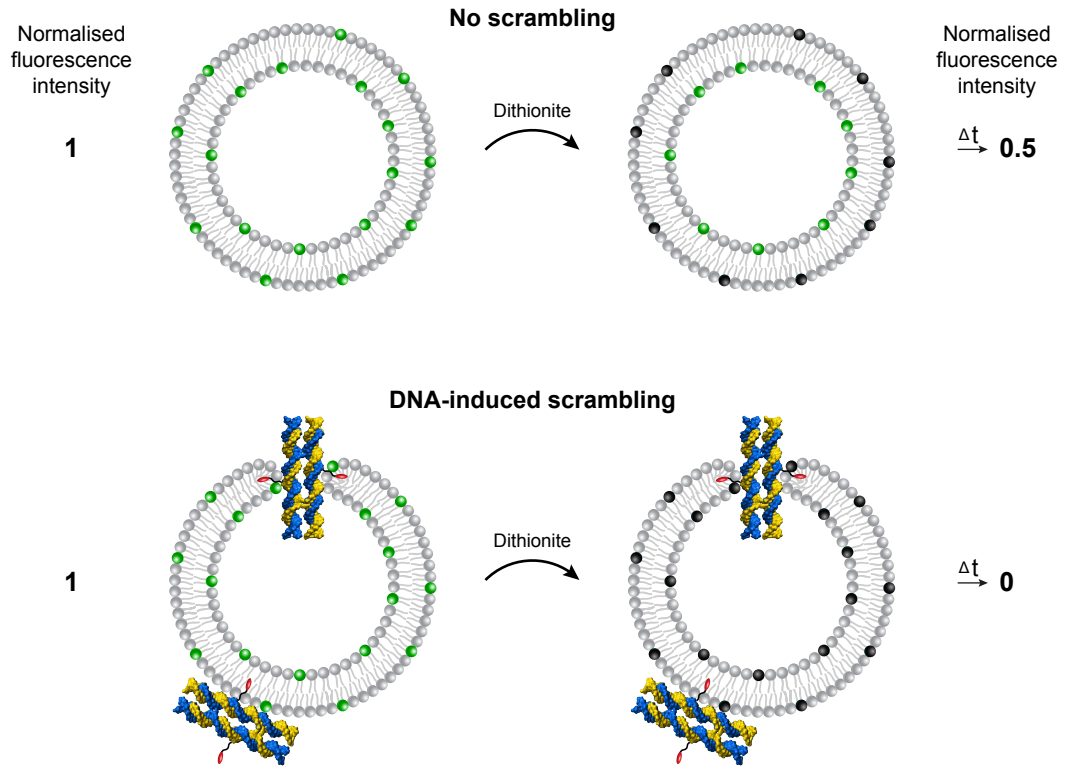

Fig. 5.1 Dithionite assay to determine lipid scrambling activity of DNA nanostructures. (**Top**) The lipid vesicles are produced containing a small fraction of NBD-labelled lipids (highlighted in green). Upon addition of dithionite, only lipids in the outer bilayer leaflet are fluorescently reduced by dithionite (black circles). When normalising the fluorescence intensity to its initial value before dithionite addition for each vesicle, it should only be reduced by dithionite to ≈ 0.5 over time in the absence of scrambling activity. (**Bottom**) DNA nanostructures can spontaneously insert into the vesicle membrane, potentially inducing and stabilising a toroidal lipid pore. Upon dithionite addition, the DNA-induced pore facilitates transport of lipids between the inner and outer bilayer leaflet. NBD-labelled lipids, previously inaccessible on the vesicle's inner membrane leaflet, are thereby transported to the outer leaflet where they are bleached by dithionite, effectively reducing the vesicle's normalised fluorescence intensity below 0.5.

5.2 Materials & Methods

5.2.1 Electrophysiology measurements

The capability of the DNA nanostructure to spontaneously self-insert into a lipid bilayer was measured with ionic current measurements using solvent-containing, free-standing membranes. The experimental design and setup were prepared together with Q. van der Spek, and she conducted the measurements and analysis [198]. Recordings were performed as described previously [7, 8, 198]. Briefly, a polytetrafluoroethylene (PTFE / Teflon) cuvette with two reservoirs separated by a hole of $\approx$ 0.28 mm diameter was employed. To *'pre-paint'* the aperture, 5 µl of 2 % (20 mg ml^{-1}) 1,2-diphytanoyl-sn-glycero-3-phosphatidylcholine lipids (DPhPC, Avanti Polar Lipids) dissolved in chloroform were deposited on the aperture and left to evaporate (typically ~5 min). The reservoirs were then each filled with 5 ml of 1 M KCl, 10 mM Tris at pH 8 and Ag / AgCl electrodes were inserted into the buffer on each side. Between 0.5 to 1 µl of 1 % DPhPC (10 mg ml^{-1}) in 90 % n-decane (Sigma) and 10 % butane were applied to a brush made from PTFE tubing. By repeatedly stroking this brush across the aperture between the reservoirs, a lipid bilayer was formed.
The current signal was amplified using an Axopatch 200B amplifier (Molecular Devices) and recorded using custom LabVIEW scripts written by Oliver Pambos and modified by Q. van der Spek [198]. Membrane formation was verified by a sudden drop in current from a few nA to close to 0 pA. Membranes with a resistance between ~50 to 80 GΩ and an I_{RMS} noise value between ~3 and 5 pA typically allowed for pore insertion which was verified with α-hemolysin transmembrane pores in preceding experiments [198, 199].
After stable membrane formation, DNA nanostructures modified with two cholesterol tags were added to the cis-side at a final concentration between 1 nM and 100 nM. Adding n-Octylpolyoxyethylene (OPOE) to a final concentration of 0.01 % to the cis-side of the cuvette significantly improved DNA nanostructure insertion. The trans-side voltage was typically varied between −100 to +100 mV and a constant voltage in that range was applied during the recording time until a spontaneous membrane insertion was observed. A sudden jump in current to a stable level typically signified the insertion of a DNA nanostructure. Subsequently, the voltage was varied in ±20 mV steps up to ±100 mV to obtain a current-voltage curve. Data was acquired using a Bessel filter of 1 kHz and a sampling rate of 3 kHz. Data analysis was carried out in OriginPro 2016.

5.2.2 Lipid mixtures for dithionite assays

To perform the dithionite reduction assay, lipid vesicles were formed from a variety of lipids which are listed in Table 5.1. Lipids were purchased as powder and dissolved in chloroform upon arrival to specific stock concentrations (C_{stock} in Table 5.1) and stored at −20 °C.

Table 5.1 Overview of lipids employed for dithionite assays. POPC was purchased from Sigma-Aldrich while all other lipids were acquired from Avanti Polar Lipids.

Abbreviation	Full lipid name	C_{stock} (mg ml^{-1})	Order #
POPC	1-palmitoyl-2-oleoyl-sn-glycero-3-phosphatidylcholine	150	42773
EColi	E. Coli Polar Lipid Extract	10	100600
eggPC	L-α-phosphatidylcholine (Egg, Chicken)	5	840051
NBD-DPhPE	1,2-diphytanoyl-sn-glycero-3-phosphoethanolamine-N-(7-nitro-2-1,3-benzoxadiazol-4-yl)	1	810142
NBD-PC	1-palmitoyl-2-{6-[(7-nitro-2-1,3-benzoxadiazol-4-yl) amino]hexanoyl}-sn-glycero-3-phosphatidylcholine	1	810130

EColi lipids are a mixture of different lipid types in themselves and will be employed in a 3:1 ratio together with eggPC, as described previously [14]. The different lipid components are listed in Fig. 5.2a. Furthermore, while eggPC exclusively contains phosphatidylcholine lipids, it is also a natural lipid mixture. An average distribution of its fatty acids is shown in Fig. 5.2b.

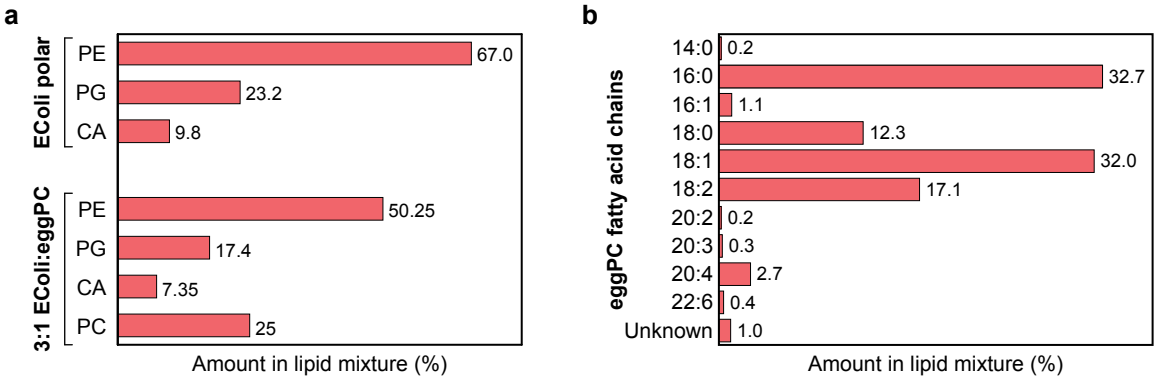

Fig. 5.2 Components of lipid mixtures used for dithionite assays. (**a**) Types of lipids in EColi polar and a 3:1 mixture of EColi polar and eggPC. PE refers to phosphatidylethanolamine, PG to phosphatidylglycerol, CA to cardiolipin, and PC to phosphatidylcholine. (**b**) Average fatty acid distribution of eggPC. Nomenclature of fatty acid chains refers to the number of carbon atoms:number of double bonds in the chain. Data for lipid compositions was obtained from Avanti Polar Lipids [200, 201].

5.2.3 Vesicle preparation and DLS analysis

Lipid vesicles were prepared from either POPC or a 3:1 mixture of EColi polar extract and eggPC. As the fluorescent reporter for the dithionite assay, 0.5 wt% (weight percent) of either NBD-DPhPE or NBD-PC were added to the mixture. Dissolved lipids (typically between 5 and 15 mg) were added to a round-bottom glass flask (Z302570, Sigma-Aldrich) and the chloroform storage solution was evaporated initially by gentle blow-drying with nitrogen followed by 1 hour desiccation under vacuum. Dried lipids were dissolved to a final concentration of 2 mM in 300 mM KCl, 1 mM EDTA and 20 mM HEPES with the pH adjusted to 7.4 using HCl (= 'buffer L'). The lipid solution was then sonicated for 15 to 30 min and stored at 4 °C.
Right before extrusion, the stored stock vesicle solution was sonicated again for 5 to 10 min. Extrusion was performed at room temperature by 15 single passes through a track-etched polycarbonate membrane (Nuclepore, Whatman) with a given average pore size using an Avanti Mini-Extruder (Avanti Polar Lipids). Before extrusion, the membrane was lined by two 10 mm polyester drain disks (WHA230300, Sigma-Aldrich) on each side and pre-equilibrated with buffer L.
Vesicle sizes were verified with dynamic light scattering (DLS). 100 µl liposome solution at ≈ 80 µM in buffer L were added to a low volume cuvette (ZEN0040) and placed in a Zetasizer Nano ZSP (Malvern Panalytical). Samples were measured at 25 °C using a lipid refractive index of 1.470, an absorption of 0.001, and water for the dispersant viscosity.

5.2.4 Dithionite assay with fluorescence spectrometer

Freshly extruded liposomes were diluted in their respective buffer to a final concentration of ≈ 80 µM lipids. 100 µl were added to a low volume quartz cuvette and the emitted fluorescence intensity was recorded at 5 Hz over time using a Cary Eclipse (Varian) fluorescence spectrometer (λ_{exc} = 460 nm, λ_{em} = 535 nm, 20 nm slit widths) at 23 °C. Dithionite (157953, Sigma-Aldrich) was diluted in 1 M Tris (pH 10 adjusted with HCl) to a concentration of either 250 mM or 1 M freshly before each experiment unless stated otherwise. Dithionite reduction assays were performed by recording the fluorescence intensity of the vesicle solution for 1 to 2 min and then pausing the data acquisition (to avoid a possible reading error of the device that stops the measurement) to add between 1 and 5 µl dithionite solution to the cuvette. The whole solution was pipetted up and down twice to facilitate mixing and data acquisition was continued. This process typically took between 10 and 15 s. The final dithionite concentration was typically 5 or 40 mM and is indicated for each experiment. For experiments where vesicles were disrupted such that dithionite can access all lipids, 2 µl of a

1:100 dilution of Triton^{TM} X-100 were added to the cuvette (pausing acquisition and mixing was also performed as described above).
Recorded traces were normalised to the averaged initial intensity F_0 before dithionite addition and the normalised intensity $F(t)/F_0$ was plotted over time using OriginPro 2016. Normalised fluorescence intensity plateaus after dithionite reduction were obtained by averaging over 10 data points before and after the six minute mark.

5.2.5 Preparation of TMEM16F scramblase proteoliposomes

Proteoliposomes were prepared according to a previously described method [14]. Briefly, human TMEM16F recombinant protein (H00196527, Abnova) pre-diluted in 300 mM KCl, 1 mM EDTA, 35 mM CHAPS, 4 mM glutathione, and 30 mM Tris at pH 8.0, was added at 5 µg per 1 mg lipids to a freshly sonicated lipid solution as described above. Final concentrations were 0.5 mM lipids and 15 nM scramblase. CHAPS detergent was subsequently removed using two to four exchanges of 200 mg Bio-Beads^{TM} SM-2 resin (Bio-Rad) per 500 µl lipid-detergent-protein solution over 36 hours at 4 °C. After detergent removal liposomes were extruded at 100 nm at room temperature as described above. Dithionite reduction assays were subsequently performed in 300 mM KCl, 1 mM EDTA and 30 mM Tris at pH 8.0. A similar but slightly optimised protocol was published recently [202] which can be of use for future experiments involving TMEM16 scramblase proteins.

5.2.6 Electroporation of LUVs

A Bio-Rad Gene Pulser^{TM} connected to a Bio-Rad Pulse Controller was used together with electroporation cuvettes with a 1 mm gap size (VWR). 40 µl of 3:1 EColi-eggPC vesicle solution (extruded at 200 nm) at ≈ 200 µM lipid concentration in buffer L were added to the electroporation cuvette and exposed to various voltage pulses.

5.3 Results & Discussion

5.3.1 Electrophysiology verifies lipid bilayer insertion

The purpose of the cholesterol modifications was to facilitate the insertion of the DNA nanostructures into a lipid bilayer. Successful membrane attachment was already verified in the previous section by observing a bright ring from the fluorescently labelled DNA structures in confocal microscopy, a similar approach as in previous work [8, 54, 74]. The next step was to prove that the cholesterol-modified DNA nanostructures could also insert into the lipid bilayer in a way that they would fully span across the membrane. Electrophysiology measurements have previously been employed successfully to demonstrate the insertion capabilities of hydrophobically modified DNA nanostructures [6, 8, 54, 66, 68, 70, 72, 74]. Solvent-containing bilayers, as the first technique for supported lipid bilayers [203], have been a proven method for studying the potential of novel proteins [204, 205] or DNA nanostructures [8, 74] to form membrane-inserted ion channels. In a cuvette made from polytetrafluoroethylene (PTFE) (see Figs. 5.3a,b) two separated reservoirs are connected by a central hole of $\approx$ 0.3 mm diameter. By placing electrodes in each reservoir and applying a voltage, the current through this aperture can be measured (Fig. 5.3c). Before membrane formation and without applied bias voltage, the current through the open aperture is typically in the range of nA. Lipids, dissolved in the organic solvent n-decane, are then spread (*'painted'*) across the aperture using a PTFE *'brush'* thereby eventually forming a lipid bilayer that seals the opening (Fig. 5.3d). The formation of such a membrane can be verified by a significant reduction in current as lipid bilayers are almost perfect insulators (Fig. 5.3f) [204]. CP2 DNA constructs with two central, diagonally-positioned cholesterol tags (2C) are then added to the cis-side of the cuvette and the current is recorded over time at a constant voltage (typically 50 to 100 mV). Spontaneous DNA nanostructure insertion is then observed by a sudden jump in the current to a stable conductance level (Figs. 5.3e,g). Similar to previous observations for a comparable DNA nanostructure [54], voltage-gating (sudden jumps between current levels at high voltages) and closure of the DNA-induced channel to a low-conductance level (voltage-switching) are observed (Fig. 5.3g). These characteristics further verify that the current jump is caused by a DNA nanostructure insertion.
Once an insertion step was observed, the voltage was reset to 0 V and a current-voltage curve (IV curve) was recorded by varying the voltage in ± 20 mV steps. In a well-sealed, plain lipid bilayer the current barely varies with the voltage staying close to 0 pA (see Fig. 5.4a). However, if a DNA nanostructure is inserted, the current changes linearly with the voltage to a much higher degree (see Fig. 5.4b), describing ohmic behaviour similar to previously reported membrane-inserted DNA nanostructures [54, 175].

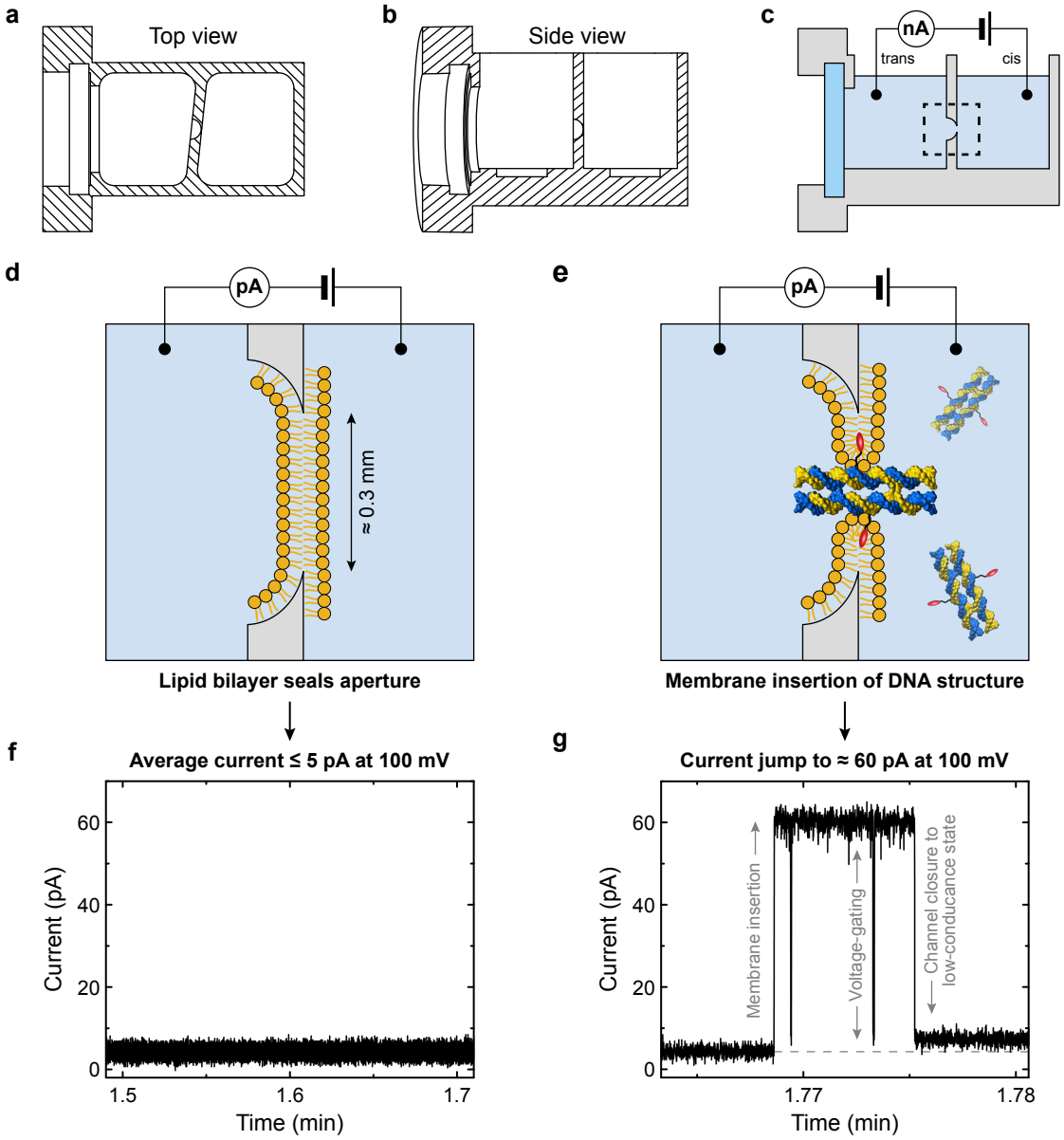

Fig. 5.3 Electrophysiology measurements to determine membrane insertion of DNA nanostructures. Top (**a**) and side (**b**) view of PTFE cuvette. (**c**) Schematic drawing of current measurement setup. The current across a central aperture (dashed rectangle) connecting two buffer-filled reservoirs is recorded. At an open aperture, and without an applied bias voltage, the current is in the low nA range. (**d**) Lipids, dissolved in n-decane, are spread across the aperture, eventually forming a lipid bilayer that seals the hole. (**e**) DNA nanostructures with two cholesterol modifications added to the cis-side of the cuvette can self-insert into the lipid bilayer, creating a passage for ions by acting as a DNA nanopore. (**f**) Current trace of a sealed bilayer. While the large size of the membrane allows for a low, residual current flow, the average current is typically $\leq$ 5 pA even at an applied voltage of 100 mV. (**g**) Current recording illustrating a current jump at constant voltage signifying the insertion of a DNA nanostructure. The trace also shows jumps between current levels (voltage-gating) and closure of the DNA nanopore to a stable, low-conductance level (voltage-switching).

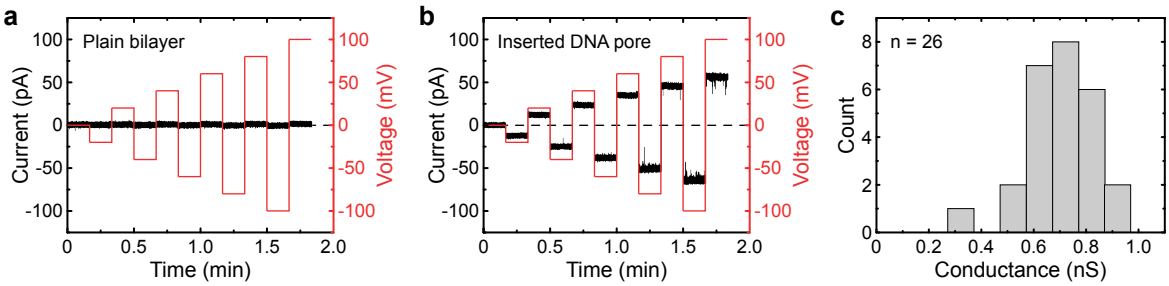

Fig. 5.4 Electrophysiological measurements of membrane-inserted DNA nanostructures. (**a**) Current-voltage trace of a sealed lipid bilayer without insertion of a DNA nanostructure. (**b**) Current-voltage trace of a lipid bilayer containing an inserted DNA nanostructure. (**c**) Conductance histogram of 26 insertion steps observed for DNA nanostructures across multiple different lipid bilayers and experiments. The mean conductance was determined to be 0.70 ± 0.14 nS (mean ± SD). The measurement buffer was 1 M KCl, 10 mM Tris at pH 8.

Over multiple lipid bilayers and experiments, insertion steps of the DNA nanostructure have been observed. The conductance levels determined from these insertion steps are plotted in Fig. 5.4c showing a mean conductance of 0.70 ± 0.14 nS (mean ± SD). The measured conductances fall well within the range determined for a similarly-sized DNA nanostructure published previously [54]. However, multiple experiments needed to be carried out and only in some of them DNA nanostructure insertion was observed. Given the comparatively large surface area of the aperture of ≈ 0.07 mm^2 (diameter equals ≈ 0.3 mm [198]) the insertion efficiency is rather low, a previously reported problem for artificial DNA-made ion channels [47]. Nevertheless, these experiments confirm that the CP2 DNA design modified with two cholesterols (2C) can insert into lipid bilayers. Furthermore, the results show that this DNA nanostructure can induce ionic currents across lipid bilayers thereby mimicking the function of naturally occurring protein ion channels.

5.3.2 Characteristics of the dithionite assay

To initially understand how the dithionite assay works and which parameters are crucial, vesicles have been formed from POPC lipids containing 0.5 wt% of NBD-DPhPE (see Fig. 5.9a for chemical structure) and extruded through membranes with a pore size of 200 nm. The vesicles were then diluted and analysed using a fluorometer (for details see Section 5.2.4). NBD is hereby excited with a laser and its emitted fluorescence is detected at a 90° angle over time. Figure 5.5a shows the absorption and emission spectrum of NBD-DPhPE in chloroform as stated by the supplier. To verify that these characteristics of NBD-DPhPE remain similar when inside a vesicle's membrane in aqueous solution, the emission spectrum of the above described vesicle suspension (80 µM final lipid concentration) was

recorded using an excitation wavelength of 460 nm (Fig. 5.5b). The maximum emission was determined at 535 nm, matching the value stated by the supplier. Therefore, NBD excitation was performed at 460 nm and emission was recorded at 535 nm for all measurements.

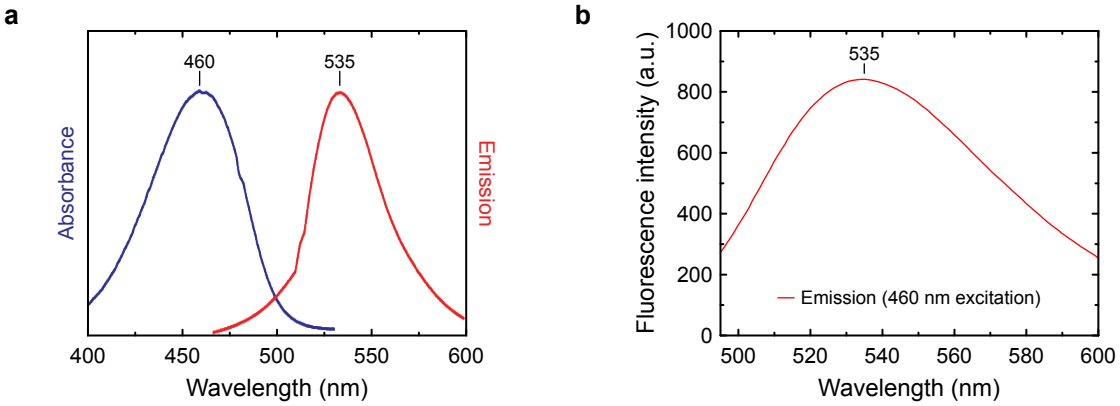

Fig. 5.5 Fluorescence spectra of NBD-DPhPE. (**a**) Absorption (blue) and emission (red) spectrum of NBD-DPhPE at 1 µg ml^{-1} in chloroform. Data provided by Avanti Polar Lipids. Image modified after [206]. (**b**) Emission spectrum from a suspension of POPC vesicles containing 0.5 wt% NBD-DPhPE. Data was recorded at 80 µM lipid concentration diluted in buffer L with an excitation wavelength of 460 nm. Trace represents the average of 3 separate scans and has been smoothed by adjacent averaging over 7 data points. Indicated values represent the wavelength of the respective local maximum.

Dithionite was then added to the vesicle solution to fluorescently reduce NBD-labelled lipids in the outer bilayer leaflet. Typical traces of the normalised fluorescence intensity observed in a dithionite reduction assay are displayed in Fig. 5.6. An initial plateau is followed by a rapid decrease in fluorescence intensity upon dithionite addition (50 mM final concentration) at $t = 2$ min. This fluorescence reduction plateaus at ~0.7 and is followed by a slow continuing decrease to ~0.6 in the time between 3 and 30 min. The initial plateau at 0.7 is higher than the expected value of ≈ 0.5 which is most likely connected to multilamellarity of the vesicles which we will discuss in Section 5.3.4. At 30 min the surfactant Triton X-100 was added, disrupting the vesicles such that all lipids are now accessible to be bleached by dithionite leading again to a rapid decrease in fluorescence. Variations in the reduction rates are most likely related to different mixing times of the solutions in the sample. Apart from this, the traces are very reproducible in multiple experiments.

A close-up of the initial rapid decrease in fluorescence is shown in Fig. 5.7a. To avoid a possible error by the device (occasionally induced by the pipette tip blocking the laser pathway), data acquisition was paused during dithionite addition. This resulted in a sudden jump between two data points (indicated by the arrow in Fig. 5.7a). As the added dithionite solution was typically less than 5 % of the total volume of the solution, this jump is partially

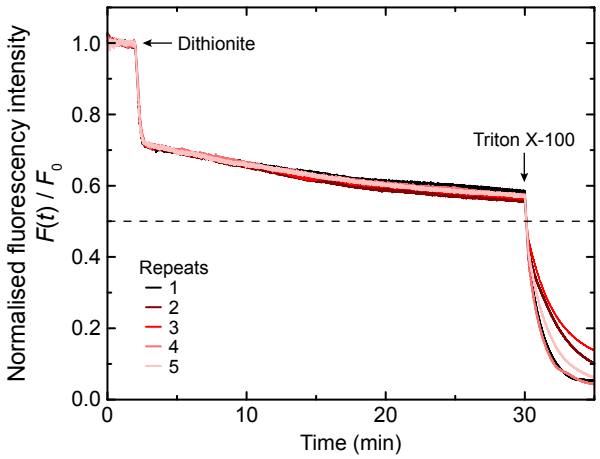

Fig. 5.6 Dithionite reduction assay on lipid vesicles. Dithionite addition induces a sudden decrease in fluorescence intensity due to bleaching of NBD lipids in the vesicles' outer bilayer leaflet. Triton X-100 addition disrupts the vesicles enabling dithionite to access lipids inside the vesicles causing a further fluorescence reduction. Traces represent independent experiments performed using the same vesicle stock solution but always fresh dithionite.

explained by sample dilution but predominantly caused by the dithionite reduction already being initiated for a brief moment before data acquisition was resumed. Dithionite has been shown to decompose in aqueous solutions due to air oxidation [207]. Therefore, a crucial element for repeatable results is that dithionite was prepared freshly every time before addition [138, 139, 208–210]. Figure 5.7b illustrates the effect of using dithionite solution 5 days after preparation resulting in a much slower fluorescence decrease. The decomposition has also been shown to happen more rapidly at low pH [24, 211]. Therefore, dithionite powder was always first prepared in 1 M Tris solution adjusted to pH 10 before it was diluted further, consistent with previously reported experimental procedures [24, 138, 208, 209].

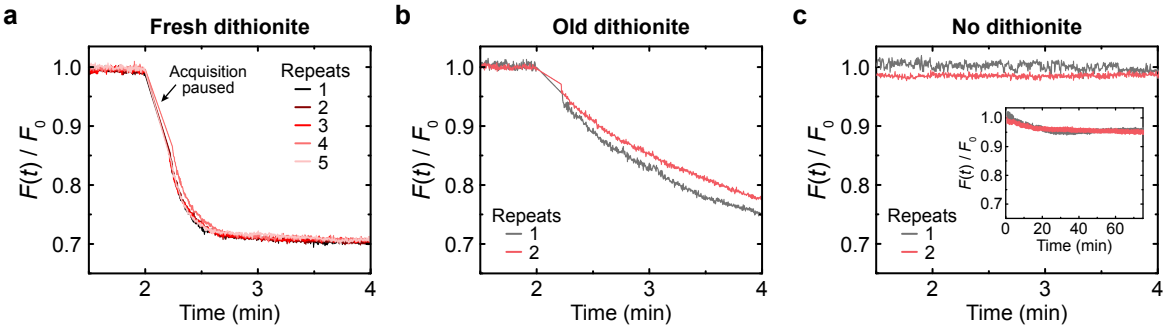

Fig. 5.7 Effect of old dithionite and NBD photobleaching. Graphs highlighting the effect on the fluorescence intensity of NBD vesicles if dithionite is (**a**) freshly prepared, (**b**) 5 days old, or (**c**) if no dithionite was added to the solution. Inset in **c** shows a larger time scale to illustrate the effect of photobleaching.

Lastly, no dithionite was added to the vesicle solution to determine the effect of photobleaching on the NBD dye during the measurement. At longer time scales an initial decrease by ~5 % within the first 20 min followed by a stable plateau is observed (inset in Fig. 5.7c). However, at relevant time scales for the dithionite assay, photobleaching had no significant effect on the fluorescence intensity (see Fig. 5.7c).
In order to correctly understand and interpret the results of the dithionite assay, the influence of its components was studied separately. Table 5.2 presents an overview of the explored conditions for five different parameters.

Table 5.2 Overview of tested conditions for dithionite assay.

Parameter	Tested conditions
Dithionite concentration (mM)	2, 4, 6, 8, 10, 50
NBD labelling position	head-labelled, tail-labelled
Lipid composition	POPC, 3:1 EColi-eggPC
Extrusion pore size (nm)	30, 100, 200, 400, 1000
OPOE concentration (%)	0.005 to 0.2

5.3.3 Influence of dithionite concentration

Previous reports in the literature typically employed final dithionite concentrations ranging from 3 to 60 mM [14, 24, 115, 131, 132, 137–141], with 10 and 20 mM being the most frequently used. In the previous section, 50 mM dithionite was employed which is on the high end of the spectrum. To investigate the influence of the dithionite concentration the assay was performed multiple times, each with a different final concentration of dithionite added to the solution (Fig. 5.8). The graph shows that for increasing concentrations the rate of fluorescence reduction is sped up, as expected. The decay traces (starting with the first point once data acquisition after dithionite addition was resumed) are well described by a single exponential which yields the characteristic decay times $\langle\tau\rangle$ (see inset in Fig. 5.8a).
At longer time scales the traces show a continuing decrease in fluorescence even after the initial exponential reduction (see Fig. 5.8b). Approximating the traces between 10 and 30 min with a linear fit yielded a percental decrease of fluorescence intensity ranging from ~10 to 25 % per hour (inset in Fig. 5.8b). In data obtained previously by Malvezzi *et al.*, similar rates of ~17 % per hour were observed, although at 40 mM dithionite concentration and a different lipid mixture (EColi-eggPC which will be discussed in the next section) [14]. These rates are higher than the ones determined for photobleaching (compare Fig. 5.7c). Furthermore, their increase with increasing dithionite concentration indicates that this could be related

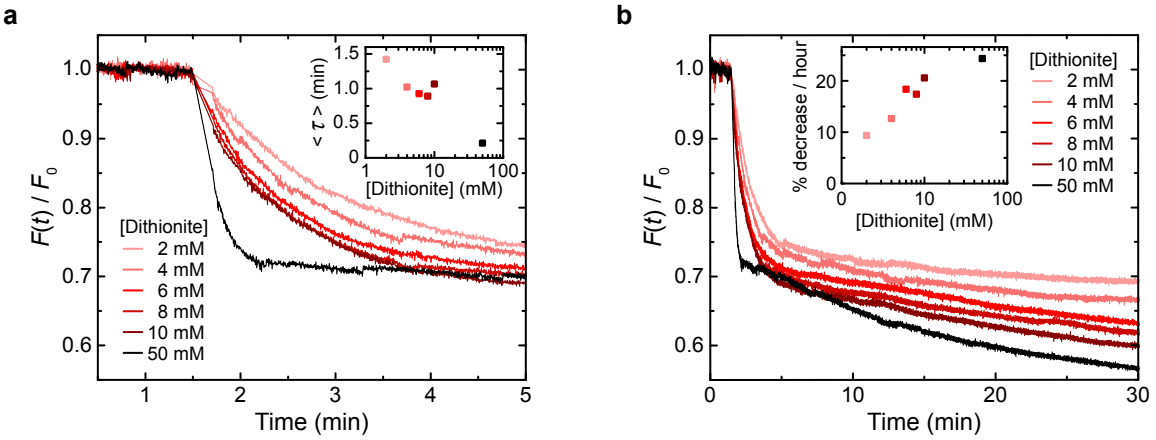

Fig. 5.8 Dithionite assay of POPC-NBD LUVs at different dithionite concentrations. (**a**) Normalised intensity over time upon addition of final dithionite concentrations ranging from 2 to 50 mM. Inset shows the time constants $\langle\tau\rangle$ obtained from single exponential fits to the traces from the point the acquisition was resumed after dithionite addition. (**b**) Longer time scale to illustrate the concentration-dependent fluorescence decrease over time even after the initial rapid reduction. Inset shows the percentage decrease per hour from a linear fit to the trace between 10 and 30 min.

to dithionite permeating through the membrane of the vesicles at a low rate. A previous study reported 5 mM dithionite to be an optimal concentration to observe NBD reduction in the outer bilayer leaflet without affecting NBD lipids in the inner bilayer leaflet [141]. However, another study that many of the here presented protocols are based on, employed 40 mM dithionite to observe more rapid reduction kinetics [14]. For further experiments we will therefore be either employing 5 or 40 mM final dithionite concentration which will be indicated for each experiment. However, the dithionite concentration will be the same within each set of experiments. It is important to note that even concentrations of as low as 0.5 mM have been reported to be sufficient to completely reduce NBD, however, longer time scales are required (~1–3 min compared to < 1 min for $\geq$ 10 mM dithionite) [24]. Ultimately, at sufficiently short time scales ($\leq$ 5 min) varying the dithionite concentration between 5 and 40 mM should only slightly affect the value where the fluorescence intensity plateaus at, but predominantly the reduction kinetics.

5.3.4 NBD labelling position, vesicle size & lipid composition

In the dithionite assay, the readout is provided by the NBD-labelled reporter lipids. The labelling position could therefore have an influence on the measured results. To test this, lipid vesicles were formed from POPC lipids with 0.5 wt% fluorescently labelled lipids with the NBD tag located either on the lipid headgroup (head*, Figs. 5.9a,c) or on a fatty acid chain via a C6 linker (tail*, Figs. 5.9b,d).

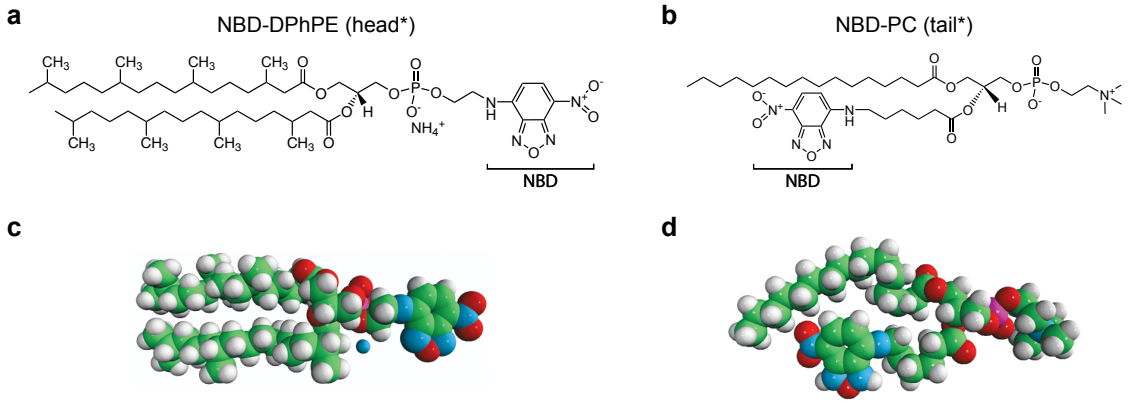

Fig. 5.9 Chemical structures of NBD-labelled lipids. (**a**) Head-labelled 16:0 NBD-DPhPE (head*) (**b**) 16:0-06:0 NBD-PC labelled with NBD on one of the fatty acid chains via a C6 linker (tail*). (**c,d**) 3D representations of the respective lipids (Colour code: C = green, H = white, O = red, N = blue, P = purple). Images taken from [206] and [212], respectively.

To simultaneously test the influence of the vesicle size, these vesicles were then extruded through polycarbonate membranes with different pore sizes ranging from 30 nm to 1 µm. Subsequently, a dithionite assay was performed and the emitted bulk fluorescence intensity was recorded. Figures 5.10a,b show the normalised fluorescence intensity before and after dithionite addition for POPC vesicles with either head-labelled (head*) or tail-labelled (tail*) NBD lipids. For all vesicle sizes and both reporter lipids, a rapid decrease in fluorescence is observed after dithionite addition (2 µl at 250 mM) at ~1.5 min, levelling off to rather stable plateaus with only a slight remaining decrease. The scatter plot in Fig. 5.10d compares the average fluorescence intensity at 6 min across different vesicle sizes. If every vesicle in the solution is unilamellar, one would expect the fluorescence intensity to approach a value of ≈ 0.5 as for each vesicle only lipids in the outer bilayer leaflet are fluorescently reduced. This is only the case for the smallest POPC vesicles with the NBD tag at the fatty acid chain. For all other vesicles, the intensity levels off at higher values, with ~0.8 for the largest vesicles. In general, the larger the vesicles, the higher the plateau. A possible explanation could be an increasing proportion of multilamellar vesicles in the solution for larger vesicles as only the NBD lipids in the furthest outer bilayer leaflet are reduced by dithionite while membranes

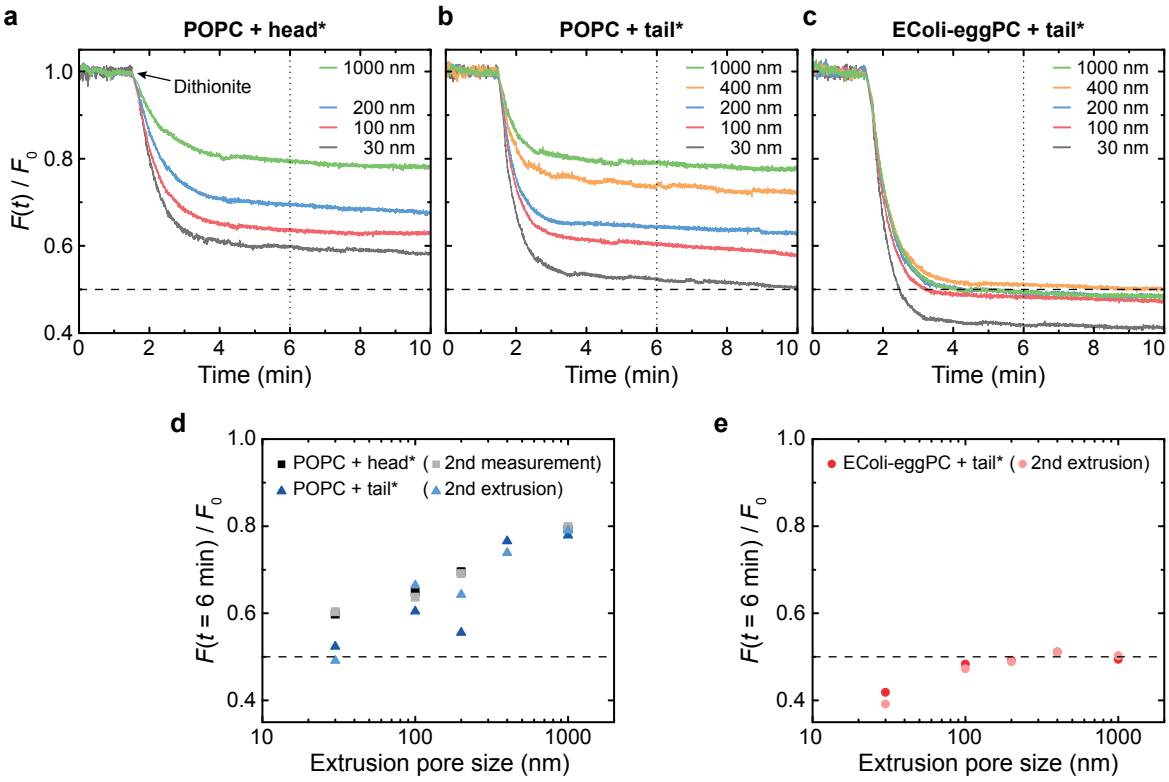

Fig. 5.10 Dithionite assay dependence on vesicle size, labelling position, and lipid type. Graphs displaying dithionite reduction assays of vesicles extruded at different membrane pore sizes and composed of POPC and a head-labelled NBD lipid (**a**), or POPC and a tail-labelled NBD lipid (**b**), or a mixture of EColi and eggPC and a tail-labelled NBD lipid (**c**). Final dithionite concentration was 5 mM. (**d,e**) Scatter plots comparing the normalised intensity at 6 min across different vesicle sizes for POPC (**d**) and EColi-eggPC vesicles (**e**). Light coloured data points refer to either a repeated measurement of the same extruded vesicle batch, or a measurement of a second extrusion from the same stock lipid batch.

inside are unaffected. While another explanation could be that NBD lipids aggregate and are therefore less accessible by dithionite, the fact that the bleaching plateaus scale with the vesicle size makes multilamellarity the more plausible explanation.

Size-dependent fluorescence reduction plateaus were observed for both head- and tail-labelled lipids with a comparable trend (see Fig. 5.10d). The most significant deviation between the two labels occurred for vesicles extruded at 30 nm. This could suggest that for small vesicles the labelling position has a more significant influence, with tail-labelled lipids being closer to a value of 0.5. However, the deviations between extrusion batches are of a comparable degree. This suggests that the labelling position might not have a significant influence on the specific fluorescence intensity value once a plateau after dithionite addition is reached. However, determining the rates of fluorescence reduction by fitting with a single exponential

reveals faster kinetics (lower $\langle\tau\rangle$) for tail-labelled reporter NBD lipids (see Fig. 5.11). This is surprising given that NBD labelled at the lipid headgroup should be easier or at least similarly accessible to be bleached by dithionite than the NBD labelled at the fatty acid chain (compare Fig. 2.9 in Chapter 2). However, choosing a lipid reporter with a faster fluorescence reduction rate is more desirable, as this allows to study faster lipid scrambling rates as the dithionite reduction rate would be less rate-limiting. Therefore, tail-labelled NBD-PC (tail*) lipids were used as the reporter lipid for further experiments.

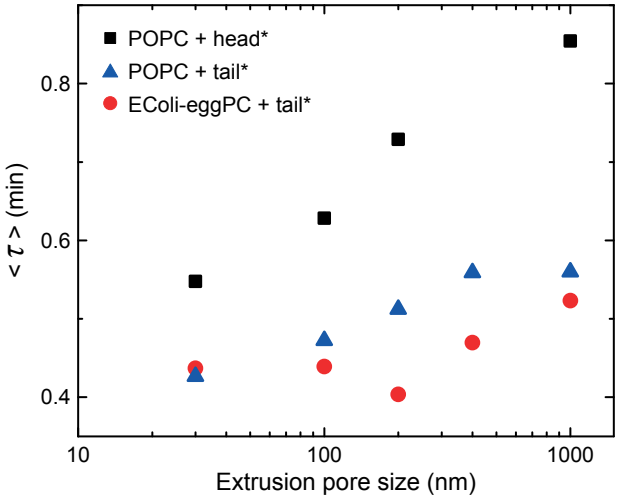

Fig. 5.11 Time constants $\langle\tau\rangle$ for different NBD lipids and lipid mixtures. Values were obtained from single exponential fits to the traces shown in Figs. 5.10a-c from the point the acquisition was resumed after dithionite addition until the five minute mark.

To gauge the robustness of the assay, deviations between performing measurement repeats of the same vesicle solution after extrusion (squares in Fig. 5.10d) and deviations between two separately extruded vesicle solutions (triangles in Fig. 5.10d) were analysed. The results show that the error between two measurements of the same sample after extrusion is comparatively small ($\leq$ 1 %), however, the error between different extrusions at the same pore size is much more relevant ($\leq$ 9 %). This could also be an explanation for the deviations observed between differently labelled lipids supporting the conclusion that the position of the fluorescent label only has a minor influence on the fluorescence intensity plateau.
Lastly, the influence of the vesicle's lipid composition was investigated. Therefore, the same experiments were repeated with vesicles composed of a 3:1 mixture of EColi and eggPC together with the tail-labelled NBD lipids. Remarkably, for all extrusion sizes except 30 nm, the fluorescence intensity plateaued almost exactly at 0.5 (see Figs. 5.10c,e) suggesting a very high degree of unilamellarity. Furthermore, the difference between two separately extruded vesicle batches was below 1 % for vesicles with a diameter $\geq$ 100 nm showing

much better reproducibility than what was observed for POPC vesicles. However, for the smallest vesicles surprisingly a value of ≈ 0.4 was reached, lower than the expected value of 0.5. This can be explained by the fact that a fluorescence reduction to 0.5 would only take place if the amount of lipids in the inner and outer bilayer leaflet was approximately the same. However, for vesicles of small diameter, the asymmetry in lipid amount between the bilayer leaflets starts to become relevant. This hypothesis can be verified by geometrical estimations of how many lipids are able to fit in the inner and outer bilayer leaflets depending on the vesicle size. The amount of lipids in the bilayer leaflets can be estimated in two ways:

a) Via the surface area of the inner and outer bilayer leaflet divided by the area of a lipid.

b) Via the volume of the inner and outer bilayer leaflet divided by the volume of a lipid.

With d_V being the outer diameter of the vesicle and d_B being the bilayer thickness, the following equations yield the number of lipids in the inner (N_i) and outer (N_o) bilayer leaflet:

Via area of a lipid:	Via volume of a lipid:
$N_o = \frac{\pi}{A_L} {d_v}^2$	$N_o = \frac{\pi}{6V_L}\left[{d_V}^3 - (d_V - d_B)^3\right]$
$N_i = \frac{\pi}{A_L}(d_V - 2d_B)^2$	$N_i = \frac{\pi}{6V_L}\left[(d_V - d_B)^3 - (d_V - 2d_B)^3\right]$

(5.1)

To estimate the asymmetry of the number of lipids between the inner and outer bilayer leaflet, POPC lipids can be used as an example as their structure within fully hydrated lipid bilayers has been well characterised previously [213] with the data shown in Table 5.3.

Table 5.3 Dimensions of POPC lipids and membranes. Values have been taken from [213] and V_L has been calculated via $V_L = \frac{1}{2} d_B A_L$.

Bilayer thickness	d_B	3.680 nm
Area of a lipid	A_L	0.683 nm^2
Volume of a lipid	V_L	1.257 nm^3

Using these values for POPC lipids, the graphs in Fig. 5.12a plot the total number N of lipids in a vesicle of diameter d_V calculated from the sum of N_o and N_i either via the surface area or the volume of the bilayer leaflets. The numbers of lipids per vesicle agree very well between calculations via surface area or via volume and deviations fall below 1 % already for vesicle diameters above ~35 nm.

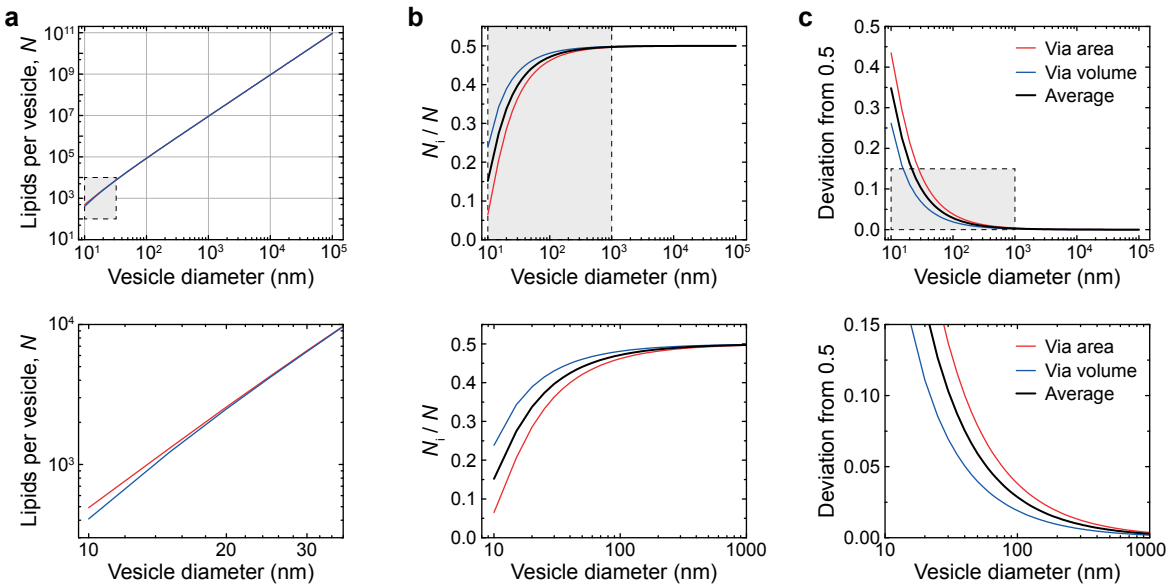

Fig. 5.12 Estimations on lipid asymmetry between the bilayer leaflets of POPC membranes. (**a**) Total number of lipids per vesicle (N) as a sum of N_o and N_i calculated either via the surface area (red) or the volume (blue) of the bilayer leaflets using Equations 5.1. (**b**) Ratio between the number of lipids in the inner bilayer leaflet (N_i) and the total number of lipids per vesicle (N). Black line represents the average of both calculations. (**c**) Deviation from an ideal value of 0.5 depending on the vesicle size. Bottom graphs highlight the lower end of the vesicle sizes (shaded areas in top row) where lipid bilayer asymmetry is most relevant.

In a dithionite assay, the value of the fluorescence plateau after dithionite addition depends on how many lipids remain inaccessible to dithionite. Given the assumptions that

- spontaneous lipid flipping happens at much longer time scales than the experiment,
- NBD-labelled lipids are distributed homogeneously within the overall lipid mixture,
- dithionite does not permeate through the membrane at the time scale of the experiment,
- and all vesicles are unilamellar,

these fluorescence intensity values should be equal to the ratio of lipids on the inner bilayer leaflet over the total number of lipids in that vesicle. Using Equations 5.1, this ratio can be calculated depending on the vesicle diameter which is plotted in Fig. 5.12b. Here, estimations performed via the area and the volume differ more significantly only reducing to less than 1 % for vesicles above ~200 nm which is why their average for the purpose of this estimation is plotted as well. Figure 5.12c allows for a direct quantification of the expected deviation from an ideal value of 0.5 induced by asymmetric lipid distribution between the bilayer lipids. For vesicles above ~200 nm this deviation falls below 2 % and below 1 % for vesicles above

~400 nm in diameter. This means that for vesicles above these diameters measurement errors become more relevant than deviations in membrane asymmetry.
Using Equations 5.1, the experimentally determined fluorescence intensity plateaus shown in Fig. 5.10e can be well explained by the asymmetry in the number of lipids between the inner and outer bilayer leaflet (Fig. 5.13). Although the dimensions of POPC lipids were used for the estimations, they agree very well with the experimental results obtained from the EColi-eggPC mixture. Calculations via volume match the data better as calculations via area seem to overestimate the asymmetry in lipid distribution between the bilayer leaflets.

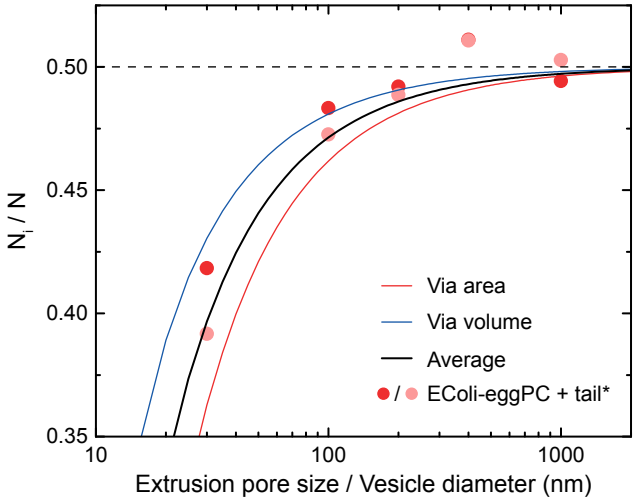

Fig. 5.13 Comparison of membrane asymmetry estimations with dithionite reduction experiments. For the calculations, the vesicle diameter d_V was assumed to be equal to the extrusion pore size. Data points from EColi-eggPC vesicles are the same as shown in Fig. 5.10e.

The fact that POPC vesicles do not agree well with the estimated asymmetry values can most likely be explained by the high degree of multilamellarity, as discussed above. In turn, vesicles formed from 3:1 EColi-eggPC seem to possess a very high degree of unilamellarity. The results would even suggest that this mixture can be used to form unilamellar vesicles up to 1 µm in diameter simply via extrusion. To verify this, DLS measurements have been performed to determine the actual size of the vesicles after extrusion (Fig. 5.14). Interestingly, vesicles formed from EColi-eggPC seem to adopt a preferred size of ~150 to 200 nm in diameter as extrusions at larger pore sizes did not affect the vesicle diameter. This is in contrast to POPC vesicles where the average diameter can yield larger values of ~450 nm or even $\geq$ 500 nm when extruded at 400 nm or 1,000 nm, respectively. The preferred size of EColi-eggPC vesicles could explain the high degree of unilamellarity determined from dithionite experiments, as unilamellarity is typically observed for vesicles below 200 nm in diameter [214, 215]. Unfortunately, this therefore rules out the EColi-eggPC mixture as a

simple way to form larger unilamellar vesicles. The increased amount of multilamellarity determined for POPC vesicles even below 200 nm could possibly be reduced by a higher number of passes through the porous membrane during extrusion. Nevertheless, the EColi-eggPC mixture performed superior in forming highly unilamellar vesicles.

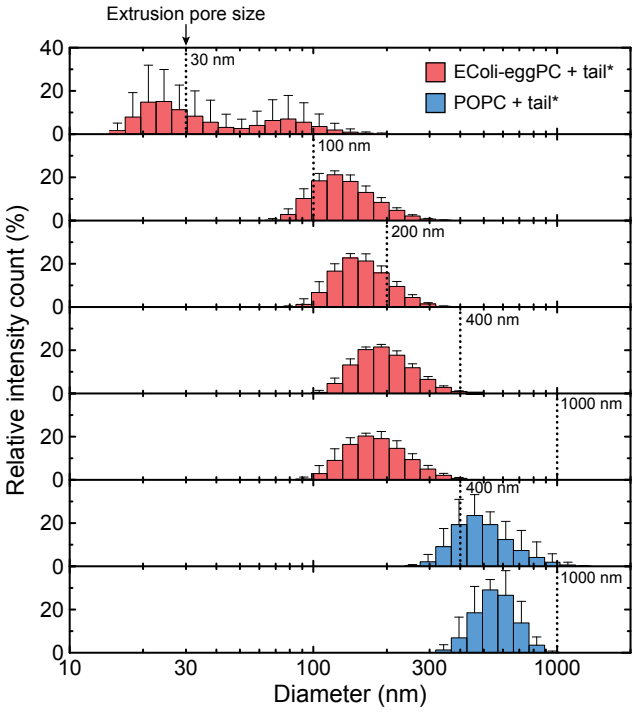

Fig. 5.14 Diameter of lipid vesicles extruded at different pore sizes measured with DLS. Extrusion pore sizes are indicated as dotted lines. Extrusions were performed from the same unextruded stock vesicle batch for both EColi-eggPC + tail* (red) and POPC + tail* (blue).

In conclusion, no significant difference between NBD labelling positions regarding the reached fluorescence plateau after dithionite addition was observed. However, lipid composition and vesicle size had a significant influence which is most likely related to the vesicles' lamellarity. Although POPC vesicles extruded at 30 nm yielded values close to 0.5, for such small vesicles a value of 0.4 would be expected due to the increased asymmetric distribution of lipids between the bilayer leaflets. As all other vesicle sizes yielded even higher fluorescence intensities it can be concluded that POPC vesicles of all sizes demonstrated a measurable degree of multilamellarity in the performed experiments. One possible reason could be that 15 single passes through the extrusion membrane was insufficient to form unilamellar POPC vesicles. Doubling the number of passes could yield a more uniform and unilamellar vesicle distribution. In contrast, EColi-eggPC vesicles showed a very high degree of unilamellarity as fluorescence intensity plateaus agreed very well with the estimated trend based on the lipid distribution between bilayer leaflets of unilamellar vesicles. Here, smaller

vesicles yield greater deviations from 0.5 but already for an extrusion pore size of 200 nm this reduced to less than 1 %. Furthermore, results were very reproducible for that lipid mixture and that size range. Therefore, vesicles formed from EColi-eggPC at a size of 200 nm are ideal for performing dithionite reduction experiments.
Lastly, the results in this section also demonstrate that the dithionite reduction assay is excellent at determining if vesicles are unilamellar. This has been successfully employed by another member of our group to demonstrate unilamellarity at the single-vesicle level of giant unilamellar vesicles formed on a microfluidic chip [216]. However, for bulk measurements on vesicles with diameters below 1 µm it is recommended to accompany the assay with DLS measurements to verify the correct vesicle formation and size.

5.3.5 Influence of OPOE concentration on dithionite assay

Surfactants have previously been employed to aid the insertion of membrane proteins and DNA nanostructures into lipid bilayers [204, 217–219], particularly poly(ethylene glycol) octyl ether (OPOE) [67, 72, 79, 217, 220]. The critical micelle concentration (CMC) of OPOE is 0.23 % ($\approx$ 6.6 mM) [217], however, for applying this surfactant to the dithionite assay, it was necessary to ensure that the surfactant does not affect the spontaneous lipid flip-flop activity in membranes of lipid vesicles already at concentrations below the CMC. Furthermore, as the dithionite assay requires that dithionite does not permeate through the vesicles' membranes, it was crucial to verify that the membrane integrity was still maintained. To reduce mixing effects where the OPOE concentration would temporarily be much higher than intended, 1 % OPOE solution was pre-diluted in buffer L to a volume of 96 µl and only then 4 µl of vesicle solution was added to yield the intended final surfactant concentration.
Figure 5.15a shows the results of the dithionite assay performed at final concentrations of OPOE ranging from 0.005 to 0.2 %. For low concentrations ($\leq$ 0.01 %) no change compared to the control without OPOE was determined. However, from concentrations of 0.05 % and higher, the reached fluorescence plateau started to decrease rapidly with increasing OPOE concentration (see Fig. 5.15b). This shows that already concentrations below the CMC can affect the results of the dithionite assay. It is however unclear, if the mechanism in the intermediate concentration range (~0.1 %) that facilitates further dithionite reduction, is based on an increased spontaneous lipid flip-flop rate or dithionite permeating through the vesicle membrane. Nevertheless, OPOE concentrations of 0.01 % or less represent a suitable range to try to aid DNA nanostructure insertion without inducing additional lipid scrambling activity on their own.

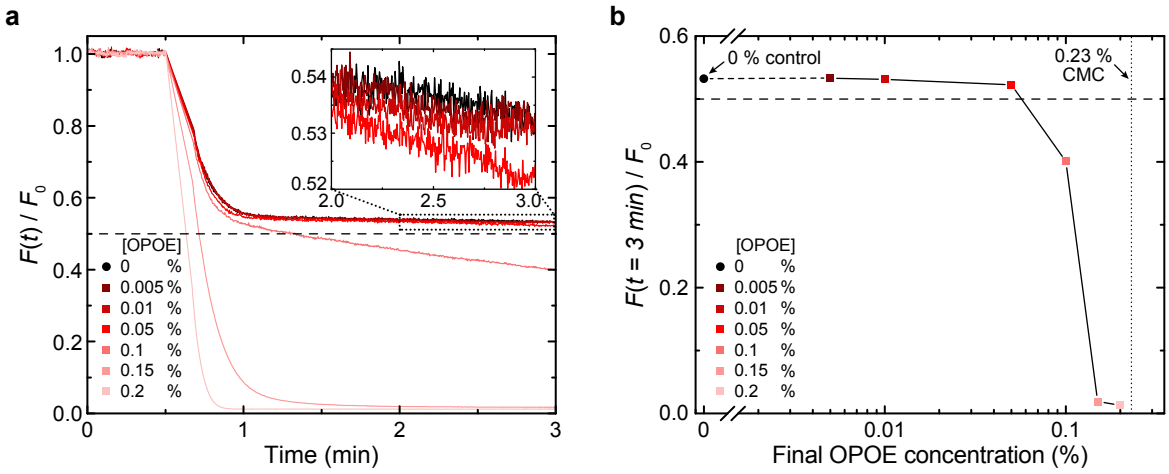

Fig. 5.15 Influence of OPOE on dithionite assay. (**a**) Dithionite assay performed in the presence of varying concentrations of OPOE. Vesicles were formed from a 3:1 EColi-eggPC mixture with NBD-PC reporter lipids extruded at 200 nm. Final lipid concentration was 80 µM and final dithionite concentration 40 mM. (**b**) Normalised fluorescence intensity at 3 min. Dotted line indicates the critical micelle concentration of OPOE.

5.3.6 TMEM16F protein scramblase assay

Having studied the influence of the different components on the dithionite assay, it was beneficial to establish a positive control to show that we can detect scrambling activity with this method. This meant to incorporate a known scramblase protein into the vesicle membrane and observe a significantly higher intensity reduction as compared to vesicles without scramblase. Although there has been some initial controversy whether the transmembrane protein TMEM16F solely regulates phospholipid scrambling or is a phospholipid scramblase itself [95, 117, 221], recent studies confirmed the scrambling activity of TMEM16F itself [21, 114, 119, 121, 222, 223]. We therefore purchased human TMEM16F recombinant protein and formed proteoliposomes according to a previously described method [14]. The protocol required the addition of the zwitterionic detergent CHAPS to facilitate protein insertion. However, as seen in the previous section with OPOE, at sufficient concentrations surfactants can destabilise the membrane leading to a false-positive result regarding scrambling activity. Therefore, it was important to first verify without scramblase protein that CHAPS can be sufficiently removed such that it does not interfere with the dithionite assay. CHAPS was added to freshly sonicated lipids (either POPC or 3:1 EColi:eggPC) and gradually removed using two or four exchanges of Bio-Beads^{TM} resin. Subsequently, vesicles were extruded and a dithionite reduction assay was performed (saturated colours in Figs. 5.16a-c). As a control, no CHAPS was added to one part of the sonicated lipids but all other steps were performed analogously (pale colours in Figs. 5.16a-c).

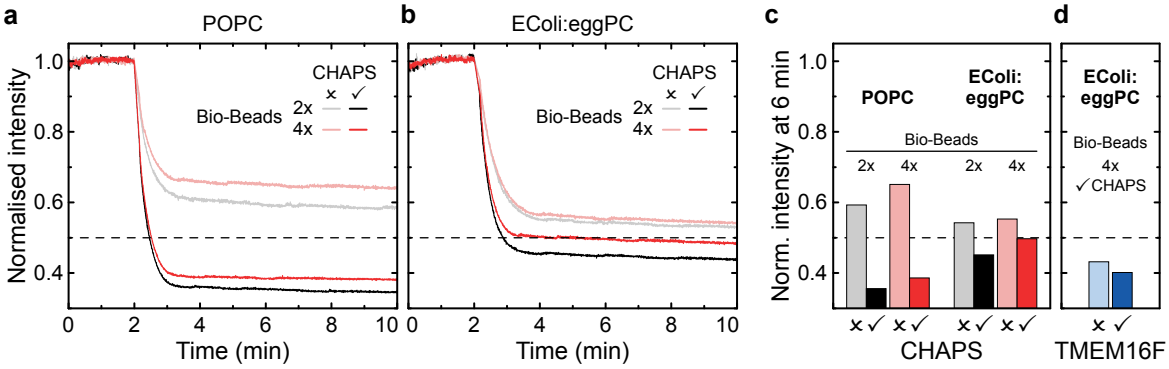

Fig. 5.16 Effect of CHAPS and TMEM16F scramblase on dithionite assay. (**a,b**) Dithionite reduction assay with (saturated colours) or without (pale colours) CHAPS performed on POPC (**a**) or 3:1 EColi:eggPC (**b**) vesicles. All samples were treated with 2 or 4 exchanges of Bio-Beads beforehand. Final dithionite concentration was 40 mM. (**c**) Bar chart comparing the normalised intensities at 6 min of traces shown in **a,b**. (**d**) Dithionite assay performed without (light blue) and with (dark blue) addition of TMEM16F scramblase protein.

The results consistently showed a shift to lower fluorescence intensities for lipids that had been treated with CHAPS compared to lipids that had not. Using 4 exchanges of Bio-Beads had a measurable improvement on removing the surfactant as the fluorescence reduction shifted again closer to 0.5. Vesicles formed from POPC without CHAPS show a similar behaviour as discussed in Section 5.3.4, in that they only approach values above 0.5 indicating some degree of multilamellarity (Fig. 5.16a). When CHAPS had been added to the lipids the fluorescence reduced to ~0.4, suggesting that dithionite can access an increased amount of NBD-labelled lipids. In contrast, vesicles formed from EColi-eggPC show again a more consistent behaviour approaching values closer to 0.5 in all cases (Fig. 5.16b). This furthermore confirms that EColi-eggPC vesicles are better suited to perform the dithionite reduction assay as they show greater reproducibility and resilience against surfactants. A comparison of the normalised intensity values at 6 min illustrates that the vesicles formed from EColi-eggPC, treated with CHAPS, and followed by 4 exchanges of Bio-Beads, approached 0.5 the closest and were therefore deemed the best system (Fig. 5.16c).

To obtain a positive control for scrambling activity, the known scramblase TMEM16F was added to freshly sonicated lipids together with CHAPS. After detergent removal and extrusion, the dithionite assay was performed. The results show a slightly decreased plateau at ≈ 0.4 after dithionite reduction (Fig. 5.16d). However, the control prepared in parallel without scramblase protein yielded a value of ≈ 0.43, reducing the effect of the scramblase to a difference of only 0.03. Although TMEM16F is calcium-activated [95], addition of calcium ions did not significantly affect these results. Furthermore, even without Ca^{2+} ions, the fluorescence intensity for a similar scramblase protein (afTMEM16) was shown to still

decrease to values below 0.3 [14]. Therefore, the results are not indicative of lipid scrambling activity given the possible deviations that can occur in the extrusion and detergent removal steps. Multiple reasons could explain the negligible influence of the scramblase:

- Too few scramblase protein was added.
- Incorporation into the membrane was too inefficient.
- Bio-Beads filtered scramblase out before membrane incorporation occurred.
- Protein not stable or not active.

The last reason could be the most likely as subsequent to these experiments the company informed us that no tests were ever performed to verify the biological activity of the provided protein. This interpretation is also supported by the fact that previously published work does not mention any scramblase protein supplier but rather that the researchers or a collaborator expressed the protein themselves. Due to this difficulty of obtaining a functioning scramblase protein, it was not possible to establish a positive scrambling control.

5.3.7 Bulk dithionite reduction assay with DNA nanostructures

Despite the lack of a positive control using a natural scramblase protein, we attempted to determine the possible scrambling activity of membrane-inserting DNA nanostructures with this bulk dithionite reduction assay. We initially verified that the DNA nanostructures are attaching to the lipid vesicles. For this, LUVs (3:1 EColi-eggPC, 0.5 wt% NBD-PC) were extruded at 200 nm and incubated with DNA nanostructures either without cholesterol or modified with 1 to 4 cholesterol tags. The DNA nanostructures were of the CP2 design and prepared as described in Chapter 4 using cholesterol-TEG and an adenine spacer (compare Fig. 4.11). Subsequent to the incubation with vesicles, DLS size measurements were performed (see Fig. 5.17). The results show an average vesicle diameter of 179 nm if DNA nanostructures were not modified with cholesterol (Fig. 5.17b). This agrees with previous observations that DNA nanostructures lacking hydrophobic modifications are not expected to attach to vesicles formed from zwitterionic lipids [8, 54, 74]. Once DNA nanostructures contained cholesterol modifications, an increased vesicle size was observed. The size shift was slightly larger for structures with only one cholesterol modification which could indicate a more loose attachment to the vesicle. However, for all constructs containing more than one cholesterol tag the average vesicle diameter increased by ~20 nm. This is in good agreement with the expected increase for DNA nanostructures attaching to the vesicles.

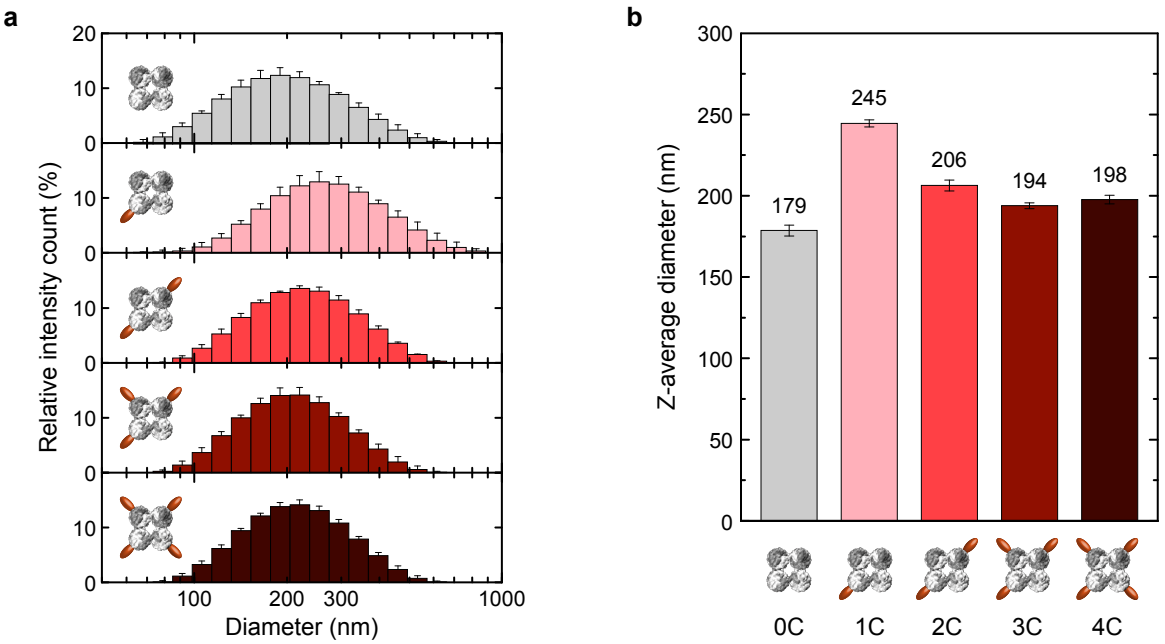

Fig. 5.17 DLS showing attachment of DNA nanostructures to LUVs. (**a**) DLS size measurements of LUVs extruded at 200 nm and incubated for 1 hour with 500 nM DNA nanostructures without or with 1 to 4 cholesterol modifications (compare Fig. 4.11). The final $MgCl_2$ concentration was 5 mM. The Z-average diameter (mean ± SD) is shown in (**b**).

As structures with only one cholesterol are not expected to form stable membrane insertion [75], the dithionite reduction assay was performed with 0C, 2C, 3C and 4C constructs only (Fig. 5.18). The traces show an initial rapid decrease to ~0.6, however, no significant difference between non-membrane-attaching (0C) and membrane-attaching structures (2C, 3C, 4C) is observed. Looking at the initial decay between 1 to 2 min, it seems that 2C structures show a more significant drop in fluorescence intensity (Fig. 5.18b, top). However, towards the end of the experiment (at 30 min) the 0C design showed the lowest fluorescence intensity (Fig. 5.18b, bottom). The comparison of initial intensity reduction levels with final ones shows only marginal differences between the different DNA nanostructures (Fig. 5.18c). These variations are within the typical deviations of performing the assay multiple times (compare Fig. 5.6). Therefore, the data does not provide a clear indication that the DNA constructs were able to induce lipid scrambling in a significant portion of the vesicles. Further experiments with the 2C design at a concentration of 100 and 200 nM and in the presence of 0.01 % OPOE still showed comparable results to Fig. 5.18a.

Although the DLS experiments indicated LUV membrane attachment of cholesterol-modified DNA nanostructures, the bulk dithionite reduction experiments were not able to demonstrate their scrambling activity. One drawback of this bulk assay is that it requires a relatively

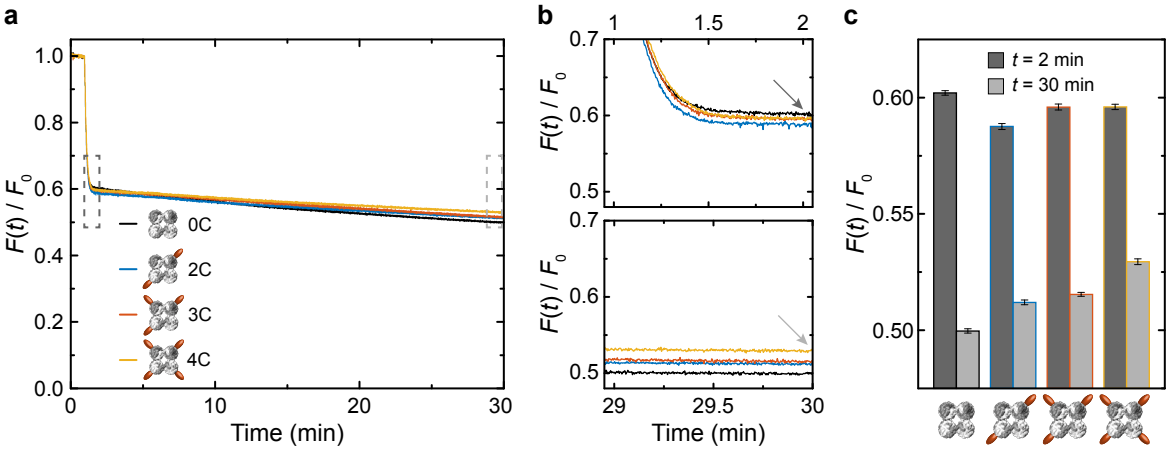

Fig. 5.18 Dithionite reduction assay with DNA nanostructures. (**a**) Dithionite reduction assay of 200 nm vesicles incubated with 100 nM DNA nanostructures without or with 2 to 4 cholesterol modifications. Final dithionite concentration was 40 mM. (**b**) Graphs focusing on the normalised fluorescence intensity right after the dithionite reduction (2 min, top) and at the end of the recording (30 min, bottom). (**c**) Histogram comparing the normalised fluorescence intensity averaged over 10 consecutive values (~2 s) at 2 and 30 min (mean ± SD).

efficient insertion of the DNA nanostructures. An adequate proportion of vesicles needs to have membrane-inserted, lipid scrambling DNA nanostructures to induce a fluorescence reduction sufficient enough to be detectable in bulk. In order to determine the minimum number of scrambled lipid vesicles that can be detected, we will use the results of the five dithionite reduction repeats shown in Fig. 5.6 to estimate the experimental errors. Averaging over 50 consecutive normalised fluorescence intensity values (~10 s) yields a standard deviation of ≈ 0.2 % representing the experimental noise (= the systematic error). This value does not significantly change once the fluorescence reduction plateau is reached (for these experiments defined as from 6 min onwards). The standard deviation of the fluorescence intensity averaged over the five experimental repeats is between 0.3 % (at 6 min) and 0.9 % (at 30 min). Therefore, the total error is on the order of ~1 %.

The electrophysiology experiments, discussed in Section 5.3.1, indicated a very low insertion efficiency. Only a single or a few insertions were observed on a lipid bilayer area of ≈ 0.07 mm^2. In comparison, the surface area of LUVs with a diameter of 100 to 200 nm is approximately 1,000,000 smaller (see Table 5.4). Assuming the same density of DNA nanostructures at the membrane surface (both assays were carried out at 100 nM DNA constructs at some point), an insertion is expected only on approximately every 1,000,000$^{\text{th}}$ vesicle. However, in order to overcome the measurement error of ~1 %, an insertion and complete lipid scrambling of more than every 100$^{\text{th}}$ vesicle is required. Even if DNA nanostructures would insert more efficiently in the curved membranes of vesicles than in

planar lipid bilayers, as suggested by a previous report [170], the insertion efficiency would have to be 10,000 times higher to have an effect in the detectable range.

Table 5.4 Comparison of the membrane area of the planar lipid bilayer used in electrophysiology experiments (A_{planar}) with the surface area ($A_{vesicle}$) of large (LUV) or giant unilamellar vesicles (GUV).

Membrane type	Diameter µm	Membrane area μm^2	Membrane area ratio $A_{vesicle}$ / A_{planar}
Planar	300	70686	1
LUV	0.1	0.03	0.4×10^{-6}
LUV	0.2	0.13	1.8×10^{-6}
GUV	5	79	0.1×10^{-2}
GUV	10	314	0.4×10^{-2}
GUV	20	1257	1.8×10^{-2}

Due to the low insertion efficiency, the current design of the bulk dithionite assay on LUVs is most likely not sensitive enough to detect the lipid scrambling activity of DNA nanostructures. Table 5.4 illustrates that using larger vesicles can enhance the probability for insertion per vesicle which we will discuss in Chapter 6. However, in the next section we will still employ LUVs but try to increase the insertion efficiency of DNA constructs using electroporation.

5.3.8 Electroporation to aid DNA nanostructure insertion

One approach to aid the membrane insertion of DNA nanostructures could be to temporarily disturb the lipid membrane of the vesicles in such a way that the energy barrier for the DNA nanostructures to insert is lowered. This could be achieved by inducing short-lived deformations to the vesicles using electric fields. Electroporation is a microbiology technique in which a strong electrical pulse is applied to create temporary pores in the lipid bilayer membranes [224, 225]. These pores create passages that are typically used for introducing molecules like proteins, DNA (transfection) or drugs into a cell [226]. The technique has previously also been applied to form temporary pores in artificial vesicles [227, 228]. DNA nanostructures that are attached to the vesicle's membrane but are not yet inserted, could then spontaneously insert into these temporary pores and stabilise them such that the nanostructures stay inserted even after the electrical pulse has decayed (see Fig. 5.19).

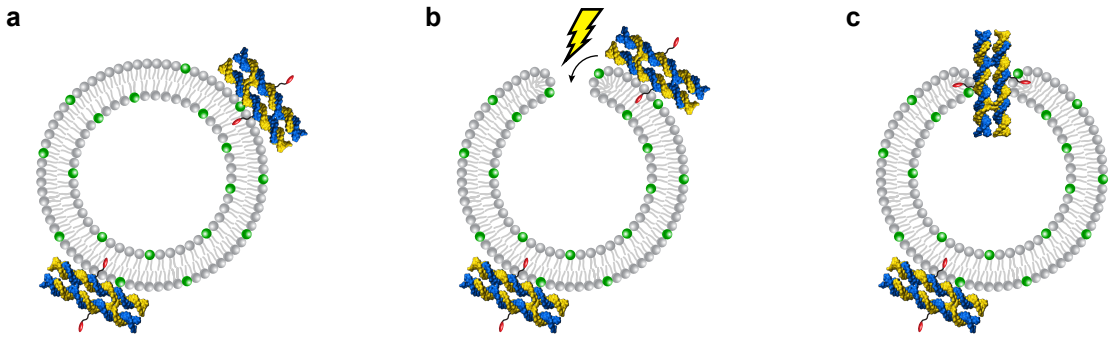

Fig. 5.19 Scheme of electroporation-assisted membrane insertion of DNA nanostructures. (**a**) Lipid vesicles with membrane-attached DNA constructs. (**b**) A strong electrical pulse induces the formation of temporary membrane pores. While diffusing on the vesicle bilayer, DNA nanostructures could spontaneously insert into these pores. (**c**) DNA structures could stabilise the temporary pores and remain in the membrane after the electrical pulse is over.

To find suitable electroporation conditions, vesicles without DNA constructs were tested first. The device generates an electric pulse with an exponential decay. The voltage initially increases rapidly reaching a peak voltage V_0 and then decreases over time following

$$\begin{aligned} V_t &= V_0\, e^{-t/\tau} \\ \text{with} \quad \tau &= RC \end{aligned} \tag{5.2}$$

being the time constant which is an expression of the pulse length. R refers to the resistance and C to the capacitance which are set on the electroporation device. The electrical field is given by

$$E_t = \frac{V_t}{d} = \frac{V_0}{d}\, e^{-\frac{1}{RC}t} \tag{5.3}$$

with d being the distance between the electrodes. Keeping d and R constant (see Section 5.2) the electrical field can be modulated by changing the voltage V_0 or the capacitance C. While the voltage alters the field strength, the capacitance can be used to change the duration the pulse is applied for. These two parameters have been explored in order to find suitable conditions where membrane pores could potentially form but the vesicles are still intact afterwards. For this, vesicle solutions were exposed to electric pulses of different voltages and pulse durations, and afterwards evaluated via DLS size measurements and a dithionite reduction assay of the same sample to see if the vesicles are still intact (see Fig. 5.20).
While for a capacitance of 1 µF vesicle sizes remained mostly unchanged, for a 3 µF capacitance larger sizes were observed from applied voltages of 1200 V onwards (Fig. 5.20a). However, the results of the dithionite assay remained relatively unchanged (Fig. 5.20b). This

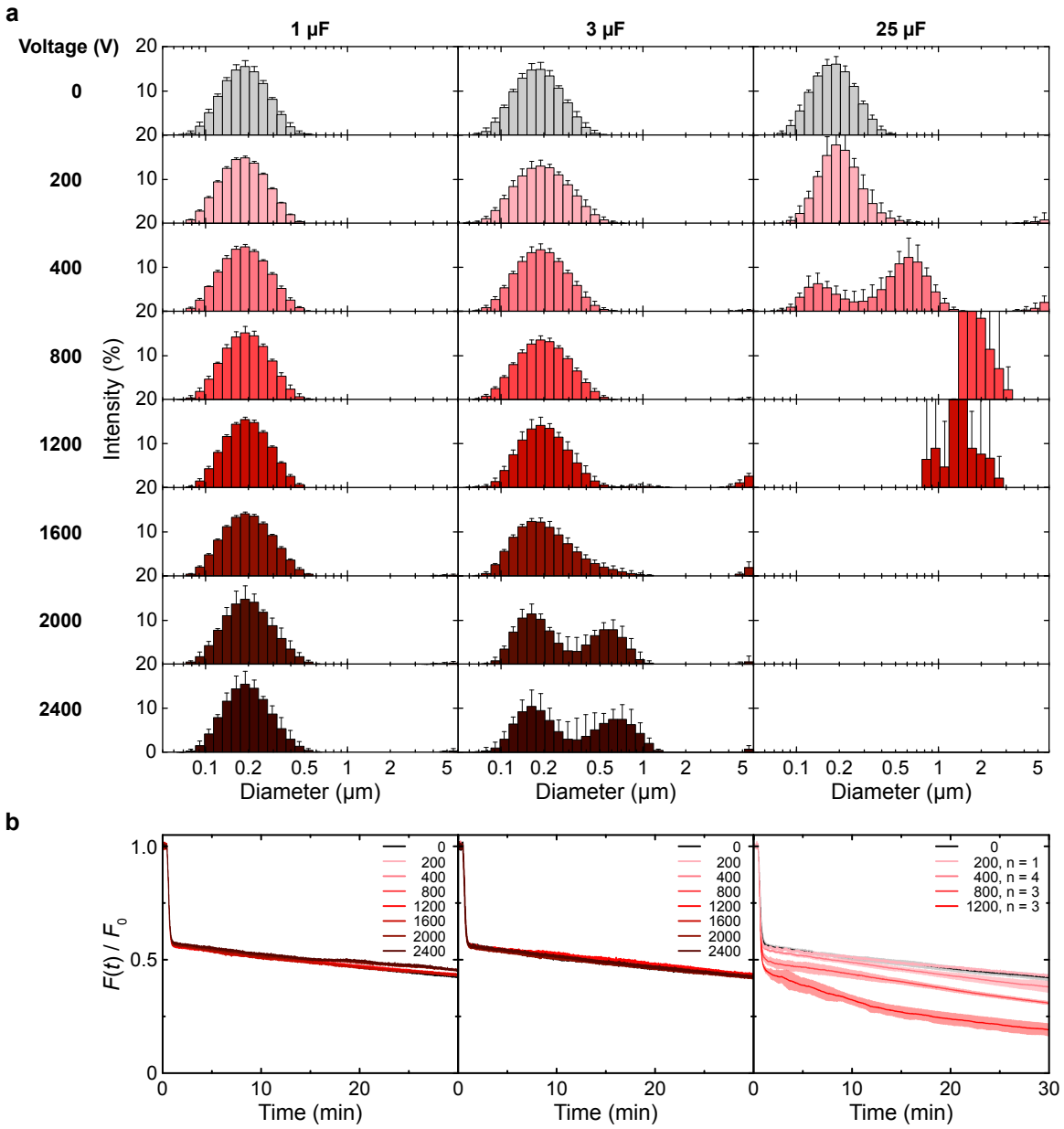

Fig. 5.20 Electroporation of LUVs at different voltages and capacitances. DLS measurements (**a**) and dithionite assays (**b**) of vesicles after exposure to voltage pulses between 0 and 2400 V at capacitances of 1, 3, and 25 µF. For 25 µF only voltages up to 1200 V were tested (as arcing and scorching of the capillaries was observed above) and the dithionite assay was repeated *n* times. Traces for the capacitance of 25 µF represent the average and standard deviation. Final dithionite concentration was 40 mM.

is in contrast to using a capacitance of 25 µF where already from 400 V onwards aggregates were observed and the bleaching plateau in the dithionite assay dropped to lower values than the 0 V control. The increased size observed for vesicles exposed to high voltages at 3 µF could indicate vesicle fusion. At the same time, the vesicles seem to remain intact such that dithionite cannot permeate to their inside as indicated by the results of the dithionite assay not significantly differing compared to if no voltage was applied (Fig. 5.20b). As vesicle fusion is a sign for temporary membrane poration [228] which could aid DNA nanostructure insertion, a pulse of 2400 V at 3 µF was selected as the most promising condition.
To test if electroporation can aid DNA nanostructure insertion, vesicles extruded at 200 nm were incubated with DNA nanostructures and exposed to an electric pulse. DLS size analysis of the vesicle suspension, after the voltage pulse was applied, showed larger vesicle diameters indicating that electroporation and vesicle fusion occurred, as intended (Fig. 5.21a). Variations in the vesicle size could be caused by different surface potentials at the lipid-buffer interface due to the presence of the DNA nanostructures.

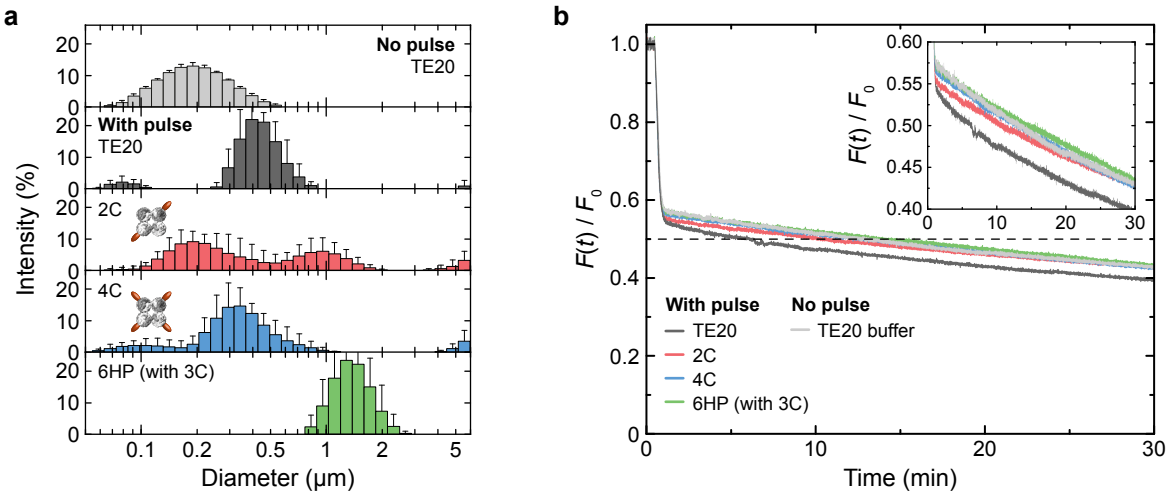

Fig. 5.21 Electroporation of LUVs after incubation with DNA nanostructures. (**a**) DLS size measurements of EColi-eggPC vesicles after their incubation with different DNA nanostructures and exposure to either no pulse or a single voltage pulse at 2400 V and 3 µF. As negative controls, DNA nanostructure buffer (TE20) was added on its own. 6HP structures were assembled with three cholesterol modifications, as described previously [72]. (**b**) Dithionite reduction assay performed on the same vesicle solutions analysed in **a**. Inset shows a close-up of the normalised intensity around 0.5. The final dithionite concentration was 40 mM.

After DLS analysis, a dithionite assay was performed. No significant difference in fluorescence reduction was observed, whether the DNA constructs were present or not (Fig. 5.21b). Therefore, although electroporation seemed to have induced vesicle fusion, it did not increase the insertion efficiency of DNA constructs significantly enough to detect scrambling activity.

5.4 Conclusion

The aim of the experiments presented in this chapter was to demonstrate the lipid scrambling activity of cholesterol-modified, membrane-inserted DNA nanostructures. The electrophysiology measurements showed that the CP2 DNA nanostructure with two cholesterol modifications is able to spontaneously self-insert into lipid bilayers and act as a synthetic DNA-built ion channel. The determined conductance of ≈ 0.7 nS was in agreement with previously determined values for a DNA nanostructure of similar size and modified with two cholesterol tags [54]. However, our experiments also demonstrated that the DNA nanostructure insertion efficiency was very low.

As frequently employed in previous research to investigate scrambling activity, the dithionite reduction assay was performed on suspended, NBD-containing LUVs using a fluorescence spectrometer. The systematic analysis of the assay parameters revealed that LUVs formed from POPC are not ideal for the dithionite assay due to a considerable degree of multilamellarity. Using a 3:1 EColi:eggPC lipid mixture proved to be far superior as vesicles showed a more consistent behaviour regarding the dithionite reduction to the expected value. Interestingly, DLS measurements demonstrated that these liposomes seemed to have a preferred size of ~200 nm in contrast to vesicles formed from POPC. The labelling position of the NBD on the lipid only had a minor influence in these experiments, however, this could become a more significant parameter once lipid scrambling activity is observed. The dithionite concentration significantly influenced the reduction kinetics which is important if scrambling rates need to be determined. While for long-term measurements higher dithionite concentrations can lead to lower fluorescence intensity plateaus over time, short-term measurements (a few minutes) are not significantly affected by that. Lastly, the presence of surfactants, specifically OPOE, was shown to induce a fluorescence reduction indicative of scrambling activity at concentrations even below the CMC. Therefore, only low concentrations can be employed and control experiments are particularly crucial.

Unfortunately, it was not possible to establish a positive control for scrambling activity using the commercially available TMEM16F scramblase. A possible cause could have been that the protein was not biologically active. Future experiments would therefore benefit from expressing a lipid scramblase protein ourselves or to collaborate with another group that could provide a functioning protein.

For cholesterol-modified DNA nanostructures the results did not show any significant indication of lipid scrambling activity for multiple different designs even though DLS experiments suggested attachment of the structures to the vesicles. A possible explanation is the low insertion efficiency of the DNA nanostructures which is in agreement with the results obtained from the electrophysiology experiments. Our calculations showed that the membrane surface

area of LUVs with a diameter of ~100 to 200 nm is approximately 10^6 times smaller than the membrane area that was employed in the electrophysiology assay. Given the determined low insertion efficiency, the number of vesicles that demonstrates scrambling activity due to a membrane-inserted DNA nanostructure is expected to be several orders of magnitude too low to be detected in the bulk dithionite assay using LUVs. This could also explain why it was not possible to determine scrambling activity despite attempts to increase the insertion efficiency by inducing transient membrane pores or vesicle fusion with electroporation.
Nevertheless, the results obtained from the bulk dithionite assays provide a valuable foundation for designing and interpreting future dithionite reduction experiments. While no lipid scrambling activity of DNA nanostructures could be demonstrated in this chapter, the question if an undoubtedly membrane-inserted construct can scramble lipids is still open. In the next chapter, we will address this question by employing molecular dynamics simulations to determine if our CP2 DNA nanostructure can, in theory, scramble lipids given it is inserted in a membrane. We will furthermore introduce a strategy to increase the probability for membrane insertion simply by increasing the size of the vesicles which will additionally allow to follow the dithionite reduction kinetics at the single-vesicle level.

Chapter 6

A lipid scramblase built from DNA

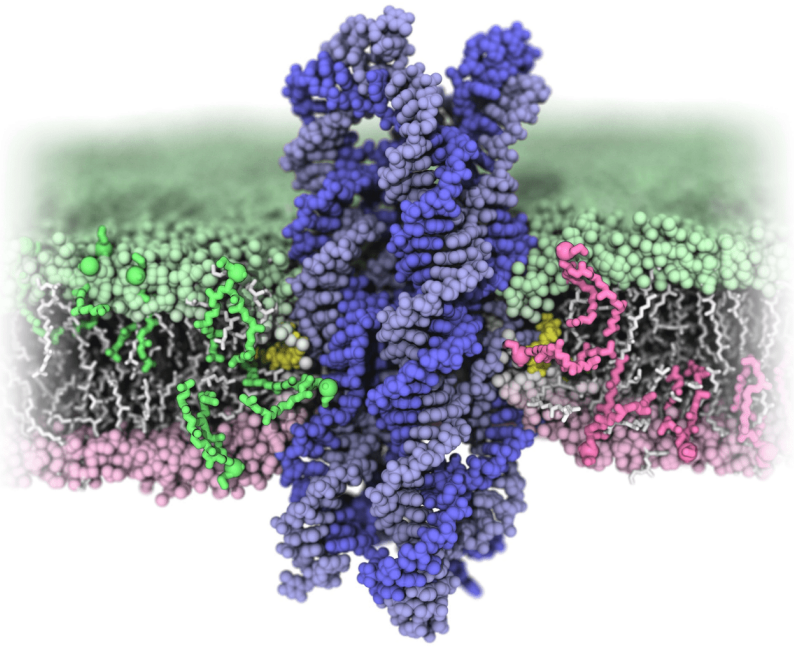

Parts of this work previously appeared in:

A. Ohmann, C. Y. Li, C. Maffeo, K. Al Nahas, K. N. Baumann, K. Göpfrich, J. Yoo, U. F. Keyser, and A. Aksimentiev. 'A synthetic enzyme built from DNA flips 10^7 lipids per second in biological membranes.' *Nature Communications*, 9:2426 (2018).

6.1 Introduction

On the molecular scale, you find it's reasonable to have a machine that does a million steps per second.
– K. Eric Drexler

In the previous chapter we have introduced the dithionite reduction assay, an established method to determine lipid scrambling activity in membranes. Although studying the characteristics of the assay provided a valuable foundation, so far we have not achieved our original aim: to determine if our membrane-inserted DNA nanostructures can induce lipid scrambling across bilayer leaflets. In this chapter we will use the CP2 DNA nanostructure modified with two cholesterol tags (2C) as a basis since we have successfully demonstrated its membrane-insertion capabilities in Chapter 5. An overview of the design with its details is shown again in Fig. 6.1. Previous experiments on a similar DNA structure have shown that this number of modifications can be sufficient for membrane insertion [54]. Furthermore, this minimal design allows to easily switch between a structure that is, in principle, able to insert into a lipid bilayer (2C) and a structure that should only attach but not insert (1C), simply by omitting one cholesterol modification in the assembly.
We will first employ atomistic MD simulations to demonstrate that this DNA nanostructure design indeed scrambles lipids when inserted into a lipid bilayer via two cholesterol anchors. Similar to the previously described results for a single membrane-spanning DNA duplex [8], the simulations reveal that the DNA nanostructure induces a toroidal lipid pore. This DNA-induced lipid pore is then shown to facilitate lipid scrambling on the order of 10^7 lipids per second for a single DNA structure.
We will furthermore introduce an improved dithionite reduction assay in order to experimentally demonstrate the lipid scrambling activity of the DNA nanostructures. The electrophysiology measurements discussed in the previous chapter showed that the insertion efficiency of the DNA constructs is rather low. This could explain why lipid scrambling was not observed in the bulk dithionite reduction experiments performed on LUVs . Given the low insertion efficiency, the number of DNA nanostructures per vesicle might not have been sufficient to achieve insertions on enough vesicles to detect a measurable decrease in NBD fluorescence with bulk fluorescence spectroscopy. In this chapter, we will discuss the advantages of employing larger vesicles in order to increase the ratio of DNA structures per vesicle. We will employ giant unilamellar vesicles (GUVs) with diameters ranging from 5 to 20 µm to perform the dithionite reduction assay which will significantly raise the chances for membrane insertion compared to the previously employed LUVs (~100 to 200 nm). It

will further allow us to directly measure scrambling activity on each individual vesicle using confocal microscopy. To the best of our knowledge, we therefore introduce a novel assay that allows the direct observation of lipid scrambling activity via monitoring the dithionite reduction kinetics at the single-vesicle level.

With this combination of atomistic MD simulations and improved dithionite reduction experiments on GUVs, we ultimately demonstrate that our DNA nanostructure can mimic a fully functional scramblase by facilitating rapid mixing of lipids between bilayer leaflets. Strikingly, the scrambling activity of our *de novo* DNA-made enzyme outperforms any known biological scramblase by several orders of magnitude. This is remarkable given that the catalytic rates of previous enzymatically active DNA nanostructures fall orders of magnitude behind natural benchmarks [229, 230].

Lastly, we will test our DNA scramblase on human breast cancer cells. We will use the Annexin V staining assay which detects the exposure of phosphatidylserine (PS) lipids on the cell surface, a task performed by lipid scramblases when they are activated during apoptosis. The results from these experiments indicate that our DNA scramblase can induce apoptosis in human cancer cells.

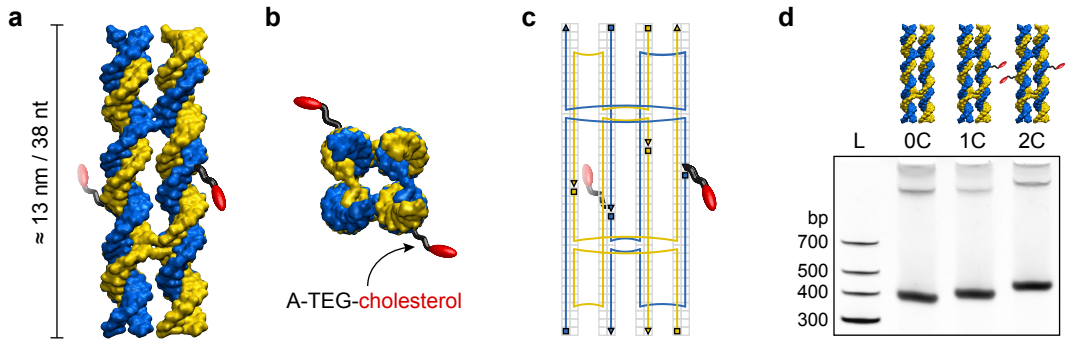

Fig. 6.1 Overview of lipid-scrambling DNA nanostructure. (**a**) Side and (**b**) top view of a 3D representation of the assembled CP2 DNA nanostructure with two cholesterol tags (red) linked to the central 3' ends via an adenine-TEG spacer (A-TEG, black). (**c**) 2D schematic illustrating the pathway of the DNA single strands as well as cholesterol modification positions. (**d**) Non-denaturing 10 % PAGE of DNA nanostructures assembled without (0C), with one (1C), or with two (2C) cholesterol modifications next to a DNA ladder (L).

6.2 Materials & Methods

6.2.1 All-atom MD simulations of lipid scrambling

MD simulations were performed and analysed by C.-Y. Li, C. Maffeo, J. Yoo and A. Aksimentiev at the University of Illinois at Urbana-Champaign. A detailed description of the methods can be found in the published article and its Supplementary Information [75]. Briefly, the caDNAno design of the DNA nanostructure was converted to an idealised all-atom representation. The design featured two centrally positioned cholesterol-TEG modifications (for chemistry see Fig. 4.1) that included an adenine spacer nucleotide (see Fig. 6.1). This atomistic representation was embedded into a lipid bilayer membrane using a previously described method [231]. The resulting model was merged with a rectangular volume of electrolyte solution, minimised and equilibrated in the constant number of particles, temperature, and pressure ensemble. The simulations employed the CHARMM36 parameter set [232] and were carried out using both NAMD [176] and Anton [233].

6.2.2 Preparation of GUVs using electroformation

Giant unilamellar vesicles were prepared by K. Al Nahas using electroformation via a Nanion Vesicle Prep Pro. 2-Oleoyl-1-palmitoyl-sn-glycero-3-phosphatidylcholine (POPC; Sigma-Aldrich) and 1-palmitoyl-2-{6-[(7-nitro-2-1,3-benzoxadiazol-4-yl)amino]hexanoyl}-sn-glycero-3-phosphatidylcholine (NBD-PC; Avanti Polar Lipids) were dissolved in chloroform and mixed in a weight/weight ratio of 200:1 (POPC:NBD-PC). These lipids were the same as the POPC:NBD-PC-C6* mixture employed in Chapter 5. 100 µl of the lipid mixture at 5 mg ml^{-1} was spin-coated on the conducting surface of an indium tin oxide (ITO)-coated glass slide (Nanion/VisionTek). Chloroform was evaporated for 1 hour in a desiccator following which 600 µl of sucrose buffer (100 mM sucrose, 20 mM HEPES at pH 7.4) was deposited within the O-ring chamber which was subsequently sealed with another ITO-coated slide (conducting surface facing the other). The electroformation chamber was then connected to the Nanion Vesicle Prep Pro and the electroformation protocol proceeded in 3 steps:

i. The A/C voltage increased linearly from 0 to 3.2 V peak-to-peak (p-p) at 10 Hz for 1 h,
ii. the voltage stayed at 3.2 V p-p and 10 Hz for 50 min,
iii. the frequency decreased linearly to 4 Hz over 10 min and was maintained for another 20 min.

The steps were adapted from previous protocols [234, 235]. Electroformation was carried out at 37 °C. Vesicles were stored at 4 °C protected from light and not used longer than 36 hours after formation.

6.2.3 Osmolality measurements

A freezing point osmometer (Automatic Micro-Osmometer Type 11, Roebling) was calibrated at 0 mOsm kg^{-1} with distilled water and at 300 mOsm kg^{-1} with a standard solution (Camlab Limited). A fresh sample was used for each measurement. 100 µl sample was deposited in a 1.5 ml Eppendorf tube and supercooled. Freezing was automatically initiated by a metal needle dipping into the solution. Due to the formation of ice crystals the sample's temperature rises until an equilibrium between melting and thawing of the ice crystals is reached and the temperature remains constant for a moment. This temperature is the real freezing point of the sample which is measured by a high-precision thermistor. From the deviation of the sample's freezing point from pure water without any solutes (freezing point = 0 °C), the osmolality of the sample is determined.

6.2.4 Dithionite reduction assay on GUVs

Assembled DNA nanostructures (1 µM) with either one (1C) or two (2C) cholesterol modifications were mixed with 0.5 % OPOE, pre-diluted in TE20 buffer, in a 7:1 ratio and incubated for 2 min at room temperature. The mixture was then diluted in glucose buffer (100 mM glucose, 4 mM $MgCl_2$, 20 mM HEPES titrated to pH 7.4 with KOH) and added to 20 µl GUV solution at a final concentration of 100 nM DNA nanostructures. Samples were then incubated for 90 to 120 min on a 1 % BSA-coated glass coverslip within an incubation chamber (Grace Bio-Labs) at room temperature. This allowed the vesicles to settle to the bottom due to the density gradient between the intravesicular sucrose and extravesicular glucose as well as the cholesterol-modified DNA nanostructures to anchor into the lipid membrane. Dithionite was freshly dissolved in 1 M Tris at pH 10 at a concentration of 1 M and then pre-diluted in 50 mM glucose, 4 mM $MgCl_2$ and 20 mM HEPES pH 7.4 to a concentration of 15 mM dithionite right before each experiment. To initiate NBD dye reduction, 30 µl of diluted dithionite solution was carefully added to the incubated vesicles to a final concentration of ~4.5 mM dithionite at approximately one minute after starting the image recording. Chambers were covered with a glass slide to prevent evaporation except when the dithionite solution was added. At all times in the protocol at least 4 mM $MgCl_2$ was present to keep the DNA nanostructures stable. A detailed overview of the buffer conditions used throughout the protocol is presented in Table 6.1 in Section 6.3.3.

Images were acquired on an Olympus FluoView filter-based FV1200F-IX83 laser scanning microscope using a 60x oil immersion objective (UPLSAPO60XO/1.35). NBD excitation was performed using a 25 mW 473 nm laser diode at 1 % laser power and emission was collected between 490 and 525 nm. Cy3 was excited with a 1.5 mW 543 nm HeNe laser at 5 % laser power and emitted light collected between 560 and 660 nm. For statistical analysis a z-stack (slice thickness 300 nm) was recorded of the field of view before and 35 min after dithionite addition with separate excitation of the 473 and 543 nm laser lines at a sampling speed of 2.0 µs pixel^{-1}. For single vesicle fluorescence reduction traces, vesicles of similar size were kept in focus and images were recorded every 10 s in between the z-stacks while exciting with both lasers simultaneously. Images were analysed using Fiji [150].
Vesicles were identified and located from the fluorescence signal collected from Cy3-labelled DNA nanostructures by applying a ring-shaped selection area over the fluorescent ring at a height close to the equatorial plane. NBD fluorescence intensity for each vesicle was then determined by measuring the mean grey value of the equivalent area in the respective images of the NBD emission channel. Values were background-subtracted by measuring and averaging over three areas without vesicles. Intensities per vesicle were normalised to the average intensity of the first five data points of each trace.

6.2.5 Dithionite leakage experiments

Several experiments were performed to test if dithionite can leak across the vesicle membrane or through the DNA-induced toroidal pore. 2-(N-(7-nitrobenz-2-oxa-1,3-diazol-4-yl)amino)-2-deoxyglucose (NBD-glucose, Invitrogen) was purchased dry and diluted to a stock concentration of 30 mM in dimethyl sulfoxide (DMSO). GUVs were then formed from POPC and NBD-PC but additionally in the presence of 50 µM NBD-glucose. Subsequently, fluorescence recovery after photobleaching (FRAP) experiments were performed using confocal microscopy on several vesicles by excitation of the whole field of view with a 473 nm laser at high intensity for several frames. Subsequently, the laser intensity was reduced to the same level as before photobleaching and the fluorescence recovery inside the vesicles was recorded over time. For data analysis the fluorescence intensity inside the vesicles was normalised to the fluorescence outside the vesicles before photobleaching.
As a second NBD-labelled probe, Amino-dPEG$_{12}$-OH (PEG12) or Amino-dPEG$_{24}$-OH (PEG24) polyethylene glycol molecules (Quanta Biodesign) were synthesised with succinimidyl 6-(N-(7-nitrobenz-2-oxa-1,3-diazol-4-yl)amino)hexanoate (NBD-SE; Invitrogen), an NHS-ester of the fluorescent dye NBD, to form NBD-PEG according to a previously described protocol [236]. For this, dried NBD-SE and PEG12 (or PEG24) were each diluted in 1:1 chloroform:methanol to final concentrations of 10 mg ml^{-1} ($\approx$ 25 mM) and

137 mg ml^{-1} ($\approx$ 128.3 mM), respectively. For the reaction, NBD-SE and PEG12 (or PEG24) were mixed at a ratio of NBD-SE:PEG of either 1:1, 1:2, or 1:10, and diluted to a final concentration of $\approx$ 5 mM NBD-SE in 1:1 chloroform:methanol. The mixture was incubated for one hour or over night at room temperature under constant movement and protected from light. The solution was then blow-dried with nitrogen, desiccated for 10 min under vacuum and subsequently dissolved in 500 µl of 20 mM HEPES (pH 7.4) for a final concentration of $\approx$ 5 mM NBD-PEG. Successful synthesis was confirmed with thin layer chromatography (TLC) on silica gel plates (Sigma-Aldrich) using 1:1 chloroform:methanol as the eluent. Imaging of the TLC plates was performed on a GelDoc-It^{TM} (UVP) imaging system using UV excitation.
GUVs were then formed from POPC in the presence of 70 µM NBD-PEG. Vesicles were diluted in glucose buffer as used for dithionite reduction assays but supplemented with 70 µM NBD-PEG (to maintain NBD-PEG concentration outside the vesicles), and incubated for two hours with 2C DNA nanostructures. FRAP experiments were performed and analysed as described for NBD-glucose above. NBD-PEG24 showed even less membrane permeability than NBD-PEG12 although not to a significant extent.

6.2.6 Annexin V staining experiments on human cancer cells

MDA-MB-231 cells were acquired from the Biorepository of the Cancer Research UK Cambridge Institute where the cells were authenticated by multiplex polymerase chain reaction (PCR) and short tandem repeat (STR) profiling including detection of mouse cell contamination. Cells were handled and maintained by K. N. Baumann. Cells were cultured in Dulbecco's modified Eagle's medium (DMEM; Sigma-Aldrich) supplemented with 10 % (v/v) heat-inactivated fetal calf serum (FCS; Thermo Scientific) at 37 °C and 5 % CO_2. A concentration of 30,000 cells per 250 µl medium was seeded on a cover glass placed in a well of a 48-well plate (day 0) and grown for two nights under the same conditions as stated above. Afterwards, cells were washed once with phosphate-buffered saline (PBS) and then covered again in fresh medium. DNA nanostructures with two cholesterols and two Cy3 tags were assembled as described in Section 4.2.1 but in PBS at pH 7.4 supplemented with 8 mM $MgCl_2$ instead of TE20 buffer. 120 µl of assembled structures were added to cells (prepared as described above) in the well plate (final structure concentration 324 nM) and incubated for one hour at 37 °C and 5 % CO_2. For control experiments performed in parallel, only the DNA folding buffer without DNA nanostructures (negative control) or 10 µM of the apoptosis-inducing agent staurosporine (S5921, Sigma-Aldrich; positive control) was added, respectively. To stain the cells with FITC-labelled Annexin V as an indicator of PS exposure, cells were first washed with 500 µl of 1x Annexin V binding buffer (Abcam) and

then incubated with 500 µl of 1x FITC-labelled Annexin V (Abcam) in binding buffer for 5 min (in accordance with the protocol provided by the manufacturer). To prepare the cells for fluorescence microscopy imaging, cells were subsequently washed with 500 µl binding buffer once again and then fixed in 250 µl of 4 % formaldehyde in binding buffer for 15 min on ice, followed by three washing steps with 250 µl binding buffer before being stored in the fridge overnight. On day four the cover glasses were transferred onto microscope slides by mounting them with Mowiol [237]. For this, 6 g of glycerol, 2.4 g of Mowiol powder (Calbiochem) and 6 ml of distilled water were added to 12 ml of 0.2 M Tris buffer (pH 8.0) and stirred for four hours. The solution was then left to rest for an additional two hours. Subsequently, the mixture was incubated for 10 min in a 50 °C water bath and finally centrifuged for 15 min at 5,000 × g. After removing the supernatant, the solution was stored at −20 °C before usage. Images were acquired on the same confocal microscope as described for the dithionite reduction assay except that a 20x air objective was used (UPLSAPO20X/0.75). Filter set and laser power for Cy3-labelled DNA nanostructures were kept the same and parameters used for the NBD dye were applied for imaging FITC-labelled Annexin V as well. Detector voltages for both channels were kept fixed and were the same for all experiments. Z-stacks (slice thickness 500 nm) of cells were acquired with separate excitation of the 473 nm and 543 nm laser lines (sampling speed 2.0 µs pixel^{-1}). The brightfield images were obtained by acquisition of the transmitted light of the 543 nm laser. Analysis was performed using Fiji [150].

6.3 Results & Discussion

6.3.1 All-atom MD simulations of lipid scrambling

Having experimentally characterised our cholesterol-modified DNA nanostructures in the preceding chapters, we employed the all-atom MD method to determine if the structures induce lipid scrambling when inserted into a lipid bilayer. For this, we collaborated again with the group of A. Aksimentiev at the University of Illinois at Urbana-Champaign who performed the MD simulations for us. Following a previously described protocol [231], an all-atom model of the DNA nanostructure modified with two cholesterol modifications (2C) embedded in a diphytanoyl phosphatidylethanolamine (DPhPE) membrane and solvated in 1 M KCl was built. The entire system was first equilibrated for ~230 ns with the DNA nanostructure constrained to its initial idealised conformation. This allowed for lipids and water to adopt an equilibrium configuration (see Fig. 6.2a).

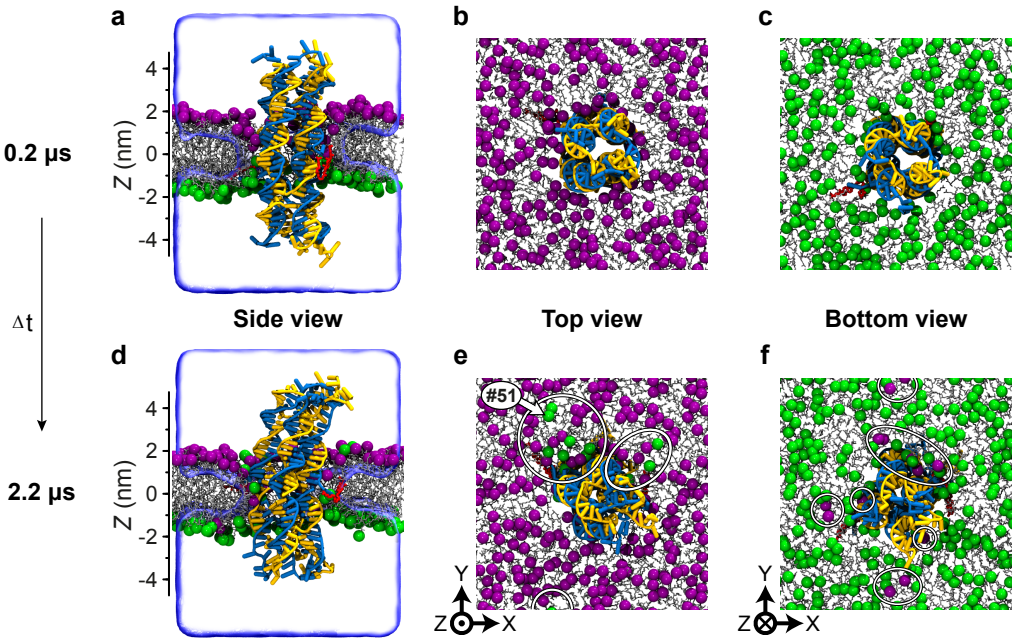

Fig. 6.2 All-atom MD simulation of lipid scrambling induced by the DNA nanostructure. Snapshots of the microscopic configuration of the simulated system at the beginning (**a-c**) and the end (**d-f**) of the free equilibration simulation. (**a,d**) Cut-away side view showing the DNA nanostructure (blue and yellow) embedded in a DPhPE lipid membrane (grey) via cholesterol tags (red). Lipid headgroups located in the upper and lower leaflet of the bilayer at 0.2 µs are highlighted using purple and green spheres, respectively. Top view (**b,e**) and bottom view (**c,f**) of the simulated system. The electrolyte solution is not shown for clarity. White ellipses in **e,f** highlight DPhPE headgroups that resided in the opposite leaflet of the bilayer at 0.2 µs. The indicated lipid #51 in **e** will be used as an example later on.

The cut-away side view shown in Fig. 6.2a illustrates that the lipid headgroups adopt a toroidal pore shape around the nanostructure. Such a toroidal pore shape at the lipid-DNA interface matches previous MD simulation performed on a single membrane-spanning DNA duplex [8]. Figures 6.2b,c illustrate the lipid headgroups residing at 0.2 µs in the upper bilayer leaflet (panel b) and lower bilayer leaflet (panel c). The system was then simulated without any constraints for ~2 µs. Comparison of initial and final configurations illustrates that throughout the simulation several lipids have completely transferred from one bilayer leaflet to the other (Figs. 6.2d-f). As the coordinates of all atoms were recorded throughout the simulation, the trajectory of how the lipids flip from one bilayer leaflet to the other could be investigated. An example of such a trajectory is depicted in Figure 6.3.

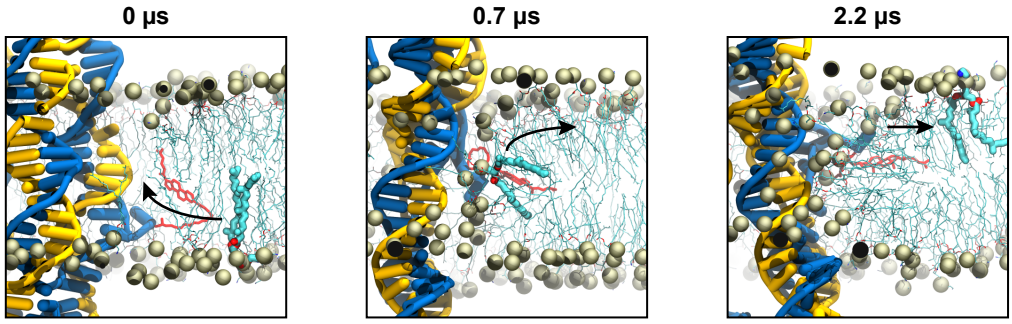

Fig. 6.3 MD simulation illustrating the trajectory of a flipping lipid. Sequence of microscopic conformations illustrating spontaneous inter-leaflet transfer of one lipid molecule (highlighted by the bold depiction; #51 in Fig. 6.2e) during the 2.2 µs MD simulation. For clarity, all other lipid molecules are shown as a different representation and the electrolyte solution is not shown. Arrows illustrate the trajectory of the lipid during the simulation.

At 0 µs the toroidal pore has not formed yet, as indicated by the parallel arrangement of the lipid headgroups. At 0.7 µs the toroidal pore has formed around the DNA nanostructure and the highlighted lipid diffuses along the DNA-lipid interface to the upper bilayer leaflet where it still remains at 2.2 µs. This visual inspection of the MD trajectory revealed, that the lipids diffused from one bilayer leaflet to the other along the walls of the DNA-induced toroidal lipid pore. The lipids forming the inner surface provide a continuous passage from one leaflet of the membrane to the other. This diffusive motion of individual lipid molecules was not correlated, occurred in both transport directions, and produced zero net transport of lipids from one leaflet to the other, as expected. Further examples of such inter-leaflet transfer events can be found in the Supplementary Information of [75].
To quantitatively characterise the inter-leaflet transport of lipids, the Z coordinate of each lipid's phosphorus atom and its radial distance R from the centre of the DNA nanostructure was computed as a function of the simulation time. Figure 6.4a shows an example of a typical

translocation, where a lipid molecule moves from the bottom leaflet ($Z < -1.75$ nm) to the top one ($Z > 1.75$ nm), while approaching the DNA construct ($R < 3$ nm) during the transfer process. These values of Z and R match well with the expectations given the geometry of the lipid bilayer and the DNA nanostructure. As the lipid molecule approaches the DNA nanostructure, it reorients itself to expose its polar headgroup to the DNA nanostructure (compare snapshot at 0.7 µs in Fig. 6.3).

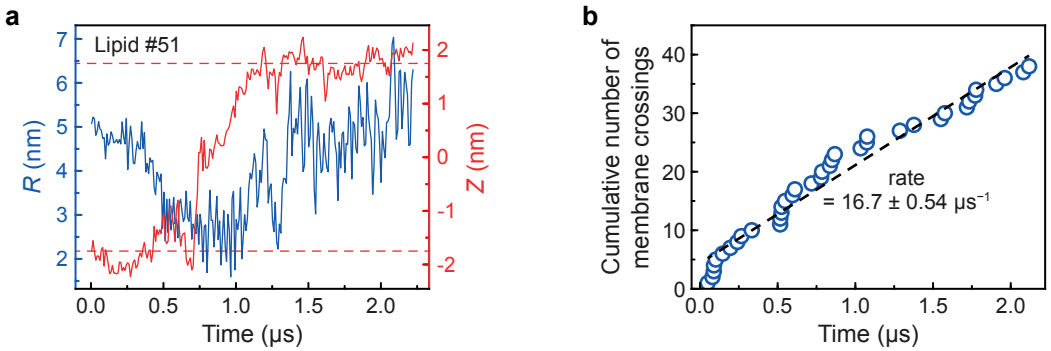

Fig. 6.4 Quantitative analysis of flipped lipids. (**a**) Graph of the radial distance R relative to the centre of mass of the nanostructure (left axis) and the Z coordinate of the phosphorus atoms (right axis) of a lipid molecule (#51, see Fig. 6.2e) undergoing a complete transfer from the lower to the upper leaflet of the bilayer. Dashed red lines indicate Z-coordinate thresholds for the upper and lower bilayer leaflet. Data shown were sampled at 0.24 ns and averaged in 9.6 ns blocks. (**b**) Cumulative number of inter-leaflet transfer events versus simulation time. A linear fit (black line) yields the average transfer rate. The error indicates the estimated standard deviation of the non-linear least squares fit.

An inter-leaflet transfer event, or a flipped lipid, was counted each time the Z coordinate of a lipid phosphorus atom changes from being less than −1.75 nm to being more than 1.75 nm or vice versa. Figure 6.4b plots the cumulative number of transfer events versus the simulation time. A linear fit yields the average transfer rate of 16.7 ± 0.54 lipids per µs. This equates to a lipid scrambling rate on the order of 10^7 lipids per second for a single DNA construct. A slower yet significant spontaneous transfer of lipids was observed in an additional 2 µs simulation of the same DNA nanostructure embedded in a diphytanoyl phosphatidylcholine (DPhPC) lipid bilayer (see Supplementary Information of [75]), suggesting that the rate of lipid transport facilitated by the same nanostructure can be lipid-type dependent.
Quantitative analysis of lipid density within the toroidal pore reveals a rather modest, of the order of 1 k_BT, free energy barrier to inter-leaflet transport (see Fig. A.5 in the Appendix), which is in accord with our earlier conclusion that transport of lipids occurred via diffusive motion. Given the general character of such transport, we can expect any membrane-spanning DNA nanostructures to exhibit lipid scrambling activity as long as they promote the formation

of a toroidal pore. Indeed, analysis of our previous MD simulations of single duplex [8] and funnel-like [74] DNA pores revealed an average inter-leaflet transport of 4 and 200 lipids per µs, respectively. In contrast, no lipid scrambling was observed for a DNA nanostructure that had a modified DNA backbone and did not allow the toroidal pore to form [68, 231].

6.3.2 Increasing the probability of DNA nanostructure insertion

In the previous section, the MD simulations determined a very high scrambling rate of 10^7 lipids per second for a single DNA nanostructure. If a comparable rate would also be observed in experiments, a single, membrane-inserted DNA nanostructure should suffice to flip most lipids of a vesicle at the typical time scales of the dithionite reduction assay even in vesicles exceeding 1 µm in diameter (compare number of lipids per vesicle in Fig. 5.12). As already briefly mentioned in Section 5.3.7, we will discuss in the following that simply by increasing the vesicle size, the probability of a single membrane insertion per vesicle increases by an even greater extent as well.
Using the previously introduced membrane parameters (see bilayer thickness d_B and volume of a lipid V_L in Table 5.3) and Equations 5.1, the number N of lipids in a vesicle of diameter d_V can be estimated as the sum of lipids in the inner (N_i) and outer bilayer leaflet (N_o) as follows:

$$\begin{aligned} N_{Lipids\ per\ vesicle} = N_i + N_o &= \frac{\pi}{6V_L}\left[\mathbf{d_V}^3 - (\mathbf{d_V} - 2d_B)^3\right] \\ &= \frac{\pi d_B}{V_L}\left[\mathbf{d_V}^2 - 2\,d_B\,\mathbf{d_V} + \frac{4}{3}{d_B}^2\right] \propto \mathbf{d_V}^2 \end{aligned} \tag{6.1}$$

The vesicle diameter d_V is highlighted in bold to illustrate that the number of lipids per vesicle has a quadratic dependency on it. In the dithionite reduction assays to detect lipid scrambling discussed in the previous chapter, typically LUVs with a diameter d_V of approximately 100 to 200 nm, a lipid concentration of $C_{Lipids} \approx 80$ µM, and a DNA concentration of $C_{DNA} \approx 100$ nM were employed. Under the assumptions that

- C_{Lipids} and C_{DNA} are kept constant,
- all lipids are used up to form vesicle membranes,
- and all DNA nanostructures homogeneously attach to the vesicles,

we can then estimate the number N of DNA nanostructures per vesicle using

$$N_{DNA\ per\ vesicle} = \frac{C_{DNA}}{C_{Lipids}}\,N_{Lipids\ per\ vesicle} \propto \mathbf{d_V}^2 \tag{6.2}$$

This equation illustrates that the number of DNA nanostructures per vesicle also has a quadratic dependency on the vesicle diameter d_V. Figure 6.5 plots how the ratio of DNA nanostructures per vesicle increases if vesicles of a larger diameter are employed.

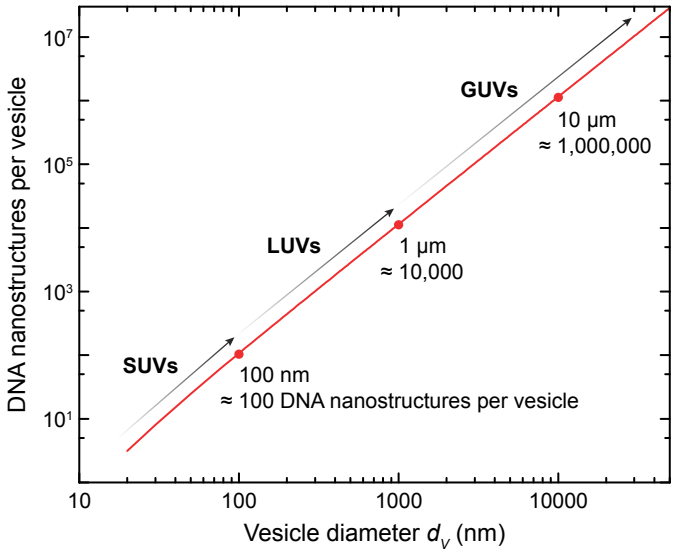

Fig. 6.5 Estimations of DNA nanostructures per lipid vesicle. Graph illustrating the number of DNA nanostructures per lipid vesicle of a given diameter d_V. Values were calculated from Equations 6.1 and 6.2 using a lipid concentration of 80 µM and DNA concentration of 100 nM. The vesicle size classification is taken from [238].

From this estimation it becomes apparent that simply by increasing the vesicle diameter from the previously employed ~100 nm to 10 µm, the chances that a single DNA nanostructure inserts can be increased 10,000 fold. Changing the system size has furthermore direct implications for the detection using fluorescently labelled lipids in the dithionite reduction assay. If a DNA nanostructure inserts in a vesicle and induces lipid scrambling, the absolute change in fluorescence signal is proportional to the number of NBD-labelled lipids that can be flipped to the outer membrane leaflet where they are bleached by dithionite. A vesicle of 10 µm in diameter is composed of approximately 10,000 times more lipids than a 100 nm vesicle. Assuming that a single DNA nanostructure insertion in a vesicle facilitates complete scrambling of the lipids such that all NBD signal is reduced by dithionite, the absolute change in fluorescence signal increases 10,000 fold as well. Therefore, simply by increasing the vesicle size by two orders of magnitude (without changing any other parameter), the insertion probability of DNA nanostructures as well as the change in fluorescence signal in case of scrambling activity can be increased by four orders of magnitude each.
It should be noted that these considerations required certain assumptions. In addition to the ones listed above, we also assumed that a single DNA construct has the same insertion

efficiency on smaller vesicles than it has on larger vesicles, disregarding the effect of membrane curvature. Furthermore, the lipid concentration can be less controlled in the electroformation process to create GUVs. Nevertheless, the fundamental advantages of employing GUVs can be of several orders of magnitude which makes them a promising improvement to the assay. Another advantage of using GUVs is that they can be observed via fluorescence microscopy enabling us to directly verify lipid scrambling at the single-vesicle level. At the same time, we can confirm the correlation of scrambling with the design and attachment of our DNA nanostructures. The increased control will also aid in understanding the results of the dithionite assay making the use of GUVs even more beneficial.

6.3.3 Dithionite assay on giant artificial vesicles

Following the benefits of using larger vesicles discussed in the previous section, it was first necessary to adapt the experimental protocols of the dithionite reduction assay to GUVs. This required reconsidering the lipid composition and particularly the buffer conditions which will be discussed in this section.

For the EColi-eggPC mixture favoured in the previous chapter, the dynamic light scattering measurements have established that this lipid mixture predominantly forms vesicles at around 200 nm in diameter. Therefore, for forming GUVs with diameters exceeding 1 µm, this lipid mixture is unsuitable. While vesicles formed from POPC lipids showed a measurable and variable degree of multilamellarity in the bulk vesicle solutions discussed in Chapter 5, by using GUVs that can be observed via confocal microscopy, each vesicle can be analysed individually and multilamellarity can be determined from the fluorescence intensity and the plateau after dithionite reduction. Furthermore, POPC lipids are ideally suited for dithionite reduction assays as they show negligible rates of spontaneous flip-flop in reconstituted vesicles (half times > 1,000 h) [239] and their fatty acid tails are the most abundant in naturally occurring lipid mixtures [239], making them particularly representative for biological membranes. Furthermore, POPC lipids minimise the differences in lipid tail chemistry between the vesicle-forming lipids and the NBD-labelled PC lipids making these tracer lipids a more accurate representation of the bulk mixture. We therefore formed GUVs from POPC and trace amounts of NBD-PC (see Section 6.2.2 and Table 5.1).

A crucial requisite for the dithionite assay to yield accurate results indicative of lipid scrambling is that dithionite does not permeate inside the lipid vesicles. Osmotic pressure differences between the inside and outside of the artificial lipid vesicles have been shown to potentially induce poration, particularly in giant unilamellar vesicles [240, 241]. Such temporary passages across the lipid bilayer could allow dithionite to leak into the vesicles. This could lead to bleaching of NBD lipids on the inner bilayer leaflet which could be falsely

interpreted as scrambling activity. To avoid this, particular care was taken that artificial vesicles were not exposed to osmotic pressure differences throughout the dithionite assay. Knowing the contribution of dithionite to the osmolality of the buffer solutions allows to account for it appropriately to minimise osmotic pressure differences. As dithionite was prepared in Tris buffer at a 1:1 molar ratio, first the osmolality of dithionite diluted in Tris buffer at a 1:1 molar ratio was determined using a freezing point osmometer. A linear fit to the measured osmolalities of different concentrations of dithionite + Tris in the low millimolar range yielded a slope of ≈ 4.3 (see Fig. 6.6a). This slope can be interpreted as the van't Hoff factor referring to the actual number of particles a dissolved substance dissociates in. The determined value matches well with a complete dissociation of dithionite into three ions ($2\ Na^+ + S_2O_4^{2-}$) and another ion contributed by Tris. Measuring Tris on its own yielded a slope of ≈ 1.2. This is slightly above 1 which could be explained by some additional ions present in the solution which were introduced when adjusting the pH to 10. This could in turn also explain the slightly higher value than 4 for dithionite + Tris. Subtraction of the two determined solutions indicates the slope for dithionite on its own, yielding a value of ≈ 3.1 (see Fig. 6.6a). These results confirm that dithionite can be expected to be fully dissociated at the low millimolar range that will be employed for the dithionite assay. At higher concentrations (100 mM and 250 mM) dithionite demonstrated incomplete dissociation (slope of ≈ 2.5, see inset in Fig. 6.6a), however, that concentration range is not relevant for the here applied protocol of a dithionite reduction assay.

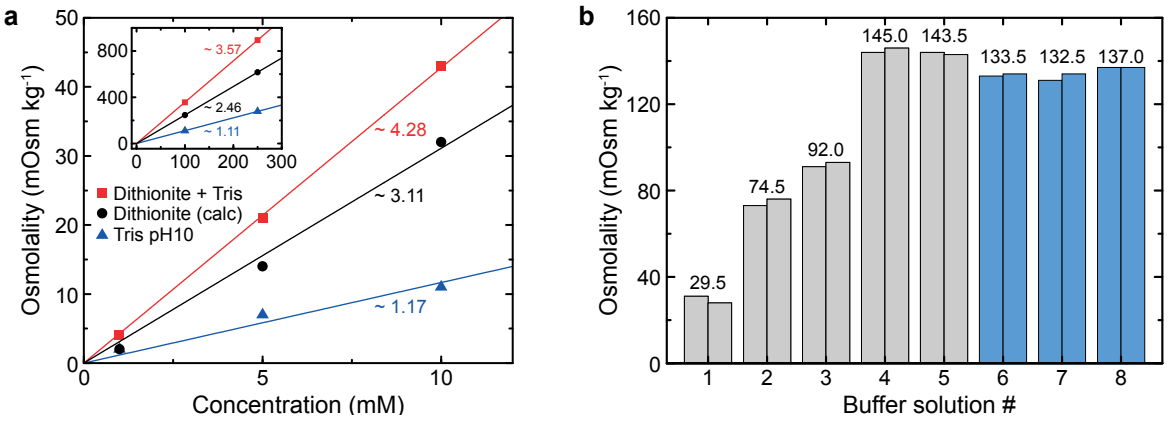

Fig. 6.6 Osmolality measurements of buffer solutions used in dithionite reduction assays. (**a**) Osmolality of Tris and dithionite + Tris (1:1 ratio) at different concentrations. Values for dithionite only were calculated by subtracting the values for Tris from the dithionite + Tris mixture. Lines denote linear fits with the intercept fixed at 0 and the slope as indicated. Inset shows the osmolality at higher concentrations. (**b**) Columns represent two measurement repeats and values their mean (for buffer solutions see Table 6.1). Blue bars denote solutions that giant unilamellar vesicles were in contact with.

Having determined the contribution of dithionite to the osmolality of the buffer solution, it could be accounted for by reducing the concentration of glucose in the buffer to maintain an osmotic balance between inside and outside the vesicles. The bar chart in Fig. 6.6b displays the determined osmolalities of the buffer solutions involved in the dithionite reduction assay. The corresponding buffer conditions are listed in Table 6.1. The bars highlighted in blue are of buffers that vesicles are in contact with. As they show very little difference between each other, dithionite addition could be assumed to not induce osmotic pressure differences significant enough to cause dithionite to leak into the vesicles. Additionally, the lack of dithionite leakage will be experimentally demonstrated by additional control experiments in the next two sections.

Table 6.1 Buffer solutions used in dithionite reduction assays.

Buffer #	Name	Buffer conditions	
1	HEPES buffer	20 mM	HEPES pH 7.4
2	TE20	20 mM	$MgCl_2$
	(containing DNA nanostructures)	10 mM	Tris pH 8.0
		1 mM	EDTA
3	Dithionite dilution solution	50 mM	glucose
		20 mM	HEPES pH 7.4
		4 mM	$MgCl_2$
4	Dithionite solution	50 mM	glucose
		20 mM	HEPES pH 7.4
		4 mM	$MgCl_2$
		15 mM	dithionite
		15 mM	Tris pH 10
5	Glucose solution	100 mM	glucose
		20 mM	HEPES pH 7.4
		4 mM	$MgCl_2$
6	Sucrose solution	100 mM	sucrose
	(containing lipid vesicles)	20 mM	HEPES pH 7.4
7	Incubation solution	7 µl	TE20 (#2)
		1 µl	0.5 % OPOE in TE20
		42 µl	glucose solution (#5)
8	Measurement solution	20 µl	sucrose solution (#6)
		50 µl	incubation solution (#7)
		30 µl	dithionite solution (#4)

6.3.4 Lipid scrambling on giant artificial vesicles

In order to determine if membrane-inserting DNA nanostructures can facilitate lipid scrambling in GUVs, the dithionite reduction assay in this chapter was performed using the 2C DNA nanostructure design (see Fig. 6.7a). This design is identical to the simulated model discussed in Section 6.3.1 apart from added Cy3-labels that enabled fluorescence visualisation. Importantly, the results will be compared to a negative control which follows exactly the same experimental procedure, except that the DNA nanostructure was only assembled with one cholesterol anchor (see Fig. 6.7b). Previously, it has been shown experimentally [54, 170] that one cholesterol tag is not sufficient to produce membrane insertion of similar-sized DNA nanostructures. Therefore, while this control construct would still attach to the lipid vesicles, membrane insertion and lipid scrambling are excluded with no other difference in experimental conditions.

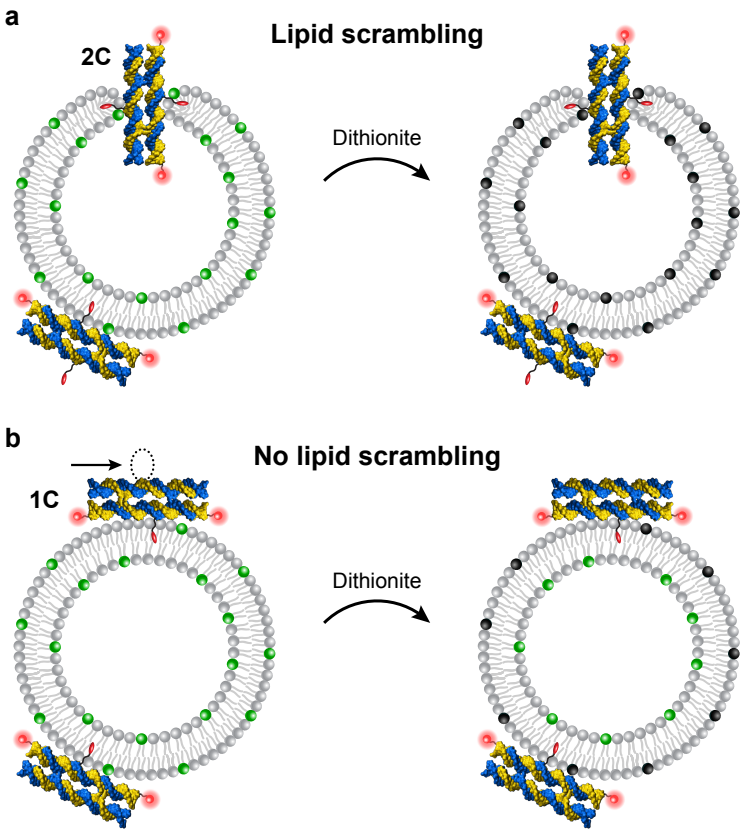

Fig. 6.7 Schematic illustration of dithionite reduction assay comparing 2C with 1C DNA nanostructures. POPC (grey) vesicles containing a fraction of NBD-labelled lipids (green) are incubated with Cy3-labelled DNA constructs. DNA nanostructures assembled with two cholesterol modifications (2C) allow for membrane insertion to induce lipid scrambling (**a**) whereas constructs with only one cholesterol (1C) do not (**b**). Cy3 labels were incorporated on strands st2 and st4 (see Table A.5 in the Appendix).

For the scrambling experiment, the vesicles were incubated in a microscope chamber in the presence of 100 nM of folded 2C DNA nanostructures at a physiological pH of 7.4 and left to settle down due to a density gradient between intravesicular sucrose and extravesicular glucose. After incubation, vesicles were imaged using confocal fluorescence microscopy. A fluorescent ring was observed in both the NBD and the DNA channel (see Fig. 6.8a). Their co-localisation (see merged image in Fig. 6.8a) demonstrates successful attachment of DNA nanostructures to the lipid vesicles [8, 54, 74].

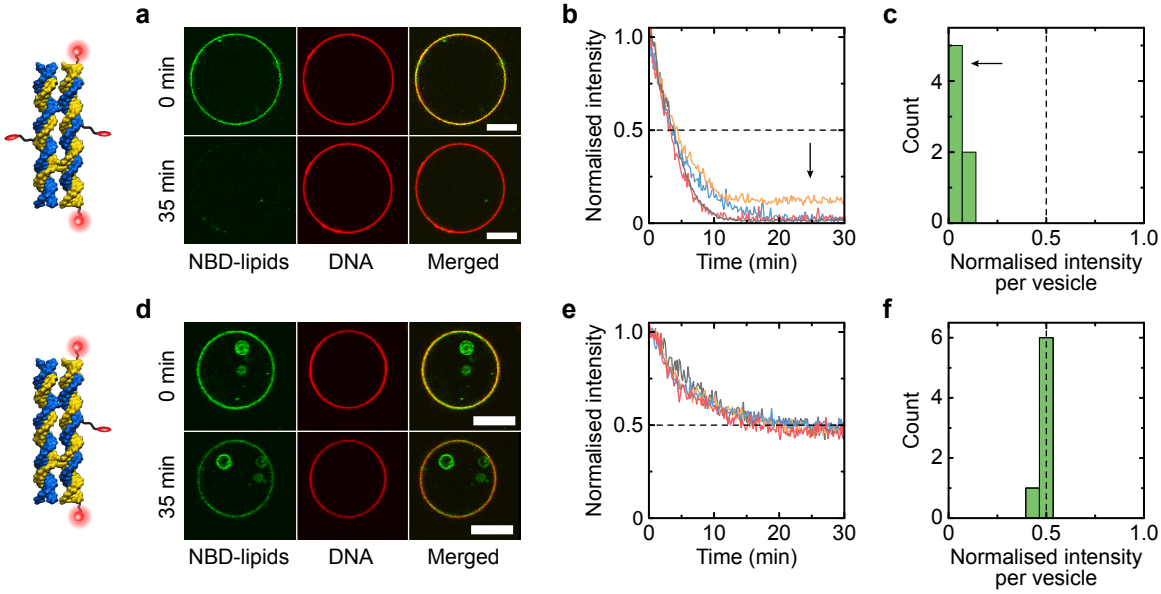

Fig. 6.8 Dithionite reduction assay on giant unilamellar vesicles. Vesicles were incubated either with 2C (top) or 1C (bottom) DNA nanostructures. (**a,d**) Confocal fluorescence microscopy images of GUVs containing fluorescently labelled NBD lipids (green) and incubated with Cy3-labelled DNA nanostructures (red) showing the same vesicle before and 35 min after dithionite addition roughly at the equatorial plane. The third column displays a merged image of the red and green channels. Scale bars are 10 µm. (**b,e**) Graphs showing four representative fluorescence intensity traces of NBD fluorescence reduction over time for 2C (**b**) and 1C (**e**) designs. Values have been normalised to the initial intensity per vesicle and aligned to the onset of dithionite reduction. (**c,f**) Histograms of residual NBD fluorescence intensity at 35 min after dithionite addition normalised to the initial intensity for each vesicle. Data were obtained from four (2C) and one (1C) experiments using the same GUV stock solution. Black arrows in **b** and **c** highlight the shifted fluorescence intensity values for 2C nanostructures in contrast to the 1C control. Data shown were collected from vesicles with a diameter above 6 µm.

After focusing on one field of view and establishing the initial intensity of NBD and DNA signals separately, dithionite solution was added (4.5 mM final concentration) while recording both channels over time. Care was taken not to move vesicles during the dithionite

addition, and the buffer conditions were optimised to avoid significant osmotic pressure, as discussed in the previous section. Figure 6.8a shows fluorescence images of a vesicle incubated with 2C nanostructures taken before and approximately 35 min after dithionite addition. The NBD signal has completely vanished suggesting that the DNA nanostructures successfully induced lipid scrambling so that inner-leaflet NBD-lipids could migrate to the outer layer where they were reduced by dithionite extinguishing any NBD fluorescence. As the DNA signal was unaffected by dithionite and the nanostructures still remained attached, the fluorescence intensity in the DNA channel could be used to localise the vesicle membrane despite the complete loss in fluorescence in the NBD channel. This enabled the acquisition of intensity traces of different vesicles over time, all showing an exponential decrease in fluorescence to almost zero (see Fig. 6.8b). About half an hour after dithionite addition all larger vesicles ($d > 6$ µm) displayed a reduction in fluorescence of over 87 % with an average residual fluorescence of only $\approx 5 \pm 4$ % ($n = 7$, Fig. 6.8c). Thus, our designed DNA nanostructures can induce lipid scrambling in biological membranes.

Upon performing the negative control by incubation of vesicles with 1C nanostructures, a fluorescent ring in the DNA channel before and after dithionite addition indicates membrane attachment similarly to the results of the 2C design (see Fig. 6.8d). However, the NBD fluorescence intensity after 35 min remained at ~50 % indicating the absence of scrambling activity. Example fluorescence intensity traces (Fig. 6.8e) show the expected exponential decrease plateauing at 48 ± 1 % ($n = 7$, Fig. 6.8f). Thus, only the outer-leaflet NBD-labelled lipids have been reduced by dithionite as the 1C DNA nanostructures could not insert into the membrane and induce lipid scrambling. Another independent set of experiments using a slightly different protocol for the dithionite reduction assay (but the same final dithionite concentration), confirmed the difference in the scrambling activity of the 1C and 2C designs (see Section A.6 in the Appendix).

For smaller vesicles ($d < 6$ µm) almost all vesicles incubated with the 1C design showed a fluorescence intensity reduction to the 0.5 value whereas the majority of vesicles incubated with the 2C design displayed a reduction considerably below the 0.5 value (see Figs. 6.9a,b). Defining a fluorescence intensity plateau after dithionite reduction of 0.44 as a threshold, more than 85 % of vesicles incubated with the 2C nanostructures showed an intensity reduction indicative of lipid scrambling (< 0.44) whereas more than 80 % of vesicles incubated with 1C structures did not (> 0.44).

Analysis of all vesicles shows no clear dependence of the fluorescence plateau after dithionite reduction on the absolute initial intensity of the vesicle (see Fig. 6.9c). This indicates that the normalisation did not obscure any possible dependence on the absolute intensity of the vesicles. Furthermore, for vesicles incubated with 1C structures, the data shows no significant

dependence of the fluorescence plateau after dithionite reduction on the vesicle's diameter. However, for vesicles incubated with 2C nanostructures, all larger vesicles (d > 6 µm) show a reduction close to 0 whereas for smaller vesicles (d < 6 µm) values have a larger spread between 0 and 0.5 (see Fig. 6.9d). As discussed in Sections 5.3.7 and 6.3.2, this could be related to their different surface area which is associated with the probability of DNA nanostructure insertion per vesicle (compare Table 5.4 in Section 5.3.7).

Lastly, no dependence of the initial absolute fluorescence intensity on the vesicle diameter was observed (Fig. 6.9e). Therefore, the only distinct feature of the vesicles presented in Fig. 6.8 is their larger size which most likely led to an increased chance for DNA nanostructure insertion to occur.

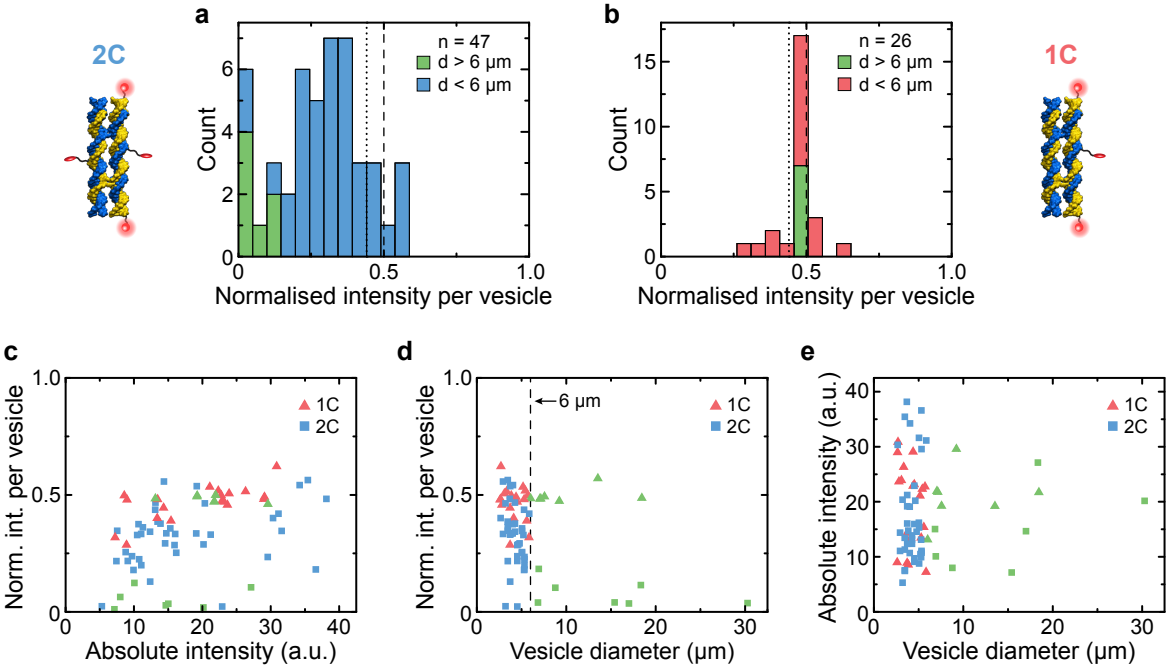

Fig. 6.9 Dependence of scrambling activity on DNA construct, vesicle intensity and vesicle diameter. (**a,b**) Histograms of residual, normalised NBD fluorescence intensity at 35 min after dithionite addition for vesicles incubated with 2C (**a**) or 1C (**b**) DNA constructs. Dotted line indicates the threshold that was set to differentiate scrambling activity (< 0.44) from no activity (> 0.44). Data for larger vesicles (diameter d > 6 µm, green) are the same as presented in Figs. 6.8c,f. Data were acquired from the same experiments as those described in Fig. 6.8. (**c,d**) Dependence of the normalised fluorescence intensity after dithionite reduction on the vesicle's initial absolute fluorescence intensity (**c**) or its diameter (**d**). (**e**) Dependence of the vesicle's initial absolute fluorescence intensity on its diameter. Green data points refer to vesicles with a diameter above 6 µm as plotted in Figs. 6.8c,f. The smallest vesicle included in the analysis was 2.6 µm in diameter.

6.3.5 Dithionite leakage through DNA-induced pores

The results presented in the previous section confirmed that DNA nanostructures capable of membrane insertion induce lipid scrambling (2C) whereas structures that should not insert, do not (1C). However, an important aspect to verify is that the membrane insertion of the DNA nanostructures does not create a passage for dithionite to permeate into the vesicles and bleach NBD lipids on the inner bilayer leaflet even without scrambling activity. As DNA is negatively charged, permeation of anions through DNA-induced lipid pores is expected to be much slower than cation permeation due to electrostatic repulsion. Previously reported simulations of a larger, membrane-inserted DNA nanostructure showed significantly decreased Cl^- ion over K^+ ion permeation [231]. In accordance with these results, the all-atom simulations of our DNA scramblase design similarly reveal a 93 % reduction of Cl^- ion permeation compared to that of K^+ ions. In the dithionite reduction assay, the NBD-reducing dithionite anion $S_2O_4^{2-}$ is larger than Cl^- ions and, most importantly, it is double negatively charged. Therefore, the negative charge of the DNA nanostructure, in combination with the low ionic strength of the buffer solution used in the experiments, is expected to present a barrier to dithionite permeation through the toroidal pore.
To experimentally demonstrate the low permeation rate of dithionite through the DNA-induced toroidal pore, we performed a series of control experiments. The experimental concept is based on employing a water-soluble NBD-labelled molecule that is present in solution both inside and outside the vesicles. Upon performing a dithionite reduction assay, only NBD dye outside the vesicles should be fluorescently reduced if no passages are present for the dithionite to cross the vesicle membrane (see Fig. 6.10).

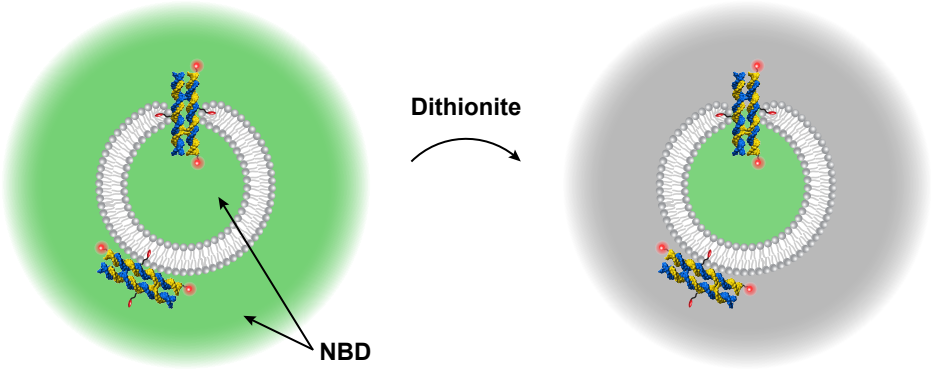

Fig. 6.10 Experimental strategy to probe for dithionite leakage through the 2D DNA nanostructure. NBD dye is present in the solution inside and outside vesicles incubated with 2C constructs. If DNA structures do not facilitate permeation of dithionite into the vesicles, addition of dithionite would only reduce NBD fluorescence outside the vesicles.

An important aspect of this experimental design is that the NBD-labelled molecule does not permeate through the vesicle membrane itself (even without any DNA nanostructures present). According to previously described protocols for bulk dithionite assays on LUVs, NBD-labelled glucose (NBD-glucose; see Fig. 6.11a) can be used to demonstrate that dithionite does not permeate inside the vesicles [14]. We therefore formed GUVs as for the dithionite assay, but this time with NBD-glucose present in solution during the formation. Vesicles were then incubated in a microscope chamber as for dithionite experiments (except without DNA structures and dithionite). We then performed fluorescence recovery after photobleaching (FRAP) experiments using confocal fluorescence microscopy. NBD-glucose inside vesicles was photobleached by excitation at a high laser power and the fluorescence recovery inside the vesicles was recorded at certain time points afterwards (see Fig. 6.11b). Already after ~10 min the fluorescence inside the vesicles has significantly recovered (see Fig. 6.11c). This indicates that under our experimental conditions, NBD-glucose can permeate across vesicle membranes within minutes even without DNA nanostructures present. A similar leakage rate of NBD-glucose has been mentioned in previous work [242]. Furthermore, with a predicted log octanol-water partition coefficient of −0.41, NBD-glucose is only moderately hydrophilic [243]. We therefore deemed NBD-glucose unsuitable for our purpose of verifying if dithionite can leak through DNA-induced toroidal pores.

Another reported approach employed NBD-labelled polyethylene glycol (NBD-PEG) [236]. The covalent attachment of the PEG chain was expected to increase the hydrodynamic radius of the NBD dye, preventing its direct permeation across the membrane or through DNA-induced toroidal pores. We therefore synthesised a fluorescent probe from NBD-SE and amino-modified 24-unit polyethylene glycol (see Fig. 6.11d). Successful synthesis was verified with thin layer chromatography (TLC) where a solvent travels through a silica gel by capillary action allowing for the separation of different analytes. NBD-SE demonstrates a shorter migration distance if co-spotted or incubated with varying ratios of NBD-SE:PEG (1:1, 1:2, 1:10; see Fig. 6.11e). Already at an NBD-SE:PEG ratio of 1:1 a complete shift of the NBD-SE spot is achieved, indicating successful conjugation to the PEG molecule.

We then formed GUVs in the presence of NBD-PEG and incubated them with 2C DNA structures, as in the dithionite reduction assay. FRAP experiments show a very slow fluorescence recovery rate with a linear slope of ~14 % per hour (Fig. 6.11f). This suggests that, at the time scale relevant for the dithionite assay, our synthesised NBD-PEG molecules are essentially membrane impermeable, even in the presence of 2C DNA structures. This makes NBD-PEG a much better probe for testing dithionite permeability than NBD-glucose.

The same batch of vesicles was then incubated with DNA scramblases, again with NBD-PEG molecules present inside and outside the vesicles. A dithionite reduction assay was

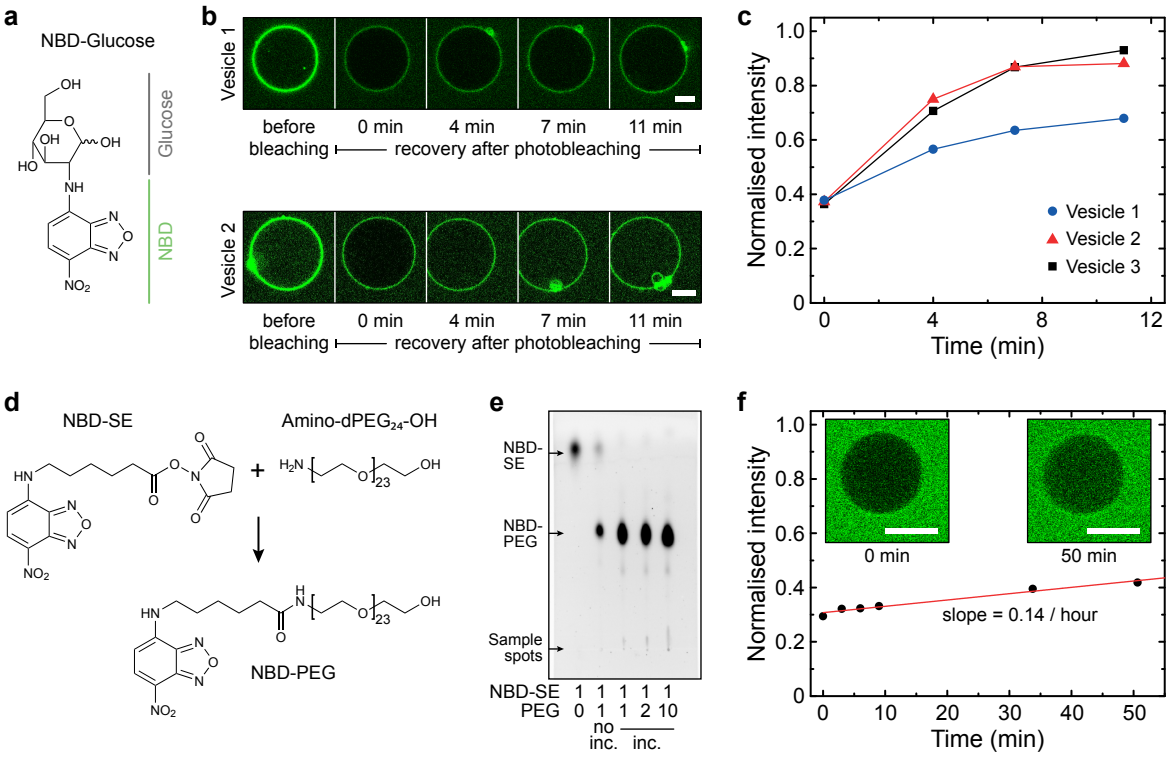

Fig. 6.11 Fluorescence recovery after photobleaching of NBD-glucose and NBD-PEG. (**a**) Chemical structure of NBD-glucose. (**b**) Confocal microscopy images of GUVs with NBD-glucose present inside and outside. Two vesicles are shown before and at various time points after photobleaching of the NBD dye. Vesicle membranes contained NBD-PC lipids as described before. (**c**) Fluorescence intensity traces of the recovery of NBD glucose inside three vesicles after they have been photobleached. Traces have been normalised to the fluorescence intensity outside the vesicles before photobleaching. (**d**) Chemical structures of NBD-SE and Amino-dPEG$_{24}$-OH (PEG24), and their reaction to NBD-PEG. (**e**) Thin layer chromatography (TLC) analysis verifying the successful conjugation of NBD to PEG. The second lane refers to a co-spot of NBD-SE and PEG whereas for the subsequent three lanes both compounds have been incubated at varying ratios over night. This TLC analysis was performed using PEG12 molecules. (**f**) Fluorescence recovery after photobleaching of NBD-PEG inside a POPC GUV that was incubated with 2C DNA nanostructures (NBD-PC was omitted in the lipid mixture). Normalisation was performed as in **c**. Red line represents a linear fit. Note the much longer time scale compared to **c**. All scale bars denote 5 µm.

carried out following the same protocol as in our lipid scrambling assays (see Fig. 6.12a). Monitoring NBD-PEG fluorescence showed that the fluorescence outside the vesicles was rapidly decreased by dithionite whereas the fluorescence inside the vesicles remained almost constant over the 45-minute time scale of the measurement (see Figs. 6.12a-c). The intensity reduction for a region outside the vesicle follows similar kinetics as observed for the dithionite reduction in the scrambling assay (see Fig. 6.12c). The NBD fluorescence intensity inside the vesicle, however, decreases at a much slower rate. This slow decrease is most likely not explained by photobleaching during the imaging (see Fig. 6.12d). A possible reason could be that the reduced background fluorescence, due to dithionite reduction outside the vesicles, could potentially contribute to the slight reduction in fluorescence intensity inside the vesicles. Alternatively it could be that there is indeed a very low permeation rate of dithionite into the vesicles. However, these experiments show that dithionite permeation through the DNA-induced pores is too slow to explain the rapid decrease in fluorescence observed in our 2C DNA construct experiments. Therefore, we do indeed observe lipid scrambling induced by the DNA scramblase nanostructures.

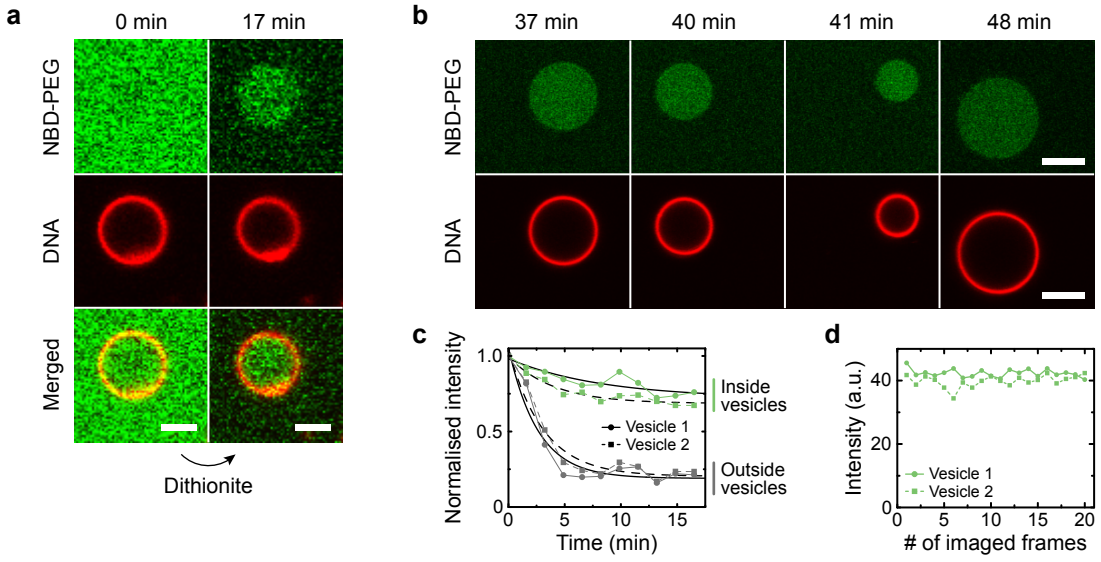

Fig. 6.12 Permeability of dithionite through vesicle membranes incubated with 2C DNA structures. (**a**) Confocal microscopy images of POPC GUVs incubated with Cy3-labelled 2C DNA structures (red) and with NBD-PEG (green) in solution at equal concentrations inside and outside the GUVs. The same vesicle is shown before and 17 min after dithionite addition. (**b**) Vesicles imaged at other locations and later time points after dithionite addition in the chamber used in **a**. All scale bars are 5 µm. (**c**) Normalised NBD-PEG fluorescence intensity inside (green) and outside (grey) two vesicles (vesicle 1 is shown in **a**). Black lines are single exponential fits. (**d**) Absolute fluorescence intensity inside the vesicles analysed in **c** imaged for 20 consecutive frames (~90 s) roughly 30 min after dithionite addition.

6.3.6 Lipid scrambling rates

To determine the lipid scrambling rate of our DNA nanostructures the traces describing the dithionite-induced fluorescence reduction presented in Fig. 6.8 were each fit with an exponential decay. For both 1C and 2C structures, traces are well described by a single exponential decay (see Figs. 6.13a,b). This is in agreement with a previous characterisation of fully activated biological scramblases that found the dithionite reduction of the NBD dye to be the rate-limiting factor in the case of rapid scrambling [14]. The exponential fits yielded characteristic decay times $\langle\tau\rangle$ of ~4 to 8 min. Using Equation 6.1, we approximated the number of lipids per vesicle N_{total} from the vesicle's diameter. With

$$k = \frac{N_{total}}{\langle\tau\rangle} \tag{6.3}$$

the lipid scrambling rates per vesicle were calculated to be between ~0.7 to 3.7 $\times$ 10^7 s^{-1} (see Fig. 6.13d). These values are in very good agreement with the simulated scrambling rates that yielded ~1.7 $\times$ 10^7 s^{-1} for individual DNA scramblases (see Section 6.3.1). No additional factor was applied to the number of lipids per vesicle in Equation 6.3 since Brownian dynamics simulations showed that the scrambling rate does not depend on the ratio of labelled to unlabelled lipids (see [75] for further details).

Experiments with pore-forming peptides determined lipid flip-flop rates between 1 and potentially 10^3 lipids per second per peptide [137, 146]. *In vitro* experiments on TMEM16 scramblases [14, 121], opsin [15] and rhodopsin [16] have assessed scrambling rates of > 10^4 s^{-1} per scramblase protein under optimal conditions. However, some of these rates were limited by the dithionite-mediated NBD reduction. Recent atomistic simulations of the G protein-coupled receptor opsin determined a characteristic time scale of ~33 µs per lipid translocation event [17]. This corresponds to a possible maximum scrambling rate of 3 $\times$ 10^4 s^{-1} in the case where dithionite is not the rate-limiting factor. In contrast, we found the simulated lipid transfer rate induced by our DNA nanostructure to be on the order of 10^7 s^{-1}, up to three orders of magnitude faster than reported for natural scramblases.

To achieve flip-flop rates equivalent to natural scramblases the free energy barrier for lipid translocation needs to be lowered from > 20 kcal mol^{-1} (uncatalysed lipid transfer) to $\approx$ 7 kcal mol^{-1} [97]. One reason for the remarkable scrambling rates of our DNA scramblase is the reduction of the free energy barrier to approximately 1 k_BT ($\approx$ 0.6 kcal mol^{-1} at room temperature), one order of magnitude lower than accomplished by natural scramblases. Furthermore, the MD simulations showed that the DNA-induced toroidal lipid pore is stable for much longer time scales than nanosecond-long, transient water passages that were previously suggested to allow for spontaneous lipid flipping and flopping [244–246].

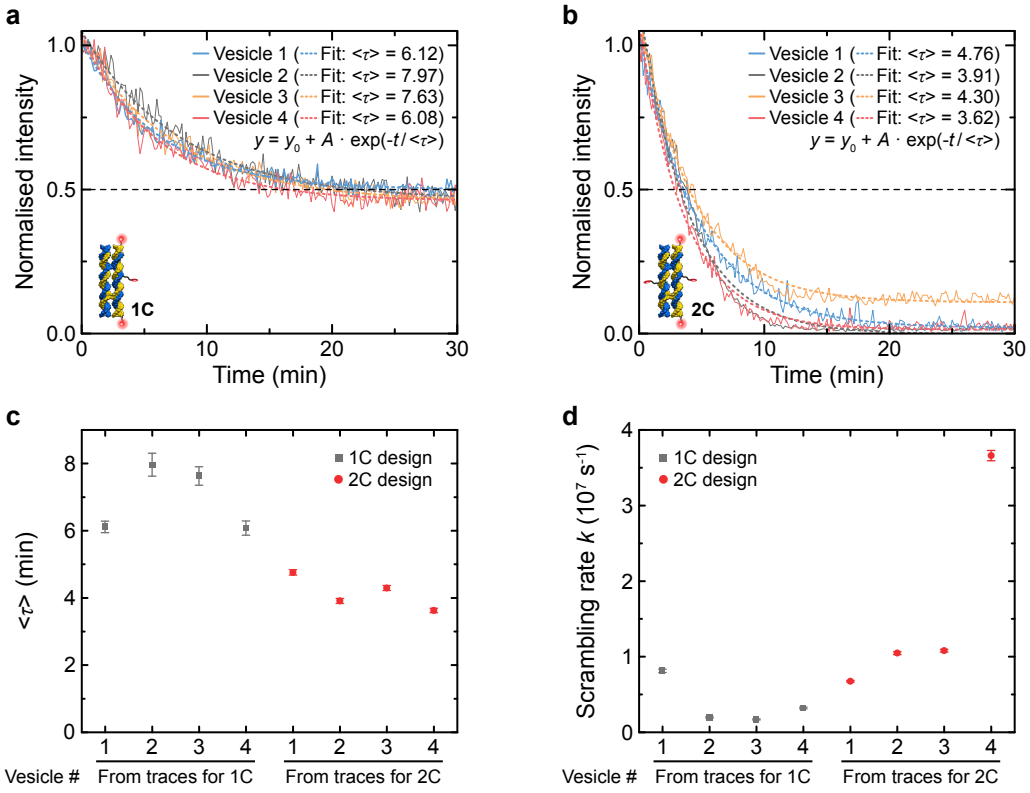

Fig. 6.13 Dithionite reduction rates determined from experiments. (**a,b**) Single exponential fits (dotted lines) of dithionite reduction traces (solid lines) shown in Figs. 6.8b,e for 1C and 2C nanostructures, respectively. Fit values $\langle\tau\rangle$ of decay rates are shown in the legend with the fitting equation below. (**c**) Graph comparing the characteristic decay times $\langle\tau\rangle$ (error bars denote fitting error) of the different dithionite reduction traces for 1C and 2C designs. (**d**) Scrambling rates approximated from characteristic decay times shown in **c** via Equation 6.3 with error bars originating from the error of $\langle\tau\rangle$. The number of lipids was calculated via the volume of a lipid as described in Equations 5.1 using the dimensions listed in Table 5.3.

Our experimentally determined average scrambling rate of $\approx 1.62 \times 10^7$ s^{-1} matches the simulation results very well, however, these rates can have multiple contributions. While several structures could insert and scramble lipids at the same time, they might only transiently insert and therefore not actively contribute for extended periods. Gummadi *et al.* previously reported calculations to estimate the mean lifetime $\langle\tau\rangle$ for a freely diffusing phospholipid to encounter a single, immobile flippase to gauge characteristic flipping times (footnote in [247]). Their estimations are based on equations regarding diffusion-controlled reactions on spherical surfaces [248–250]. Sano *et al.* [249] state (in their Equation 6.1) that the mean reaction time $\langle\tau\rangle$ for two particles that diffuse on a circle, one particle immobile in the centre

and the other initially uniformly distributed within the circle, is given by

$$\frac{\langle\tau\rangle}{\tau_Q} = \frac{2}{1-\frac{d^2}{4R^2}} \ln\left(\frac{2R}{d}\right) - \frac{3}{2} + \frac{d^2}{8R^2} + \frac{2D}{pd}\left(1-\frac{d^2}{4R^2}\right) \tag{6.4}$$

with $\tau_Q = R^2/D$ being the characteristic time, D the diffusion constant of the diffusing particle, d the distance at which both particles react with each other, and p measuring the reactivity once the particles encounter each other at the distance d. R denotes the radius of a sphere whose surface area equates to the same area as the circle of radius $2R$ that the particles are diffusing on. The boundary of the circle is assumed to be perfectly reflective.
We can now use this equation to estimate the mean interaction time for a phospholipid to be flipped (= captured) once it encounters a DNA-induced toroidal pore. For this, we first assume a direct absorption upon encounter ($p \to \infty$) meaning the lipid is flipped upon reaching the toroidal pore. This simplifies Equation 6.4 to

$$\frac{\langle\tau\rangle}{\tau_Q} \approx \frac{2}{1-\frac{d^2}{4R^2}} \ln\left(\frac{2R}{d}\right) - \frac{3}{2} + \frac{d^2}{8R^2} \tag{6.5}$$

In our case, the encounter distance d equates to the radius of the toroidal pore r_p (lipid headgroups are hereby assumed as point-like). With $d_V = 2R$ as the diameter of the lipid vesicle, and therefore $\tau_Q = d_V^2/4D$, the equation can be rewritten to

$$\langle\tau\rangle \approx \frac{d_V^2}{4D}\left[\frac{2}{1-\left(\frac{r_p}{d_V}\right)^2} \ln\frac{d_V}{r_p} - \frac{3}{2} + \frac{1}{2}\left(\frac{r_p}{d_V}\right)^2\right] \tag{6.6}$$

In the scramblase experiments, the GUV diameter was in the range of several micrometres while the radius of the DNA nanostructures (and therefore of the toroidal pores) was only a few nanometres. As this satisfies the condition of $1 \gg r_p^2/d_V^2$, the equation can ultimately be simplified to

$$\langle\tau\rangle \approx \frac{d_V^2}{2D}\left(\ln\frac{d_V}{r_p} - \frac{3}{4}\right) \tag{6.7}$$

Performing an analogous transformation with Equation 6.2 from Sano *et al.* [249], we obtain an expression for the mean reaction time of a pair of freely diffusing particles on a spherical surface as

$$\langle\tau\rangle \approx \frac{d_V^2}{2D}\left(\ln\frac{d_V}{r_p} - \frac{1}{2}\right) \tag{6.8}$$

While Equation 6.7 agrees with other previous work [250], it should be noted that neither of the two equations agree with the equation used for flippase activity presented in a footnote in Gummadi *et al.* as their second term in the brackets was -1 which might be an inaccuracy in the derivation of the equation. Nevertheless, we can now use Equation 6.7 to calculate $\langle\tau\rangle$ for the average diameter of the vesicles used for the determination of scrambling rates (see Fig. 6.13b) and compare it to the experimentally determined values (see Table 6.2).

Table 6.2 Calculated and experimentally determined scrambling rates. The radius of the toroidal pore r_p was approximated from the transition path of a lipid headgroup at the toroidal pore determined from calculations of the 2D potential of mean force (see Fig. A.5 in the Appendix). D denotes the diffusion coefficient of POPC lipids in GUVs [251]. d_V is the average diameter of the vesicles used for 2C rate calculations in Fig. 6.13b. N_{total} refers to the total number of lipids in a vesicle of diameter d_V and was calculated with Equation 6.1. k is the lipid scrambling rate per scramblase calculated using Equation 6.3.

r_p	D	d_V	N_{total}	Term in	$\langle\tau\rangle_{calc}$	$\langle\tau\rangle_{exp}$	k_{calc}	k_{exp}
nm	$\mu m^2\ s^{-1}$	µm	10^9	equation	min	min	$10^7\ s^{-1}$	$10^7\ s^{-1}$
2.3	7	19.4	3.46	$-3/4$	3.72	4.15	1.55	1.62
				$-1/2$	3.83	4.15	1.51	1.62
				-1	3.60	4.15	1.60	1.62

The calculated mean lifetime is ≈ 3.7 min, which is only slightly lower than the averaged experimental value of ≈ 4.2 min. Furthermore, the scrambling rate k, defined as in Equation 6.3, is calculated to be $1.55 \times 10^7\ s^{-1}$ assuming only a single DNA nanostructure is active, which agrees very well with the simulated and experimentally observed rates (see Table 6.2). These values vary only slightly with respect to the second term in the brackets in Equations 6.7 and 6.8, or the -1 used in Gummadi *et al.* [247] (compare Table 6.2). While Equation 6.7 ($-3/4$) assumes an immobile toroidal pore (= absorbing region), Equation 6.8 ($-1/2$) assumes two diffusing particles on a spherical surface. A diffusion coefficient of $D = 1\ \mu m^2\ s^{-1}$ was previously reported for a 6-helical DNA nanostructure that was potentially membrane-inserted (6HP design with 3 cholesterol modifications, compare Fig. 3.8 for general design) [78]. Assuming a similar diffusion coefficient for the DNA-induced toroidal pore, the calculated value for the mean lifetime $\langle\tau\rangle$ will most likely be in between Equations 6.7 and 6.8. These results together with the calculated low energy barrier for lipid translocation suggest, that lipid diffusion in our GUVs is not rate limiting even if only one DNA scramblase is active. If multiple structures scramble lipids simultaneously, a faster fluorescence reduction would be expected. But in the current assay protocol, the slow kinetics of the dithionite reduction are ultimately rate limiting.

6.3.7 DNA scramblase experiments on human cancer cells

To show the potential of our DNA scramblase for *in vivo* applications, we tested it on human cells. As discussed in Chapter 2, lipid scrambling is part of the signalling pathway to induce cell apoptosis. An established method to detect apoptosis in cells is to use a fluorescently labelled protein called Annexin V which has a high affinity for phosphatidylserine (PS) lipids [252, 253]. In healthy cells, due to the asymmetric lipid distribution in the the cell membrane, PS lipids are primarily located in the inner bilayer leaflet [102, 254, 255]. Therefore, Annexin V should not significantly bind to the cell membrane (see Fig. 6.14a). However, if apoptosis or lipid scrambling is induced, the lipid composition is equilibrated exposing PS lipids on the cell's outer bilayer leaflet (see Figs. 6.14b,c). The binding of fluorescently labelled Annexin V can then be detected via confocal microscopy.

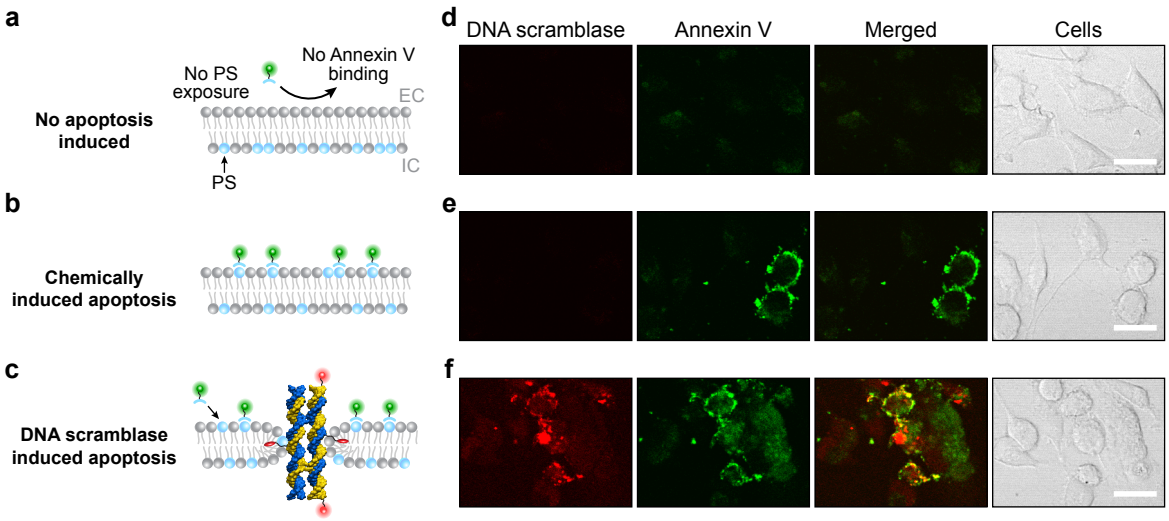

Fig. 6.14 Annexin V staining experiments on human cancer cells. (**a-c**) Schematic illustration of FITC-labelled Annexin V (green) binding assay without apoptosis (**a**), with chemically induced apoptosis (**b**), and DNA scramblase induced apoptosis (**c**). Phosphatidylserine (PS) lipids are highlighted in light blue. (**d-f**) Confocal microscopy images of fixed cells after incubation with only DNA folding buffer (**d**), 10 µM staurosporine (**e**), or with Cy3-labelled 2C DNA scramblases (**f**). While no Annexin V binding occurs in the negative control, incubation with DNA scramblases showed cell attachment of the DNA nanostructures (red) associated with increased Annexin V (green) binding (see merged signal of both channels) due to PS exposure. All imaging settings were the same for the equivalent images in all experiments. Corresponding brightfield images illustrate cell locations (scale bar is 20 µm).

To test our DNA scramblases, we employed MDA-MB-231 breast cancer cells as they naturally possess a low level of PS in the outer membrane leaflet [210]. First, as a negative control, we incubated the cells with DNA scramblase buffer only. Subsequent staining with Annexin V and imaging of the fixed cells with confocal microscopy confirmed the

low amount of Annexin V binding under these conditions (see Fig. 6.14d). Second, as a positive control, we incubated the cells with the apoptosis-inducing microbial alkaloid staurosporine which resulted in binding of Annexin V to the cell's membrane indicated by bright fluorescent edges (see Fig. 6.14e). No signal was detected in the red channel illustrating sufficient spectral separation of the FITC dye from the Cy3 channel.
Ultimately, cells were incubated with Cy3-labelled 2C DNA nanostructures where successful scrambling activity would be indicated by an elevated level of surface-exposed PS resulting in increased binding of FITC-Annexin V (see Fig. 6.14c). Confocal microscopy images presented in Fig. 6.14f show not only that the DNA nanostructures attached to the cells but also that Annexin V binding increased in their vicinity. The recorded fluorescence intensity is comparable to the positive control performed with the apoptosis-inducing agent. The elevated level of surface-exposed PS demonstrates that our DNA scramblase is able to induce lipid scrambling in human cells.

6.4 Conclusion

One of the biggest challenges in determining if our DNA nanostructures can induce lipid scrambling was their low insertion efficiency. In this chapter, we addressed this issue in two ways. First, we performed atomistic MD simulations in which we could investigate how our 2C DNA structure interacts with the lipid bilayer when it is membrane inserted. In accordance with our previous work on a membrane-inserted DNA duplex [8], the DNA construct induces a toroidal DNA-lipid pore that was stable throughout the entire 2.2 µs simulation. This DNA-stabilised, toroidal pore establishes a pathway for lipid molecules to diffusively translocate from one bilayer leaflet to the other only needing to cross an energy barrier of $\approx 1\ k_BT$. From these simulations we could furthermore determine a lipid scrambling rate on the order of 10^7 lipids per second thereby outperforming biological scramblases by up to three and reported artificial scramblases by up to six orders of magnitude [97, 131, 132].
Second, we adapted the dithionite reduction assay to giant unilamellar vesicles in the micrometre range. This allowed us to increase the probability for a membrane-inserted DNA nanostructure by several orders of magnitude while at the same time being able to follow the lipid scrambling activity of each individual vesicle. To the best of our knowledge, this is the first demonstration of directly recording the dithionite-induced fluorescence reduction, and thereby lipid scrambling activity, at the single-vesicle level. Particularly for vesicles larger than 6 µm in diameter, almost complete fluorescence reduction was observed for all vesicles incubated with 2C DNA structures, indicating rapid lipid scrambling activity. Importantly, vesicles incubated with 1C constructs consistently showed an intensity reduction to only

half, indicating the absence of scrambling activity and no leakage of dithionite into the vesicles. Controls performed with our synthesised NBD-PEG molecule further verified that the fluorescence decrease induced by the 2C DNA scramblase design could not be explained by leakage of dithionite through the membrane, the DNA-induced toroidal pore, or the DNA construct itself. This demonstrated that we do indeed observe lipid scrambling activity.
The experimentally determined scrambling rates were on the order of 10^7, agreeing well with the simulation results. While these rates could have several contributions, e.g. multiple, simultaneously inserted structures, the previously determined low insertion efficiency indicates that most likely only very few of the membrane-attached DNA structures actually contribute to lipid scrambling activity. Estimations on the characteristic lipid flipping time scales for a single DNA scramblase (or rather the toroidal pore it induces) confirmed that a single membrane-inserted structure could potentially be sufficient to explain the experimentally observed scrambling kinetics. However, ultimately the rate-limiting step in the current assay design is the dithionite reduction reaction. Therefore, future protocols using higher dithionite or lower DNA nanostructure concentrations might allow to investigate a regime where lipid scrambling activity can be differentiated from dithionite reduction kinetics.
Lastly, experiments with human breast cancer cells indicated that, similar to the role of lipid scramblases in nature, our DNA scramblases can induce cell apoptosis. Future flow cytometry experiments would be beneficial to further quantify the scrambling and apoptosis-inducing activity of our DNA nanostructures on cells.
In summary, with our combined approach of all-atom MD simulations and single-vesicle scrambling experiments, we successfully demonstrated the application of DNA nanotechnology to design synthetic lipid scramblases that can even outperform their natural counterparts by several orders of magnitude.

Chapter 7

Conclusions & Outlook

There are lots and lots of little problems out there, all of which can probably be solved on the nanometre scale using these systems or systems derived from them.

– Nadrian C. Seeman

The aim of this thesis was to determine if a DNA-induced toroidal lipid pore facilitates mixing of lipid molecules between the leaflets of a lipid bilayer. We thereby envisioned to design and build synthetic mimics of natural lipid scramblase proteins using DNA nanotechnology. As previous work demonstrated the feasibility of mimicking protein ion channels using DNA as a building material, DNA nanotechnology presented itself as an ideal tool to expand the range of synthetic membrane protein mimics to lipid scramblases. Gaining control over a cell membrane's lipid composition has numerous applications in biomedicine and for therapeutics, making this objective a worthwhile endeavour.

Throughout this thesis, we gradually increased the complexity of the DNA nanostructure as well as the experimental methods. After a structural analysis of the DNA constructs, we studied their behaviour once modified with cholesterol, and ultimately investigated their interaction with lipid membranes on planar bilayers (current measurements), large and giant unilamellar vesicles (dithionite reduction assays), and via all-atom MD simulations.

In Chapter 3, we introduced the design of our DNA nanostructure consisting of eight ssDNA strands that self-assemble into four interconnected dsDNA helices. Using a non-scaffolded DNA nanostructure facilitated an assembly at µM concentrations while minimising DNA material cost. This is in contrast to DNA origami structures whose concentration is often limited to the nM range by the viral ssDNA scaffold strand. These fundamental advantages make our approach scaleable and cost-efficient, two essential aspects for possible future applications in medicine. The DNA nanostructures consistently showed a high folding

yield at $MgCl_2$ concentrations above ~5 mM which allowed to work at a broader range of buffer conditions, another advantage over DNA origami. It was crucial to use a loading dye without additional EDTA which should always be kept in mind for experiments where the Mg^{2+} concentration is an integral parameter. While our AFM measurements lacked the resolution, TEM imaging enabled us to confirm the correct assembly of the monomeric DNA nanostructures as their dimensions matched well with the expectations. Four DNA nanostructure designs have been developed throughout this thesis. Particularly, the CP3 short and CP4 layouts could be useful alternatives to explore in the future as they exclusively formed monomeric structures. However, the chosen CP2 design presented the most balanced layout due to its high folding yield and numerous, centrally located modification positions. This in-depth analysis of the design and assembly characteristics of the DNA nanostructure provided a valuable foundation for the rest of the thesis work to build up on.

To insert hydrophilic DNA nanostructures into a lipid bilayer, hydrophobic moieties were required on the DNA. The commercial availability and compatibility with lipid membranes made cholesterol the most prominent molecule to anchor DNA into a lipid bilayer. As hydrophobic tags typically induce aggregation we needed to better understand this aspect first, in order to optimise the design of our synthetic lipid scramblase. We therefore characterised in Chapter 4 the behaviour of cholesterol-modified ssDNA, dsDNA, and DNA nanostructures. Their transient interactions or complete aggregation could be efficiently analysed using non-denaturing (native) PAGE. We avoided the use of denaturing gels, as they have been shown to mask cholesterol-mediated interactions [81]. Our studies revealed a sequence-dependent aggregation behaviour of cholesterol-modified ssDNA. Particularly the terminal bases preceding the cholesterol modification and tendencies to form dimers or multimers had a significant influence. This should be prevented by optimising the sequence to minimise secondary structure formation using a structure prediction tool such as NUPACK [38]. We showed that preventing stable secondary structure formation, by using poly-T DNA sequences, can avoid chol-DNA aggregation. All-atom MD simulations were employed to investigate the mode of action demonstrating that the ssDNA wraps around the cholesterol at the nanosecond time scale thereby shielding the hydrophobic group. We hypothesised that this interaction between ssDNA and cholesterol is a mechanism by which cholesterol-mediated aggregation can be prevented. We proved this hypothesis by controlling the hydrophobically mediated interaction of a cholesterol-modified DNA duplex by varying the length of an adjacent ssDNA overhang. A 6 nt overhang was sufficient to prevent cholesterol-mediated aggregation. This approach also succeeded at shielding tocopherol modifications suggesting that our method is universally applicable to other types of hydrophobic tags.

The aggregation behaviour of the CP2 DNA constructs was mostly determined by the choles-

terol number and modification position, and less by the linker chemistry. While up to two cholesterol modifications showed consistent band shifts in native PAGE, for higher numbers aggregation dominated. However, we could successfully prevent aggregation both in native PAGE and DLS experiments in solution using our ssDNA shielding strategy. Importantly, we verified that the ssDNA overhangs do not inhibit binding to lipid membranes. Here, the versatile modification positions of the CP2 design were crucial for the systematic study of cholesterol-mediated aggregation and its prevention. The combination of eight thymine overhangs to prevent stacking interactions, four cholesterol groups to facilitate membrane interaction, four ssDNA overhangs to prevent cholesterol-mediated aggregation, and two Cy3-molecules to allow tracking with fluorescence microscopy, demonstrates the impressive amount of complexity that can be engineered into such a small DNA structure.

As the ssDNA shielding strategy was only developed at the end of this thesis work, the 2C CP2 design was favoured at that time as it did not tend to aggregate. In Chapter 5, we then investigated its interaction with planar lipid bilayers and LUVs. Electrophysiology measurements demonstrated that this design can insert into lipid bilayers and induce ionic currents across them. We have thereby successfully mimicked the function of natural protein ion channels. However, these experiments also indicated that the insertion efficiency of these DNA structures is very low. Next, the bulk dithionite reduction assay on LUVs was employed to gauge the DNA nanostructure's lipid scrambling activity. The higher degree of unilamellarity rendered vesicles formed from a 3:1 EColi:eggPC lipid mixture superior compared to POPC. It was even possible to detect the asymmetric lipid distribution across bilayer leaflets due to geometrical constraints for vesicles smaller than ~100 nm in diameter. Combined with a second method to confirm vesicle formation (e.g. DLS or confocal microscopy), the dithionite assay proved to be an excellent tool to determine the unilamellarity of artificial lipid vesicles which our group already employed in another publication [216].

While the NBD labelling position slightly affected the reduction kinetics, no significant influence on the reached fluorescence plateaus was observed. Dithionite concentrations ranging from 10 to 40 mM are ideal if rapid lipid scrambling kinetics are studied in bulk. However, a concentration of ~5 mM presents a good balance between sufficiently fast kinetics and low permeation across vesicle membranes which was of great importance in experiments with GUVs. Final OPOE concentrations of approximately one order of magnitude below the CMC proved to be acceptable (~0.02 %) but above that membrane permeability was compromised. If rapid scrambling kinetics are expected, concentrations up to ~0.05 % could be employed together with appropriate controls in future experiments.

Unfortunately, we could not establish a positive scrambling control using a commercially available TMEM16F scramblase, possibly due to its lack of biological activity. Collabora-

tions with other research groups that can provide scramblase proteins would be beneficial to directly compare natural with synthetic scramblases in the same assay. Also, it was not possible to detect scrambling activity of various DNA nanostructure designs using the bulk dithionite assay with LUVs. Given the low DNA nanostructure insertion efficiency and the small surface area of LUVs, the percentage of vesicles containing membrane-inserted, lipid-scrambling DNA nanostructures is expected to be significantly too low to be differentiated from the measurement error. Neither employing OPOE nor electroporation could remedy this circumstance significantly enough to observe scrambling activity in these bulk experiments. Nevertheless, the ease of working with LUVs allowed for the characterisation of multiple assay parameters which aided in optimising the protocols for subsequent experiments.

In Chapter 6, we introduced two ways to analyse the lipid scrambling activity of our DNA nanostructures despite their low insertion efficiency. With MD simulations of the 2C CP2 nanostructure we could directly study its interaction with the lipid bilayer when membrane-inserted. Electrostatic forces between the charged DNA and the hydrophilic lipid headgroups causes the lipids to rearrange forming a toroidal DNA-lipid pore. Stabilised by the DNA nanostructure, this toroidal lipid pore connects the two bilayer leaflets allowing lipids to diffusively translocate between the leaflets. Re-analysing previous MD simulations showed that lipid scrambling activity depends on the size of the DNA nanostructure (DNA duplex [8] vs. DNA origami porin [74]) while no scrambling activity is observed when a hydrophobic belt prevented the formation of a continuous toroidal pore [68, 231] (compare Section 6.3.1). We therefore suggest that any membrane-spanning DNA nanostructure (or hydrophilic object in general) induces lipid scrambling as long as it allows for the formation of a toroidal lipid pore whose shape will be the rate-determining factor of the scrambling activity.

Lastly, the simulations established a scrambling rate on the order of 10^7 lipids per second. This high scrambling rate could be explained by the low energy barrier of $\approx 1\ k_BT$ and the fact that the toroidal pore completely surrounds the DNA construct. In contrast, natural scramblases primarily facilitate lipid translocations through an aqueduct-like pathway, possibly requiring conformational changes, although the precise mechanisms are still unclear [120].

Adapting the dithionite assay to GUVs was a key experimental development to demonstrate the lipid scrambling ability of our 2C DNA nanostructure. Raising their chances for a single insertion per vesicle and directly observing the dithionite assay at the single-vesicle level were vital advantages. As 1C structures consistently did not scramble lipids, and proving with our synthesised NBD-PEG molecule that dithionite permeation into the vesicles had significantly slower kinetics, we could conclusively demonstrate the lipid scrambling activity of our 2C DNA structures. The experimentally measured scrambling rates and theoretical calculations both make the rates determined from MD simulations plausible, particularly taking

into consideration the low insertion efficiency of the DNA nanostructures. However, further experiments should employ higher dithionite or lower DNA concentrations to eventually enter a regime where the dithionite reduction is not rate-limiting providing further insight into the scrambling kinetics. Lastly, we demonstrated that our DNA scramblase can induce the surface exposure of PS-lipids in human cancer cells, a role in the apoptosis mechanism taken over by lipid scramblases. Future flow cytometry experiments can provide a more quantitative analysis of the lipid scrambling capabilities of our DNA scramblase in cells.

In summary, in this thesis we introduced a novel strategy to control cholesterol-mediated aggregation with the length of adjacent ssDNA overhangs. This allows for DNA nanostructures with increased number of hydrophobic tags while maintaining the close structure-function-relationship enabled by DNA nanotechnology. This will facilitate greater control in interfacing DNA nanostructures with lipid bilayers and cell membranes. The higher free energy gained from more membrane-anchored cholesterol groups could balance the energy penalty of DNA membrane penetration [74] which could potentially improve insertion efficiencies of DNA nanostructures, a long-standing problem in the field [47]. We envision that our easy-to-implement method will expand the design space of membrane-interfacing DNA nanosystems with applications in research and biomedicine.

We furthermore established an advanced protocol for the dithionite reduction assay that enables tracing of lipid scrambling activity at the single-vesicle level. Our designed DNA nanostructure can reproduce the biological function of a scramblase protein by mixing lipids that reside on opposite leaflets of a biological membrane *in vitro* and in human cells. Our synthetic DNA scramblase flips lipids much more rapidly, outperforming biological and reported artificial scramblases by several orders of magnitude. These exceptional rates are promoted by a stable DNA-induced toroidal lipid pore directly interconnecting the membrane leaflets without any substrate specificity or covalent bond formation.

Next steps will focus on gaining control over the scrambling activity by establishing an activation mechanism and design-specific rates. Modulating the toroidal pore will be key which could for example be achieved by using a single, membrane-spanning DNA duplex with internal modifications of varying hydrophobicity. Recent experiments in our group already showed that this is a promising approach to rationally design DNA scramblases with different rates. For biomedical applications we envision future designs to be equipped with a targeting mechanism for membranes of specific cell types. On demand, target cell-specific lipid scrambling could help patients suffering from impaired scrambling activity, or trigger phagocytic uptake of PS-exposing intruder cells by macrophages, including cells carrying cancer-specific plasma membrane antigens. As the mechanism of our DNA scramblase is independent of the cell-specific apoptosis pathways, it can be applied to a variety of cell

types. Control over lipid homeostasis with synthetic DNA nanostructures opens up a novel direction for designing personalised drugs and therapeutics for a variety of health conditions. Ultimately, the ability to outperform naturally evolved proteins allowed for a glimpse at the tremendous opportunities yet to be explored in nucleic acid-based nanotechnology.

Summary of key insights gained in this dissertation

- A DNA nanostructure design was devised that assembles under a range of Mg^{2+}-concentrations with the expected dimensions. The design provides an ideal balance between high assembly yield and versatile modification options.
- Aggregation of cholesterol-modified ssDNA is sequence-dependent while for DNA nanostructures, cholesterol number and modification position are the determining factors. Hydrophobically-mediated interactions can be controlled by the length of ssDNA overhangs adjacent to the hydrophobic groups allowing for an increased number of cholesterol tags per DNA nanostructure while preventing aggregation.
- Stable currents are induced by the spontaneous insertion of the 2C CP2 nanostructures in a lipid bilayer classifying them as 'DNA-built synthetic ion channels'. However, the insertion efficiency is very low. The bulk dithionite reduction assay using a fluorometer is optimised by using a lipid mixture of EColi:eggPC leading to more unilamellar vesicles. While cholesterol-modified DNA nanostructures attached to the vesicles, lipid scrambling was not detected, most likely due to their low insertion efficiency.
- MD simulations showed that the DNA construct induces a stable, toroidal DNA-lipid pore allowing lipids to rapidly diffuse between bilayer leaflets. By adapting the dithionite assay to GUVs, we experimentally demonstrated lipid scrambling activity of our 2C DNA scramblase. Both experiments and simulations support a lipid scrambling rate on the order of 10^7 lipids per second. This high rate is most likely explained by the low energy barrier of 1 k_BT for lipids to cross between bilayer leaflets and the fact that the toroidal pore completely surrounds the DNA nanostructure, which is in contrast to the mode of lipid flipping of natural lipid scramblase proteins. We thereby pioneered the use of DNA nanotechnology to create artificial lipid scramblases which can outperform synthetic and natural scramblases by several orders of magnitude.
- Future experiments should focus on controlling scrambling activity by modulating the size of the toroidal pore or by changing the hydrophilicity of the membrane-inserted region. With an activation mechanism and cell-targeting capabilities, synthetic DNA-built scramblases open up exciting opportunities for patient-specific therapeutics.

References

[1] R. P. Feynman. 'There's plenty of room at the bottom.' *California Institute of Technology, Engineering and Science Magazine*, 23(5):22–36 (1960). URL http://www.zyvex.com/nanotech/feynman.html.

[2] N. C. Seeman. 'Nucleic acid junctions and lattices.' *Journal of Theoretical Biology*, 99(2):237–247 (1982). doi:10.1016/0022-5193(82)90002-9.

[3] N. C. Seeman and H. F. Sleiman. 'DNA nanotechnology.' *Nature Reviews Materials*, 3:17068 (2017). doi:10.1038/natrevmats.2017.68.

[4] M. Vinther and J. Kjems. 'Interfacing DNA nanodevices with biology: Challenges, solutions and perspectives.' *New Journal of Physics*, 18(8):085005 (2016). doi:10.1088/1367-2630/18/8/085005.

[5] K. Göpfrich, I. Platzman, and J. P. Spatz. 'Mastering complexity: Towards bottom-up construction of multifunctional eukaryotic synthetic cells.' *Trends in Biotechnology*, 36(9):938–951 (2018). doi:10.1016/j.tibtech.2018.03.008.

[6] M. Langecker, V. Arnaut, T. G. Martin, J. List, S. Renner, M. Mayer, H. Dietz, and F. C. Simmel. 'Synthetic lipid membrane channels formed by designed DNA nanostructures.' *Science*, 338(6109):932–936 (2012). doi:10.1126/science.1225624.

[7] K. Göpfrich. 'Rational design of DNA-based lipid membrane pores.' *Ph.D. Thesis, University of Cambridge* (2016). doi:10.17863/CAM.15517.

[8] K. Göpfrich, C. Y. Li, I. Mames, S. P. Bhamidimarri, M. Ricci, J. Yoo, A. Mames, A. Ohmann, M. Winterhalter, E. Stulz *et al.* 'Ion channels made from a single membrane-spanning DNA duplex.' *Nano Letters*, 16(7):4665–4669 (2016). doi:10.1021/acs.nanolett.6b02039.

[9] M. S. Bretscher. 'Asymmetrical lipid bilayer structure for biological membranes.' *Nature New Biology*, 236(61):11–12 (1972). doi:10.1038/newbio236011a0.

[10] A. Castegna, C. M. Lauderback, H. Mohmmad-Abdul, and D. A. Butterfield. 'Modulation of phospholipid asymmetry in synaptosomal membranes by the lipid peroxidation products, 4-hydroxynonenal and acrolein: Implications for Alzheimer's disease.' *Brain Research*, 1004(1-2):193–197 (2004). doi:10.1016/j.brainres.2004.01.036.

[11] H. Mohmmad Abdul and D. A. Butterfield. 'Protection against amyloid beta-peptide (1–42)-induced loss of phospholipid asymmetry in synaptosomal membranes by tricyclodecan-9-xanthogenate (D609) and ferulic acid ethyl ester: Implications for Alzheimer's disease.'

Biochimica et Biophysica Acta (BBA) - Molecular Basis of Disease, 1741(1-2):140–148 (2005). doi:10.1016/j.bbadis.2004.12.002.

[12] S. K. Sahu, S. N. Gummadi, N. Manoj, and G. K. Aradhyam. 'Phospholipid scramblases: An overview.' *Archives of Biochemistry and Biophysics*, 462(1):103–114 (2007). doi:10.1016/j.abb.2007.04.002.

[13] P. F. Devaux, A. Herrmann, N. Ohlwein, and M. M. Kozlov. 'How lipid flippases can modulate membrane structure.' *Biochimica et Biophysica Acta - Biomembranes*, 1778(7-8):1591–1600 (2008). doi:10.1016/j.bbamem.2008.03.007.

[14] M. Malvezzi, M. Chalat, R. Janjusevic, A. Picollo, H. Terashima, A. K. Menon, and A. Accardi. 'Ca^{2+}-dependent phospholipid scrambling by a reconstituted TMEM16 ion channel.' *Nature Communications*, 4:2367 (2013). doi:10.1038/ncomms3367.

[15] I. Menon, T. Huber, S. Sanyal, S. Banerjee, P. Barré, S. Canis, J. D. Warren, J. Hwa, T. P. Sakmar, and A. K. Menon. 'Opsin is a phospholipid flippase.' *Current Biology*, 21(2):149–153 (2011). doi:10.1016/j.cub.2010.12.031.

[16] M. A. Goren, T. Morizumi, I. Menon, J. S. Joseph, J. S. Dittman, V. Cherezov, R. C. Stevens, O. P. Ernst, and A. K. Menon. 'Constitutive phospholipid scramblase activity of a G protein-coupled receptor.' *Nature Communications*, 5:5115 (2014). doi:10.1038/ncomms6115.

[17] G. Morra, A. M. Razavi, K. Pandey, H. Weinstein, A. K. Menon, and G. Khelashvili. 'Mechanisms of lipid scrambling by the G protein-coupled receptor opsin.' *Structure*, 26(2):356–367 (2018). doi:10.1016/j.str.2017.11.020.

[18] A. Zachowski. 'Phospholipids in animal eukaryotic membranes: Transverse asymmetry and movement.' *Biochemical Journal*, 294(1):1–14 (1993). doi:10.1042/bj2940001.

[19] E. M. Bevers, P. Comfurius, D. W. Dekkers, M. Harmsma, and R. F. A. Zwaal. 'Transmembrane phospholipid distribution in blood cells: Control mechanisms and pathophysiological significance.' *Biological Chemistry*, 379(8-9):973–986 (1998). URL https://europepmc.org/abstract/med/9792430.

[20] T. Pomorski, J. C. M. Holthuis, A. Herrmann, and G. van Meer. 'Tracking down lipid flippases and their biological functions.' *Journal of Cell Science*, 117(6):805–813 (2004). doi:10.1242/jcs.01055.

[21] K. Yu, J. M. Whitlock, K. Lee, E. A. Ortlund, Y. Y. Cui, and H. C. Hartzell. 'Identification of a lipid scrambling domain in ANO6/TMEM16F.' *eLife*, 4:e06901 (2015). doi:10.7554/eLife.06901.

[22] R. F. A. Zwaal, P. Comfurius, and E. M. Bevers. 'Scott syndrome, a bleeding disorder caused by defective scrambling of membrane phospholipids.' *Biochimica et Biophysica Acta - Molecular and Cell Biology of Lipids*, 1636(2-3):119–128 (2004). doi:10.1016/j.bbalip.2003.07.003.

[23] K. S. Ravichandran and U. Lorenz. 'Engulfment of apoptotic cells: Signals for a good meal.' *Nature Reviews Immunology*, 7(12):964–974 (2007). doi:10.1038/nri2214.

[24] J. C. McIntyre and R. G. Sleight. 'Fluorescence assay for phospholipid membrane asymmetry.' *Biochemistry*, 30(51):11819–11827 (1991). doi:10.1021/bi00115a012.

[25] S. Khalid, P. J. Bond, J. Holyoake, R. W. Hawtin, and M. S. P. Sansom. 'DNA and lipid bilayers: Self-assembly and insertion.' *Journal of the Royal Society Interface*, 5(Suppl.3):S241–S250 (2008). doi:10.1098/rsif.2008.0239.focus.

[26] J. D. Watson and F. H. C. Crick. 'Molecular structure of nucleic acids: A structure for deoxyribose nucleic acid.' *Nature*, 171(4356):737–738 (1953). doi:10.1038/171737a0.

[27] R. E. Franklin and R. G. Gosling. 'Molecular configuration in sodium thymonucleate.' *Nature*, 171(4356):740–741 (1953). doi:10.1038/171740a0.

[28] E. Benson, A. Mohammed, J. Gardell, S. Masich, E. Czeizler, P. Orponen, and B. Högberg. 'DNA rendering of polyhedral meshes at the nanoscale.' *Nature*, 523(7561):441–444 (2015). doi:10.1038/nature14586.

[29] N. C. Seeman. 'DNA in a material world.' *Nature*, 421(6921):427–431 (2003). doi:dv2cm8.

[30] P. W. K. Rothemund. 'Folding DNA to create nanoscale shapes and patterns.' *Nature*, 440(7082):297–302 (2006). doi:10.1038/nature04586.

[31] W. Bae, S. Kocabey, and T. Liedl. 'DNA nanostructures *in vitro*, *in vivo* and on membranes.' *Nano Today*, 26:98–107 (2019). doi:10.1016/j.nantod.2019.03.001.

[32] J. Chen and N. C. Seeman. 'Synthesis from DNA of a molecule with the connectivity of a cube.' *Nature*, 350(6319):631–633 (1991). doi:10.1038/350631a0.

[33] T. J. Fu and N. C. Seeman. 'DNA double-crossover molecules.' *Biochemistry*, 32(13):3211–3220 (1993). doi:10.1021/bi00064a003.

[34] W. M. Shih, J. D. Quispe, and G. F. Joyce. 'A 1.7-kilobase single-stranded DNA that folds into a nanoscale octahedron.' *Nature*, 427(6975):618–621 (2004). doi:10.1038/nature02307.

[35] S. M. Douglas, H. Dietz, T. Liedl, B. Högberg, F. Graf, and W. M. Shih. 'Self-assembly of DNA into nanoscale three-dimensional shapes.' *Nature*, 459(7245):414–418 (2009). doi:10.1038/nature08016.

[36] S. M. Douglas, A. H. Marblestone, S. Teerapittayanon, A. Vazquez, G. M. Church, and W. M. Shih. 'Rapid prototyping of 3D DNA-origami shapes with caDNAno.' *Nucleic Acids Research*, 37(15):5001–5006 (2009). doi:10.1093/nar/gkp436.

[37] C. E. Castro, F. Kilchherr, D. N. Kim, E. L. Shiao, T. Wauer, P. Wortmann, M. Bathe, and H. Dietz. 'A primer to scaffolded DNA origami.' *Nature Methods*, 8(3):221–229 (2011). doi:10.1038/nmeth.1570.

[38] J. N. Zadeh, C. D. Steenberg, J. S. Bois, B. R. Wolfe, M. B. Pierce, A. R. Khan, R. M. Dirks, and N. A. Pierce. 'NUPACK: Analysis and design of nucleic acid systems.' *Journal of Computational Chemistry*, 32(1):170–173 (2011). doi:10.1002/jcc.21596.

[39] T. E. Ouldridge, A. A. Louis, and J. P. K. Doye. 'Structural, mechanical, and thermodynamic properties of a coarse-grained DNA model.' *Journal of Chemical Physics*, 134(8):085101 (2011). doi:10.1063/1.3552946.

[40] B. E. K. Snodin, F. Randisi, M. Mosayebi, P. Šulc, J. S. Schreck, F. Romano, T. E. Ouldridge, R. Tsukanov, E. Nir, A. A. Louis *et al.* 'Introducing improved structural properties and salt dependence into a coarse-grained model of DNA.' *Journal of Chemical Physics*, 142(23):234901 (2015). doi:10.1063/1.4921957.

[41] R. Veneziano, S. Ratanalert, K. Zhang, F. Zhang, H. Yan, W. Chiu, and M. Bathe. 'Designer nanoscale DNA assemblies programmed from the top down.' *Science*, 352(6293):1534 (2016). doi:10.1126/science.aaf4388.

[42] J. Yoo, A. N. Sobh, C. Y. Li, and A. Aksimentiev. 'Cadnano to PDB file converter.' (2016). URL https://nanohub.org/resources/cadnanocvrt.

[43] P. Wang, T. A. Meyer, V. Pan, P. K. Dutta, and Y. Ke. 'The beauty and utility of DNA origami.' *Chem*, 2(3):359–382 (2017). doi:10.1016/j.chempr.2017.02.009.

[44] A. Samanta and I. L. Medintz. 'Nanoparticles and DNA – a powerful and growing functional combination in bionanotechnology.' *Nanoscale*, 8(17):9037–9095 (2016). doi:10.1039/c5nr08465b.

[45] N. V. Voigt, T. Tørring, A. Rotaru, M. F. Jacobsen, J. B. Ravnsbæk, R. Subramani, W. Mamdouh, J. Kjems, A. Mokhir, F. Besenbacher *et al.* 'Single-molecule chemical reactions on DNA origami.' *Nature Nanotechnology*, 5(3):200–203 (2010). doi:10.1038/NNANO.2010.5.

[46] G. Ke, M. Liu, S. Jiang, X. Qi, Y. R. Yang, S. Wootten, F. Zhang, Z. Zhu, Y. Liu, C. J. Yang *et al.* 'Directional regulation of enzyme pathways through the control of substrate channeling on a DNA origami scaffold.' *Angewandte Chemie - International Edition*, 55(26):7483–7486 (2016). doi:10.1002/anie.201603183.

[47] N. A. W. Bell and U. F. Keyser. 'Nanopores formed by DNA origami: A review.' *FEBS Letters*, 588(19):3564–3570 (2014). doi:10.1016/j.febslet.2014.06.013.

[48] J. J. Funke, P. Ketterer, C. Lieleg, S. Schunter, P. Korber, and H. Dietz. 'Uncovering the forces between nucleosomes using DNA origami.' *Science Advances*, 2(11):e1600974 (2016). doi:10.1126/sciadv.1600974.

[49] P. C. Nickels, B. Wünsch, P. Holzmeister, W. Bae, L. M. Kneer, D. Grohmann, P. Tinnefeld, and T. Liedl. 'Molecular force spectroscopy with a DNA origami-based nanoscopic force clamp.' *Science*, 354(6310):305–307 (2016). doi:10.1126/science.aah5974.

[50] J. Li, C. Fan, H. Pei, J. Shi, and Q. Huang. 'Smart drug delivery nanocarriers with self-assembled DNA nanostructures.' *Advanced Materials*, 25(32):4386–4396 (2013). doi:10.1002/adma.201300875.

[51] Y. J. Chen, B. Groves, R. A. Muscat, and G. Seelig. 'DNA nanotechnology from the test tube to the cell.' *Nature Nanotechnology*, 10(9):748–760 (2015). doi:10.1038/nnano.2015.195.

[52] F. Hong, F. Zhang, Y. Liu, and H. Yan. 'DNA origami: Scaffolds for creating higher order structures.' *Chemical Reviews*, 117(20):12584–12640 (2017). doi:10.1021/acs.chemrev.6b00825.

[53] B. Wei, M. Dai, and P. Yin. 'Complex shapes self-assembled from single-stranded DNA tiles.' *Nature*, 485(7400):623–626 (2012). doi:10.1038/nature11075.

[54] K. Göpfrich, T. Zettl, A. E. C. Meijering, S. Hernández-Ainsa, S. Kocabey, T. Liedl, and U. F. Keyser. 'DNA-tile structures induce ionic currents through lipid membranes.' *Nano Letters*, 15(5):3134–3138 (2015). doi:10.1021/acs.nanolett.5b00189.

[55] T. G. Martin and H. Dietz. 'Magnesium-free self-assembly of multi-layer DNA objects.' *Nature Communications*, 3:1103 (2012). doi:10.1038/ncomms2095.

[56] S. M. Douglas. 'DNA origami folding animation.' (2011). URL https://www.youtube.com/watch?v=p4C_aFlyhfI.

[57] A. Ohmann. 'Establishing a method to couple a defined number of Kinesin-1 motors to a cargo using DNA origami.' *Diploma Thesis, Technische Universität Dresden* (2014).

[58] A. Shaw, E. Benson, and B. Högberg. 'Purification of functionalized DNA origami nanostructures.' *ACS Nano*, 9(5):4968–4975 (2015). doi:10.1021/nn507035g.

[59] H. Bila, E. E. Kurisinkal, and M. M. C. Bastings. 'Engineering a stable future for DNA-origami as a biomaterial.' *Biomaterials Science*, 7(2):532–541 (2019). doi:10.1039/c8bm01249k.

[60] H. Shen, Y. Wang, J. Wang, Z. Li, and Q. Yuan. 'Emerging biomimetic applications of DNA nanotechnology.' *ACS Applied Materials & Interfaces*, 11(15):13859–13873 (2019). doi:10.1021/acsami.8b06175.

[61] E. Pozharski and R. C. MacDonald. 'Thermodynamics of cationic lipid-DNA complex formation as studied by isothermal titration calorimetry.' *Biophysical Journal*, 83(1):556–565 (2002). doi:10.1016/S0006-3495(02)75191-6.

[62] J. J. McManus, J. O. Rädler, and K. A. Dawson. 'Does calcium turn a zwitterionic lipid cationic?' *Journal of Physical Chemistry B*, 107(36):9869–9875 (2003). doi:10.1021/jp034463d.

[63] S. Gromelski and G. Brezesinski. 'DNA condensation and interaction with zwitterionic phospholipids mediated by divalent cations.' *Langmuir*, 22(14):6293–6301 (2006). doi:10.1021/la0531796.

[64] M. Langecker, V. Arnaut, J. List, and F. C. Simmel. 'DNA nanostructures interacting with lipid bilayer membranes.' *Accounts of Chemical Research*, 47(6):1807–1815 (2014). doi:10.1021/ar500051r.

[65] S. Hernández-Ainsa, M. Ricci, L. Hilton, A. Aviñó, R. Eritja, and U. F. Keyser. 'Controlling the reversible assembly of liposomes through a multistimuli responsive anchored DNA.' *Nano Letters*, 16(7):4462–4466 (2016). doi:10.1021/acs.nanolett.6b01618.

[66] J. R. Burns, K. Göpfrich, J. W. Wood, V. V. Thacker, E. Stulz, U. F. Keyser, and S. Howorka. 'Lipid-bilayer-spanning DNA nanopores with a bifunctional porphyrin anchor.' *Angewandte Chemie - International Edition*, 52(46):12069–12072 (2013). doi:10.1002/anie.201305765.

[67] A. Seifert, K. Göpfrich, J. R. Burns, N. Fertig, U. F. Keyser, and S. Howorka. 'Bilayer-spanning DNA nanopores with voltage-switching between open and closed state.' *ACS Nano*, 9(2):1117–1126 (2015). doi:10.1021/nn5039433.

[68] J. R. Burns, E. Stulz, and S. Howorka. 'Self-assembled DNA nanopores that span lipid bilayers.' *Nano Letters*, 13(6):2351–2356 (2013). doi:10.1021/nl304147f.

[69] J. R. Burns, N. Al-Juffali, S. M. Janes, and S. Howorka. 'Membrane-spanning DNA nanopores with cytotoxic effect.' *Angewandte Chemie - International Edition*, 53(46):12466–12470 (2014). doi:10.1002/anie.201405719.

[70] S. Krishnan, D. Ziegler, V. Arnaut, T. G. Martin, K. Kapsner, K. Henneberg, A. R. Bausch, H. Dietz, and F. C. Simmel. 'Molecular transport through large-diameter DNA nanopores.' *Nature Communications*, 7:12787 (2016). doi:10.1038/ncomms12787.

[71] L. Parolini, B. M. Mognetti, J. Kotar, E. Eiser, P. Cicuta, and L. Di Michele. 'Volume and porosity thermal regulation in lipid mesophases by coupling mobile ligands to soft membranes.' *Nature Communications*, 6:5948 (2015). doi:10.1038/ncomms6948.

[72] J. R. Burns, A. Seifert, N. Fertig, and S. Howorka. 'A biomimetic DNA-based channel for the ligand-controlled transport of charged molecular cargo across a biological membrane.' *Nature Nanotechnology*, 11(2):152–156 (2016). doi:10.1038/nnano.2015.279.

[73] L. Messager, J. R. Burns, J. Kim, D. Cecchin, J. Hindley, A. L. B. Pyne, J. Gaitzsch, G. Battaglia, and S. Howorka. 'Biomimetic hybrid nanocontainers with selective permeability.' *Angewandte Chemie - International Edition*, 55(37):11106–11109 (2016). doi:10.1002/anie.201604677.

[74] K. Göpfrich, C. Y. Li, M. Ricci, S. P. Bhamidimarri, J. Yoo, B. Gyenes, A. Ohmann, M. Winterhalter, A. Aksimentiev, and U. F. Keyser. 'Large-conductance transmembrane porin made from DNA origami.' *ACS Nano*, 10(9):8207–8214 (2016). doi:10.1021/acsnano.6b03759.

[75] A. Ohmann, C. Y. Li, C. Maffeo, K. Al Nahas, K. N. Baumann, K. Göpfrich, J. Yoo, U. F. Keyser, and A. Aksimentiev. 'A synthetic enzyme built from DNA flips 10^7 lipids per second in biological membranes.' *Nature Communications*, 9:2426 (2018). doi:10.1038/s41467-018-04821-5.

[76] A. Czogalla, D. J. Kauert, H. G. Franquelim, V. Uzunova, Y. Zhang, R. Seidel, and P. Schwille. 'Amphipathic DNA origami nanoparticles to scaffold and deform lipid membrane vesicles.' *Angewandte Chemie - International Edition*, 54(22):6501–6505 (2015). doi:10.1002/anie.201501173.

[77] H. G. Franquelim, A. Khmelinskaia, J. P. Sobczak, H. Dietz, and P. Schwille. 'Membrane sculpting by curved DNA origami scaffolds.' *Nature Communications*, 9:811 (2018). doi:10.1038/s41467-018-03198-9.

[78] O. Birkholz, J. R. Burns, C. P. Richter, O. E. Psathaki, S. Howorka, and J. Piehler. 'Multifunctional DNA nanostructures that puncture and remodel lipid membranes into hybrid materials.' *Nature Communications*, 9:1521 (2018). doi:10.1038/s41467-018-02905-w.

[79] J. R. Burns and S. Howorka. 'Structural and functional stability of DNA nanopores in biological media.' *Nanomaterials*, 9(4):490 (2019). doi:10.3390/nano9040490.

[80] J. List, M. Weber, and F. C. Simmel. 'Hydrophobic actuation of a DNA origami bilayer structure.' *Angewandte Chemie - International Edition*, 53(16):4236–4239 (2014). doi:10.1002/anie.201310259.

[81] A. Johnson-Buck, S. Jiang, H. Yan, and N. G. Walter. 'DNA-cholesterol barges as programmable membrane-exploring agents.' *ACS Nano*, 8(6):5641–5649 (2014). doi:10/f58jz4.

[82] A. Czogalla, H. G. Franquelim, and P. Schwille. 'DNA nanostructures on membranes as tools for synthetic biology.' *Biophysical Journal*, 110(8):1698–1707 (2016). doi:10/f8j655.

[83] A. Khmelinskaia, H. G. Franquelim, E. P. Petrov, and P. Schwille. 'Effect of anchor positioning on binding and diffusion of elongated 3D DNA nanostructures on lipid membranes.' *Journal of Physics D: Applied Physics*, 49(19):194001 (2016). doi:10.1088/0022-3727/49/19/194001.

[84] A. Khmelinskaia, J. Mücksch, E. P. Petrov, H. G. Franquelim, and P. Schwille. 'Control of membrane binding and diffusion of cholesteryl-modified DNA origami nanostructures by DNA spacers.' *Langmuir*, 34(49):14921–14931 (2018). doi:10.1021/acs.langmuir.8b01850.

[85] K. Jahnke, M. Weiss, C. Frey, S. Antona, J. W. Janiesch, I. Platzman, K. Göpfrich, and J. P. Spatz. 'Programmable functionalization of surfactant-stabilized microfluidic droplets via DNA-tags.' *Advanced Functional Materials*, 29(23):1808647 (2019). doi:10.1002/adfm.201808647.

[86] A. Lopez and J. Liu. 'DNA oligonucleotide-functionalized liposomes: Bioconjugate chemistry, biointerfaces, and applications.' *Langmuir*, 34(49):15000–15013 (2018). doi:10/c9cq.

[87] Z. Cao, R. Tong, A. Mishra, W. Xu, G. C. L. Wong, J. Cheng, and Y. Lu. 'Reversible cell-specific drug delivery with aptamer-functionalized liposomes.' *Angewandte Chemie - International Edition*, 48(35):6494–6498 (2009). doi:10.1002/anie.200901452.

[88] F. He, H. Liu, X. Guo, B. C. Yin, and B. C. Ye. 'Direct exosome quantification via bivalent-cholesterol-labeled DNA anchor for signal amplification.' *Analytical Chemistry*, 89(23):12968–12975 (2017). doi:10.1021/acs.analchem.7b03919.

[89] Y. Yang, J. Wang, H. Shigematsu, W. Xu, W. M. Shih, J. E. Rothman, and C. Lin. 'Self-assembly of size-controlled liposomes on DNA nanotemplates.' *Nature Chemistry*, 8(5):476–483 (2016). doi:10.1038/nchem.2472.

[90] Z. Zhang, Y. Yang, F. Pincet, M. C. Llaguno, and C. Lin. 'Placing and shaping liposomes with reconfigurable DNA nanocages.' *Nature Chemistry*, 9(7):653–659 (2017). doi:10.1038/nchem.2802.

[91] G. Stengel, R. Zahn, and F. Höök. 'DNA-induced programmable fusion of phospholipid vesicles.' *Journal of the American Chemical Society*, 129(31):9584–9585 (2007). doi:10.1021/ja073200k.

[92] W. Xu, J. Wang, J. E. Rothman, and F. Pincet. 'Accelerating SNARE-mediated membrane fusion by DNA-lipid tethers.' *Angewandte Chemie - International Edition*, 54(48):14388–14392 (2015). doi:10.1002/anie.201506844.

[93] P. M. Arnott and S. Howorka. 'A temperature-gated nanovalve self-assembled from DNA to control molecular transport across membranes.' *ACS Nano*, 13(3):3334–3340 (2019). doi:10.1021/acsnano.8b09200.

[94] B. Alberts, A. Johnson, J. Lewis, M. Raff, K. Roberts, and P. Walter. *Molecular biology of the cell*. Garland Science, New York, 5th edition (2008).

[95] J. Suzuki, M. Umeda, P. J. Sims, and S. Nagata. 'Calcium-dependent phospholipid scrambling by TMEM16F.' *Nature*, 468(7325):834–840 (2010). doi:10.1038/nature09583.

[96] R. D. Kornberg and H. M. McConnell. 'Inside-outside transitions of phospholipids in vesicle membranes.' *Biochemistry*, 10(7):1111–1120 (1971). doi:10.1021/bi00783a003.

[97] T. G. Pomorski and A. K. Menon. 'Lipid somersaults: Uncovering the mechanisms of protein-mediated lipid flipping.' *Progress in Lipid Research*, 64:69–84 (2016). doi:10/f9h8wm.

[98] R. M. Epand and J. M. Ruysschaert. *The biophysics of cell membranes: Biological consequences*, volume 19. Springer Series in Biophysics, Springer Nature, Singapore (2017). doi:10.1007/978-981-10-6244-5.

[99] F. X. Contreras, L. Sánchez-Magraner, A. Alonso, and F. M. Goñi. 'Transbilayer (flip-flop) lipid motion and lipid scrambling in membranes.' *FEBS Letters*, 584(9):1779–1786 (2010). doi:10.1016/j.febslet.2009.12.049.

[100] M. R. Clark. 'Flippin' lipids.' *Nature Immunology*, 12(5):373–375 (2011). doi:10.1038/ni.2024.

[101] K. Segawa and S. Nagata. 'An apoptotic 'Eat Me' signal: Phosphatidylserine exposure.' *Trends in Cell Biology*, 25(11):639–650 (2015). doi:10.1016/j.tcb.2015.08.003.

[102] G. van Meer, D. R. Voelker, and G. W. Feigenson. 'Membrane lipids: Where they are and how they behave.' *Nature Reviews Molecular Cell Biology*, 9(2):112–124 (2008). doi:10.1038/nrm2330.

[103] V. A. Fadok, D. R. Voelker, P. A. Campbell, J. J. Cohen, D. L. Bratton, and P. M. Henson. 'Exposure of phosphatidylserine on the surface of apoptotic lymphocytes triggers specific recognition and removal by macrophages.' *Journal of Immunology*, 148(7):2207–2216 (1992). URL http://www.jimmunol.org/content/148/7/2207.

[104] B. R. Lentz. 'Exposure of platelet membrane phosphatidylserine regulates blood coagulation.' *Progress in Lipid Research*, 42(5):423–438 (2003). doi:10.1016/S0163-7827(03)00025-0.

[105] S. M. van den Eijnde, M. J. B. van den Hoff, C. P. M. Reutelingsperger, W. L. van Heerde, M. E. R. Henfling, C. Vermeij-Keers, B. Schutte, M. Borgers, and F. C. S. Ramaekers. 'Transient expression of phosphatidylserine at cell-cell contact areas is required for myotube formation.' *Journal of Cell Science*, 114(20):3631–3642 (2001). URL https://jcs.biologists.org/content/114/20/3631.article-info.

[106] H. W. A. Ehlen, M. Chinenkova, M. Moser, H. M. Munter, Y. Krause, S. Gross, B. Brachvogel, M. Wuelling, U. Kornak, and A. Vortkamp. 'Inactivation of Anoctamin-6/TMEM16F, a regulator of phosphatidylserine scrambling in osteoblasts, leads to decreased mineral deposition in skeletal tissues.' *Journal of Bone and Mineral Research*, 28(2):246–259 (2013). doi:10.1002/jbmr.1751.

[107] J. Ousingsawat, P. Wanitchakool, R. Schreiber, M. Wuelling, A. Vortkamp, and K. Kunzelmann. 'Anoctamin-6 controls bone mineralization by activating the calcium transporter NCX1.' *Journal of Biological Chemistry*, 290(10):6270–6280 (2015). doi:10.1074/jbc.M114.602979.

[108] L. A. Barber, M. B. Palascak, C. H. Joiner, and R. S. Franco. 'Aminophospholipid translocase and phospholipid scramblase activities in sickle erythrocyte subpopulations.' *British Journal of Haematology*, 146(4):447–455 (2009). doi:10.1111/j.1365-2141.2009.07760.x.

[109] T. Lhermusier, H. Chap, and B. Payrastre. 'Platelet membrane phospholipid asymmetry: From the characterization of a scramblase activity to the identification of an essential protein mutated in Scott syndrome.' *Journal of Thrombosis and Haemostasis*, 9(10):1883–1891 (2011). doi:10.1111/j.1538-7836.2011.04478.x.

[110] J. Rosing, E. M. Bevers, P. Comfurius, H. C. Hemker, G. van Dieijen, H. J. Weiss, and R. F. A. Zwaal. 'Impaired factor X and prothrombin activation associated with decreased phosopholipid exposure in platelets from a patient with a bleeding disorder.' *Blood*, 65(6):1557–1561 (1985). URL http://www.bloodjournal.org/content/65/6/1557.

[111] J. D. Brunner, N. K. Lim, S. Schenck, A. Duerst, and R. Dutzler. 'X-ray structure of a calcium-activated TMEM16 lipid scramblase.' *Nature*, 516(7530):207–212 (2014). doi:10.1038/nature13984.

[112] W. Humphrey, A. Dalke, and K. Schulten. 'VMD: Visual molecular dynamics.' *Journal of Molecular Graphics*, 14(1):33–38 (1996). doi:10.1016/0263-7855(96)00018-5.

[113] H. M. Berman, J. Westbrook, Z. Feng, G. Gilliland, T. N. Bhat, H. Weissig, I. N. Shindyalov, and P. E. Bourne. 'The protein data bank.' *Nucleic Acids Research*, 28(1):235–242 (2000). doi:10.1093/nar/28.1.235.

[114] J. Suzuki, T. Fujii, T. Imao, K. Ishihara, H. Kuba, and S. Nagata. 'Calcium-dependent phospholipid scramblase activity of TMEM 16 protein family members.' *Journal of Biological Chemistry*, 288(19):13305–13316 (2013). doi:10.1074/jbc.M113.457937.

[115] M. Malvezzi, K. K. Andra, K. Pandey, B. C. Lee, M. E. Falzone, A. Brown, R. Iqbal, A. K. Menon, and A. Accardi. 'Out-of-the-groove transport of lipids by TMEM16 and GPCR scramblases.' *Proceedings of the National Academy of Sciences*, 115(30):E7033–E7042 (2018). doi:10.1073/pnas.1806721115.

[116] E. Castoldi, P. W. Collins, P. L. Williamson, and E. M. Bevers. 'Compound heterozygosity for 2 novel TMEM16F mutations in a patient with Scott syndrome.' *Blood*, 117(16):4399–4400 (2011). doi:10.1182/blood-2011-01-332502.

[117] H. Yang, A. Kim, T. David, D. Palmer, T. Jin, J. Tien, F. Huang, T. Cheng, S. R. Coughlin, Y. N. Jan *et al.* 'TMEM16F forms a Ca^{2+}-activated cation channel required for lipid scrambling in platelets during blood coagulation.' *Cell*, 151(1):111–122 (2012). doi:10.1016/j.cell.2012.07.036.

[118] S. Grubb, K. A. Poulsen, C. A. Juul, T. Kyed, T. K. Klausen, E. H. Larsen, and E. K. Hoffmann. 'TMEM16F (Anoctamin 6), an anion channel of delayed Ca^{2+} activation.' *Journal of General Physiology*, 141(5):585–600 (2013). doi:10.1085/jgp.201210861.

[119] L. K. Schenk, U. Schulze, S. Henke, T. Weide, and H. Pavenstädt. 'TMEM16F regulates baseline phosphatidylserine exposure and cell viability in human embryonic kidney cells.' *Cellular Physiology and Biochemistry*, 38(6):2452–2463 (2016). doi:10.1159/000445596.

[120] M. E. Falzone, M. Malvezzi, B. C. Lee, and A. Accardi. 'Known structures and unknown mechanisms of TMEM16 scramblases and channels.' *Journal of General Physiology*, 150(7):933–947 (2018). doi:10.1085/jgp.201711957.

[121] R. Watanabe, T. Sakuragi, H. Noji, and S. Nagata. 'Single-molecule analysis of phospholipid scrambling by TMEM16F.' *Proceedings of the National Academy of Sciences*, 115(12):3066–3071 (2018). doi:10.1073/pnas.1717956115.

[122] R. J. C. Gilbert, M. D. Serra, C. J. Froelich, M. I. Wallace, and G. Anderluh. 'Membrane pore formation at protein-lipid interfaces.' *Trends in Biochemical Sciences*, 39(11):510–516 (2014). doi:10.1016/j.tibs.2014.09.002.

[123] S. S. Metkar, B. Wang, E. Catalan, G. Anderluh, R. J. C. Gilbert, J. Pardo, and C. J. Froelich. 'Perforin rapidly induces plasma membrane phospholipid flip-flop.' *PLoS ONE*, 6(9):e24286 (2011). doi:10.1371/journal.pone.0024286.

[124] M. A. Kol, A. van Dalen, A. I. P. M. de Kroon, and B. de Kruijff. 'Translocation of phospholipids is facilitated by a subset of membrane-spanning proteins of the bacterial cytoplasmic membrane.' *Journal of Biological Chemistry*, 278(27):24586–24593 (2003). doi:10.1074/jbc.M301875200.

[125] M. Langer, R. Sah, A. Veser, M. Gütlich, and D. Langosch. 'Structural properties of model phosphatidylcholine flippases.' *Chemistry & Biology*, 20(1):63–72 (2013). doi:10.1016/j.chembiol.2012.11.006.

[126] T. Pomorski and A. K. Menon. 'Lipid flippases and their biological functions.' *Cellular and Molecular Life Sciences*, 63(24):2908–2921 (2006). doi:10.1007/s00018-006-6167-7.

[127] A. Ballesteros and K. J. Swartz. 'Lipids surf the groove in scramblases.' *Proceedings of the National Academy of Sciences*, 115(30):7648–7650 (2018). doi:10.1073/pnas.1809472115.

[128] J. M. Whitlock and H. C. Hartzell. 'A pore idea: The ion conduction pathway of TMEM16/ANO proteins is composed partly of lipid.' *Pflügers Archiv - European Journal of Physiology*, 468(3):455–473 (2016). doi:10.1007/s00424-015-1777-2.

[129] T. Jiang, K. Yu, H. C. Hartzell, and E. Tajkhorshid. 'Lipids and ions traverse the membrane by the same physical pathway in the nhTMEM16 scramblase.' *eLife*, 6:e28671 (2017). doi:10.7554/eLife.28671.

[130] S. Feng, S. Dang, T. W. Han, W. Ye, P. Jin, T. Cheng, J. Li, Y. N. Jan, L. Y. Jan, and Y. Cheng. 'Cryo-EM studies of TMEM16F calcium-activated ion channel suggest features important for lipid scrambling.' *Cell Reports*, 28(2):567–579.e4 (2019). doi:10.1016/j.celrep.2019.06.023.

[131] J. M. Boon, T. N. Lambert, A. L. Sisson, A. P. Davis, and B. D. Smith. 'Facilitated phosphatidylserine (PS) flip-flop and thrombin activation using a synthetic PS scramblase.' *Journal of the American Chemical Society*, 125(27):8195–8201 (2003). doi:10.1021/ja029670q.

[132] H. Nakao, K. Ikeda, Y. Ishihama, and M. Nakano. 'Membrane-spanning sequences in endoplasmic reticulum proteins promote phospholipid flip-flop.' *Biophysical Journal*, 110(12):2689–2697 (2016). doi:10.1016/j.bpj.2016.05.023.

[133] P. F. Devaux, P. Fellmann, and P. Hervé. 'Investigation on lipid asymmetry using lipid probes: Comparison between spin-labeled lipids and fluorescent lipids.' *Chemistry and Physics of Lipids*, 116(1-2):115–134 (2002). doi:10.1016/S0009-3084(02)00023-3.

[134] D. Marquardt, F. A. Heberle, T. Miti, B. Eicher, E. London, J. Katsaras, and G. Pabst. '^{1}H NMR shows slow phospholipid flip-flop in gel and fluid bilayers.' *Langmuir*, 33(15):3731–3741 (2017). doi:10.1021/acs.langmuir.6b04485.

[135] M. Doktorova, F. A. Heberle, D. Marquardt, R. Rusinova, R. L. Sanford, T. A. Peyear, J. Katsaras, G. W. Feigenson, H. Weinstein, and O. S. Andersen. 'Gramicidin increases lipid flip-flop in symmetric and asymmetric lipid vesicles.' *Biophysical Journal*, 116(5):860–873 (2019). doi:10.1016/j.bpj.2019.01.016.

[136] R. G. Sleight and R. E. Pagano. 'Transport of a fluorescent phosphatidylcholine analog from the plasma membrane to the Golgi apparatus.' *Journal of Cell Biology*, 99(2):742–751 (1984). doi:10.1083/jcb.99.2.742.

[137] K. Matsuzaki, O. Murase, N. Fujii, and K. Miyajima. 'An antimicrobial peptide, magainin 2, induced rapid flip-flop of phospholipids coupled with pore formation and peptide translocation.' *Biochemistry*, 35(35):11361–11368 (1996). doi:10.1021/bi960016v.

[138] Q. L. Chang, S. N. Gummadi, and A. K. Menon. 'Chemical modification identifies two populations of glycerophospholipid flippase in rat liver ER.' *Biochemistry*, 43(33):10710–10718 (2004). doi:10.1021/bi049063a.

[139] K. John, S. Schreiber, J. Kubelt, A. Herrmann, and P. Müller. 'Transbilayer movement of phospholipids at the main phase transition of lipid membranes: Implications for rapid flip-flop in biological membranes.' *Biophysical Journal*, 83(6):3315–3323 (2002). doi:10.1016/S0006-3495(02)75332-0.

[140] C. Angeletti and J. W. Nichols. 'Dithionite quenching rate measurement of the inside-outside membrane bilayer distribution of 7-nitrobenz-2-oxa-1,3-diazol-4-yl-labeled phospholipids.' *Biochemistry*, 37(43):15114–15119 (1998). doi:10.1021/bi9810104.

[141] A. Bhalla, M. C. Chicka, W. C. Tucker, and E. R. Chapman. 'Ca^{2+}-synaptotagmin directly regulates t-SNARE function during reconstituted membrane fusion.' *Nature Structural & Molecular Biology*, 13(4):323–330 (2006). doi:10.1038/nsmb1076.

[142] S. Haldar and A. Chattopadhyay. 'Application of NBD-labeled lipids in membrane and cell biology.' In Y. Mély and G. Duportail (eds.), 'Fluorescent methods to study biological membranes. Springer Series on Fluorescence (Methods and Applications),' volume 13, pp. 37–50. Springer, Berlin, Heidelberg (2012). doi:10.1007/4243_2012_43.

[143] A. Chattopadhyay and E. London. 'Parallax method for direct measurement of membrane penetration depth utilizing fluorescence quenching by spin-labeled phospholipids.' *Biochemistry*, 26(1):39–45 (1987). doi:10.1021/bi00375a006.

[144] A. Chattopadhyay. 'Chemistry and biology of N-(7-nitrobenz-2-oxa-1,3-diazol-4-yl)-labeled lipids: Fluorescent probes of biological and model membranes.' *Chemistry and Physics of Lipids*, 53(1):1–15 (1990). doi:10.1016/0009-3084(90)90128-E.

[145] I. Sarkar and A. K. Mishra. 'Fluorophore tagged bio-molecules and their applications: A brief review.' *Applied Spectroscopy Reviews*, 53(7):552–601 (2018). doi:10/c9b7.

[146] E. Fattal, S. Nir, R. A. Parente, and F. C. Szoka Jr. 'Pore-forming peptides induce rapid phospholipid flip-flop in membranes.' *Biochemistry*, 33(21):6721–6731 (1994). doi:10.1021/bi00187a044.

[147] A. Pluen, P. A. Netti, R. K. Jain, and D. A. Berk. 'Diffusion of macromolecules in agarose gels: Comparison of linear and globular configurations.' *Biophysical Journal*, 77(1):542–552 (1999). doi:10.1016/S0006-3495(99)76911-0.

[148] D. L. Holmes and N. C. Stellwagen. 'Estimation of polyacrylamide gel pore size from Ferguson plots of linear DNA fragments. II. Comparison of gels with different crosslinker concentrations, added agarose and added linear polyacrylamide.' *Electrophoresis*, 12(9):612–619 (1991). doi:10.1002/elps.1150120903.

[149] N. C. Stellwagen. 'Apparent pore size of polyacrylamide gels: Comparison of gels cast and run in Tris-acetate-EDTA and Tris-borate-EDTA buffers.' *Electrophoresis*, 19(10):1542–1547 (1998). doi:10.1002/elps.1150191004.

[150] J. Schindelin, I. Arganda-Carreras, E. Frise, V. Kaynig, M. Longair, T. Pietzsch, S. Preibisch, C. Rueden, S. Saalfeld, B. Schmid *et al.* 'Fiji: An open-source platform for biological-image analysis.' *Nature Methods*, 9(7):676–682 (2012). doi:10.1038/nmeth.2019.

[151] D. Nečas and P. Klapetek. 'Gwyddion: An open-source software for SPM data analysis.' *Central European Journal of Physics*, 10(1):181–188 (2012). doi:10.2478/s11534-011-0096-2.

[152] F. C. Simmel and W. U. Dittmer. 'DNA nanodevices.' *Small*, 1(3):284–299 (2005). doi:10.1002/smll.200400111.

[153] S. Fischer, C. Hartl, K. Frank, J. O. Rädler, T. Liedl, and B. Nickel. 'Shape and interhelical spacing of DNA origami nanostructures studied by small-angle X-ray scattering.' *Nano Letters*, 16(7):4282–4287 (2016). doi:10.1021/acs.nanolett.6b01335.

[154] R. D. Shannon. 'Revised effective ionic radii and systematic studies of interatomic distances in halides and chalcogenides.' *Acta Crystallographica Section A*, 32(5):751–767 (1976). doi:10.1107/S0567739476001551.

[155] Y. Marcus. 'Ionic radii in aqueous solutions.' *Chemical Reviews*, 88(8):1475–1498 (1988). doi:10.1021/cr00090a003.

[156] C. Maffeo, B. Luan, and A. Aksimentiev. 'End-to-end attraction of duplex DNA.' *Nucleic Acids Research*, 40(9):3812–3821 (2012). doi:10.1093/nar/gkr1220.

[157] F. Kilchherr, C. Wachauf, B. Pelz, M. Rief, M. Zacharias, and H. Dietz. 'Single-molecule dissection of stacking forces in DNA.' *Science*, 353(6304):aaf5508 (2016). doi:10.1126/science.aaf5508.

[158] X. Qiu, K. Andresen, L. W. Kwok, J. S. Lamb, H. Y. Park, and L. Pollack. 'Inter-DNA attraction mediated by divalent counterions.' *Physical Review Letters*, 99(3):038104 (2007). doi:10.1103/PhysRevLett.99.038104.

[159] R. F. Brown, C. T. Andrews, and A. H. Elcock. 'Stacking free energies of all DNA and RNA nucleoside pairs and dinucleoside-monophosphates computed using recently revised AMBER parameters and compared with experiment.' *Journal of Chemical Theory and Computing*, 11(5):2315–2328 (2015). doi:10.1021/ct501170h.

[160] D. C. Harris. *Quantitative chemical analysis*. W.H. Freeman, New York, 9th edition (2015).

[161] J. Zhai and E. Bakker. 'Complexometric titrations: New reagents and concepts to overcome old limitations.' *Analyst*, 141(14):4252–4261 (2016). doi:10.1039/c6an00538a.

[162] A. Kuzuya, Y. Sakai, T. Yamazaki, Y. Xu, and M. Komiyama. 'Nanomechanical DNA origami 'single-molecule beacons' directly imaged by atomic force microscopy.' *Nature Communications*, 2:449 (2011). doi:10.1038/ncomms1452.

[163] G. Tikhomirov, P. Petersen, and L. Qian. 'Fractal assembly of micrometre-scale DNA origami arrays with arbitrary patterns.' *Nature*, 552(7683):67–71 (2017). doi:10.1038/nature24655.

[164] J. S. Villarrubia. 'Algorithms of scanned probe microscope image simulation, surface reconstruction, and tip estimation.' *Journal of Research of the National Institute of Standards and Technology*, 102(4):425–454 (1997). doi:10.6028/jres.102.030.

[165] F. Moreno-Herrero, J. Colchero, and A. M. Baró. 'DNA height in scanning force microscopy.' *Ultramicroscopy*, 96(2):167–174 (2003). doi:10.1016/S0304-3991(03)00004-4.

[166] Y. Ke, S. M. Douglas, M. Liu, J. Sharma, A. Cheng, A. Leung, Y. Liu, W. M. Shih, and H. Yan. 'Multilayer DNA origami packed on a square lattice.' *Journal of the American Chemical Society*, 131(43):15903–15908 (2009). doi:10.1021/ja906381y.

[167] H. Dietz, S. M. Douglas, and W. M. Shih. 'Folding DNA into twisted and curved nanoscale shapes.' *Science*, 325(5941):725–730 (2009). doi:10.1126/science.1174251.

[168] X. C. Bai, T. G. Martin, S. H. W. Scheres, and H. Dietz. 'Cryo-EM structure of a 3D DNA-origami object.' *Proceedings of the National Academy of Sciences*, 109(49):20012–20017 (2012). doi:10.1073/pnas.1215713109.

[169] C. R. Zobel and M. Beer. 'Electron stains. I. Chemical studies on the interaction of DNA with uranyl salts.' *Journal of Cell Biology*, 10(3):335–346 (1961). doi:10.1083/jcb.10.3.335.

[170] J. R. Burns and S. Howorka. 'Defined bilayer interactions of DNA nanopores revealed with a nuclease-based nanoprobe strategy.' *ACS Nano*, 12(4):3263–3271 (2018). doi:10.1021/acsnano.7b07835.

[171] W. L. Whitehouse, J. E. Noble, M. G. Ryadnov, and S. Howorka. 'Cholesterol anchors enable efficient binding and intracellular uptake of DNA nanostructures.' *Bioconjugate Chemistry*, 30(7):1836–1844 (2019). doi:10.1021/acs.bioconjchem.9b00036.

[172] S. Kocabey, S. Kempter, J. List, Y. Xing, W. Bae, D. Schiffels, W. M. Shih, F. C. Simmel, and T. Liedl. 'Membrane-assisted growth of DNA origami nanostructure arrays.' *ACS Nano*, 9(4):3530–3539 (2015). doi:10.1021/acsnano.5b00161.

[173] R. A. Brady, N. J. Brooks, P. Cicuta, and L. Di Michele. 'Crystallization of amphiphilic DNA C-stars.' *Nano Letters*, 17(5):3276–3281 (2017). doi:10.1021/acs.nanolett.7b00980.

[174] P. Chidchob, D. Offenbartl-Stiegert, D. McCarthy, X. Luo, J. Li, S. Howorka, and H. F. Sleiman. 'Spatial presentation of cholesterol units on a DNA cube as a determinant of membrane protein-mimicking functions.' *Journal of the American Chemical Society*, 141(2):1100–1108 (2019). doi:10.1021/jacs.8b11898.

[175] H. Joshi and P. K. Maiti. 'Structure and electrical properties of DNA nanotubes embedded in lipid bilayer membranes.' *Nucleic Acids Research*, 46(5):2234–2242 (2018). doi:10.1093/nar/gkx1078.

[176] J. C. Phillips, R. Braun, W. Wang, J. Gumbart, E. Tajkhorshid, E. Villa, C. Chipot, R. D. Skeel, L. Kalé, and K. Schulten. 'Scalable molecular dynamics with NAMD.' *Journal of Computational Chemistry*, 26(16):1781–1802 (2005). doi:10.1002/jcc.20289.

[177] D. A. Case, V. Babin, J. Berryman, R. M. Betz, Q. Cai, D. S. Cerutti, T. E. Cheatham III, T. A. Darden, R. E. Duke, H. Gohlke *et al.* *Amber 14*. University of California, San Francisco (2014). URL http://orbilu.uni.lu/handle/10993/16614.

[178] K. Vanommeslaeghe, E. Hatcher, C. Acharya, S. Kundu, S. Zhong, J. Shim, E. Darian, O. Guvench, P. Lopes, I. Vorobyov *et al.* 'CHARMM general force field: A force field for drug-like molecules compatible with the CHARMM all-atom additive biological force fields.' *Journal of Computational Chemistry*, 31(4):671–690 (2010). doi:10.1002/jcc.21367.

[179] G. J. Martyna, D. J. Tobias, and M. L. Klein. 'Constant pressure molecular dynamics algorithms.' *Journal of Chemical Physics*, 101(5):4177–4189 (1994). doi:10.1063/1.467468.

[180] S. E. Feller, Y. Zhang, R. W. Pastor, and B. R. Brooks. 'Constant pressure molecular dynamics simulation: The Langevin piston method.' *Journal of Chemical Physics*, 103(11):4613–4621 (1995). doi:10.1063/1.470648.

[181] D. J. Sindhikara, S. Kim, A. F. Voter, and A. E. Roitberg. 'Bad seeds sprout perilous dynamics: Stochastic thermostat induced trajectory synchronization in biomolecules.' *Journal of Chemical Theory and Computation*, 5(6):1624–1631 (2009). doi:10.1021/ct800573m.

[182] N. Foloppe and A. D. Mackerell Jr. 'All-atom empirical force field for nucleic acids: I. Parameter optimization based on small molecule and condensed phase macromolecular target data.' *Journal of Computational Chemistry*, 21(2):86–104 (2000). doi:10.1002/(SICI)1096-987X(20000130)21:2<86::AID-JCC2>3.0.CO;2-G.

[183] K. Hart, N. Foloppe, C. M. Baker, E. J. Denning, L. Nilsson, and A. D. MacKerell Jr. 'Optimization of the CHARMM additive force field for DNA: Improved treatment of the BI/BII conformational equilibrium.' *Journal of Chemical Theory and Computation*, 8(1):348–362 (2012). doi:10.1021/ct200723y.

[184] J. Yoo and A. Aksimentiev. 'Improved parametrization of Li^+, Na^+, K^+, and Mg^{2+} ions for all-atom molecular dynamics simulations of nucleic acid systems.' *Journal of Physical Chemistry Letters*, 3(1):45–50 (2012). doi:10.1021/jz201501a.

[185] J. Yoo and A. Aksimentiev. 'New tricks for old dogs: Improving the accuracy of biomolecular force fields by pair-specific corrections to non-bonded interactions.' *Physical Chemistry Chemical Physics*, 20(13):8432–8449 (2018). doi:10.1039/c7cp08185e.

[186] S. Miyamoto and P. A. Kollman. 'Settle: An analytical version of the SHAKE and RATTLE algorithm for rigid water models.' *Journal of Computational Chemistry*, 13(8):952–962 (1992). doi:10.1002/jcc.540130805.

[187] H. C. Andersen. 'Rattle: A "velocity" version of the shake algorithm for molecular dynamics calculations.' *Journal of Computational Physics*, 52(1):24–34 (1983). doi:10.1016/0021-9991(83)90014-1.

[188] D. R. Roe and T. E. Cheatham III. 'PTRAJ and CPPTRAJ: Software for processing and analysis of molecular dynamics trajectory data.' *Journal of Chemical Theory and Computation*, 9(7):3084–3095 (2013). doi:10.1021/ct400341p.

[189] K. Göpfrich, B. Haller, O. Staufer, Y. Dreher, U. Mersdorf, I. Platzman, and J. P. Spatz. 'One-pot assembly of complex giant unilamellar vesicle-based synthetic cells.' *ACS Synthetic Biology*, 8(5):937–947 (2019). doi:10.1021/acssynbio.9b00034.

[190] X. Hou, Y. S. Zhang, G. Trujillo-de Santiago, M. M. Alvarez, J. Ribas, S. J. Jonas, P. S. Weiss, A. M. Andrews, J. Aizenberg, and A. Khademhosseini. 'Interplay between materials and microfluidics.' *Nature Reviews Materials*, 2(5):17016 (2017). doi:10.1038/natrevmats.2017.16.

[191] B. Haller, K. Göpfrich, M. Schröter, J. W. Janiesch, I. Platzman, and J. P. Spatz. 'Charge-controlled microfluidic formation of lipid-based single- and multicompartment systems.' *Lab on a Chip*, 18(17):2665–2674 (2018). doi:10.1039/c8lc00582f.

[192] S. Elhadj, G. Singh, and R. F. Saraf. 'Optical properties of an immobilized DNA monolayer from 255 to 700 nm.' *Langmuir*, 20(13):5539–5543 (2004). doi:10.1021/la049653+.

[193] R. Bar-Ziv and A. Libchaber. 'Effects of DNA sequence and structure on binding of RecA to single-stranded DNA.' *Proceedings of the National Academy of Sciences*, 98(16):9068–9073 (2001). doi:10.1073/pnas.151242898.

[194] A. Ohmann, K. Göpfrich, H. Joshi, R. F. Thompson, D. Sobota, N. A. Ranson, A. Aksimentiev, and U. F. Keyser. 'Controlling aggregation of cholesterol-modified DNA nanostructures.' *Nucleic Acids Research*, 47(21):11441–11451 (2019). doi:10.1093/nar/gkz914.

[195] R. I. Zhdanov, E. P. D'yachkov, N. B. Strazhevskaya, A. S. Shmyrina, A. S. Krylov, P. N. D'yachkov, W. Lorenz, and A. A. Kubatiev. 'Cholesterol and its fatty acid esters in native DNA preparations: Lipid analysis, computer simulation of their interaction with DNA and cholesterol binding to immobilized oligodeoxyribonucleotides.' *Russian Chemical Bulletin*, 54(9):2204–2210 (2005). doi:10.1007/s11172-006-0097-2.

[196] S. M. Gryaznov and D. H. Lloyd. 'Modulation of oligonucleotide duplex and triplex stability via hydrophobic interactions.' *Nucleic Acids Research*, 21(25):5909–5915 (1993). doi:10.1093/nar/21.25.5909.

[197] N. Arashiki, M. Saito, I. Koshino, K. Kamata, J. Hale, N. Mohandas, S. Manno, and Y. Takakuwa. 'An unrecognized function of cholesterol: Regulating the mechanism controlling membrane phospholipid asymmetry.' *Biochemistry*, 55(25):3504–3513 (2016). doi:10.1021/acs.biochem.6b00407.

[198] Q. van der Spek. 'Synthetic membrane pores with varying hydrophobicity and conductivity made from DNA.' *Part III Project Report, University of Cambridge* (2017).

[199] L. Song, M. R. Hobaugh, C. Shustak, S. Cheley, H. Bayley, and J. E. Gouaux. 'Structure of staphylococcal α-hemolysin, a heptameric transmembrane pore.' *Science*, 274(5294):1859–1865 (1996). doi:10.1126/science.274.5294.1859.

[200] Avanti Polar Lipids. 'E. coli Extract Polar (100600).' (2019). URL https://avantilipids.com/product/100600.

[201] Avanti Polar Lipids. 'Egg PC (840051).' (2019). URL https://avantilipids.com/product/840051.

[202] J. D. Brunner and S. Schenck. 'Preparation of proteoliposomes with purified TMEM16 protein for accurate measures of lipid scramblase activity.' In G. Drin (ed.), '*Intracellular lipid transport. Methods in molecular biology, vol 1949*,' pp. 181–199. Humana Press, New York, NY (2019). doi:10.1007/978-1-4939-9136-5_14.

[203] P. Mueller, D. O. Rudin, H. T. Tien, and W. C. Wescott. 'Reconstitution of cell membrane structure *in vitro* and its transformation into an excitable system.' *Nature*, 194(4832):979–980 (1962). doi:10.1038/194979a0.

[204] T. Gutsmann, T. Heimburg, U. Keyser, K. R. Mahendran, and M. Winterhalter. 'Protein reconstitution into freestanding planar lipid membranes for electrophysiological characterization.' *Nature Protocols*, 10(1):188–198 (2015). doi:10.1038/nprot.2015.003.

[205] S. Nekolla, C. Andersen, and R. Benz. 'Noise analysis of ion current through the open and the sugar-induced closed state of the LamB channel of Escherichia coli outer membrane: evaluation of the sugar binding kinetics to the channel interior.' *Biophysical Journal*, 66(5):1388–1397 (1994). doi:10.1016/S0006-3495(94)80929-4.

[206] Avanti Polar Lipids. '4ME 16:0 NBD PE (NBD-DPhPE; 810142).' (2019). URL https://avantilipids.com/product/810142.

[207] R. G. Rinker, T. P. Gordon, D. M. Mason, R. R. Sakaida, and W. H. Corcoran. 'Kinetics and mechanism of the air oxidation of the dithionite ion ($S_2O_4^=$) in aqueous solution.' *Journal of Physical Chemistry*, 64(5):573–581 (1960). doi:10.1021/j100834a015.

[208] J. G. Stout, F. Bassé, R. A. Luhm, H. J. Weiss, T. Wiedmer, and P. J. Sims. 'Scott syndrome erythrocytes contain a membrane protein capable of mediating Ca^{2+}-dependent transbilayer migration of membrane phospholipids.' *Journal of Clinical Investigation*, 99(9):2232–2238 (1997). doi:10.1172/JCI119397.

[209] P. Williamson, A. Christie, T. Kohlin, R. A. Schlegel, P. Comfurius, M. Harmsma, R. F. A. Zwaal, and E. M. Bevers. 'Phospholipid scramblase activation pathways in lymphocytes.' *Biochemistry*, 40(27):8065–8072 (2001). doi:10.1021/bi001929z.

[210] S. D. Vallabhapurapu, V. M. Blanco, M. K. Sulaiman, S. L. Vallabhapurapu, Z. Chu, R. S. Franco, and X. Qi. 'Variation in human cancer cell external phosphatidylserine is regulated by flippase activity and intracellular calcium.' *Oncotarget*, 6(33):34375–34388 (2015). doi:10.18632/oncotarget.6045.

[211] W. J. Lem and M. Wayman. 'Decomposition of aqueous dithionite. Part I. Kinetics of decomposition of aqueous sodium dithionite.' *Canadian Journal of Chemistry*, 48(5):776–781 (1970). doi:10.1139/v70-126.

[212] Avanti Polar Lipids. '16:0-06:0 NBD PC (810130).' (2019). URL https://avantilipids.com/product/810130.

[213] N. Kučerka, S. Tristram-Nagle, and J. F. Nagle. 'Structure of fully hydrated fluid phase lipid bilayers with monounsaturated chains.' *Journal of Membrane Biology*, 208(3):193–202 (2006). doi:10.1007/s00232-005-7006-8.

[214] M. J. Hope, M. B. Bally, L. D. Mayer, A. S. Janoff, and P. R. Cullis. 'Generation of multilamellar and unilamellar phospholipid vesicles.' *Chemistry and Physics of Lipids*, 40(2-4):89–107 (1986). doi:10.1016/0009-3084(86)90065-4.

[215] L. D. Mayer, M. J. Hope, and P. R. Cullis. 'Vesicles of variable sizes produced by a rapid extrusion procedure.' *Biochimica et Biophysica Acta - Biomembranes*, 858(1):161–168 (1986). doi:10.1016/0005-2736(86)90302-0.

[216] M. Schaich, J. Cama, K. Al Nahas, D. Sobota, H. Sleath, K. Jahnke, S. Deshpande, C. Dekker, and U. F. Keyser. 'An integrated microfluidic platform for quantifying drug permeation across biomimetic vesicle membranes.' *Molecular Pharmaceutics*, 16(6):2494–2501 (2019). doi:10.1021/acs.molpharmaceut.9b00086.

[217] P. Neves, S. C. D. N. Lopes, I. Sousa, S. Garcia, P. Eaton, and P. Gameiro. 'Characterization of membrane protein reconstitution in LUVs of different lipid composition by fluorescence anisotropy.' *Journal of Pharmaceutical and Biomedical Analysis*, 49(2):276–281 (2009). doi:10.1016/j.jpba.2008.11.026.

[218] A. J. Wolfe, Y. C. Hsueh, A. R. Blanden, M. M. Mohammad, B. Pham, A. K. Thakur, S. N. Loh, M. Chen, and L. Movileanu. 'Interrogating detergent desolvation of nanopore-forming proteins by fluorescence polarization spectroscopy.' *Analytical Chemistry*, 89(15):8013–8020 (2017). doi:10.1021/acs.analchem.7b01339.

[219] A. J. Wolfe, W. Si, Z. Zhang, A. R. Blanden, Y. C. Hsueh, J. F. Gugel, B. Pham, M. Chen, S. N. Loh, S. Rozovsky *et al.* 'Quantification of membrane protein-detergent complex interactions.' *Journal of Physical Chemistry B*, 121(44):10228–10241 (2017). doi:10.1021/acs.jpcb.7b08045.

[220] J. Cama, H. Bajaj, S. Pagliara, T. Maier, Y. Braun, M. Winterhalter, and U. F. Keyser. 'Quantification of fluoroquinolone uptake through the outer membrane channel OmpF of *Escherichia coli*.' *Journal of the American Chemical Society*, 137(43):13836–13843 (2015). doi:10.1021/jacs.5b08960.

[221] P. Scudieri, E. Caci, A. Venturini, E. Sondo, G. Pianigiani, C. Marchetti, R. Ravazzolo, F. Pagani, and L. J. V. Galietta. 'Ion channel and lipid scramblase activity associated with expression of TMEM16F/ANO6 isoforms.' *Journal of Physiology*, 593(17):3829–3848 (2015). doi:10.1113/JP270691.

[222] C. Muratori, A. G. Pakhomov, E. Gianulis, J. Meads, M. Casciola, P. A. Mollica, and O. N. Pakhomova. 'Activation of the phospholipid scramblase TMEM16F by nanosecond pulsed electric fields (nsPEF) facilitates its diverse cytophysiological effects.' *Journal of Biological Chemistry*, 292(47):19381–19391 (2017). doi:10.1074/jbc.M117.803049.

[223] C. Bricogne, M. Fine, P. M. Pereira, J. Sung, M. Tijani, Y. Wang, R. Henriques, M. K. Collins, and D. W. Hilgemann. 'TMEM16F activation by Ca^{2+} triggers plasma membrane expansion and directs PD-1 trafficking.' *Scientific Reports*, 9:619 (2019). doi:10/c7kw.

[224] I. G. Abidor, V. B. Arakelyan, L. V. Chernomordik, Y. A. Chizmadzhev, V. F. Pastushenko, and M. P. Tarasevich. 'Electric breakdown of bilayer lipid membranes. I. The main experimental facts and their qualitative discussion.' *Journal of Electroanalytical Chemistry and Interfacial Electrochemistry*, 104:37–52 (1979). doi:10.1016/S0022-0728(79)81006-2.

[225] J. C. Weaver and Y. A. Chizmadzhev. 'Theory of electroporation: A review.' *Bioelectrochemistry and Bioenergetics*, 41(2):135–160 (1996). doi:10.1016/S0302-4598(96)05062-3.

[226] M. L. Yarmush, A. Golberg, G. Serša, T. Kotnik, and D. Miklavčič. 'Electroporation-based technologies for medicine: Principles, applications, and challenges.' *Annual Review of Biomedical Engineering*, 16:295–320 (2014). doi:10.1146/annurev-bioeng-071813-104622.

[227] J. Teissie and T. Y. Tsong. 'Electric field induced transient pores in phospholipid bilayer vesicles.' *Biochemistry*, 20(6):1548–1554 (1981). doi:10.1021/bi00509a022.

[228] R. Dimova, K. A. Riske, S. Aranda, N. Bezlyepkina, R. L. Knorr, and R. Lipowsky. 'Giant vesicles in electric fields.' *Soft Matter*, 3(7):817–827 (2007). doi:10.1039/b703580b.

[229] K. Schlosser and Y. Li. 'Biologically inspired synthetic enzymes made from DNA.' *Chemistry & Biology*, 16(3):311–322 (2009). doi:10.1016/j.chembiol.2009.01.008.

[230] S. K. Silverman. 'Catalytic DNA: Scope, applications, and biochemistry of deoxyribozymes.' *Trends in Biochemical Sciences*, 41(7):595–609 (2016). doi:10.1016/j.tibs.2016.04.010.

[231] J. Yoo and A. Aksimentiev. 'Molecular dynamics of membrane-spanning DNA channels: Conductance mechanism, electro-osmotic transport, and mechanical gating.' *Journal of Physical Chemistry Letters*, 6(23):4680–4687 (2015). doi:10.1021/acs.jpclett.5b01964.

[232] A. D. MacKerell Jr, D. Bashford, M. Bellott, R. L. Dunbrack Jr, J. D. Evanseck, M. J. Field, S. Fischer, J. Gao, H. Guo, S. Ha *et al.* 'All-atom empirical potential for molecular modeling and dynamics studies of proteins.' *Journal of Physical Chemistry B*, 102(18):3586–3616 (1998). doi:10.1021/jp973084f.

[233] D. E. Shaw, J. P. Grossman, J. A. Bank, B. Batson, J. A. Butts, J. C. Chao, M. M. Deneroff, R. O. Dror, A. Even, C. H. Fenton *et al.* 'Anton 2: Raising the bar for performance and programmability in a special-purpose molecular dynamics supercomputer.' In '*SC14: Proceedings of the International Conference for High Performance Computing, Networking, Storage and Analysis*,' pp. 41–53. IEEE Press, New Orleans, LA (2014). doi:10.1109/SC.2014.9.

[234] T. Pott, H. Bouvrais, and P. Méléard. 'Giant unilamellar vesicle formation under physiologically relevant conditions.' *Chemistry and Physics of Lipids*, 154(2):115–119 (2008). doi:10.1016/j.chemphyslip.2008.03.008.

[235] O. Mertins, N. P. da Silveira, A. R. Pohlmann, A. P. Schröder, and C. M. Marques. 'Electroformation of giant vesicles from an inverse phase precursor.' *Biophysical Journal*, 96(7):2719–2726 (2009). doi:10.1016/j.bpj.2008.12.3928.

[236] S. Li, P. Hu, and N. Malmstadt. 'Confocal imaging to quantify passive transport across biomimetic lipid membranes.' *Analytical Chemistry*, 82(18):7766–7771 (2010). doi:10.1021/ac1016826.

[237] Leica Microsystems CMS GmbH. 'The guide to STED sample preparation.' (2019). URL https://www.leica-microsystems.com/science-lab/the-guide-to-sted-sample-preparation/.

[238] D. van Swaay and A. DeMello. 'Microfluidic methods for forming liposomes.' *Lab on a Chip*, 13(5):752–767 (2013). doi:10.1039/c2lc41121k.

[239] M. Nakano, M. Fukuda, T. Kudo, N. Matsuzaki, T. Azuma, K. Sekine, H. Endo, and T. Handa. 'Flip-flop of phospholipids in vesicles: Kinetic analysis with time-resolved small-angle neutron scattering.' *Journal of Physical Chemistry B*, 113(19):6745–6748 (2009). doi:10.1021/jp900913w.

[240] C. Taupin, M. Dvolaitzky, and C. Sauterey. 'Osmotic pressure-induced pores in phospholipid vesicles.' *Biochemistry*, 14(21):4771–4775 (1975). doi:10.1021/bi00692a032.

[241] S. U. A. Shibly, C. Ghatak, M. A. S. Karal, M. Moniruzzaman, and M. Yamazaki. 'Experimental estimation of membrane tension induced by osmotic pressure.' *Biophysical Journal*, 111(10):2190–2201 (2016). doi:10.1016/j.bpj.2016.09.043.

[242] M. Chabanon, J. C. S. Ho, B. Liedberg, A. N. Parikh, and P. Rangamani. 'Pulsatile lipid vesicles under osmotic stress.' *Biophysical Journal*, 112(8):1682–1691 (2017). doi:10.1016/j.bpj.2017.03.018.

[243] H. Sträuber and S. Müller. 'Viability states of bacteria – Specific mechanisms of selected probes.' *Cytometry Part A*, 77(7):623–634 (2010). doi:10.1002/cyto.a.20920.

[244] A. H. de Vries, A. E. Mark, and S. J. Marrink. 'Molecular dynamics simulation of the spontaneous formation of a small DPPC vesicle in water in atomistic detail.' *Journal of the American Chemical Society*, 126(14):4488–4489 (2004). doi:10.1021/ja0398417.

[245] A. A. Gurtovenko and I. Vattulainen. 'Molecular mechanism for lipid flip-flops.' *Journal of Physical Chemistry B*, 111(48):13554–13559 (2007). doi:10.1021/jp077094k.

[246] A. A. Gurtovenko, O. I. Onike, and J. Anwar. 'Chemically induced phospholipid translocation across biological membranes.' *Langmuir*, 24(17):9656–9660 (2008). doi:10.1021/la801431f.

[247] S. N. Gummadi and A. K. Menon. 'Transbilayer movement of dipalmitoylphosphatidylcholine in proteoliposomes reconstituted from detergent extracts of endoplasmic reticulum.' *Journal of Biological Chemistry*, 277(28):25337–25343 (2002). doi:10.1074/jbc.M203809200.

[248] H. C. Berg and E. M. Purcell. 'Physics of chemoreception.' *Biophysical Journal*, 20(2):193–219 (1977). doi:10.1016/S0006-3495(77)85544-6.

[249] H. Sano and M. Tachiya. 'Theory of diffusion-controlled reactions on spherical surfaces and its application to reactions on micellar surfaces.' *Journal of Chemical Physics*, 75(6):2870–2878 (1981). doi:10.1063/1.442360.

[250] B. Goldstein, C. Wofsy, and G. Bell. 'Interactions of low density lipoprotein receptors with coated pits on human fibroblasts: Estimate of the forward rate constant and comparison with the diffusion limit.' *Proceedings of the National Academy of Sciences*, 78(9):5695–5698 (1981). doi:10.1073/pnas.78.9.5695.

[251] R. Macháň and M. Hof. 'Lipid diffusion in planar membranes investigated by fluorescence correlation spectroscopy.' *Biochimica et Biophysica Acta - Biomembranes*, 1798(7):1377–1391 (2010). doi:10.1016/j.bbamem.2010.02.014.

[252] I. Vermes, C. Haanen, H. Steffens-Nakken, and C. Reutellingsperger. 'A novel assay for apoptosis flow cytometric detection of phosphatidylserine expression on early apoptotic cells using fluorescein labelled Annexin V.' *Journal of Immunological Methods*, 184(1):39–51 (1995). doi:10.1016/0022-1759(95)00072-I.

[253] M. van Engeland, L. J. W. Nieland, F. C. S. Ramaekers, B. Schutte, and C. P. M. Reutelingsperger. 'Annexin V-affinity assay: A review on an apoptosis detection system based on phosphatidylserine exposure.' *Cytometry*, 31:1–9 (1998). doi:10.1002/(SICI)1097-0320(19980101)31:1<1::AID-CYTO1>3.0.CO;2-R.

[254] J. A. F. Op den Kamp. 'Lipid asymmetry in membranes.' *Annual Review of Biochemistry*, 48(1):47–71 (1979). doi:10.1146/annurev.bi.48.070179.000403.

[255] J. E. Rothman and J. Lenard. 'Membrane asymmetry.' *Science*, 195(4280):743–753 (1977). doi:10.1126/science.402030.

Appendix

A.1 Advice and troubleshooting for PAGE

- To prevent gel mixture leakage, place a 1 ml pipette tip behind the spring-loaded clamp in the casting stand to increase the pressure on the glass plates into the gaskets.
- Filling should be performed quickly. Bubbles formed when pipetting the gel mixture in usually rise to the top and disappear. It is recommended to fill spacer plates all the way to the top as it reduces the risk of bubbles in the gel pockets when inserting the comb.
- Leaving the glass pipette in the unused portion of the gel mixture after pouring can be used as a rough confirmation that polymerisation was successful.
- Polymerisation durations between 1 to 2 hours provided the most consistent results. At longer durations drying of the gel becomes a factor which starts to deform the gel pockets.
- If the same gel pockets repeatedly show filaments in them, using a new comb or new spacer plates typically resolves the problem.
- TEMED should be added last to the gel mixture, as it catalyses the polymerisation reaction and from then onwards the gel starts to rapidly solidify.
- TEMED should be used from small aliquots rather than the stock bottle as oxidation decreases its catalytic activity. Oxidised TEMED solution has a yellowish colour.
- APS solution is not stable for long periods of time in aqueous solutions and for best results should be prepared freshly. However, storing frozen aliquots at $-20\ ^{\circ}\mathrm{C}$ and thawing them upon use has proven sufficient, although aliquots should not be stored longer than 6 months or until gels show inconsistent polymerisation.
- For best results, polyacrylamide solution should ideally not be older than 12 months.
- Inconsistent polymerisation and band separation is often resolved by using fresh solutions.
- Recommended final concentrations of APS and TEMED are typically 0.05 %. The here described protocol uses slightly more than that which has proven to facilitate faster

polymerisation (without clouding of the gel) and might also compensate for degradation of APS and TEMED allowing them to be stored for longer.

- Many DNA ladders contain mixed DNA sequences for bands referring to the same base pair length (particularly some ladders from New England Biolabs). Due to the sequence specificity of PAGE, these will split up, providing a less accurate reference. To avoid this, the used ladder L: GeneRuler Low Range (Thermo Fisher Scientific) proved a good choice.
- Freshly vortexing the DNA ladder and loading it last typically yields the sharpest bands.
- Many commercially available loading dyes contain SDS or EDTA. Care must be taken that this does not interfere with the DNA samples upon loading onto the gel.
- The comb should only be taken out after the chamber was filled with running buffer such that no air bubbles enter the pockets.
- It is highly recommended to clean the glass edges and gel pockets from gel filaments before loading. Flushing the pockets with the running buffer or air helps to remove particles from the pockets (pipetting repeatedly with a gel loading tip and about 100 to 150 µl volume). Applying suction with the pipette upon making contact with a loose particle can aid to remove it from the pocket. Care must be taken not to poke the bottom of the gel pocket.
- Gel-loading tips are recommended for sample loading. It is best to pipette slowly and always slightly less than the total volume of prepared sample to avoid air at the end of the pipette tip which can cause difficulties for ejecting the sample into the gel pocket. To pipette small volumes, the adapter on 2 and 10 µl Gilson pipettes can be reversed to accommodate 200 µl tip sizes.
- Running the gel at room temperature and the typical buffer conditions (11 mM $MgCl_2$ present) leads to temperatures of ~30 °C (at 100 V for 90 min) or ~37 °C (at 200 V for 45 min) inside the central reservoir. The outer reservoir typically stays below 30 °C. Surrounding the gel chamber with crushed ice some minutes prior the run typically yields temperatures in the outer chamber reservoir of 18 °C before and ~10 °C after running the gel for 90 min at 100 V. Temperatures are higher when two gels are run in parallel. Temperatures are generally lower for the gel located more centrally rather than the one closest to the wall of the gel chamber.
- At 100 V and the above described running buffer, the current is typically ~24 mA (for one gel, double for two gels) at the beginning and decreases to < 15 mA towards the end.
- To avoid possible tearing of the gel slab edges, separate the gel from the glass by passing with a scalpel once on each side before releasing the gel slab into the staining solution.

- It is recommended to keep the gel slab always well moistened. A dry gel slab easily tears or breaks while a wet gel slab can even fold without breaking (but is still prone to tearing).
- The GelRed® staining solution can be used multiple times, especially for PAGE gels that do not absorb much of the dye. The staining solution should be stored in the dark.
- Rinsing the gel slab with distilled water after staining can improve the signal to noise ratio as excess dye is removed.
- The UV lamp used for gel imaging requires ~5 min to warm up. This results in a continuously increasing contrast if the gel is imaged multiple times after the lamp is switched on. To avoid this, switch the lamp on already a few minutes before imaging.
- Gel imaging at various exposure times is recommended as for analysis the bands should not be saturated but for presentation purposes more intense bands aid contrast.
- The gel slab should be aligned horizontally focussing on the gel pockets (not the bottom edge of the gel as it can be skewed). Digitally rotating the image after imaging can reduce the sharpness of the bands.

A.2 Sequences of DNA nanostructures

Table A.1 Sequences of DNA nanostructures with various ssDNA overhangs included to prevent stacking interactions.

Name	5' overhang	Double-stranded core sequence (5' to 3')	3' overhang
sc1		CCTTTCCACGAACACAGGGTTGTCCGATCCTATATTACGACTCC	-/C/G/A/T/TT/TTT
sc2	-/C/G/A/T/TT/TTT	GGGAAGGGGTTCGCAAGTCGCACCCTAAACG	
sc3		TCTTATCCTGCATCGAAAGCTCAATCATGCATC	-/C/G/A/T/TT/TTT
sc4	-/C/G/A/T/TT/TTT	ATGTTGAAGGCTCAGGATGC	
st1	-/C/G/A/T/TT/TTT	ATCGGACATTCAACATGGAGTCGTGGTGCGACT	
st2		TGCGAACAGGATAAGACGTTTAGAATATAGG	-/C/G/A/T/TT/TTT
st3	-/C/G/A/T/TT/TTT	TTCGATGCCCCTTCCCGATGCATGAAGGGCATCCTGAGCCACCC	
st4		TGTGTTCGTGGAATTGAGCT	-/C/G/A/T/TT/TTT

Table A.2 DNA strands employed for DNA nanostructures assembled with different number of TTT overhangs as analysed in Fig. 3.3. For detailed sequences see Table A.3.

TTT overhangs	DNA strands with TTT overhangs
0 / 0	—
1 / 0	st1
1 / 1	st1, sc3
2 / 1	st1, sc3, sc1
2 / 2	st1, sc3, sc1, st3
3 / 2	st1, sc3, sc1, st3, sc4
3 / 3	st1, sc3, sc1, st3, sc4, st4
4 / 3	st1, sc3, sc1, st3, sc4, st4, st2
4 / 4	st1, sc3, sc1, st3, sc4, st4, st2, sc2
4 / 0	st1, sc1, sc4, st2

Table A.3 Sequences of different DNA nanostructure designs.

Design	Strand	Sequence (5' to 3')	nt
CP1	U1R1	AAAACGCTAAGCCACCTTTAGATCCAAA	28
	U1R2	GGTCGTGCGGACTGTCGAACACCAACGATGCCTGATAGAAGT	42
	U2R1	GGATCTAAAGGACTTCTATCAAAGACGGGACGACTCCGGGAG	42
	U2R2	GGCATCGTTGGAAAAAATTTCGGATCCA	28
	U3R1	AAACTCCCGGAGTCCGCTGCTGATCAAA	28
	U3R2	GTCCCGTCTTTGGATCCGAAAGCCATAATATATCGAGACGGG	42
	U4R1	GATCAGCAGCGCCCGTCTCGACCGCACGACCTGGCTTAGCGT	42
	U4R2	TATATTATGGCAAAAAATGTTCGACAGT	28
CP2	sc1	CCTTTCCACGAACACAGGGTTGTCCGATCCTATATTACGACTCCTTT	47
	sc2	TTTGGGAAGGGGTTCGCAAGTCGCACCCTAAACG	34
	sc3	TCTTATCCTGCATCGAAAGCTCAATCATGCATCTTT	36
	sc4	TTTATGTTGAAGGCTCAGGATGC	23
	st1	TTTATCGGACATTCAACATGGAGTCGTGGTGCGACT	36
	st2	TGCGAACAGGATAAGACGTTTAGAATATAGGTTT	34
	st3	TTTTTCGATGCCCCTTCCCGATGCATGAAGGGCATCCTGAGCCACCC	47
	st4	TGTGTTCGTGGAATTGAGCTTTT	23
CP3	sc11	TTTTACCGCGAGGAGCTAGCGGCTTT	26
	sc12	TTTAGGTAGCGCCGCTGCGAACGTTT	26
	sc21	ATAACCGTGTGAGCCTGACGGTCGGCCAGAGAGGCTCGATTA	42
	sc22	AGACATTTCGGCCGGCGTAGACCGGACAGGTATTCATGCAGG	42
	st11	CACACGGTTATCCTCGCGGTACGTTCGCAGCCCTGCATGAAT	42
	st12	CCGAAATGTCTGGCGCTACCTGCCGCTAGCTTAATCGAGCCT	42
	st21	TTTCCGTCAGGCTACCTGTCCGGTTT	26
	st22	TTTTCTACGCCGGCTCTGGCCGATTT	26
CP3 short	sc11	TTTTCGCATCAGGGCACATTGGCTTT	26
	sc12	TTTTGCGGCTAAGACTTGCCAGGTTT	26
	sc21	GCCGACGTGTACGGATCTGGCA	22
	sc22	GCGACATTGCGGCCGATTCGGA	22
	st11	TTTTACACGTCGGCCCTGATGCGACCTGGCAAGTTCCGAATCGGCTTT	48
	st12	TTTCGCAATGTCGCCTTAGCCGCAGCCAATGTGCTGCCAGATCCGTTT	48
CP4	sc1	AGTGTCGACAAGACGGCTGTGGCTTGTGTGGTGTGTCAATCCTTCGGACTAG	52
	sc2	AGTCACATGCGTAGGTTTCCGCGTTCTCGCCAGGATGAGATTT	43
	sc3	TTTAGGGCTGCTAAGTCGT	19
	st1	AGCCACAGATGTGACTTGTGTGGTGTGTCTAGTCCGACGACTTAACCTACGC	52
	st2	TTTACGCGGAAGCAGCCCTTCTCATCCTCGACACTAAGGATTG	43
	st3	CCGTCTTGTGGCGAGATTT	19
6HP	sc1	AGCGAACGTGGATTTTGTCCGACATCGGCAAGCTCCCTTTTTCGACTATT	50
	sc2	CGAAGATCGTGTTTTTCCACAGTTGATTGCCCTTCACTTTTCCCAGCAGG	50
	sc3	TCACCAGTGAGATTTTTGTCGTACCAGGTGCATGGATTTTTGCATTCTAA	50
	st1	CCGATGTCGGACTTTTACACGATCTTCGCCTGCTGGGTTTTGGGAGCTTG	50
	st2	AATCAACTGTGGTTTTTCTCACTGGTGATTAGAATGCTTTTGTGAAGGGC	50
	st3	CCTGGTACGACATTTTTCCACGTTCGCTAATAGTCGATTTTATCCATGCA	50

A.3 Cholesterol-modified ssDNA and dsDNA

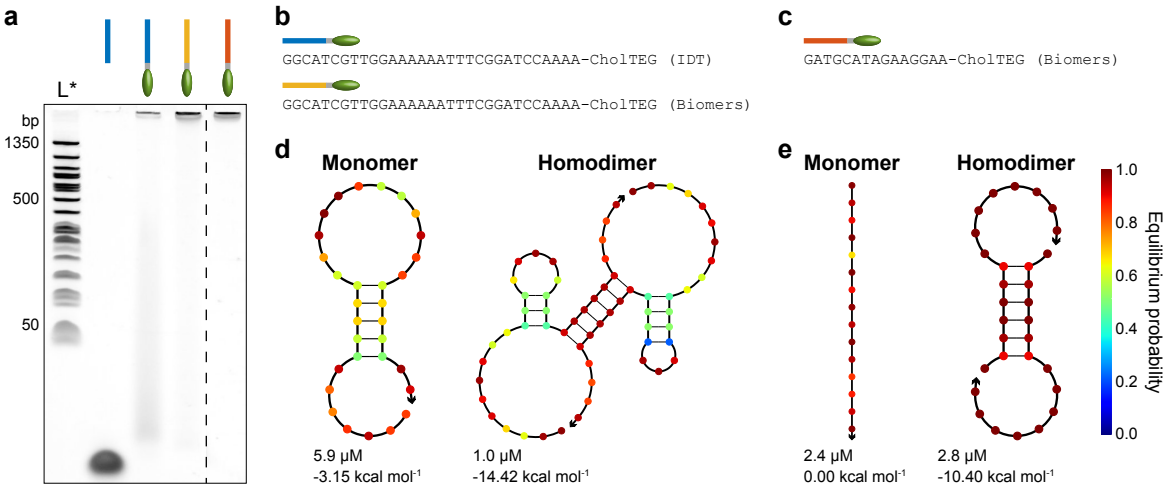

Fig. A.1 Analysis of other DNA sequences with dimerisation tendencies. (**a**) PAGE of one unmodified and three cholesterol-modified DNA sequences as shown in **b** and **c**. Samples were run on the same gel but space between lanes was omitted as indicated by the dashed line. (**d,e**) Probability shading representation of NUPACK free energy calculations of DNA sequences shown in **b** and **c**, respectively, illustrating a tendency for dimerisation.

Table A.4 DNA sequences used for dsDNA aggregation prevention experiments with ssDNA overhangs. The sequence of the 'ss' chol-DNA strand equals sequence (b) analysed previously. 5' tocopherol-modified ssDNA was purchased from biomers.net covalently linked to the DNA via an octyl (C8) spacer.

DNA strand	Sequence (5' to 3')
ss	AAACTCCCGGAGTCCGCTGCTGATCAAA
ss chol	AAACTCCCGGAGTCCGCTGCTGATCAAA-CholTEG
comp −6	CAGCAGCGGACTCCGGGAGTTT
comp 0	TTTGATCAGCAGCGGACTCCGGGAGTTT
comp +2	CCTTTGATCAGCAGCGGACTCCGGGAGTTT
comp +4	TACCTTTGATCAGCAGCGGACTCCGGGAGTTT
comp +6	ACTACCTTTGATCAGCAGCGGACTCCGGGAGTTT
comp +8	GTACTACCTTTGATCAGCAGCGGACTCCGGGAGTTT
comp +10	TCGTACTACCTTTGATCAGCAGCGGACTCCGGGAGTTT
ss toco	TocoC8-ATATATTATGGCAAAAAATGTTCGACAGT
comp 0	ACTGTCGAACATTTTTTGCCATAATATAT
comp +3	ACTGTCGAACATTTTTTGCCATAATATATCTG
comp +6	ACTGTCGAACATTTTTTGCCATAATATATCTGTCA
comp +10	ACTGTCGAACATTTTTTGCCATAATATATCTGTCACTTG

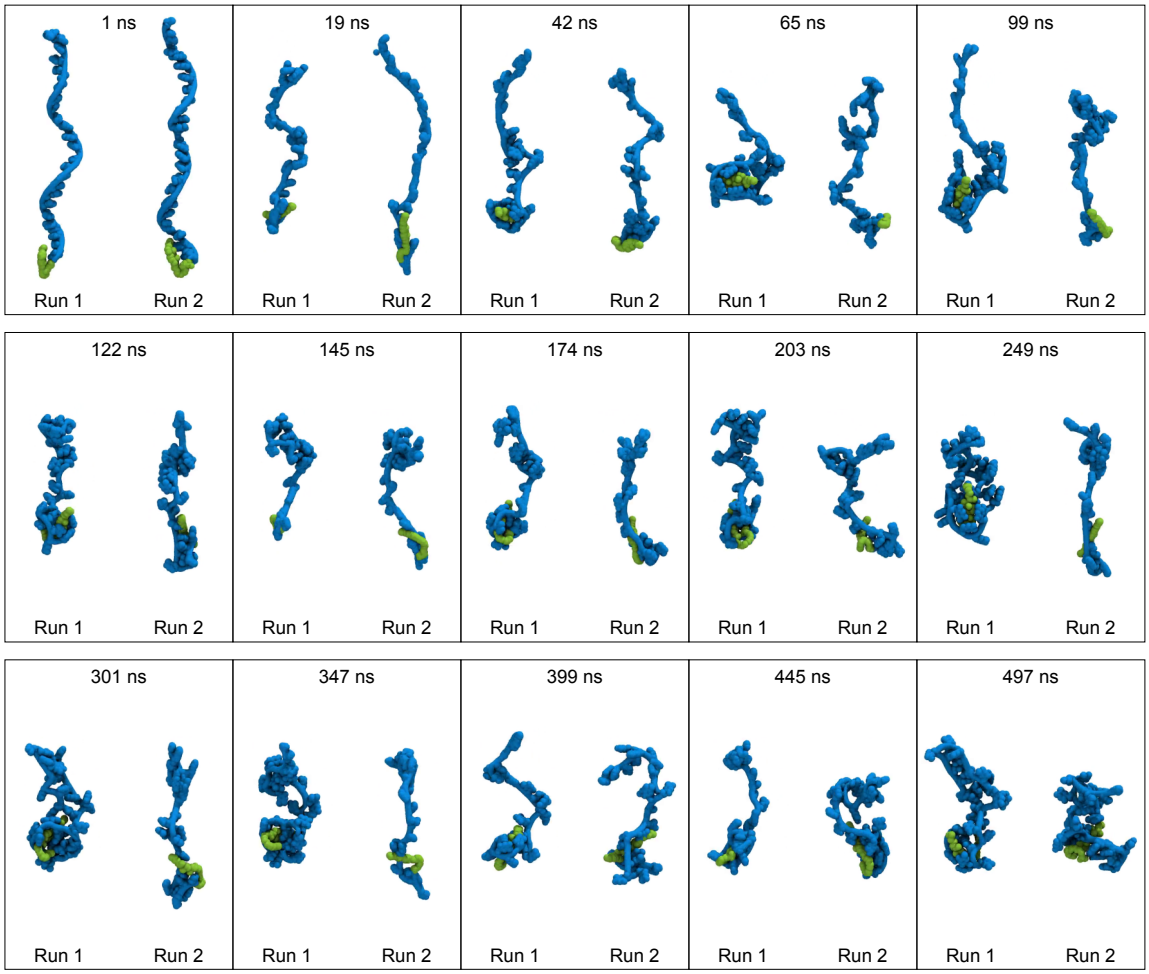

Fig. A.2 Image sequence of MD simulations of cholesterol-modified 30T ssDNA. Instantaneous snapshots of all-atom MD simulations of cholesterol-modified 30 thymine ssDNA (30T) taken at various time points throughout two independent 0.5 µs long simulation runs (Run 1 and Run 2) starting from the same initial configuration. The ssDNA wraps around the cholesterol group throughout both simulation runs. Water and ions are not shown for clarity. A movie of the simulation can be found in the Supplementary Information of the published article [194].

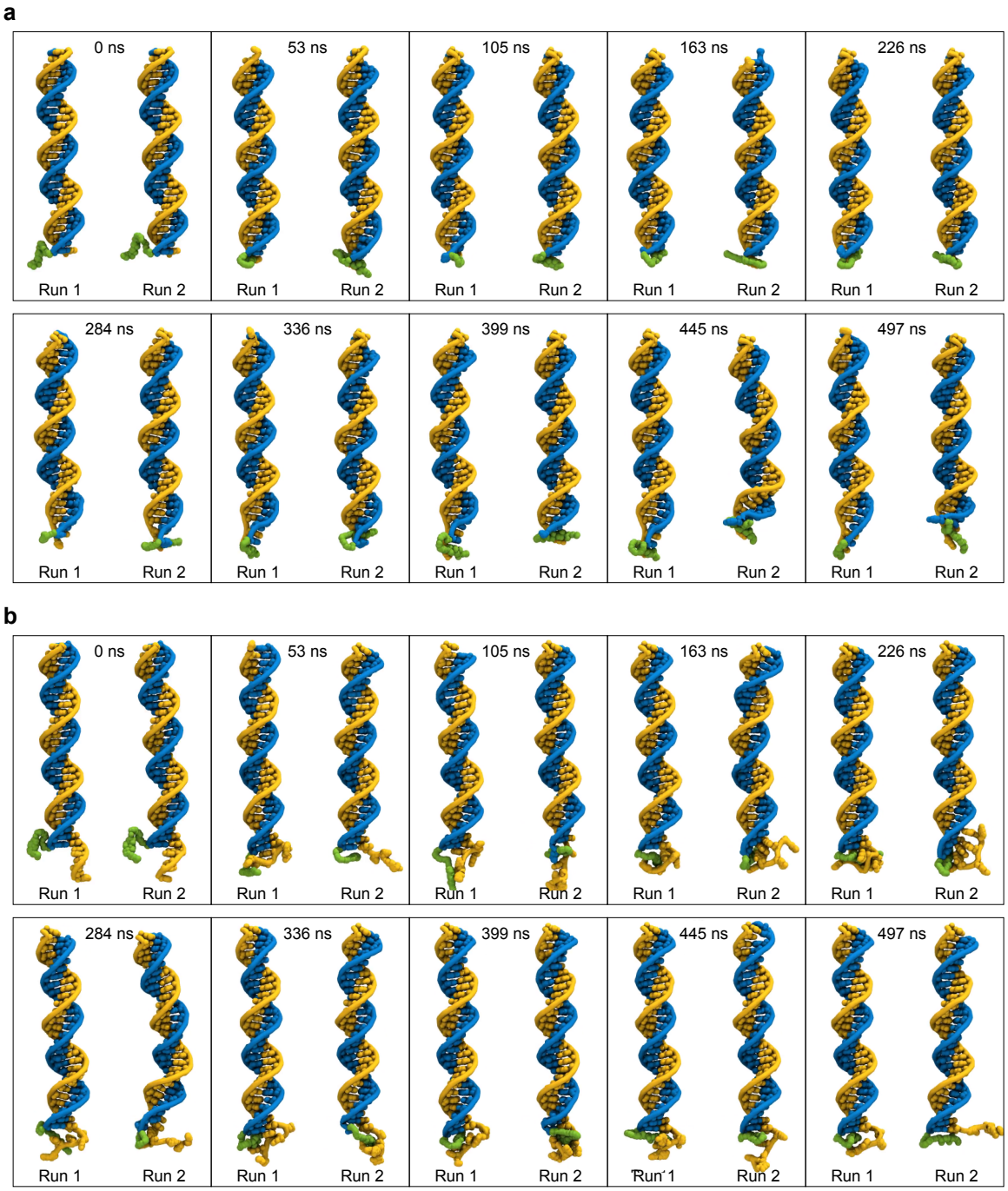

Fig. A.3 Image sequences of MD simulations of cholesterol-modified DNA duplexes. Instantaneous snapshots of all-atom MD simulations of the cholesterol-modified DNA duplex without (**a**) and with a 6 nt overhang (**b**) on the complementary strand. For each system two independent 0.5 µs long simulation runs (Run 1 and Run 2) starting from the same initial configuration were performed. Water and ions are not shown for clarity. Movies of the simulations can be found in the Supplementary Information of the published article [194].

A.4 Cholesterol-modified CP2 DNA nanostructure

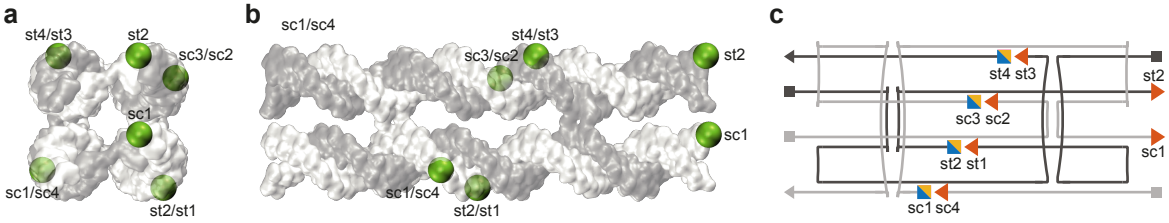

Fig. A.4 Overview of modification positions and DNA strand names for the DNA nanostructure design. Top (**a**) and side view (**b**) of a 3D representation of the DNA nanostructure with cholesterol modification positions highlighted as green spheres. (**c**) 2D scheme illustrating the ssDNA pathways and modification positions within the DNA nanostructure design.

Table A.5 DNA sequences of cholesterol-modified (C) and Cy3-modified (F) strands employed for the assembly of the CP2 DNA nanostructure.

DNA strand	Modification	Sequence (5' to 3')
sc4C	3' TEG	TTTATGTTGAAGGCTCAGGATGCA
sc2C	3' TEG	TTTGGGAAGGGGTTCGCAAGTCGCACCCTAAACGA
st3C	3' TEG	TTTTTCGATGCCCCTTCCCGATGCATGAAGGGCATCCTGAGCCACCCA
st1C	3' TEG	TTTATCGGACATTCAACATGGAGTCGTGGTGCGACTA
sc1C	5' TEG / 5' C6	ACCTTTCCACGAACACAGGGTTGTCCGATCCTATATTACGACTCCTTT
sc3C	5' TEG / 5' C6	ATCTTATCCTGCATCGAAAGCTCAATCATGCATCTTT
st4C	5' TEG / 5' C6	ATGTGTTCGTGGAATTGAGCTTTT
st2C	5' TEG / 5' C6	ATGCGAACAGGATAAGACGTTTAGAATATAGGTTT
sc1C	3' TEG	CCTTTCCACGAACACAGGGTTGTCCGATCCTATATTACGACTCCTTT
st2C	3' TEG	TGCGAACAGGATAAGACGTTTAGAATATAGGTTT
st2F	3' Cy3	TGCGAACAGGATAAGACGTTTAGAATATAGGTTT
st4F	3' Cy3	TGTGTTCGTGGAATTGAGCTTTT

Table A.6 DNA sequences employed for DNA nanostructures assembled with different cholesterol linker types.

Cholesterol number	Linker type	DNA strands with cholesterol
1	3' TEG	sc4C
2	3' TEG	sc4C, sc2C
3	3' TEG	sc4C, sc2C, st3C
4	3' TEG	sc4C, sc2C, st3C, st1C
1	5' TEG / 5' C6	sc1C
2	5' TEG / 5' C6	sc1C, sc3C
3	5' TEG / 5' C6	sc1C, sc3C, st4C
4	5' TEG / 5' C6	sc1C, sc3C, st4C, st2C

A.5 Additional MD results: Energetics of lipid scrambling

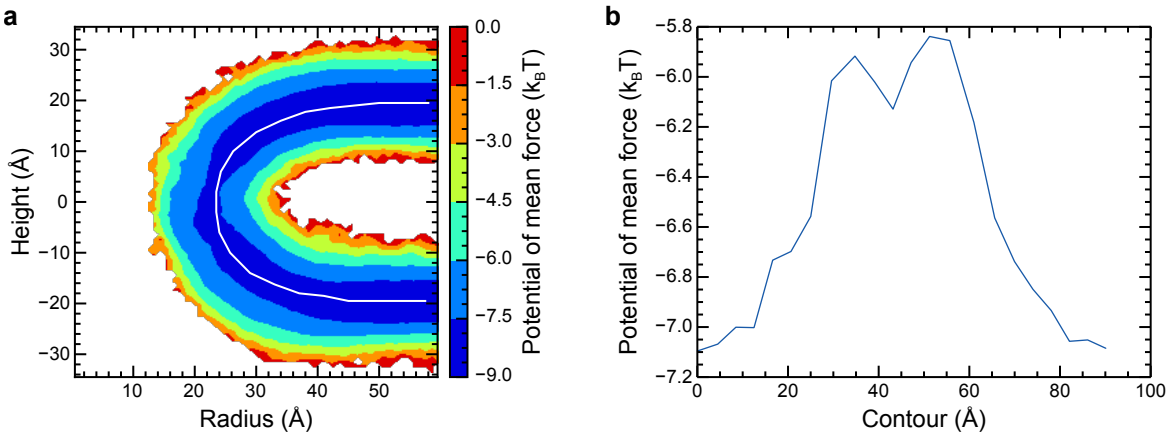

Fig. A.5 Energetics of lipid scrambling. (**a**) Two-dimensional potential of mean force (PMF) for a lipid headgroup near the toroidal pore. The PMF was obtained by Boltzmann inversion of the average density of lipid phosphorus atoms. To obtain the density, the system was translated at each frame of the trajectory so that the centre of mass of all lipid atoms within 2 nm of DNA was at the origin. Following that, a two-dimensional histogram was constructed by binning the radial- and Z-coordinates of each phosphorus atom during the 2 µs MD trajectory. An approximate transition path for moving a lipid molecule from one leaflet to the other is drawn as a white line. The transition path was obtained by selecting all bins with a density greater than 1 % of the maximum and iteratively removing bins from the edges until a single path of bins remained. (**b**) Free energy profile along the transition path for a lipid moving from one leaflet to the other. To compute the free energy profile, all bins in the 2D histogram were assigned to the nearest transition path bin. The free energy at each transition path bin was calculated from the Boltzmann-weighted average of the free energies of its assigned bins from panel **a**. The contour at zero corresponds to the bin with radial and Z-coordinates of 59 and −20 Å, respectively.

A.6 Alternative dithionite reduction protocol

In the alternative experimental protocol, the final concentration of dithionite was similar (≈ 5 mM), however, the amount of dithionite solution added was greater (see Table A.7).

Table A.7 Alternative protocol of dithionite reduction assay.

Amount	Buffer conditions
20 µl	GUV solution in 100 mM sucrose, 20 mM HEPES pH 7.4
24.5 µl	100 mM glucose, 20 mM HEPES pH 7.4
0.5 µl	0.5 % OPOE in TE20 buffer
5 µl	DNA nanostructures at 1 µM in TE20 buffer –> Incubation for ≈ 150 min at room temperature –> Record z-stacks of multiple areas containing vesicles
50 µl	10 mM dithionite in 80 mM glucose, 20 mM HEPES pH 7.4 –> Record z-stacks of multiple areas containing vesicles after 1 hour
100 µl	Total volume

The greater amount of added solution caused the vesicles to move upon dithionite addition in most cases. Therefore, it was rarely possible to compare the intensity before and after addition for the same vesicle. Alternatively, z-stacks of several areas containing vesicles were acquired before and one hour after dithionite addition. NBD fluorescence intensities before and after dithionite addition were determined similarly as described in Section 6.2. Intensity values were background subtracted and their count was normalised to the highest intensity column in each graph (see Figs. A.6a,c). The fairly large spread in the intensity distribution can be explained by the use of a 20x air objective (UPLSAPO20X, NA = 0.75) in these experiments which resulted in a larger focal volume in z-direction. This caused the fluorescence intensity to depend on the size meaning that larger vesicles had a higher fluorescence intensity than smaller ones. However, the data still showed that for vesicles incubated with 2C nanostructures the highest peak is associated with a complete NBD reduction (red column in Fig. A.6a) which is in contrast to 1C nanostructure experiments where the highest peak is located at a much higher remaining fluorescence intensity (Fig. A.6c). A small fraction of vesicles in the case of 1C nanostructures is completely reduced in their fluorescence which could be caused by dithionite leakage into the vesicles while they were moved upon dithionite addition. Fluorescence intensity traces show an exponential decay to almost 0 or to 0.5 for vesicles incubated with 2C or 1C nanostructures, respectively (see Figs. A.6b,d). Spikes in intensity are caused by vesicles temporarily being out of focus during image acquisition. Although the results are comparable to the ones presented in Chapter 6, improvements in the protocol prevented vesicles from moving, while still not exposing them to an osmotic shock,

which allowed to normalise the fluorescence intensity reduction for each vesicle making the overall results much more consistent.

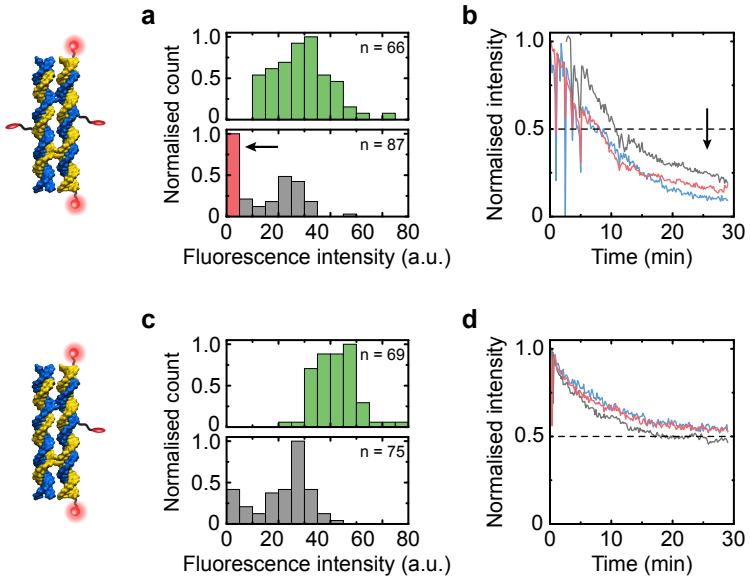

Fig. A.6 Results of dithionite reduction assays using an alternative protocol. (**a,c**) Absolute NBD fluorescence intensities before (green) and ~1 hour after (grey) dithionite addition of vesicles incubated with 2C (**a**) or 1C (**c**) DNA nanostructures. Arrow and red column highlight the shifted population down to no residual fluorescence. Counts were normalised to the maximum for each histogram. Number of analysed vesicles is denoted by n. (**b,d**) NBD fluorescence intensity traces from vesicles incubated with 2C and 1C nanostructures and imaging very 5 s over time. Values have been normalised to the initial intensity per vesicle and aligned to the onset of dithionite reduction. The shifted grey trace in the top graph is caused by the vesicle entering the field of view only some moments after dithionite addition.